

**2023 WORKSHOP ON
INNOVATIVE NANOSCALE
DEVICES AND SYSTEMS**

OUTRIGGER KONA RESORT AND SPA, KAILUA-KONA, HI, USA

DECEMBER 3 –8, 2023

BOOK OF ABSTRACTS

EDITORS:

JOHN CONLEY

BEREND JONKER

ALEXANDER BALANDIN

DEEP JARIWALA

JOSEF WEINBUB

STUART PARKIN

JAROSLOV FABIAN

AKIRA OIWA

MATTHEW GILBERT

STEPHEN GOODNICK

The 2023 Workshop on Innovative Nanoscale Devices and Systems (WINDS) is held December 3 – 8, 2023, at the Outrigger Kona Resort and Spa, Kailua-Kona, HI, USA.

WINDS is a week-long, international, and interactive workshop designed to explore the fundamental properties of nanoscale devices and applications thereof. In particular, WINDS provides a forum for material, device, and characterization as well as experimental and modeling researchers to interact.

The program consists of invited talks, regular talks, and poster presentations. All contributions have been peer-reviewed by the program committee.

This workshop is composed of morning and evening sessions, with afternoons free for ad hoc meetings to encourage extended interaction and discussion among participants. It is the successor of the original WINDS and the International Symposium on Advanced Nanodevices and Nanotechnology (ISANN), which were held on alternate years. WINDS itself began as an outgrowth of the successful Advanced Heterostructures Workshop, which has a long history dating from the 1980s.

WINDS 2023 is an AVS Sponsored Topical Conference, with financial support from the American Institute of Physics. The conference committee greatly appreciates their support.



**Sponsored
Topical
Conference**
www.avs.org

Applied Physics Letters

CONFERENCE CHAIRS

General Chair: **John F. Conley, Jr.** Oregon State University, USA

Europe Co-Chair: **Stuart Parkin**, Max-Planck Institute of
Microstructure Physics, Germany

Japan Co-Chair: **Akira Oiwa**, Osaka University, Japan

US Co-Chair: **Alexander Balandin**, Univ. California Los
Angeles, USA

**Communications
Chair:** **Josef Weinbub**, TU Wien, Austria

**Local arrangements
Chair:** **Stephen Goodnick**, University of Arizona, USA

PROGRAM COMMITTEE

Jaroslav Fabian	University of Regensburg, Germany
Claudia Felser	Max Planck Institute for Chemical Physics of Solids, Germany
David K. Ferry	Arizona State University, USA
Eric E. Fullerton	University of California, San Diego, USA
Matthew Gilbert	University of Illinois Urbana-Champaign, USA
Koji Ishibashi	RIKEN, Japan
Satoshi Iwamoto	University of Tokyo, Japan
David Janes	Purdue University, USA
Deep Jariwala	University of Pennsylvania, USA
Berend (Berry) Jonker	Naval Research Lab, USA
Victor Klimov	Los Alamos National Laboratory, USA
Valeria Lauter	Oak Ridge National Laboratory, USA
Tomoki Machida	University of Tokyo, Japan
Kazuhiko Matsumoto	Osaka University, Japan
Wolfgang Porod	University of Notre Dame, USA
Ian Sellers	University of Oklahoma, USA
Viktor Sverdlov	TU Wien, Austria
Igor Zutic	University at Buffalo, USA

Program

- General sessions are in Kaleiopapa Convention Center (KCC) Keauhou Rooms One and Two
- Registration will be open each day in the Kaleiopapa Convention Center Foyer starting on Sunday from 15:00-1800, Monday starting 60 minutes before the AM1 session, and remaining days starting 30 minutes before the AM1 session.

Sunday, December 3

15:00-18:00	Registration Kaleiopapa Convention Center Foyer
18:00-20:00	Gala Reception Pa'akai Point (Rays on the Bay if rain)

Monday, December 4

08:45-09:00	Opening remarks (Keauhou Two) John Conley (Oregon State University, General Chair) and Stephen Goodnick (Arizona State University, Local Arrangements)
-------------	--

MAM1: Keynote Session - Advanced devices (Keauhou Two) Session chair: John Conley (Oregon State University, USA)	
09:00-09:30 (Invited)	Michael Fuhrer (Monash University, Australia) <i>Two-Dimensional Topological Materials for Low-Voltage Transistors</i>
09:30-10:00 (Invited)	Xiangfeng Duan (UCLA, USA) <i>Towards Designable Artificial Quantum Solid with High-Order van der Waals Superlattices</i>
10:00-10:30 (Invited)	Tomoki Machida (University of Tokyo, Japan) <i>Subband electronics and symmetry engineering using van der Waals assembly of transition metal dichalcogenides</i>
10:30-11:00	Coffee break

MAM2: 2D Materials I - Light-Matter Interactions and van der Waals structures (Keauhou Two)	
Session chair: Berry Jonker (Naval Research lab)	
11:00-11:30 (Invited)	Dmitri Basov (Columbia University, USA) <i>Polaritons at van der Waals interfaces</i>
11:30-11:45	Jeffrey Schwartz (University of Maryland, USA) <i>Mid-Infrared, Near-Infrared, and Visible Nanospectroscopy of Hydrogen-Intercalated MoO₃</i>
11:45-12:00	Slava V. Rotkin (Pennsylvania State University, USA) <i>Optical imaging of low-dimensional materials beyond diffraction limit</i>
12:00-12:15	Momoko Onodera (University of Tokyo, Japan) <i>All-dry flip-over stacking of 2D crystal flakes using polyvinyl chloride</i>
12:15-12:30	Ramesh Kudalippalliyalil (University of Maryland, USA) <i>Probing Slow and Fast Transient Responses in Ultrafast-Excited Multilayer MoS₂ Flakes on a Microdisk Resonator</i>
12:30-19:00	Ad hoc session

MPM: Ferroelectrics & oxides (Keauhou Two)	
Session Chairs: John Conley (Oregon State University, USA) & David Henry (Sandia National Labs, USA)	
19:00-19:30 (Invited)	Jon Ihlefeld (University of Virginia, USA) <i>Phase Stabilizing Mechanisms to Achieve High-Performing Ferroelectric Hafnium Zirconium Oxide for Memory Applications</i>
19:30-19:45	M. David Henry (Sandia National Laboratory, USA) <i>Multilevel Resistance for Ta/Hf_{0.6}Zr_{0.4}O₂/TaN Ferroelectric Tunnel Junction Devices</i>
19:45-20:00	John F. Conley, Jr. (Oregon State University, USA) <i>Internal Photoemission (IPE) Spectroscopy Measurement of Conduction Band Offsets in Pristine and Poled Ferroelectric ALD HfZrOx Metal/Ferroelectric/Semiconductor (MFS) Devices</i>
20:00-20:15	Zirun Han (University of Pennsylvania, USA) <i>Multistate 20, 10, and 5 nm Al_{1-x}Sc_xN Ferroelectric Diodes</i>
20:15-20:30	Detlev Gruetzmacher (Forschungszentrum Jülich, Germany) <i>Ferroelectric Polarization Modulated Schottky Diodes Enabling Improved Neuromorphic Functionality</i>
21:00	Adjourn

Tuesday, December 5

TAM1: Topology & Chirality I (Keauhou One)	
Session Chairs: Jaroslav Fabian and Stuart Parkin	
09:00-09:30 (Invited)	Ron Naaman (Weizmann Institute, Rehovot, Israel) <i>The Electron's Spin and Chirality- a Miraculous Match</i>
09:45-10:00	Denis Kochan (Slovak Academy of Sciences, Bratislava, Slovakia) <i>Dirac-type charge carrier dynamics and Landau levels on curved surfaces</i>
10:00-11:00	Coffee break
10:30	Group photo by Aloha sign

TAM2: 2D Materials II - Advanced Device Applications (Keauhou Two)	
Session Chairs: Tomoki Machida and Berry Jonker	
09:00-09:15	Teja Potocnik (University of Cambridge, UK) <i>High throughput characterization and automated fabrication of lateral TMD heterostructure devices</i>
09:15-09:30	Kazuhiko Matsumoto (Osaka University, Japan) <i>Enhancement of Sensitivity for Influenza Virus Detection by Integrated Graphene FET Biosensor using Surface Potential Modulator</i>
09:30-09:45	Sanjaya Lohani (University of Illinois Chicago, USA) <i>Control variational quantum algorithm meets artificial intelligence</i>
09:45-10:00	Arisa Chiba (Institute for Materials Research, Japan) <i>Analysis of Wear Morphology of Concentrated Polymer Brushes under Various Conditions Using Coarse-Grained Molecular Dynamics</i>
10:00-10:15	Alexander Balandin (UCLA, USA) <i>Charge-Density-Wave Domain Depinning in Quasi-Two-Dimensional van der Waals Materials – Novel Functionality for Electronic Applications</i>
10:15-10:30	Denis Mamaluy (Sandia National Laboratory, USA) <i>Si:P δ-layer Resonant Tunnel Junctions for TeraHertz applications</i>
10:30	Group photo by Aloha sign
10:30-11:00	Coffee break

TAM3: Light-Matter (Keauhou One)	
Session Chairs: Kazuhiko Matsumoto and Igor Zutic	
11:00-11:15	Fei Yao (University at Buffalo, USA) <i>Two-dimensional van der Waals Materials and Their Mixed Low-Dimensional Hybrids for Clean Energy Applications</i>
11:15-11:30	Mahmoud Jalali Mehrabad (University of Maryland, USA) <i>Chiral optical nanocavity with atomically thin mirrors</i>
11:30-11:45	Kouichi Semba (National Institute of Information and Communications Technology, Japan) <i>Can the qubit frequency remain finite even under the very strong Lamb shift from an infinite number of electromagnetic modes?</i>
11:45-12:00	Hirofumi Shiraki (Osaka Research Institute of Industrial Science and Technology, Japan) <i>Superfluorescence-induced optical force in structural environment</i>
12:00-12:15	Shuva Mitra (University of Wisconsin, USA) <i>Enhanced optical nonlinearity in graphene nanomeshes</i>
12:15-12:45 (Invited)	Taishi Nishihara (Kyoto University, Japan) <i>Distinctive high-temperature light emission originating from one-dimensional excitons of carbon nanotubes</i>
12:45-13:00	Zizwe Chase (University of Illinois at Chicago, USA) <i>Strong Coupling of Cd3As2 Ribbons and Photons in a Terahertz Photonic Crystal Cavity</i>
13:00-19:00	Ad hoc session

TAM4: 2D Materials III - Quantum Science (Keauhou Two)	
Session Chair: Alexander Balandin (UCLA)	
11:00-11:30 (Invited)	Lee Bassett (University of Pennsylvania, USA) <i>Optically addressable single spins in hexagonal boron nitride</i>
11:30-11:45	Berry Jonker (Naval Research Laboratory, USA) <i>Single Photon Emitters in 2D Materials</i>
11:45-12:00	Herbert F. Fotso (University at Buffalo SUNY, USA) <i>Enabling Efficient Photon-Mediated Operations Between Spectrally Different Quantum Bits</i>
12:00-12:15	Igor Zutic (University at Buffalo, USA) <i>Fusion and Braiding of Majorana Zero Modes in Topological Planar Josephson Junctions</i>
13:00-19:00	Ad hoc session

TPM: Light-matter, Solar, Superconductivity (Keauhou Two)	
Session chairs: Victor Klimov and Stuart Parkin	
19:00-19:15	Victor I. Klimov (Los Alamos National Laboratory, USA) <i>Colloidal Quantum Dot Laser Diodes: Three Decades in the Making</i>
19:15-19:30	Stuart Parkin (Max Planck Institute of Microstructure Physics, Germany) <i>The Josephson Diode effect</i>
19:30-19:45	Bryan M. Wong (University of California-Riverside, USA) <i>Harnessing Laser-Driven Excitations to Control Polarization Switching in Ferroelectric Materials</i>
19:45-20:00	Gunuk Wang (Korea University, Korea) <i>Robust and skin-attachable memristor synaptic array for pattern and real-time finger motion recognition</i>
20:00-20:15	Sangita Regmi (University of Illinois Chicago, USA) <i>Data-informed prior for Bayesian state tomography</i>
20:15-22:30	Gerhard Klimeck (Purdue University, USA) <i>Bridging Communities in Chipshub on nanoHUB.org - From Advanced Materials and Devices to Full Chip Design</i>
20:30	Adjourn

Wednesday, December 6

WAM1: 2D Materials IV – Transport Properties (Keauhou Two)	
Session Chair: Berry Jonker (NRL)	
09:00-09:30 (Invited)	Daniel Rhodes (University of Wisconsin, USA) <i>Topologically Nontrivial States, Superconductivity, and Ferroelectricity in Few-layer 2M and Td-TMDs</i>
09:30-10:00 (Invited)	Elisabetta Paladino (University of Catania, Italy) <i>Noise mechanisms in short ballistic graphene Josephson junctions</i>
10:00-10:15	Huamin Li (University at Buffalo, USA) <i>Tunable Charge Transport at 2D/3D Integrated Interfaces</i>
10:15-10:30	Hui Zhao (University of Kansas, USA) <i>Generating free charge carriers in graphene in a van der Waals multilayer heterostructure</i>
10:30-11:00	Coffee break

WAM2: Modeling, Simulations, and Computations (Keauhou One)	
Session Chairs: Ian Sellers and Takahashi Ishikawa	
09:00-09:15	Ryoya Kano (Tohoku University, Japan) <i>Investigation of PtCo Alloy Catalyst Composition for Suppression of H₂O₂ Formation in Polymer Electrolyte Fuel Cell Anodes by First-Principles Calculations</i>
09:15-09:30	Shogo Fukushima (Tohoku University, Japan) <i>Molecular Dynamics Simulation on Stress Corrosion Cracking of High Entropy Alloys in Water Environment</i>
09:30-09:45	Jonah Shoemaker (Arizona State University, USA) <i>Influence of Deformation Potential Scattering on Impact Ionization and Critical Field in Ultra-Wide Bandgap Materials</i>
09:45-10:00	Xujiao Gao (Sandia National Laboratories, USA) <i>TCAD-Optimization Informed Modeling of Commercial SiC MOSFET</i>
10:00-10:15	Takashi Ishikawa (Tohoku University, Japan) <i>Reactive Molecular Dynamics Simulation for Revealing Splitting Phenomena and Mechanism of Ni Particles in Solid Oxide Fuel Cell Anode</i>
10:15-10:30	Ryutaro Kudo (Tohoku University, Japan) <i>Effect of Ethylene Glycol Additives on the Water Lubrication of Silicon Nitride - Molecular Dynamics Simulation with Neural Network Potential -</i>
10:30-11:00	Coffee break

WAM3: Spintronics & Quantum (Keauhou One)	
Session Chair: Wolfgang Porod and Akira Oiwa	
11:00-11:15	Akira Oiwa (Osaka University, Japan) <i>Shortcut to adiabaticity for adiabatic passage of a single electron spin</i>
11:15-11:30	Josef Weinbub (TU Wien, Austria) <i>Controlling Single Electrons by Non-Uniform Magnetic Fields</i>
11:30-11:45	Samuel Belling University of Wisconsin, USA <i>Scattering in the Wigner Equation</i>
11:45-12:00	Juan Mendez (Sandia National Laboratories, USA) <i>Atomic Precision Advanced Manufacturing (APAM) devices for quantum sensing</i>
12:00-12:15	Alexander Khitun (University of California – Riverside, USA) <i>Magnonic Combinatorial Memory</i>
12:15-12:30	Deepak K. Singh (University of Missouri, USA) <i>Magnetic charge quasi-particle dynamics for spintronics and reservoir computing applications</i>
12:30-12:45	Wolfgang Porod (University of Notre Dame, USA) <i>Interference-based computing using nonlinear spin waves</i>
13:00-18:30	Ad hoc session

WAM4: Topology & Chirality (Keauhou Two)	
Session Chair: Matt Gilbert	
11:00-11:30 (Invited)	Dieter Weiss (University of Regensburg, Germany) <i>Quantum transport in HgTe topological insulators and HgTe-superconductor hybrids</i>
11:30-11:45	Saurav Islam (Pennsylvania State University, USA) <i>Topological Hall effect in Dirac semimetal</i>
11:45-12:15 (Invited)	Kirstin Alberi (NREL, USA) <i>Epitaxial Topological Semimetal Thin Film Platforms for Device Applications</i>
12:15-12:45 (Invited)	Takis Kontos (ESN, Paris, France) <i>Quantum sensing of axion dark matter with a phase resolved haloscope</i>
13:00-18:30	Ad hoc session

18:30-21:00	Banquet at Bayview Grounds (Rays on the Bay if rain)
-------------	--

Thursday, December 7

RAM1: 2D Materials V - Strain & Thermal Properties (Keauhou Two)	
Session chair: Igor Zutic (YSUNY Buffalo, USA)	
09:00-09:30 (Invited)	Clivia M. Sotomayor Torres (Catalan Institute of Nanoscience and Nanotechnology, Spain) <i>Phonons in free-standing nanostructured membranes of MoSe and Si</i>
09:30-09:45	Davoud Adinehloo (University at Buffalo, USA) <i>Emergent Wetting Behavior and Strain Engineering in 2D Materials on Nanostructured Substrates</i>
09:45-10:00	Laleh Avazpour (University of Wisconsin, USA) <i>Modeling Long-Wavelength Phonon Dynamics for Enhanced Thermal Transport in Nanomaterials</i>
10:00-10:15	Fereshte Ghahari (George Mason University, USA) <i>Thermal probe of Fractional quantum Hall states in Bilayer graphene</i>
10:15-11:00	Coffee break

RAM2: 2D Materials VI - Magnetic & Spin-dependent Properties (Keauhou Two)	
Session Chair: Victor I. Klimov and Clivia Sotomayor Torres	
11:00-11:30 (Invited)	Scott Crooker (Los Alamos National Lab, USA) <i>Asymmetric proximity interactions and chiral quantum light generation in 2D magnet/semiconductor van der Waals heterostructures</i>
11:30-11:45	Igor Zutic (University of Buffalo) <i>Terahertz Spin-Light Coupling in Proximitized Dirac Materials</i>
11:45-12:00	Fariborz Kargar (UCLA, USA) <i>Electron Transport in Vertical Quasi-Two-Dimensional Antiferromagnetic Semiconductor Devices</i>
12:00-12:15	Jaroslav Fabian (University of Regensburg, Germany) <i>Correlated phases in proximitized (untwisted) graphene multilayers</i>
12:15-12:30	Gerhard Klimeck (Purdue University, USA) <i>Materials screening for spin orbit torque in two-dimensional van der Waals heterostructures</i>
12:30-12:45	Maciej Kalka (AGH University of Krakow, Poland) <i>Phase-space approach for the topological phase transitions in silicene</i>
12:45-19:00	Ad hoc session

RPM Rapid Poster Talks (Keauhou One)	
Session Chair: Alex Balandin and Jaroslav Fabian	
19:00-19:10	Alexander Balandin (UCLA, USA) <i>Publishing in APL</i>
19:10-19:15	<i>Intro to poster talks</i>
19:15-19:20	Bonhwi Gu (Sungkyunkwan University, Korea) <i>Novel probe metal pads design for IC test in DRAM</i>
19:20-19:25	Hyojin Park (Sungkyunkwan University, Korea) <i>The mask stack efficiency for improving gate oxide reliability of DRAM</i>
19:25-19:30	Izabella Wojciechowska (AGH University of Science and Technology, Poland) <i>Charge-to-spin conversion in twisted graphene on transition metal dichalcogenides</i>
19:30-19:35	Piotr Pigon (AGH University of Science and Technology, Poland) <i>Electronic and Topological Properties of a Topological Insulator Thin Film Sandwiched between Ferromagnetic Insulators</i>
19:35-19:40	Shahabaj Mundaganur (University at Buffalo, USA) <i>Asymmetrically Engineered Nanoscale Transistors for On-Demand Sourcing of Terahertz Plasmons</i>
19:40-19:45	Kota Jojima (Tohoku University, Japan) <i>Coarse-grained molecular dynamics simulation study on the dispersion mechanism of organically modified nanoparticles in mixed solvent - Analysis of nanoparticle/solvent/nanoparticle interface structure</i>
19:45-19:50	Yasushi Shoji (National Institute of Advanced Industrial Science and Technology, Japan) <i>2.1 eV AlGaInP photovoltaic device for use in radiation environment</i>
19:50-21:00	<i>Poster discussion and drinks</i>
21:00	Adjourn

Friday, December 8

FAM1: 2D Topology & Chirality (Keauhou Two)	
Session Chair: Matthew Gilbert and Valeria Lauter	
09:00-09:30 (Invited)	Claudia Felser (Max-Planck Institute Dresden, Germany) <i>Chirality and Topology</i>
09:30-09:45	Masashi Kawasaki (University of Tokyo, Japan) Proximity effect of an emergent field from spin ice in an oxide heterostructure
09:45-10:00	Luis Jauregui (University of California - Irvine, USA) <i>Dominant Surface State Transport in HfTe5 thin films</i>
10:00-10:15	Valeria Lauter (Oak Ridge National Laboratory, USA) <i>Quasi-two-Dimensional Chromium Telluride: Thickness Dependent magnetism and Strain-tunable Berry curvature</i>
10:15-10:30	Wenyao Liu (Boston College, USA) <i>Evidence of 1D propagating topological superconducting mode along edge of Fe(Te,Se)</i>
10:30-11:00	Coffee break

FAM2: Advanced Devices & Neuromorphic (Keauhou Two)	
Session Chair: Steve Goodnick and Marius Orłowski	
11:00-11:15	Viktor Sverdlov (TU Wien, Austria) <i>Multi-bit Operation in an MRAM Cell with a Composite Free Layer</i>
11:15-11:30	Marius Orłowski (Virginia Tech, USA) <i>Electron Tunneling between Vibrating Cu Atoms in a Cu Filament in a Neuromorphic ReRAM Device</i>
11:30-11:45	Saulius Marcinkevicius (KTH Royal Institute of Technology, Sweden) <i>Experimental evidence of a novel mechanism of hole injection into quantum wells of long wavelength GaN-based LEDs</i>
11:45-12:00	Dong Sik Park (Sungkyunkwan University, Korea) <i>New Method for Improving AI Void and Refresh Characteristics in sub 25nm DRAM</i>
12:00-12:15	Minhyung Kim (Sungkyunkwan University, Korea) <i>A novel technology for edge patterning in processes using SOH masks in sub-20nm DRAM</i>
12:30	Closing Remarks / Conference Ends

Two-Dimensional Topological Materials for Low-Voltage Transistors

Michael S. Fuhrer^{1,2}

¹*School of Physics and Astronomy, Monash University, Victoria 3800, Australia*

²*ARC Centre of Excellence in Future Low-Energy Electronics Technologies, Monash University, Victoria 3800, Australia*
michael.fuhrer@monash.edu

Keywords: 2d materials, topology

The impending end of Moore's Law has prompted a search for a new computing technology with vastly lower energy consumed per operation than silicon CMOS. The recent discovery of topological phases of matter offers a possible solution: a "topological transistor" in which an electric field tunes a two-dimensional material from a conventional insulator "off" state to a topological insulator "on" state, in which topologically protected edge modes carry dissipationless current (Fig. 1). This electric field-tuned topological transition has advantages over current MOSFETs: (1) Due to the combined effects of Rashba spin-orbit interaction and electric field control of the bandgap, the topological transistor may switch at lower voltage, overcoming "Boltzmann's tyranny"[1] (Fig. 2), and (2) true electric field-controlled switching opens the possibility of using the full power of negative capacitance structures as an electric field amplifier to achieve further reductions in switching voltage[2] (Fig. 3). We have studied thin films of Na₃Bi grown in ultra-high vacuum by molecular beam epitaxy as a platform for topological electronic devices. When thinned to a few atomic layers Na₃Bi is a large gap (>300 meV) 2D topological insulator, and electrical transport measurements demonstrate that the current is carried by helical topological edge modes over millimeter-scale distances[3]. Electric field applied by proximity of an STM tip can close the bandgap completely and reopen it as a conventional insulator[4] demonstrating the basis of electric field-switched topology (Fig. 4).

[1] M. Nadeem, *et al.*, *Nano Letters* **21**, 3155–3161 (2021).

[2] M.S. Fuhrer, *et al.*, *Proceedings of the 2021 International Electron Devices Meeting*, pp. 38.2.1-38.2.4 (2021).

[3] C. Liu, *et al.*, *Nano Letters* **9**, 6306 (2020).

[4] J.L. Collins, *et al.*, *Nature* **564**, 390-394 (2018).

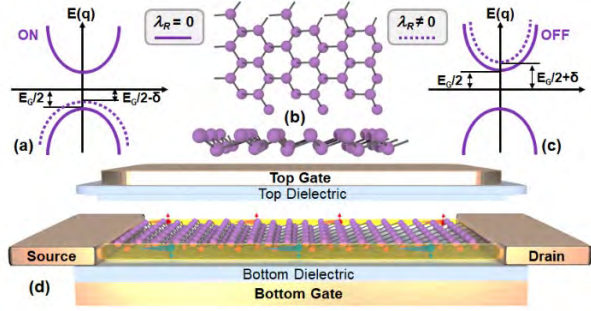


Fig.1: Topological quantum field effect transistor. In the absence of a gate electric field, a QSH insulator hosts dissipationless helical conducting channels with a minimum value of the quantized conductance $2 e^2/h$ (ON state of TQFET (a)). When the gate electric field exceeds a threshold limit, the thin QSH insulator layer (staggered honeycomb lattice (b)) enters into the trivial regime, in which the minimum value of the conductance drops to zero (OFF state of TQFET (c)). Such electric field switching is accompanied by the topological quantum field effect which enhances the topological phase transition driven by a gate electric field and reduces the subthreshold swing (a, c). Here, δ represents the shift in nontrivial (a) and trivial (c) band gap E_G due to topological quantum field effect. (d) Geometry of topological quantum field effect transistor. Adapted from [1].

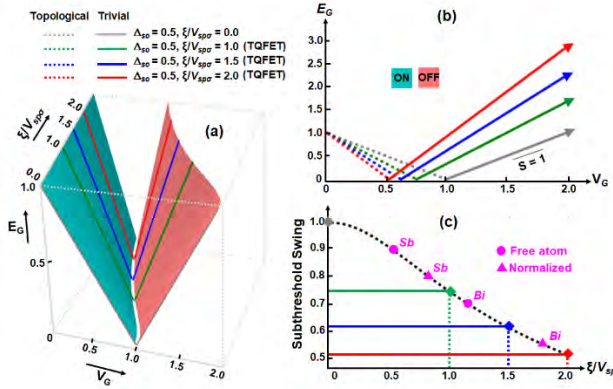


Fig.2: Topological quantum field effect on band gap, threshold gate voltage, and subthreshold swing. The green, blue, and red lines represent the variation of band gap (a), threshold gate voltage (b), and subthreshold swing (c) corresponding to atomic spin-orbit interaction (SOI) and Slater-Koster parameter ratio $\zeta/V_{spo} = 1, 1.5, 2$ respectively which encodes the topological quantum field effect. (a) Nontrivial (trivial) bulk band gap E_G decreases (increases) sharply with increasing ζ/V_{spo} . Accordingly, the threshold gate voltage (b) and subthreshold swing (c) decreases with increasing ζ/V_{spo} . Magenta circles (triangles) represent the subthreshold swing for TQFET based on antimonene and bismuthene with free atomic (normalized) SOI. Adapted from [1].

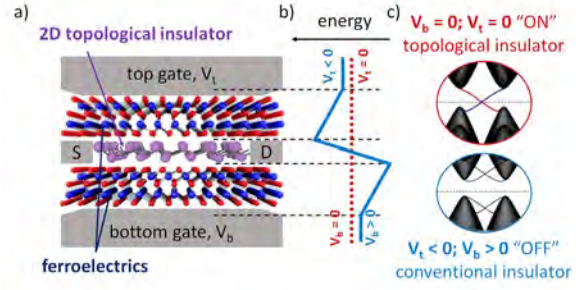


Fig.3: Schematic of negative capacitance topological quantum field-effect transistor. (a) Structure of the device. (b) Electrostatic potential energy as a function of distance across the device in “on” (red) and “off” (blue) states. (c) Band diagrams in “on” (topological insulator, red) and “off” (conventional insulator, blue) states. Adapted from [2].

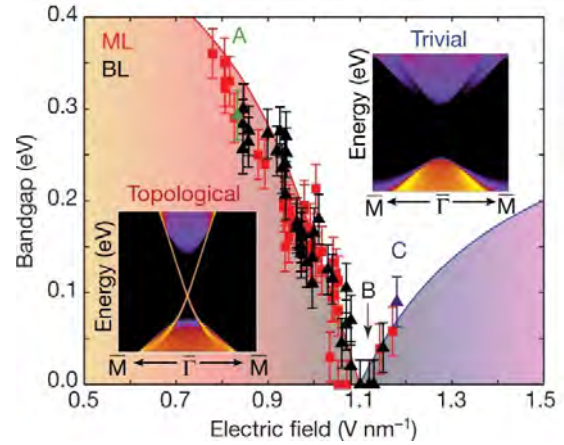


Fig.4: Electric field dependence of the bandgap in monolayer (ML; red) and bilayer (BL, black) Na_3Bi , showing switching from topological insulator (orange shading) to trivial insulator (purple shading). The edge-projected electronic spectrum from density functional theory calculations are shown as insets for Na_3Bi monolayer without (lower right) and with (upper left) electric field. Adapted from [4].

Towards Designable Artificial Quantum Solid with High-Order van der Waals Superlattices

Xiangfeng Duan¹

¹*Department of Chemistry and Biochemistry, California NanoSystems Institute, University of California Los Angeles, Los Angeles, CA, USA*
xduan@chem.ucla.edu

Keywords: 2d materials, quantum materials, nanostructures

The advent of two-dimensional atomic crystals (2DACs) and van der Waals heterostructures (vdWHs) has inspired a new thinking on heterostructure construction beyond the limits of lattice matching requirement [1]. However, the vdWHs explored to date have been largely limited to relatively simple systems with a small number of building blocks. The preparation of high-order vdW superlattices with a larger number of alternating units is exponentially more challenging due to the limited yield and scalability of the commonly used exfoliation-and-restacking strategy. Here I will discuss strategies to create high-order vdW superlattices (vdWSLs) consisting alternating 2D crystalline atomic layers of diverse electronic properties and/or self-assembled molecular layers of designable chemical motifs and structural topologies. First, by exploiting a capillary-force-driven rolling-up process, we show a series of synthetic VdWHs can be transformed into high-order vdWSLs with alternating atomic layers of widely variable material compositions, electronic band offset dimensions, chirality and topology [2]. Alternatively, we further introduce a molecular intercalation approach to prepare a new family of hybrid superlattices consisting of alternating layers of covalently bonded 2D atomic layers and self-assembled molecular layers, which opens the door to exploit highly versatile molecular design strategies to tailor solid-state materials, enabling artificial materials with designable structural motifs and tunable electronic and optical properties [3,4]. We will particularly highlight a recent example of a new class of chiral molecular intercalation superlattices that exhibit robust chiral-induced spin selectivity and unconventional superconducting ordering parameter [5,6]. The formation of high-order vdW superlattices defines a rich artificial materials platform to unlock previously inaccessible physical limits and enable new device concepts beyond the reach of the existing materials.

[1] Y. Liu, Y. Huang and X. Duan. Van der Waals integration before and beyond two-dimensional materials. *Nature* **567**, 323-333 (2019) (DOI: 10.1038/s41586-019-1013-x)

[2] B. Zhao *et al.* High-order superlattices by rolling up van der Waals heterostructures. *Nature* **591**, 385–390 (2021). (DOI: 10.1038/s41586-021-03338-0).

[3] C. Wang, *et al.* Monolayer atomic crystal molecular superlattices. *Nature* **555**, 231-236 (2018) (DOI: 10.1038/nature25774).

[4] B. Zhou *et al.* A chemical-dedoping strategy to tailor electron density in molecular-intercalated bulk monolayer MoS₂. *Nat. Synthesis* (2023) (DOI: 10.1038/s44160-023-00396-2).

[5] Q. Qian *et al.* Chiral molecular intercalation superlattices. *Nature*, **606**, 902-908 (2022). (DOI: 10.1038/s41586-022-04846-3).

[6] Z. Wan *et al.* Signatures of Chiral Superconductivity in Chiral Molecule Intercalated Tantalum Disulfide. *arXiv* (2023). (arXiv:2302.05078).

Subband electronics and symmetry engineering using van der Waals assembly of transition metal dichalcogenides

Tomoki Machida

Institute of Industrial Science, University of Tokyo, Tokyo 153-8505, Japan
tmachida@iis.u-tokyo.ac.jp

Keywords: 2d materials, quantum transport

Few-layer transition metal dichalcogenides (TMDs) exhibit subband quantization induced by the out-of-plane quantum confinement of the wavefunctions, i.e., a few-layer TMDs are naturally-formed quantum wells (QWs). Using momentum-conserved resonant tunneling, we investigate the QW states in 3L-WSe₂/h-BN/3L-WSe₂ van der Waals (vdW) tunnel junctions with twist angles θ_{tunnel} . Current–voltage characteristics exhibit multiple resonant tunneling peaks whose positions shift as θ_{tunnel} was varied over the 0–60° range. These results were in good agreement with calculated angular dispersion in conduction band in 3L-WSe₂, which indicated the presence of a spin-polarized subband crossing and a saddle point. Our twist-controlled resonant tunneling approach overcomes the difficulties associated with momentum-resolved electronic structure measurements and reveals the unique vdW-QW states in the conduction band of multi-layer WSe₂.

We demonstrate that the spatial inversion symmetry and hence the spin splitting in band structure can be controlled by van der Waals (vdW) assembly with a controlled twist angle. Twisted bilayer WTe₂ with twist angle $\theta_{\text{twist}} = 0^\circ$ and 180° are investigated. The intensity of second harmonic generation changes by two orders of magnitude depending on θ_{twist} , indicating that 1L WTe₂ + 1L WTe₂ (0°) possesses the spatial inversion symmetry, whereas 1L WTe₂ + 1L WTe₂ (180°) lacks the inversion symmetry. The electronic structure of the 1L WTe₂ + 1L WTe₂ are significantly modulated by θ_{twist} . The spin splitting emerges when $\theta_{\text{twist}} = 180^\circ$ as a consequence of the broken inversion symmetry. The effect induced by controlling the symmetry is quite robust with respect to θ_{twist} fluctuation and inhomogeneity, suggesting the feasibility of pursuing new physical phenomena in 2D materials based on symmetry engineering.

Finally, we demonstrate 3D manipulation of 2D material flakes, such as sliding, rotating, and folding. A PVC/PDMS micro-dome structure functions as a point-of-contact manipulator for 2D material flakes. The adhesion between the PVC polymer and 2D material is fully tunable with temperature. Our method could facilitate the expansion of van der Waals heterostructure fabrication technology for constructing more complex vdW structures.

- [1] K. Takeyama, R. Moriya, S. Okazaki, Y. Zhang, S. Masubuchi, K. Watanabe, T. Taniguchi, T. Sasagawa, and T. Machida, *Nano Lett.* **21**, 3929 (2021).
- [2] K. Kinoshita, R. Moriya, S. Okazaki, Y. Zhang, S. Masubuchi, K. Watanabe, T. Taniguchi, T. Sasagawa, and T. Machida, *Nano Lett.* **22**, 4640 (2022).
- [3] K. Kinoshita, R. Moriya, S. Okazaki, Y. Zhang, S. Masubuchi, K. Watanabe, T. Taniguchi, T. Sasagawa, and T. Machida (in press).
- [4] Y. Zhang, K. Kamiya, T. Yamamoto, M. Sakano, X. Yang, S. Masubuchi, S. Okazaki, K. Shinokita, T. Chen, K. Aso, Y. Y.-Takamura, Y. Oshima, K. Watanabe, T. Taniguchi, K. Matsuda, T. Sasagawa, K. Ishizaka, and T. Machida, *Nano Lett.* **23** (in press).
- [5] Y. Wakafuji, R. Moriya, S. Masubuchi, K. Watanabe, T. Taniguchi, and T. Machida, *Nano Lett.* **20**, 2486 (2020).

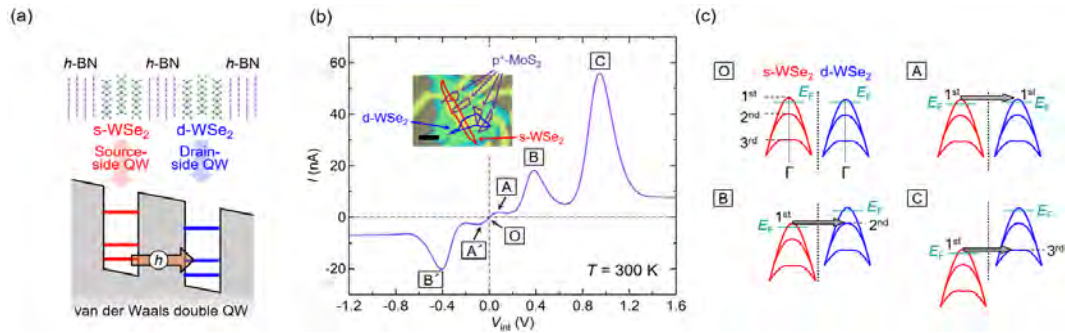


Fig. 1 Resonant tunneling through quantized subbands in multi-layer WSe₂.

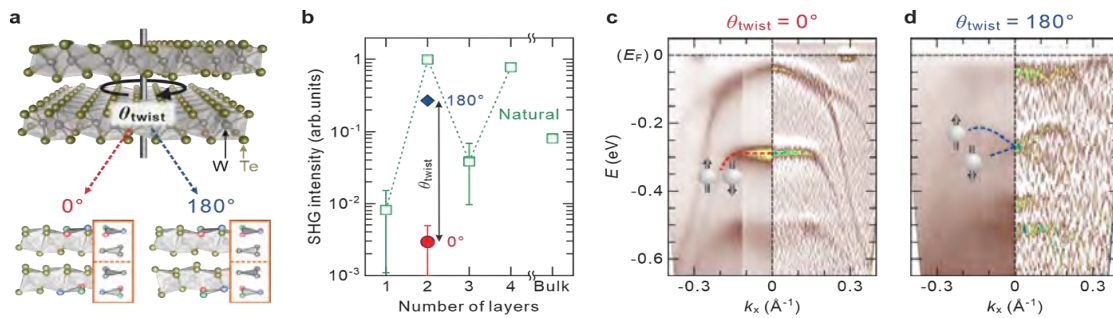


Fig. 2 Control of inversion symmetry in twisted bilayer WTe₂.

Polaritons at van der Waals interfaces

D.N. Basov

Columbia University, New York, New York USA <https://infrared.cni.columbia.edu>

Keywords: 2d materials, plasmonics

Van der Waals (vdW) interfaces are emerging as a versatile platform to control and investigate electronic, magnetic and optical properties of quantum materials. I will discuss nano-optical studies of charge transfer across an interface of vdW materials with different work functions[1]. I will also discuss an interface of two vdW insulators MoO₃ and hBN revealing strong polaritonic coupling and negative refraction [2].

[1] Kim et al. Nature Materials 22, 838 (2023)

[2] Sternbach et al. Science 379, 555 (2023)

Mid-Infrared, Near-Infrared, and Visible Nanospectroscopy of Hydrogen-Intercalated MoO₃

Jeffrey J. Schwartz^{1,2,3,4}, Sergiy Krylyuk⁵, Devon S. Jakob²,
Albert V. Davydov⁵, and Andrea Centrone²

¹*Laboratory for Physical Sciences, College Park, Maryland 20740, United States*

²*Physical Measurement Laboratory, National Institute of Standards and Technology,
Gaithersburg, Maryland 20899, United States*

³*Institute for Research in Electronics and Applied Physics, University of Maryland,
College Park, Maryland 20742, United States*

⁴*Department of Electrical and Computer Engineering, University of Maryland,
College Park, Maryland 20742, United States*

⁵*Material Measurement Laboratory, National Institute of Standards and Technology,
Gaithersburg, Maryland 20899, United States*

jjschwa@lps.umd.edu

Keywords: 2d materials, light-matter interactions

Control over the local chemical composition and spatial heterogeneities in nanomaterials provides a means to impart new functions and to tailor their properties in many applications. For two-dimensional (2D) van der Waals materials, intercalation is one useful strategy to exert such control, by inserting or removing atomic, molecular, or ionic species in their lattice. For example, hydrogen intercalation and the creation of oxygen vacancies in MoO₃ locally increase electrical conductivity, optical absorption, and electrochemical activity, thereby enabling its use in electrochromic, photochromic, catalytic, and energy storage applications. Here, after thermal annealing of MoO₃ crystals in H₂, we show that the resulting hydrogen molybdenum bronzes and/or oxygen-deficient, substoichiometric molybdenum oxides (MoO_{3-δ}) display highly heterogeneous, optically dark, topographically protruding patterns at the nanoscale. We leverage the nanoscale resolution of photothermal induced resonance absorption spectra and maps in the visible, mid-, and near-infrared⁵ to characterize these features that are spectrally distinct from the surrounding regions. Subsequent annealing in O₂ enables partial recovery of the initial Mo:O stoichiometry, though some absorption peaks linked to intercalation persist. The high-resolution imaging and spectroscopic analyses employed here enable precise measurements of nanoscale heterogeneities that foster the adoption of 2D and other materials in advanced applications.

Optical imaging of low-dimensional materials beyond diffraction limit

Slava V. Rotkin

Materials Research Institute and Department of Engineering Science & Mechanics, The Pennsylvania State University, Millennium Science Complex, University Park, PA 16802, USA

Recent success in synthesis of new two- and one-dimensional materials (21DM) (including graphene, TMDCs, heteronanotubes, MXenes and atomic polar metals), was followed by a large number of works exploring their optical properties and seeking for novel applications in quantum technologies, biosensing, energy and computing. Atomically thin 21DMs have an ultimate surface-to-volume ratio. While it helps biosensing, electronics and other applications, any surface non-uniformities drastically increase variability of materials properties. Modulation of optical properties at the nanometer scale due to atomic impurities or adsorbates or defects, wrinkles or ruptures, lattice mismatch, doping and work function variation is important to be able to control. However, even before developing a synthetic approach to mitigate such a problem, appropriate characterization tools are needed to detect such a modulation and study it.

In this talk, several methods for nanoscale (sub-diffractive) optical characterization will be presented. Correlated multiplexed (multidimensional) optical imaging technique will be introduced and demonstrated using a few examples: a vertical heterostructure comprised of monolayer graphene and single layer flakes of MoS₂,^[1] heteronanotubes comprised of radial heterostructure with carbon core and hBN/MoS₂ shell,^[2] glass nanoindentations,^[3] rhombohedral/hexagonal stacked graphene,^[4] and heterostructures of graphene/Ag/SiC atomic layers^[5]. The correlation of several information channels, including scattering Scanning Near-field Optical Microscopy (sSNOM) and microRaman^[6,7], allows one to obtain information on, e.g., local Fermi level and strain tensor components^[1] or distribution of chemical bonds in a glassy material^[3].

Acknowledgement: This work is partially supported by NSF DMR-2011839 and DMR-2039351.

- | | |
|---|--|
| 1. T. Ignatova, et.al, ACS Nano 2022, 16 , 2598. | 5. SV. Rotkin, in <i>Proc. of WINDS</i> , 2019, (12/1-6, HI, USA). |
| 2. Y. Feng, et.al, ACS Nano 2021, 15 , 5600. | 6. C. Neumann, et.al, Nature Comm 2015, 6 , 8429. |
| 3. H. He, et.al, Acta Materialia 2021, 208 , 116694. | 7. T. Ignatova, et.al, J Mat Chem B 2017, 5 , 6536. |
| 4. S. Bachu, et.al, ACS Nano 2023, 17 , 12140. | |

All-dry flip-over stacking of 2D crystal flakes using polyvinyl chloride

Momoko Onodera¹, Yusai Wakafuji¹, Taketo Hashimoto,² Satoru Masubuchi,¹ Rai Moriya,¹ Yijin Zhang,¹ Kenji Watanabe,³ Takashi Taniguchi,^{1,4} Tomoki Machida^{1,2}

¹*Institute of Industrial Science, University of Tokyo, Tokyo, Japan*

²*Riken Technos Corporation, Japan*

³*Research Center for Functional Materials, NIMS, Japan*

⁴*International Center for Materials Nanoarchitectonics, NIMS, Japan*

Keywords: 2d materials

Development of transfer technique of 2D materials is highly important for both fundamentals and applications of 2D materials. Recently, versatile manipulation—including sliding, folding, and peeling—of 2D flakes has been demonstrated using polyvinyl chloride (PVC) [1]. The key point of the manipulation was the strong adhesion of PVC, which enabled the control of the entire 2D flake only with a small part of the flake contacted by PVC. Here, we evaluate the adhesion of PVC to 2D flakes using a novel approach, distinguishing the effects of the surface and edge of the 2D flakes on the pickup force. We prepared a PVC/ poly(dimethylpolysiloxane) (PDMS) stamp on a glass slide for 2D flake pickup. We conducted pickup test of circular-shaped h-BN flakes varying contact region and contact area of PVC stamp (Figure 1a-c), and the result is summarized in Figure 1d. In this plot, we can identify the pickup region of PVC/PDMS stamp, in which pickup is likely to occur (yellow-shaded region). The feature of PVC/PDMS stamp is that it can pick up h-BN flakes by the surface contact alone, indicating that PVC is strongly adhesive to the 2D flakes surface [2].

Next, we show that the pickup and release temperature of PVC is modulated by the PVC film thickness. To make PVC/PDMS stamp, a PVC layer was fabricated from commercially available PVC powder. A plasticizer (dioctyl phthalate, DOP) was mixed with PVC powder, and the mixture was dissolved in cyclohexanone. The PVC/cyclohexanone solution was coated on a glass slide and solidified on a hotplate. The PVC layer was then laid on a dome-shaped piece of PDMS on a glass slide. We found that the pickup and release temperatures of h-BN flakes, T_{pickup} and T_{release} , of PVC decrease by the PVC film thickness rather than the DOP content. Utilizing the difference in the T_{pickup} and T_{release} , 2D flakes can be transferred from thick to thin PVC films (Figure 2), which we call polymer-to-polymer transfer. This is highly useful for device fabrication because it enables us to turn over van der Waals heterostructures [3].

[1] Y. Wakafuji *et al.*, Nano Lett. **20**, 2486 (2020).

[2] Y. Wakafuji, M. Onodera *et al.*, npj 2D Mater Appl **6**, 44 (2022).

[3] M. Onodera *et al.*, Sci. Rep. **12**, 21963 (2022).

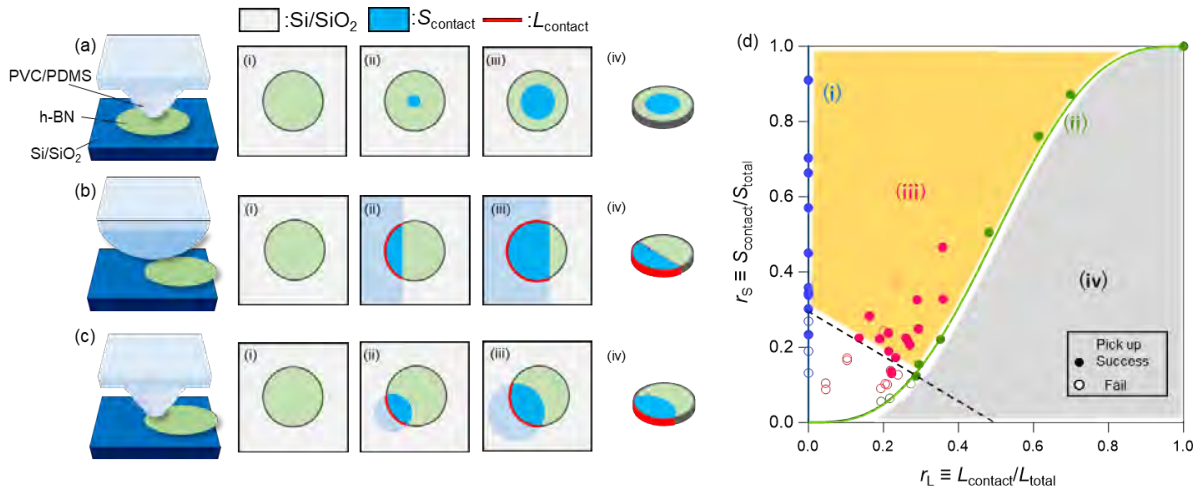


Figure 1. (a) Pickup by surface contact alone using the PVC/triple PDMS dome. (b) Pickup by edge contact with minimal surface contact area using the PVC/semicylindrical PDMS, where the relationship between r_s and r_L is given by Equation (1). (c) Pickup by edge and surface contact using the PVC/triple PDMS dome. The sky blue and red regions in (i)–(iv) indicate the areas of surface contact and edge contact between the PVC and *h*-BN, respectively. (d) Plot of pickup test results versus relative contact surface area and relative contact edge length. Closed circles indicate successful pickups and open circles indicate unsuccessful pickups. The blue, green, and red colors correspond to the pickup by (i) surface contact alone, (ii) mainly edge contact, and (iii) edge and surface contact, respectively. The yellow shaded region is the region in which pickup occurs (the pickup region), and the white region is the region in which pickup is impossible. The gray-shaded region (iv) is the experimentally unfeasible region.

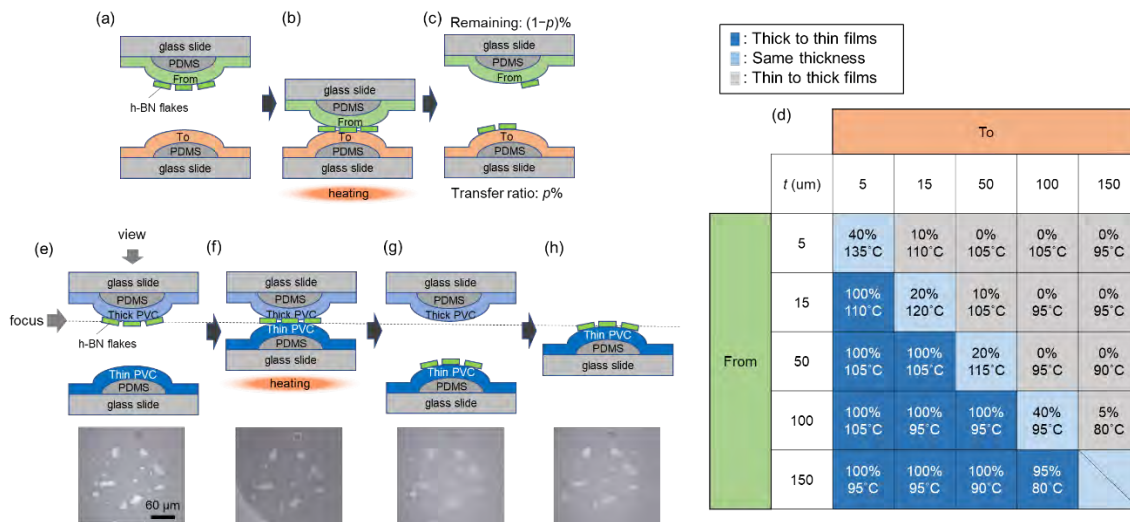


Figure 2. (a-c) Schematics of the polymer-to-polymer transfer test. (a) The from-stamp with *h*-BN flakes was set above the to-stamp. (b) The from- and to-stamps were contacted and (c) detached at a certain temperature, and the transfer ratio of *h*-BN flakes and the stage temperature were recorded. (d-g) Schematics and photographs of the polymer-to-polymer transfer of *h*-BN flakes. (d) A thin PVC/PDMS stamp with *h*-BN flakes was set above the thick PVC/PDMS stamp, and the two stamps were (e) contacted and (d) detached at a certain temperature. (g) *h*-BN flakes were transferred to the thick PVC/PDMS stamp. The dotted line shows the focus of the photographs. (h) Result of the polymer-to-polymer transfer test.

Probing Slow and Fast Transient Responses in Ultrafast-Excited Multilayer MoS₂ Flakes on a Microdisk Resonator

Ramesh Kudalippallyalil^{1,2*}, Gyan Prakash^{1,2}, Thomas. E. Murphy¹ and Karen E. Grutter²

¹*Institute for Research in Electronics & Applied Physics, University of Maryland,
College Park, MD 20742, USA*

²*Laboratory for Physical Sciences, College Park, MD 20740, USA,*

**rameshk@lps.umd.edu*

Keywords: 2D materials, light-matter interactions.

Molybdenum disulphide (MoS₂), a prominent member of the transition metal dichalcogenide (TMDC) family, stands out as one of the most extensively explored two-dimensional (2D) materials. It possesses layer-dependent nonlinear characteristics and carrier dynamics [1]. The absorption, photoconductivity, and photoluminescence properties of MoS₂ can be tuned with the number of layers, making it suitable for many high-performance integrated optoelectronics applications [2]. However, ultrafast carrier dynamics in MoS₂ flakes have been most commonly studied using Z-scan and transient absorption spectra measurements at normal incidence [3, 4], but these methods do not clearly reveal how the material would respond when incorporated into a guided-mode integrated photonic device. In this work, we exfoliate multi-layer flakes of MoS₂ onto a SiN microdisk resonator. Using ultrafast laser pulses of 50 fs duration and wavelength 800 nm, we photo-excite these MoS₂ flakes at normal incidence and use a second, continuous-wave probe laser (~1550 nm) coupled into the SiN resonator to monitor its transient response. We observe pump fluence-dependent transient blue and red shift in the resonance wavelength, each with distinctly different time-scales. We attribute the blue-shift to carrier dynamics in MoS₂ (~ps) and the red-shift to the carrier-induced thermo-optic effect at MoS₂/SiN interface (μs). Leveraging a high-Q integrated photonic resonator significantly enhances both the sensitivity and precision of optical property measurement and facilitates insights into carrier dynamics within these atomically thin materials. Such devices show promise as high-efficiency optical modulators or switches.

[1] Chaves, A., et al. npj 2D Materials and Applications 4.1, 29 (2020).

[2] Tian, He, et al., Nano Research 9, 1543-1560 (2016).

[3] N. Dong et al., Sci. Reports 5, 1–10 (2015).

[4] S. Das et al., Light. Sci. & Appl. 10, 1–9 (2021).

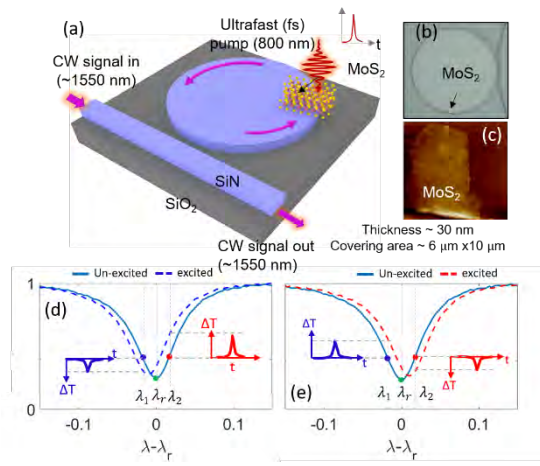


Fig. 1: (a) Schematic of the studied device, (b) microscope image of the fabricated resonator with a multi-layer MoS₂ flake, (c) AFM image of the MoS₂ flake, (d) and (e) represent the blue-shifted and red-shifted spectrum, respectively, before and after UF excitation. The transient responses at λ_1 and λ_2 are also shown for reference.

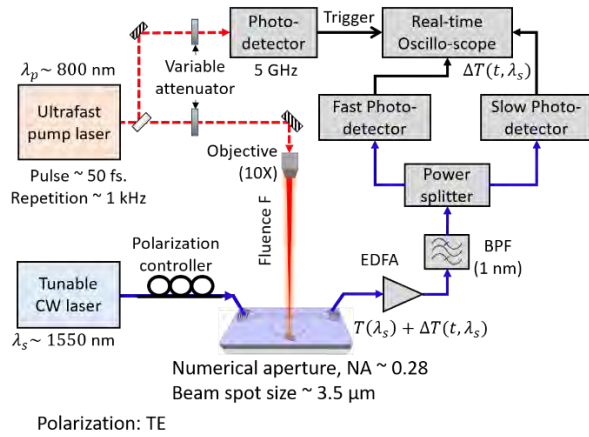


Fig. 2: Ultrafast characterization setup. EDFA- Erbium doped fiber amplifier, BPF – band pass filter. The bandwidth of fast and slow detectors are 10 GHz and 10 MHz, respectively.

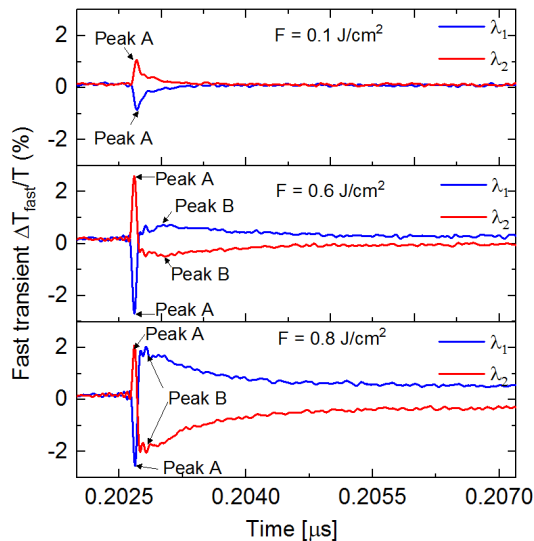


Fig. 3: Fluence (F) dependent differential transient signal ($\Delta T/T$) recorded using the fast photo-receiver at two symmetric wavelengths (λ_1, λ_2) near resonance (λ_r). Peak A and peak B represent the two peaks of the transient signal.

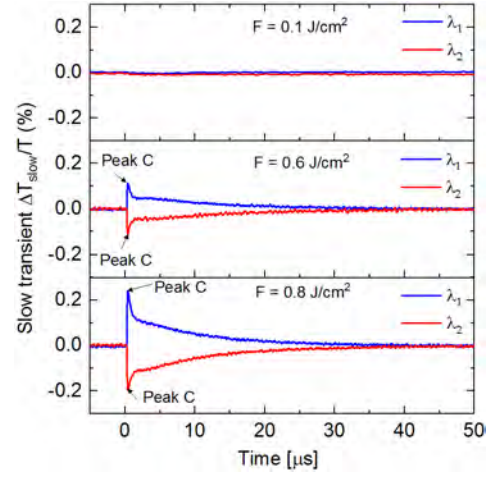


Fig. 4: Fluence (F) dependent differential transient signal ($\Delta T/T$) recorded using the slow photo-receiver at two symmetric wavelengths (λ_1, λ_2) near resonance (λ_r). Peak C represents the peak of the transient signal.

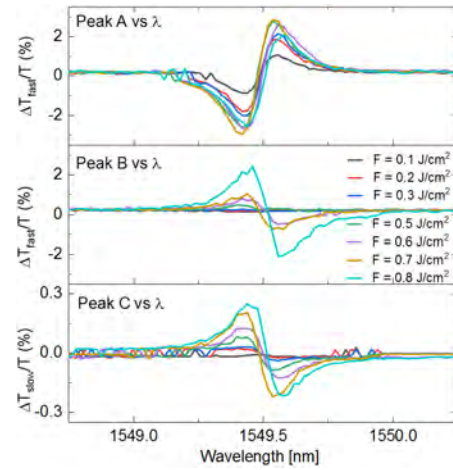


Fig. 5: Peak of differential transmission versus signal (CW) wavelength across the resonance for different fluence levels.

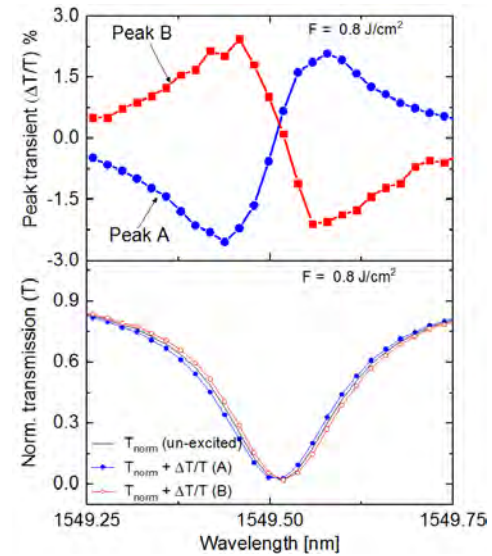


Fig. 6: (Top) Peaks of the fast (peak A) and slow (peak B) transients corresponding to the maximum fluence $F = 0.8 \text{ J/cm}^2$, and (bottom) the resultant spectral shifts, which is extracted by adding the peaks with the un-excited transmission (black).

Phase Stabilizing Mechanisms to Achieve High-Performing Ferroelectric Hafnium Zirconium Oxide for Memory Applications

S.T. Jaszewski,¹ S.S. Fields,¹ and J.F. Ihlefeld^{1,2}

¹*Department of Materials Science and Engineering, University of Virginia, Charlottesville, Virginia 22904, USA*

²*Charles L. Brown Department of Electrical and Computer Engineering, University of Virginia, Charlottesville, Virginia 22904, USA*
jihlefeld@virginia.edu

Keywords: oxides and ferroelectrics

Ferroelectric hafnia is positioned to serve as low energy, non-volatile computing memory elements as well as in compute-in-memory applications owing to its inherent large scale semiconductor fabrication compatibility and ability to display considerable ferroelectric responses at nano-scale film thickness. A challenge preventing the implementation of this material in commercial devices is an inability to prepare materials that possess only the ferroelectric phase. In this presentation, we will discuss progress toward identifying and quantifying the various factors that lead to stabilization of the ferroelectric phase. The presentation will focus on two primary factors: 1) oxygen vacancies and 2) mechanical strain. It will be shown that significant oxygen vacancy concentrations are needed to stabilize the ferroelectric phase in otherwise compositionally pure hafnium oxide.[1, 2] The majority of these oxygen vacancies are charge neutral and, owing to this, have been largely undercounted in prior works. It will also be shown that there is a direct correlation between biaxial stress and the polarization magnitude in hafnium zirconium oxide films.[2] We will show that the presence of a top electrode ‘capping’ layer during thermal processing aids in stabilizing the ferroelectric phase. The mechanism of the capping effect is not a thermal expansion mismatch between the electrode and underlying film as is widely reported. Rather, the mechanism is a membrane force that prevents out-of-plane displacements and the formation of the larger molar volume equilibrium monoclinic phase.[3] Knowledge of these two phase stabilizing factors can help process design to realize phase-pure, high-performing hafnia for variety of microelectronic applications.

1. Jaszewski, S.T., *et al.*, *Acta Mater.* **239**, 118220 (2022)
2. Ihlefeld, J.F., *et al.*, *Appl. Phys. Lett.* **121**, 240502 (2022)
3. Fields, S.S., *et al.*, *Adv. Electron. Mater.* **8**, 2200601 (2022)

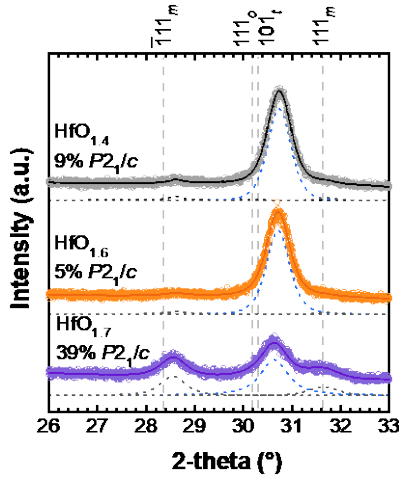


Fig.1: X-ray diffraction patterns of HfO_{2-x} films prepared via sputtering. The vertical dashed lines indicate the positions of the various possible phases. The monoclinic phase percentages are quantified and shown.

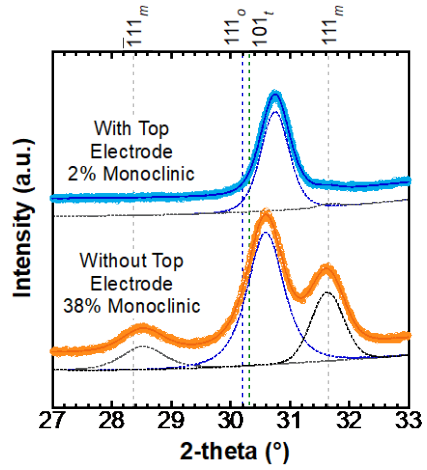


Fig.4: X-ray diffraction patterns of hafnium zirconium oxide films prepared with (blue) and without (orange) top electrodes. The phase percentage of monoclinic phase is provided.

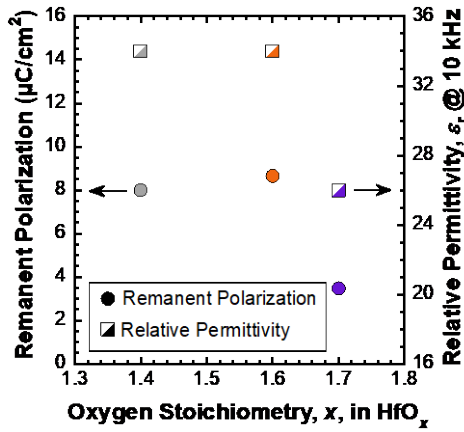


Fig.2: Remanent polarization (left) and relative permittivity (right) of HfO_{2-x} films prepared via sputtering showing the effect of oxygen non-stoichiometry on performance.

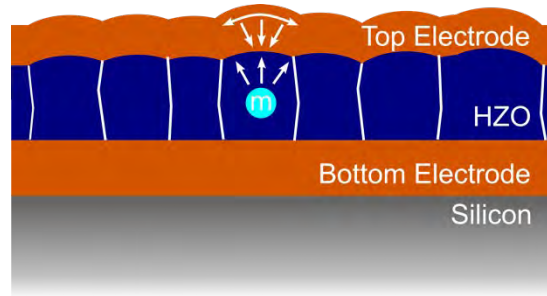


Fig.5: Illustration of the role that the top electrode plays in preventing formation of the equilibrium monoclinic phase in hafnium zirconium oxide thin films.

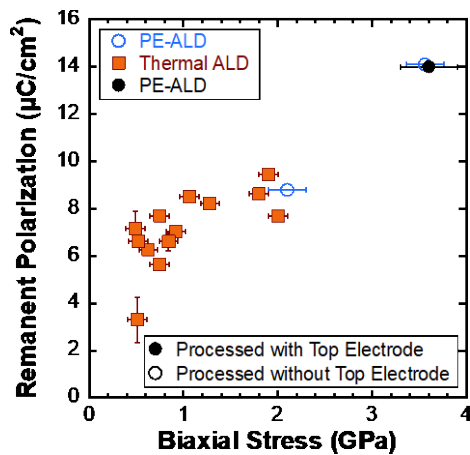


Fig.3: Remanent polarization as a function of biaxial stress in hafnium zirconium oxide thin films prepared via thermal and plasma enhanced atomic layer deposition (ALD).

Multilevel Resistance for Ta/Hf_{0.6}Zr_{0.4}O₂/TaN Ferroelectric Tunnel Junction Devices

M.D. Henry¹, J. Haglund^{1,2}, M. Lenox³, T.R. Young¹, J.F. Conley, Jr.², and J. Ihlefeld³

¹MESA Fabrication Facility, Sandia National Labs, Albuquerque NM, USA

²Dept. of Electrical Engineering, Oregon State University, Corvallis, OR, USA

³Dept. of Material Science and Engineering, University of Virginia, Charlottesville, VA, USA
mdhenry@sandia.gov

Keywords: Oxides, ferroelectrics, ferroelectric tunnel junctions, advanced electronic devices

Hafnia based ferroelectric devices have demonstrated advantages in the semiconductor and microelectronics industry with their high integration potential in fabs and compatibility with complementary metal oxide semiconductor (CMOS) technologies in both the front and back end of the line (FEOL, BEOL) [1]. Further, hafnium zirconium oxides (HZO) achieve a particular interest due to their thickness scaling ability via atomic layer deposition (ALD), coercive voltage compatibility with CMOS technology, and wide range of devices such as ferroelectric random-access memory (FeRAM), ferroelectric field effect transistors (FeFET), ferroelectric tunnel junctions (FTJ) [2, 3].

This work demonstrates the utilization of 7.8 nm thick Hf_{0.6}Zr_{0.4}O₂ layer utilizing Ta and TaN asymmetric electrodes for FTJ devices. With Ta as the top electrode and TaN as the bottom electrode, these devices switch from a high resistance state to low resistance state upon application of positive voltage, with better than a 10x resistance ratio between states. Since FTJ devices are inherently a current density transport device, area scaling permits device resistances to be tuned for circuit design. However, by appropriate selection of a pulse read voltage, we can modulate the resistance ratio and absolute resistance of the "on" and "off" state of the device, an attribute also useful for circuit design. This feature suggests that read voltages offer the potential for a multistate resistor useful in multistate applications.

This work was supported by the Laboratory Directed Research and Development program at Sandia National Laboratories, a multimission laboratory managed and operated by National Technology and Engineering Solutions of Sandia LLC, a wholly owned subsidiary of Honeywell International Inc. for the U.S. Department of Energy's National Nuclear Security Administration under contract DE-NA0003525.

[1] T. Mikolajick *et al.*, *Adv. Mater.*, **2206042** (2022).

[2] M. Kobayashi *et al.*, *IEEE Journal of the Electron Devices Society* **7** (2018).

[3] K. Nair *et al.*, *ACS Appl. Electron. Mater.* **5**, 1478 (2023).

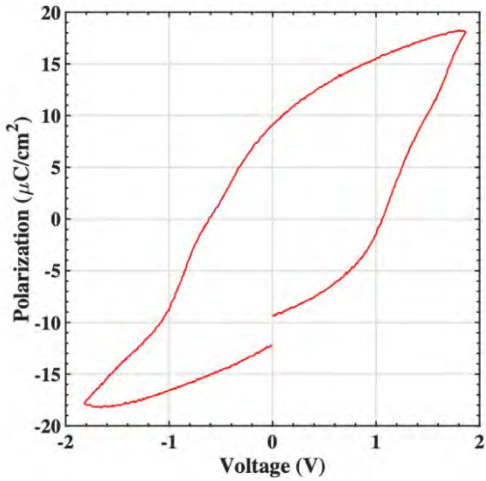


Fig.1: Polarization loop of the TaN/7.8nm $Hf_{0.7}Zr_{0.3}O_2/Ta$ ferroelectric tunneling junction.

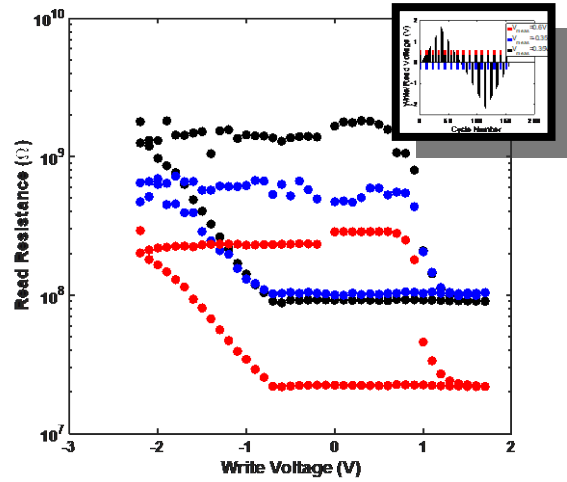


Fig.4: Pulsed hysteresis curves showing the FTJ resistance at the 0.35V (black), -0.35V (blue) and 0.6V (red) read voltages. Inset shows the pulse sequence used to generate measurements.

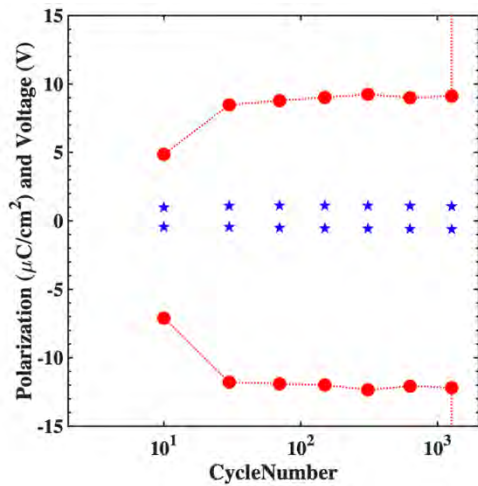


Fig.2: Polarization and coercive voltage as the device is cycled for endurance of the 7.8 nm HZO.

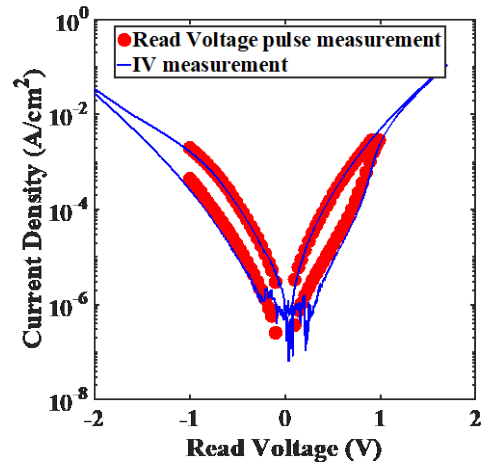


Fig.5: Swept IV measurement (blue) with pulsed read states overlaid (red) showing the current at discrete read states.

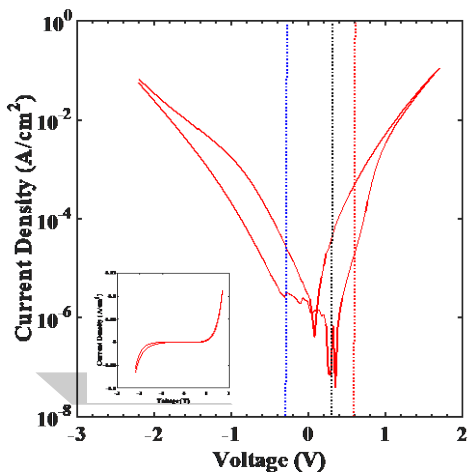


Fig.3: J-V measurements from -2.2 V to 1.7 to -2.2 V showing a switch from high to low resistance states; dash lines indicating read voltages of 0.35V (black), -0.35V (blue), and 0.6V (red) for

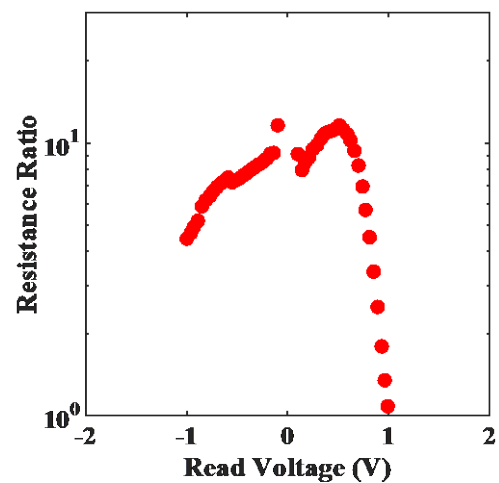


Fig.6: Resistance ratio of high/low resistance modulation based on the value of the read voltage suggesting an optimized resistance ratio.

Internal Photoemission (IPE) Spectroscopy Measurement of Conduction Band Offsets in Pristine and Poled Ferroelectric ALD HfZrO_x Metal/Ferroelectric/Semiconductor (MFS) Devices

Jessica L. Peterson,¹ Takanori Mimura,² Jon Ihlefeld,² and John F. Conley, Jr.¹

¹*School of EECS, Oregon State University, Corvallis, OR, 97331*

²*Depts. of MSE and ECE, University of Virginia, Charlottesville, Virginia 22904*

*jconley@eeecs.oregonstate.edu

Keywords: oxides and ferroelectrics

Due to the already widespread use of HfO₂ as a gate dielectric, ferroelectric Hf_{0.5}Zr_{0.5}O₂ (HZO) has attracted much attention for CMOS non-volatile memory and logic applications. Optimizing HZO for these applications will require knowledge of the interfacial energy barriers with the electrodes in the specific device structures used. The only method of measuring barrier heights in working devices is internal photoemission (IPE) spectroscopy. We previously reported IPE measurement of the energy barriers in pristine as-deposited HZO in metal/insulator/metal structures (MIM) with various electrodes [1]. Here we present the first report of the impact of "waking" and "poling" on energy barriers in operating metal/ferroelectric/semiconductor (MFS) devices, operations necessary to stabilize and truly exploit ferroelectric behavior of HZO devices [2].

20 nm HZO thin films were deposited on p-Si using 102 atomic layer deposition supercycles of HfO₂ and ZrO₂. Next, a 20 nm blanket TaN film was deposited, annealed for 30 seconds at 600°C, stripped away, and then replaced by an optically transparent top electrode (5nm TaN / 5 nm Pd). TaN/HZO/Si devices were woken by performing 5000 ±5V cycles at 1 kHz and then poled by applying a +4 V / -4 V square pulses. During IPE, devices were biased and current measured while simultaneously sweeping incident monochromatic photon energy from 1.7 to 5.5 eV. Extracted spectral thresholds were plotted vs. square root electric field and extrapolated to zero to account for any Schottky field induced barrier lowering.

For pristine devices, TaN, Si conduction, and Si valance band (CB and VB) barriers were measured at 2.5, 3.5, and 4.4 eV, respectively. Following waking, the TaN barrier was reduced to 2.1 eV, possibly indicating redistribution of oxygen defects toward the TaN interface, while The Si CB and VB remained roughly the same. Following positive poling, barriers were within error of the woken devices, but the negative poling resulted in an increase in the TaN barrier to 2.8 eV and a decrease in the Si CB and VB barriers to 3.1 and 4.4 eV respectively. This suggests oxygen vacancy movement away from the TaN interface. IPE results provide insight into HZO device operation. Additional measurements on the impact of cycling fatigue on barrier heights along with capacitance vs. voltage and current vs. voltage measurements will also be reported at the meeting.

[1] M. A. Jenkins *et al.*, *ACS AMI* 13, 14634–14643, (2021).

[2] E. D. Grimley *et al.*, *AEM2* 1600173, (2016).

Multistate 20, 10, and 5 nm $\text{Al}_{1-x}\text{Sc}_x\text{N}$ Ferroelectric Diodes

Zirun Han^{1,2†}, Kwan-Ho Kim^{1†}, Roy H. Olsson III¹, Deep Jariwala^{1*}

¹*Department of Electrical and Systems Engineering, University of Pennsylvania, Philadelphia PA 19104*

²*Department of Physics and Astronomy, University of Pennsylvania, Philadelphia PA 19104*

[†] These authors equally contributed to this work.

* *Corresponding Author, email: dmj@seas.upenn.edu*

Keywords: oxides and ferroelectrics, neuromorphic

We demonstrate Back-End-of-Line-compatible, high-performance ferroelectric diodes (FE-diodes) using 5, 10, and 20 nm $\text{Al}_{0.72}\text{Sc}_{0.28}\text{N}$ films. Through the inclusion and engineering of an AlO_x interlayer (IL), substantial improvements in the On-Off / rectification ratios for scaled 5 and 10 nm ferroelectric diodes are obtained, increasing by 590/251 and 10/92 times respectively compared to devices without insulator interlayers. This enables stable 5-bit multi-state operation with a stable retention, making the devices promising for neuromorphic computing applications. An in-depth analysis into the transport mechanisms of the devices was performed, and our compact model aligns well with the experimental results. Leveraging the unique ferroelectric properties of $\text{Al}_{1-x}\text{Sc}_x\text{N}$, we demonstrate theoretically and experimentally that the inclusion of an interlayer can reduce the switching voltage of the ferroelectric diode. Additionally, the impact of the interlayer on the retention and endurance characteristics of the devices are analyzed.

Ferroelectric Material	AlScN
Remanent Polarization ($\mu\text{C}/\text{cm}^2$)	70 - 135
Coercive Field (MV/cm)	2 - 10
Dielectric Constant	10 - 20
Processing Temperature ($^\circ\text{C}$)	350

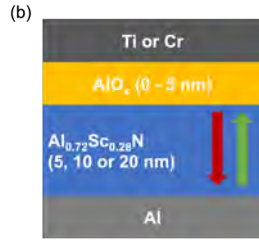


Fig.1: (a) Table for the ferroelectric properties and process temperature of AlScN. (b) Schematic diagram of $\text{Al}_{0.72}\text{Sc}_{0.28}\text{N}$ ferroelectric diode.

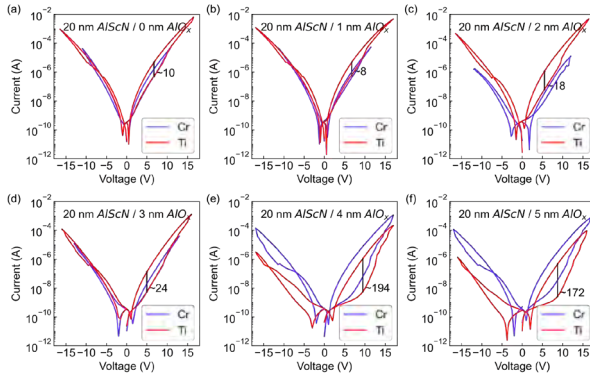


Fig.2: I-V characteristics of 20 nm $\text{Al}_{0.72}\text{Sc}_{0.28}\text{N}$ FE-diode with AlO_x IL thickness of (a) 0 nm, (b) 1 nm, (c) 2 nm, (d) 3 nm, (e) 4 nm, and (f) 5 nm. For all devices, Al is the bottom electrode, and Ti (red) or Cr (purple) is the top electrode.

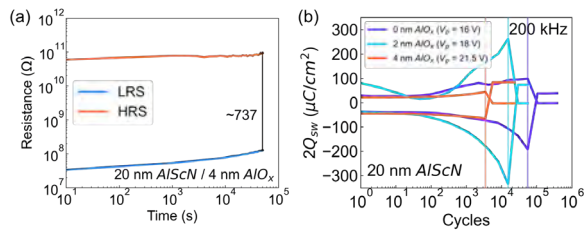


Fig.3: (a) LRS/HRS retention measurement of 20 nm AlScN FE-diode with 4 nm AlO_x IL up to 50,000 s. (b) Endurance measurements of the LRS/HRS memory states of the 20 nm AlScN FE-diode with 0, 2, and 4 nm AlO_x IL. The points of device failure are 5.6×10^4 cycles (0 nm IL), 1.5×10^4 cycles (2 nm IL), and 3.5×10^3 cycles (4 nm IL). V_p denotes the pulse amplitude of the applied voltage.

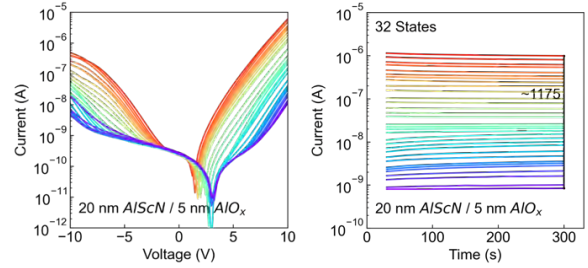


Fig.4: I-V curves of FE-diode obtained after gradual switching by applying 0.5 V steps and 32 multi-states retention of FE-diode up to 300 s.

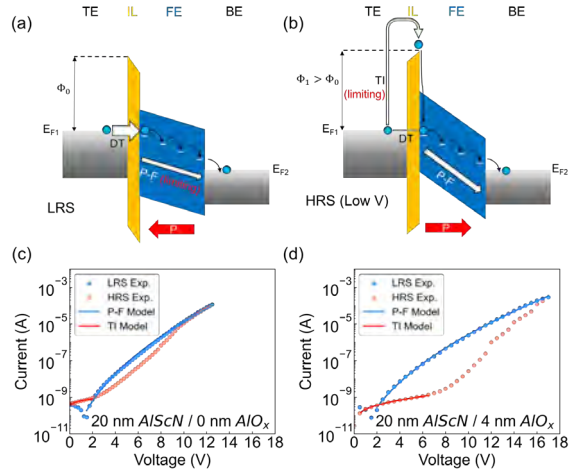


Fig.5: Energy band diagram and active transport mechanisms of AlScN FE-diode for the (a) low-resistance state (LRS) (b) high-resistance state (HRS). (c-d) Fitting of the Poole-Frenkel (P-F) and thermionic emission (TI) models.

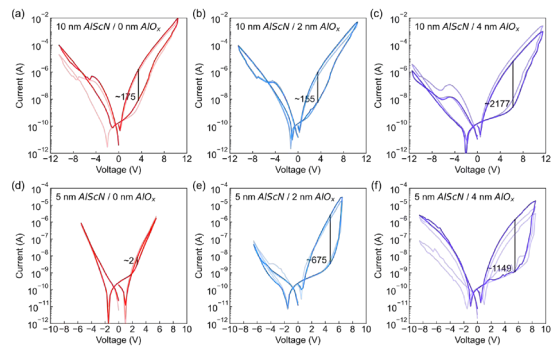


Fig.6: I-V characteristics of 10 nm $\text{Al}_{0.72}\text{Sc}_{0.28}\text{N}$ FE-diode with AlO_x IL thickness of (a) 0 nm, (b) 2 nm, and (c) 4 nm; 5 nm $\text{Al}_{0.72}\text{Sc}_{0.28}\text{N}$ FE-diode with AlO_x thickness of (d) 0 nm, (e) 2 nm, and (f) 4 nm. Each plot includes I-V curves obtained from three different devices to confirm the device-to-device variation.

Ferroelectric Polarization Modulated Schottky Diodes Enabling Improved Neuromorphic Functionality

Andreas Grenmyr, Jiayuan Zhang, Fengben Xi, Qing-Tai Zhao, Detlev Grützmacher
Peter Grünberg Institute (PGI-9, PGI-10) and JARA Institute for Green-IT,
Forschungszentrum Jülich, 52428 Jülich, Germany
d.gruetzmacher@fz-juelich.de

Keywords: neuromorphic

Rapid progress in artificial intelligence has been achieved employing conventional CMOS technology platforms. However, these suffer from high energy consumption and limitations in data transfer capacity (von Neumann bottleneck) [1]. To solve these problems, neuromorphic devices mimicking the behavior of synapses and neurons in the human brain are envisioned [2]. Ferroelectric field-effect transistor (FeFET) are powerful contenders, but typically designs show degraded linearity when applying potentiating or depressing pulses. As illustrated in Fig. 1a, forming Schottky diodes at the drain and source can solve this problem and allow ferroelectric polarization to control the device, improving linearity, as previously shown [3]. The device can be further improved by employing a dual gate (Fig. 1b). The 4th terminal enables heterosynaptic functionality. It acts as a modulatory neuron impacting the synapse [4].

Fig. 2 compares the long-term potentiation/depression (LTP/LTD) results obtained from both 3-terminal (Fig. 2a) and 4-terminal (Fig. 2b, c) devices. In the homosynaptic device (3-terminals), 50 potentiating pulses with an amplitude of -0.7V followed by 50 depressing pulses with an amplitude of 0.5V. In the 4-terminal devices, voltage pulses are applied to the programming gate on the source side, and the modulation of the synaptic characteristics by the modulatory neuron enables heterosynaptic plasticity. The effect of the input voltage at the fourth terminal, V_{MOD} , is clearly visible in Fig. 2b-c by the higher current and lower noise at $V_{MOD} = -1V$. Comparing devices with homosynaptic and heterosynaptic plasticity, the reduction of positive feedback is advantageous increasing controllability for potentiation and depression of synapses. The fourth terminal enables logic gates for in-memory computing [1]. As shown in Fig. 3, if either one of V_{MOD} or V_{PRO} is negative, the current is low. If both are negative at the same time, the current becomes high, enabling the AND function using only a single device. Similarly all logic gates can be demonstrated using 1 or 2 devices, enabling simple integration of synaptic functions and in-memory computing leading to more efficient and compact systems.

[1] S. H. Jo, T. Chang, et al., *Nano Lett.*, 10, 1297 (2010)

[2] G. Pedretti and D. Ielmini, *Electronics.*, 10, 1063, (2021)

[3] F. Xi et al., *ACS Appl. Mater. Interfaces*, vol. 13, no. 27, 2021

[4] F. Xi et al., *Adv. Electron. Mater.*, 2022

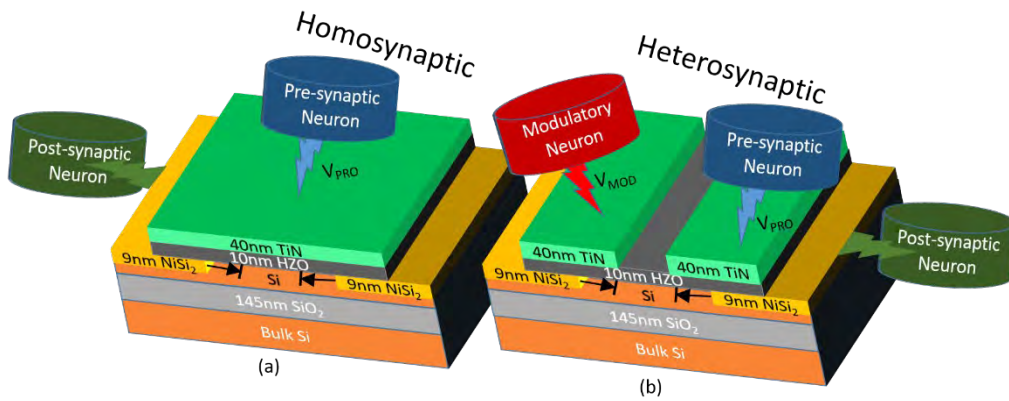


Figure 1. Illustration of FE-SBFET structures of: a) three terminals, and b) four terminal devices with dual-gate. The second gate can be used as a modulatory neuron. Hf_{0.5}Zr_{0.5}O₂ (HZO) is used as the ferroelectric layer.

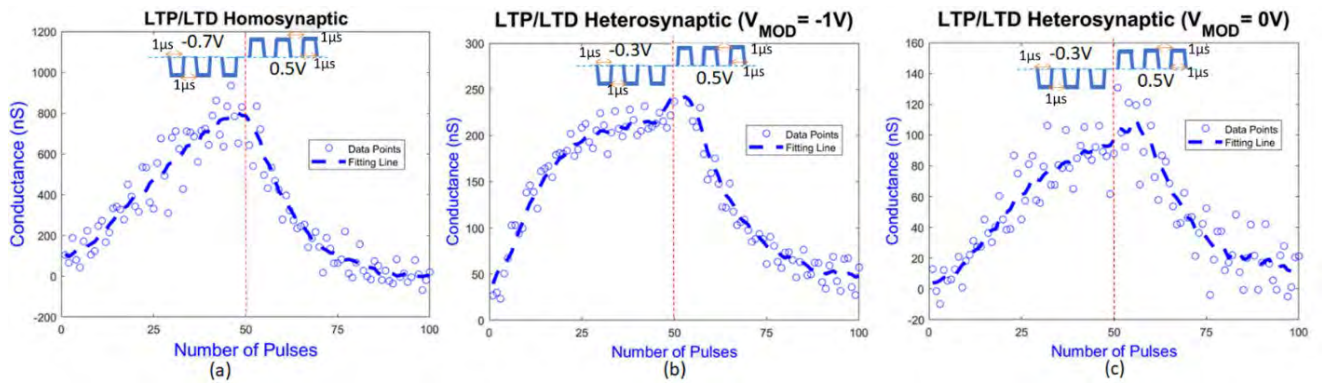


Figure 2. a) Measured LTP/LTD results for the homosynaptic 3-terminal device, 50/50 potentiating/depressing pulses are applied. b) For the heterosynaptic 4-terminal device, the modulating voltage influence the conductive states. For a modulating gate voltage $V_{MOD} = -1V$ the conductivity of the weight states increases, and the noise decreases

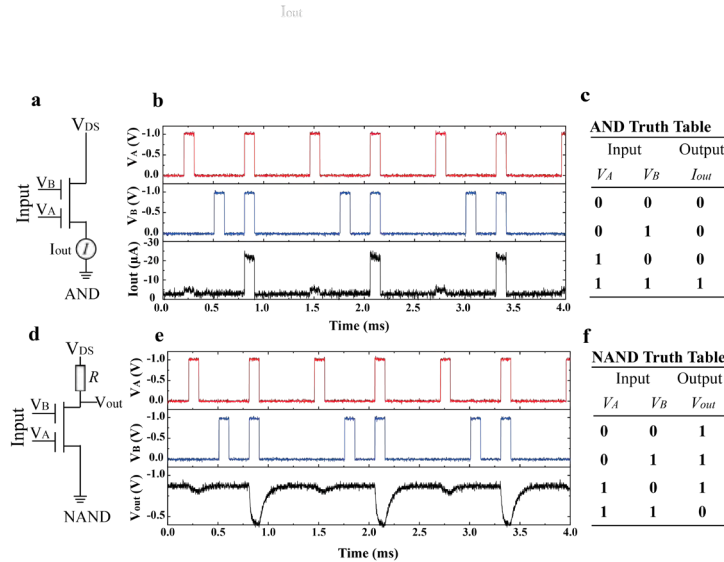


Figure 3. Logic AND and NAND function implemented by using a single heterosynaptic device.

The Electron's Spin and Chirality- a Miraculous Match

R. Naaman

Department of Chemical and Biological Physics, Weizmann Institute of Science,

Rehovot 76100, Israel

Ron.naaman@weizmann.ac.il

Keywords: Chirality, spin, magnetoresistance, spintronics, CISS.

Spin based properties, applications, and devices are commonly related to magnetic effects and to magnetic materials. However, we established that chiral material could act as spin filters for photoelectrons transmission, in electron transfer, and in electron transport [1,2]. The effect, termed Chiral Induced Spin Selectivity (CISS), has interesting implications in wide range of fields like spintronics [3], spin controlled chemistry, long range electron transfer, enantirecognition and enantioseparation. The mechanism of the effect, and its applications and implications, will be presented.

[1] R. Naaman, Y. Paltiel, D.H. Waldeck, *Acc. Chem. Res.*, **53**, 2659 (2020).

[2] D.H. Waldeck, R. Naaman, Y. Paltiel, *App. Phys. Lett. Material*, **9**, 040902 (2021).

[3] S.-H. Yang, R. Naaman, Y. Paltiel, S. Parkin, *Nat. Rev. Phys.* **3**, 328 (2021)

Magnetostrictive Evolution of Singular Anisotropic Magnetoresistance in Topological Metals

Matthew J. Gilbert

¹Department of Electrical and Computer Engineering, University of Illinois Urbana-Champaign, USA

²Institute for Condensed Matter Theory, University of Illinois Urbana-Champaign, USA

³Institute for Quantum Information Science and Technology Center, University of Illinois Urbana-Champaign, USA

⁴Department of Physics, University of Illinois Urbana-Champaign, USA

The ubiquity of topology within physics has been the source of much of our understanding of how symmetry both stabilizes and enhances observable phases of matter. Within condensed matter physics, the examination of topological phases of matter has led to the discovery of both new phenomena and the explication of previously overlooked physical responses that have been directly tied to the presence of a topology. The emergent importance of topological phases of matter has not only driven the examination of insulating, superconducting, magnetic, and heavy fermion materials. Of this diverse set of materials, magnetic materials, both ferromagnetic and antiferromagnetic, have been of particular interest due to the presence of broken time-reversal symmetry, that may lead to the presence of Weyl or Dirac fermions. Furthermore, the corresponding high Curie temperatures (T_c) well-known to exist in magnetic metals provides the possibility of finding and manipulating interesting topological phases at elevated temperatures.

In this work, we seek to clarify the interdependence of magnetic structure and topology by studying the interplay between magnetostriction and topology in elemental thin-film Holmium (Ho) using a combined experimental and theoretical effort. In our examination, we find C_6 rotationally symmetric discontinuous spikes in the anisotropic magnetoresistance (AMR) of the antiferromagnetic (AF) phase in Holmium when the magnetic field is aligned with the a -axis that are superimposed on a typical C_2 rotationally symmetric. As the temperature is increased and Holmium transitions to a conical ferromagnetic (FM) phase, the C_6 peaks begin to blend into a more dominant C_2 AMR. We explain this transition via magnetostrictive changes in the Holmium lattice that are associated with the applied in-plane as the material transitions from the AF phase to the FM phase.

Dirac-type charge carrier dynamics and Landau levels on curved surfaces

D. Kochan¹, M. Fürst², C. Gorini³ and K. Richter²

¹*Institute of Physics, Slovak Academy of Sciences, 84511 Bratislava, Slovakia*

²*Institute for Theoretical Physics, University of Regensburg, 93040 Regensburg, Germany*

³*SPEC, CEA, CNRS, Université Paris-Saclay, 91191 Gif-sur-Yvette, France*

denis.kochan@savba.sk

Keywords: topological insulators (, quantum transport)

Studies of the formation of Landau levels based on the Schrodinger equation for electrons constrained to curved surfaces have a long history. These include as prime examples surfaces with constant positive and negative curvature, the sphere and the pseudosphere. Now, topological insulators [1], hosting Dirac-type surface states, provide a unique platform to experimentally examine such quantum Hall physics in curved space. Hence, here we consider solutions of the Dirac equation for curved surfaces. In particular we study the pseudosphere for both, the case of an overall perpendicular magnetic field and a homogeneous co-axial, thereby locally varying, magnetic field. For both magnetic-field configurations, in particular the latter experimentally relevant case, we provide analytical solutions for spectra and eigenstates in the strong-field limit and compare with numerical solutions. We discuss implications of these results for quantum transport and orbital magnetism [2].

[1] R. Kozlovsky, A. Graf, D. Kochan, K. Richter, C. Gorini, *Phys. Rev. Lett.* **124**, 126804 (2020).

[2] M.Fürst, D. Kochan, C. Gorini, K. Richter, arXiv:2307.09221.

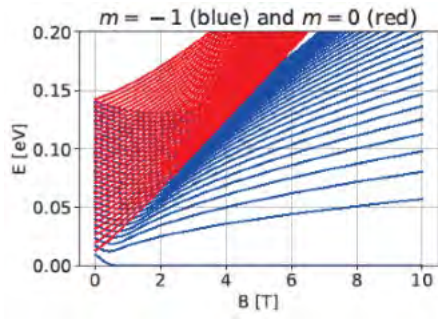


Fig.1: Landau level spectrum for Dirac equation on curved surface with negative curvature (pseudosphere) in perpendicular constant magnetic field, for states with two different angular momenta.

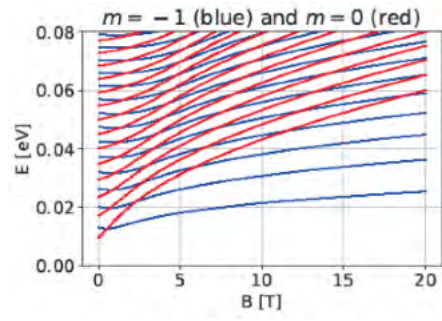


Fig.2 Landau level spectrum for Dirac equation on curved surface with negative curvature (pseudosphere) in a coaxial constant magnetic field, for states with two different angular momenta..

High throughput characterization and automated fabrication of lateral TMD heterostructure devices

T. Potocnik^{1*}, O. Burton¹, R. Mouthaan¹, P. Christopher¹, P. K. Sahoo², S. Hofmann¹, H. Joyce¹ and J.A. Alexander-Webber^{1*}

¹*Department of Engineering, University of Cambridge*

²*Quantum Materials and Device Research Laboratory, Indian Institute of Technology Kharagpur*

tp503@cam.ac.uk, jaa59@cam.ac.uk

Keywords: 2d materials, other advanced devices

Transition metal dichalcogenides (TMD) heterostructures offer a range of physical and optical properties with applications in environmental and image sensing. However, their growth and resulting properties are difficult to control, and their integration into devices remains a challenge. Here, we present high-throughput methods for identifying and characterizing 2D transition metal dichalcogenide (TMD) lateral heterostructures and for automatically designing electrode patterns to automatically fabricate hundreds of TMD photodiodes. We introduce spectroscopic ellipsometric contrast microscopy (SECM)[1] as a tool for mapping material and layer numbers in lateral TMD heterostructures. We optimize the ellipsometric angles to enhance the image contrast based on measured and calculated reflection coefficients of incident light. In addition, we introduce an optimized machine-readable, lithographically processable, and multi-scale fiducial marker system — dubbed LithoTag — which provides nanostructure position determination of individual flakes at the nanometer scale [2]. A grid of uniquely defined LithoTag markers patterned across a substrate enables image alignment and nanometer-accurate position, and combined with SECM, gives a database of individual TMD material properties, crucial for understanding the complexities of growth and nucleation within heterostructure material systems. We use position information to automatically route electrode patterns to TMD flakes of specific properties, automatically designing and fabricating >100 TMD photodiodes from a random arrangement of flakes on a substrate. Finally, we encapsulate some devices with atomic layer deposition Al₂O₃ to optimize their photocurrent performance. The presented methods enable automation of nanodevice processing and are agnostic to microscopy modality and nanostructure type. Such high-throughput experimental methodology coupled with data-extensive science can help overcome the characterization bottleneck and improve the yield of nanodevice fabrication, driving the development and applications of nanostructured materials.

- [1] T. Potočnik *et al.*, “Fast Twist Angle Mapping of Bilayer Graphene Using Spectroscopic Ellipsometric Contrast Microscopy,” *Nano Lett.*, Jun. 2023, doi: 10.1021/acs.nanolett.3c00619.
- [2] T. Potočnik *et al.*, “Automated Computer Vision-Enabled Manufacturing of Nanowire Devices,”

ACS Nano, Sep. 2022, doi: 10.1021/acsnano.2c08187.

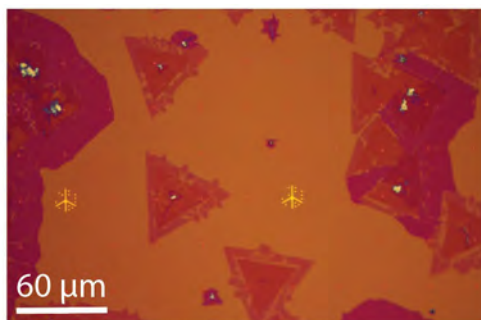


Fig.1: Optical microscope of $\text{MoSe}_2/\text{WSe}_2$ lateral heterostructures on a SiO_2/Si substrate with LithoTag fiducial markers (Ti/Au).

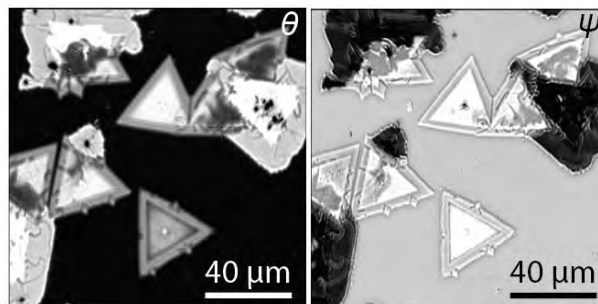


Fig.2: Delta (left) and psi (right) ellipsometric maps taken in rotating compensator (RCE) mode at 478 nm showing the contrast between two heterostructure materials.

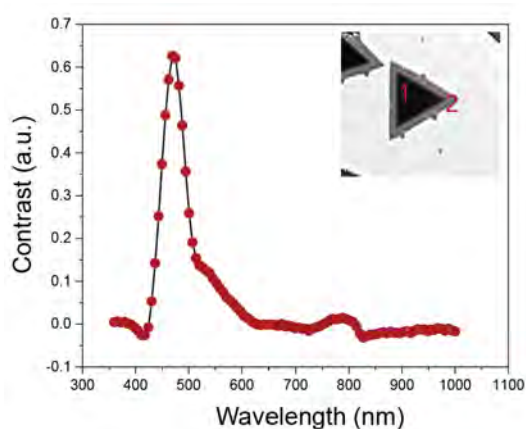


Fig.3: Contrast between MoSe_2 and WSe_2 (inset, material 1 and 2, respectively) as a function of wavelength, showing enhanced contrast at 475 nm.



Fig.4 Optical microscope image of an automatically fabricated two-terminal device with a 4 μm channel across the interface between MoSe_2 and WSe_2 .

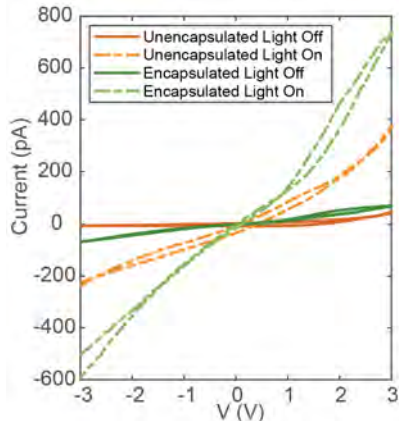


Fig.5: IV characteristics of a $\text{MoSe}_2/\text{WSe}_2$ device before and after encapsulation with ALD Al_2O_3 . Encapsulated devices show increased current both with and without white light illumination.

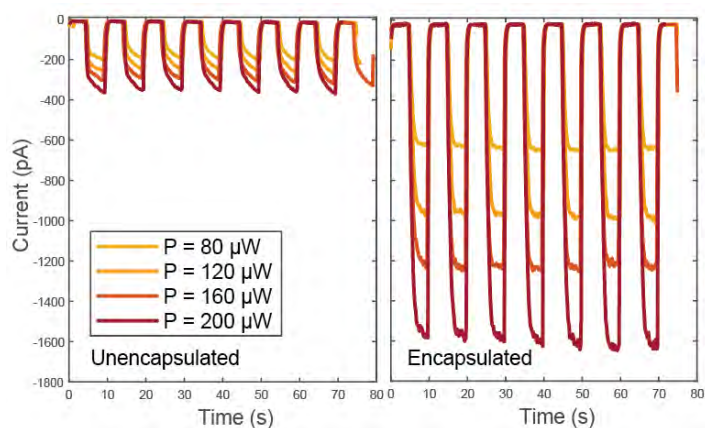


Fig.6: Photocurrent measurements of $\text{MoSe}_2/\text{WSe}_2$ at different laser power settings. Encapsulated devices show increased current and more stable device switching.

Enhancement of Sensitivity for Influenza Virus Detection by Integrated Graphene FET Biosensor using Surface Potential Modulator

Kazuhiko Matsumoto¹, Kaori Yamamoto¹, Natsuki Sato¹, Kiyoji Sakano¹, Takao Ono¹,
Shota Ushiba², Naruto Miyakawa², Shinsuke Tani²,
Youhei Watanabe³, Hidekazu Tanaka¹, Masahiko Kimura²

¹ Osaka University, Ibaraki, Osaka 567-0047, Japan

² Murata Manufacturing Co., Ltd., 1-10-1 Higashikotari, Nagaokakyo-shi, Kyoto 617-8555, Japan

³ Kyoto Prefecture University of Medicine, Kajii-cho, Kamigyo-ku, Kyoto-shi, 602-8566

*E-mail: k-matsumoto@sanken.osaka-u.ac.jp

Keywords: bioelectronics, sensors

We have been studying to detect the influenza virus using the integrated G-FET with high sensitivity. Fig.1 (a) shows the optical image of the integrated 32 G-FET, and (b) the expanded view of the G-FET. The channel length and width of G-FET was 10 μm and 100 μm respectively. The graphene channel was deposited after the Ti/Au source/drain electrodes were formed on the silicon substrate. The microfluidic channel as shown in Fig. 2 was installed on to the graphene FET array in order to flow Phosphoric Buffer Saline(PBS) from the right hand side of the optical image, pass over the FETs, and drain out from the left hand side. Using the microfluidic channel, the exchange of the PBS solution and washing of the physisorbed virus becomes possible for the precise detection of virus.

Fig. 3 shows the relationship between the surface potential V_l and the surface charge Q_e in the 0.01xPBS solution which is obtained from the Poisson-Boltzmann equation. The graph shows the linear relation near 0 surface potential or 0 surface charge, and shows the nonlinear relation at the larger surface potential area. The differential dV_l/dQ_e , means the sensitivity and is shown by the green line. The sensitivity shows the highest value at $Q_e = 0$ and $V_l = 0$. In the real device, however, there are large amount of charges on the surface of graphene due to the spontaneously induced electron and to the induced electron by the modulated antibody. The calculated surface potential and the induced electron are $\sim 100\text{mV}$ and $\sim 6 \times 10^{12}/\text{cm}^2$, respectively. Therefore, the sensitivity of the graphene FET is not high enough as it is. In order to get the higher sensitivity from Fig.3, the surface charge Q_e and surface potential V_l should be as small as possible. For this purpose, we introduced the surface potential modulator(SPM) on to the graphene surface, which includes the amino group and has the positive charge. We expect the surface potential modulator with positive charge cancels out the negative charge on the graphene surface and improve the sensitivity.

Fig. 4 shows the schematic structure of the graphene FET modified with antibody. PBASE (1-Pyrenebutyric acid N-hydroxy-succinimide ester) was first modified on graphene as a linker and then the influenza antibody was introduced to bind to it. Furthermore, in order to control the surface potential of graphene FET, surface potential modulator(SPM) with positive charge was newly added to G-FET to enhance the sensitivity.

Fig. 5 shows the comparison of the sensitivity of the graphene FET with and without the surface potential modulator when the influenza virus was introduced into the system. Without SPM, the Dirac point shift was as small as 2.6mV before and after the introduction of influenza virus. On the other hand, with SPM, the Dirac point shift becomes as large as 51mV. Figure 6 shows the average of Dirac point shift of 6 graphene FETs with and without SPM before and after the introduction of the influenza virus. ~ 10 times larger Dirac point shift was obtained by SPM.

Thus, by introducing the SPM, the sensitivity of the graphene FET biosensor can be improved drastically.

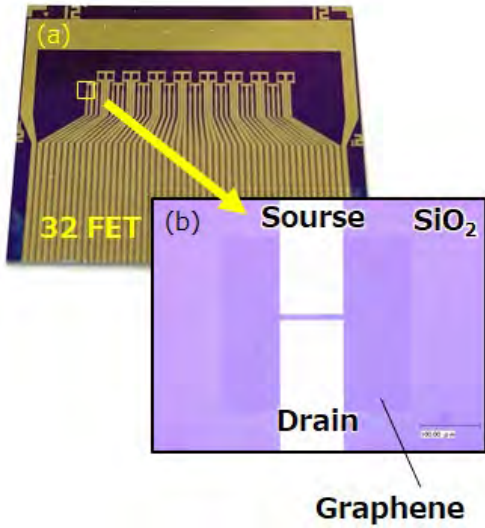


Fig. 1. (a) The optical image of integrated 32 G-FET. (b) The optical image of expanded view of G-FET.

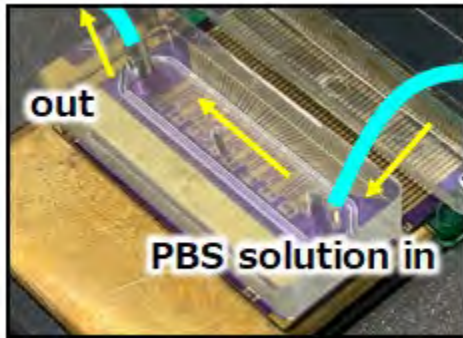


Fig. 2. Microfluidic channel installed on to the graphene FET array.

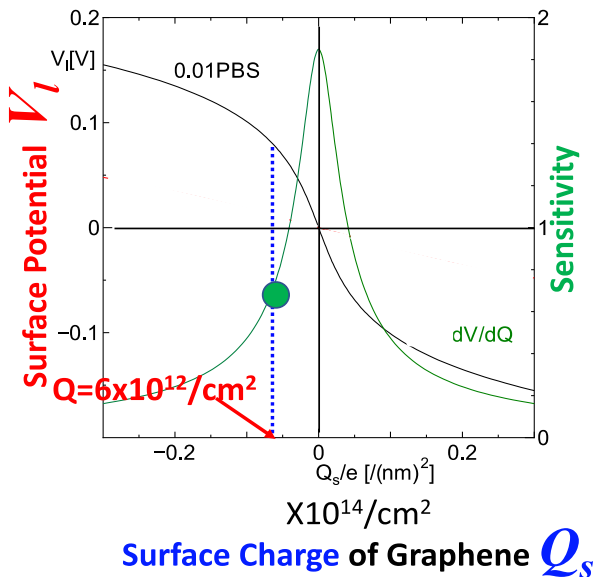


Fig. 3. Relationship between surface potential V_I v.s. surface charge Q_s . The differential dV_I/dQ_s means the sensitivity and is shown by green line. The sensitivity shows the highest value at 0 charge and 0 Potential.

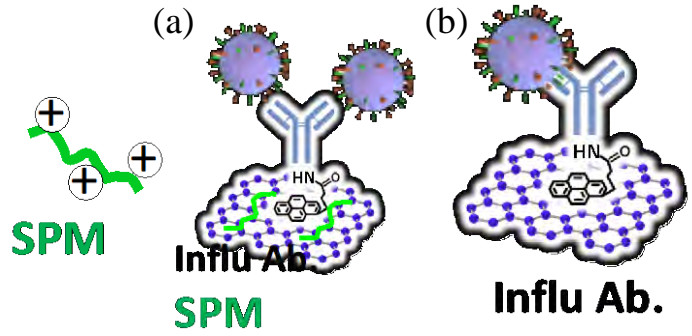


Fig. 4. Schematic structure of graphene FET modified by influenza antibody (a) with and (b) without surface potential modulator (SPM) which includes the amino group with positive charge.

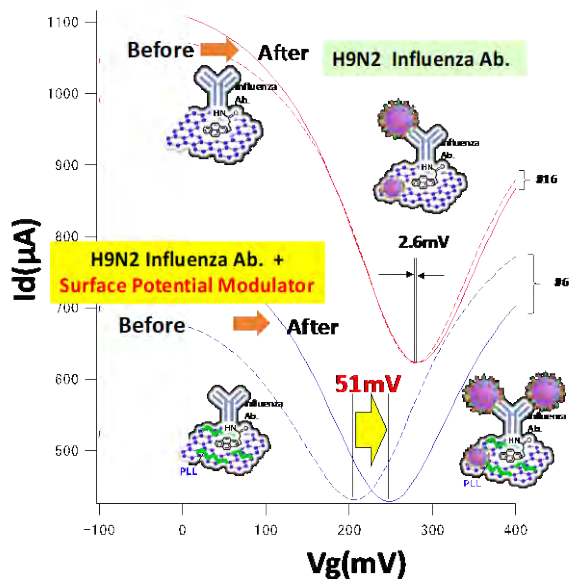


Fig. 5. Detection of Influenza virus using graphene FET with and without surface potential modulator.

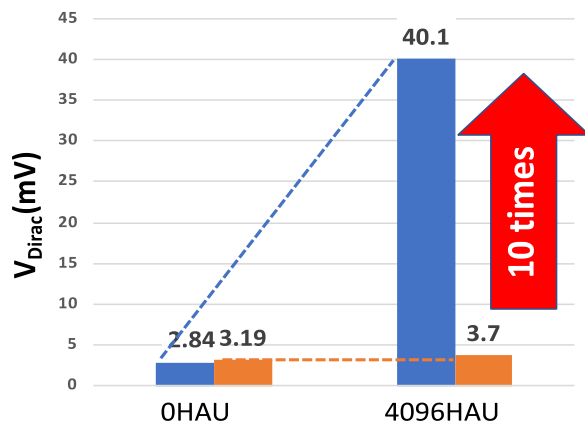


Fig. 6. Comparison of Dirac point shift, i.e., the sensitivity with and without surface potential modulator.

Control variational quantum algorithm meets artificial intelligence

Sanjaya Lohani^{1, +}, Chenxu Liu², Yanzhu Chen³, Brian T Kirby^{4, 5}, Sophia Economou³, Thomas A Searles¹

¹*University of Illinois Chicago, Chicago, IL 60607, USA*

²*Pacific Northwest National Laboratory, Richland, WA 99354*

³*Virginia Tech University, Blacksburg, VA 24061*

⁴*Tulane University, New Orleans, LA 70118, USA*

⁵*DEVCOM Army Research Laboratory, Adelphi, MD 20783, USA*

⁺*slohan3@uic.edu*

Keywords: variational quantum algorithm, machine learning, pulse optimization

Ctrl-VQE, a pulse-based VQE algorithm, can drastically reduce the circuit depth compared to gate-based methods. The flexibility of pulse shaping, while providing circuit depth reduction, also brings the challenge of optimizing a large number of variational parameters. Here, we build a machine learning (ML) assisted ctrl-VQE algorithm framework. Our approach leverages reinforcement learning (RL) techniques to train and optimize the control pulses to provide better performance than classical optimization techniques. We have successfully designed and constructed a deep Q learning (DQN) agent that automatically explores the space of possible bang-bang pulse sequences required to implement ctrl-VQE. The simulation results show that our RL-based approach can find compact pulse sequences for the H₂ molecule Hamiltonian. The RL-assisted ctrl-VQE is expected to provide similar advantages in optimizing control pulses for large systems with higher correlations.

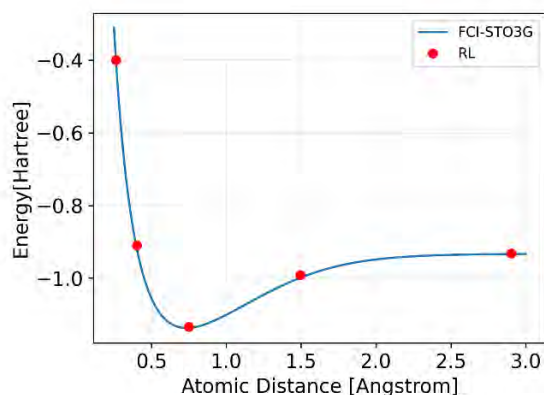


Figure 1: Ground state energy versus atomic distance for Hydrogen molecule. Blue: energy curve from the full configuration interaction (FCI) in a minimal STO-3G basis set. Red dots: energy curve obtained from the reinforcement learning assisted optimized ctrl-VQE.

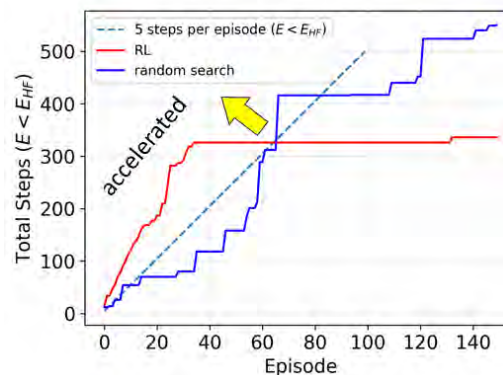


Figure 2: Total constructive pulse steps with the energy less than Hartree Fock versus the number episodes for an agent. Red line: using reinforcement learning agent. Blue: an agent following the random search. Dotted line: a threshold where an agent is expected to build 5 pulse sequences per episode. The curve lying left to the threshold is assumed to have accelerated learning.

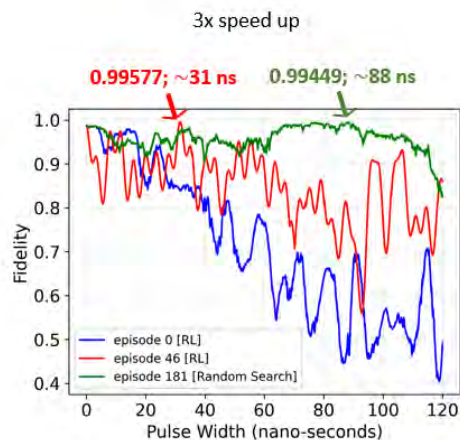


Figure 3: Fidelity of the quantum state generated by the optimized sequence of pulses versus the pulse width in nano seconds. Episode 0 represents the beginning of the learning task. A reinforcement learning agent finds the optimized sequence of pulses in 31 nano seconds (red curve), where a random search takes 88 nano seconds (green).

Lohani, Sanjaya, et al. "Data-centric machine learning in quantum information science." *Machine Learning: Science and Technology* 3.4 (2022): 04LT01.

Asthana, Ayush, et al. "Minimizing state preparation times in pulse-level variational molecular simulations." *arXiv preprint arXiv:2203.06818* (2022).

Analysis of Wear Morphology of Concentrated Polymer Brushes under Various Conditions Using Coarse-Grained Molecular Dynamics

Arisa Chiba¹, Ryutaro Kudo¹, Mizuho Yokoi¹, Masayuki Kawaura¹, Yuta Asano¹, Shogo Fukushima¹, Yusuke Ootani¹, Nobuki Ozawa^{2,1}, and Momoji Kubo^{1,2}

¹ Institute for Materials Research, Tohoku University, Miyagi, Japan

² New Industry Creation Hatchery Center, Tohoku University, Miyagi, Japan

chiba.arisa.q3@dc.tohoku.ac.jp

Keywords: nanostructures

In the mechanical engineering, reduction of friction is strongly demanded to improve the energy conversion efficiency of machine system. Thus, the development of new low-friction materials is required. We focus on concentrated polymer brush (CPB). CPB has superior properties as a low friction material [1, 2]. However, durability of CPB is not satisfactory for commercial use [3], therefore, elucidation of the wear mechanism is required. Thus, we analyzed the CPB wear phenomena under various load and speed conditions by sliding simulation using coarse-grained molecular dynamics.

Figure 1 shows the sliding simulation model. The CPB is composed of linear polymer chains grafted on a flat substrate. The CPB model is soaked in good solvent. The polymer chain is modeled by a bead-spring model. A slider was pressed and slid on the CPB. Load force was $96.8 \sim 1161.3 \epsilon/\sigma$, sliding speed was $0.4 \sim 1.2 \sigma/\tau$, where σ , ϵ , and τ were the units of length, energy, and time, respectively. Simulations were performed until the slider slid on CPB 10 cycles or the number of breaking events reached 100.

As a result, we found out that the dynamics of the sliding interface can be divided into 3 types by the polymer peeling off and the slider penetration (Figure 2). Type I was observed at low load/high speed; the slider always floated and did not penetrate into the CPB. Type II was observed at low speed; the slider penetrated into the CPB. Type III was observed at high load/high speed; the slider penetrated into the CPB and the CPB peeled off behind the slider. The penetration was observed at high load. Moreover, the peeling off was observed when the load was large and the sliding speed was high. The wear process was investigated by analyzing the location of breaking points of polymer chains (Figure 3). Interestingly, each type has its own wear mode. In type I, breaking mainly occurs at the surface area of CPB. In type II, breaking occurred at surface area, the internal part of CPB and in front of the slider. In type III, breaking mainly occurred in front of the slider as well as the surface area. No internal breaking was observed in type III. We will discuss the details of the wear mechanism that day.

[1] C. Yoshikawa *et al.*, Chem. Lett., **39**, 142-143 (2010)

[2] C. Yoshikawa *et al.*, J. Mater. Chem. B, **9**, 5794-5804 (2021)

[3] M. Miyazaki *et al.*, Wear, **482-483**, 203984 (2021).

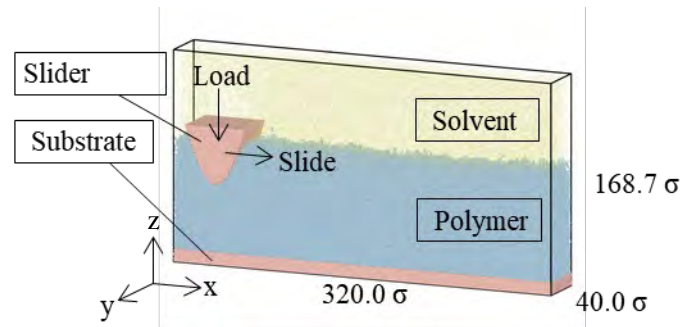


Fig.1: Sliding simulation model of CPB system. The yellow beads indicate solvent. The blue beads indicate polymer. The pink beads indicate substrate and slider.

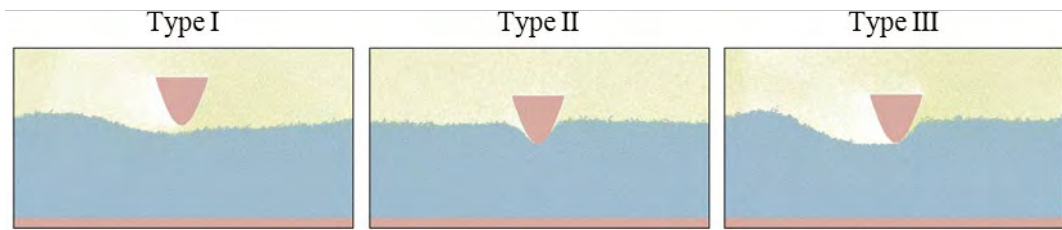


Fig.2: Typical snapshot of the sliding simulations classified into type I (load force: $96.8 \epsilon/\sigma$, sliding speed: $1.2 \sigma/\tau$), type II (load force: $774.2 \epsilon/\sigma$, sliding speed: $0.4 \sigma/\tau$), type III (load force: $1161.3 \epsilon/\sigma$, sliding speed: $1.2 \sigma/\tau$).

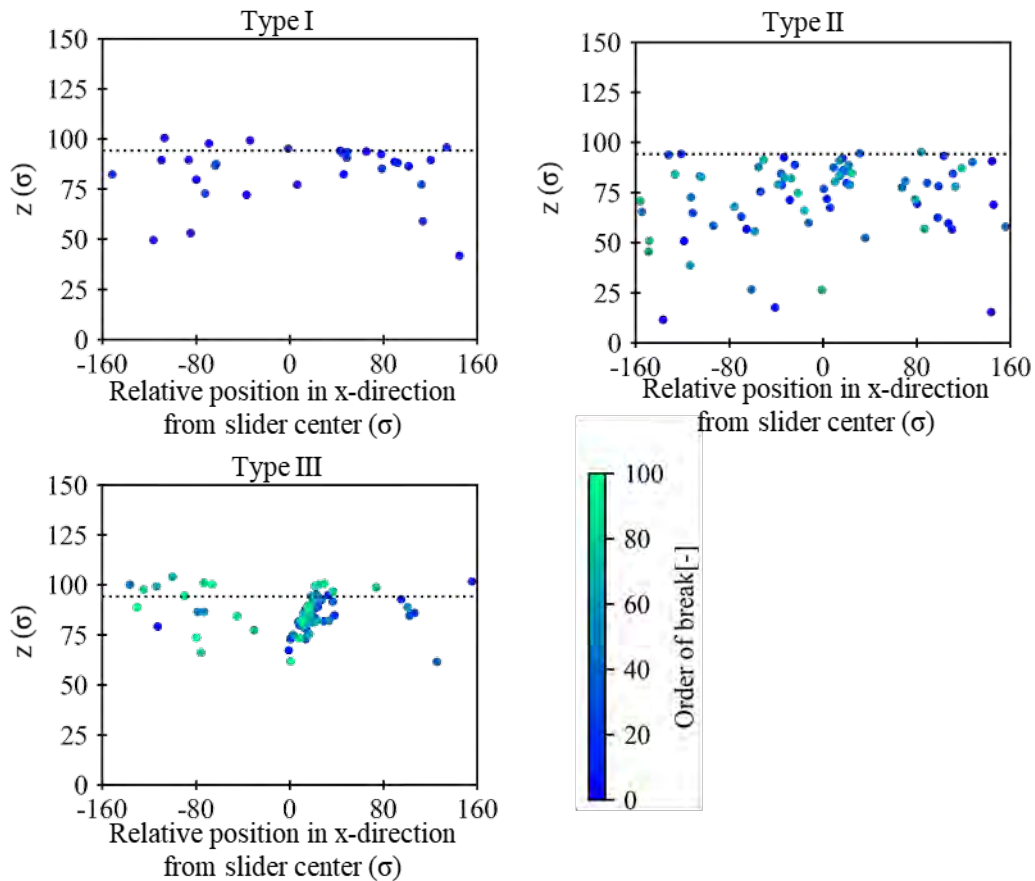


Fig.3: Location of breaking points observed in sliding simulation classified into type I (load force: $96.8 \epsilon/\sigma$, sliding speed: $1.2 \epsilon/\sigma$), type II (load force: $774.2 \epsilon/\sigma$, sliding speed: $0.4 \epsilon/\sigma$), and type III (load force: $1161.3 \epsilon/\sigma$, sliding speed: $1.2 \epsilon/\sigma$). The dotted line indicates the equilibrium position of the CPB surface during relaxation.

Charge-Density-Wave Domain Depinning in Quasi-Two-Dimensional van der Waals Materials – Novel Functionality for Electronic Applications

Jonas O. Brown¹, Maedeh Taheri², Fariborz Kargar^{1,2}, and Alexander A. Balandin^{1,2}

¹*Department of Materials Science and Engineering, UCLA, California 90095 USA*

²*Department of Electrical and Computer Engineering, UCR, California 92521 USA*

balandin@seas.ucla.edu

Keywords: 2D materials, quantum materials, quantum transport, nanostructures,

The charge-density-wave (CDW) phase is a macroscopic quantum state consisting of a periodic modulation of the electronic charge density accompanied by a periodic distortion of the atomic lattice. Early work on CDW effects in bulk samples of the quasi-one-dimensional (1D) metallic crystals revealed oscillating current for constant voltages, giant dielectric response, and other intriguing phenomena. Recently, one can witness a rebirth of the field of CDW materials and devices, partially driven by an interest in quasi-two-dimensional (2D) van der Waals materials where CDW phases can manifest themselves at room temperature [1]. The process of depinning and sliding of CDWs is important for understanding the physics of the CDW condensate phases and for novel device functionalities. For bulk 1D crystals, the temperature dependence of CDW depinning has been used as an important characteristic allowing one to experimentally assess the predictions of different models of collective electron transport. In this presentation, we report on the temperature-dependent depinning of the CDW domains in quasi-2D 1T-TaS₂ – van der Waals layered material with the transition between the nearly commensurate CDW (NC-CDW) and the incommensurate CDW (IC-CDW) phases at ~350 K. We use the derivative current-voltage (I-V) characteristics, *i.e.* current fluctuations, to monitor the evolution of the depinning field with temperature (see Figures 1 – 3). The spikes and fluctuations in the derivative I-Vs indicate the onset of the CDW phase transitions and domain depinning. Within the NC-CDW phase, we observe an increase in the depinning threshold field as the temperature decreases [2]. We establish the dependence of the threshold field on the thickness of 1T-TaS₂ channels, revealing the surface pinning effects on CDWs in quasi-2D materials (see Figure 4). Finally, we describe the differences between CDW depinning and sliding in the quasi-1D bulk crystals and in the thin films of the 2D van der Waals materials. The prospects of electronic device applications of 1T-TaS₂ and other quasi-2D CDW materials are also discussed.

A.A.B. acknowledges the support of the U.S. DOE Office of Basic Energy Sciences (DE-SC0021020) and the Vannevar Bush Faculty Fellowship (N00014-21-1-2947).

[1] M. Taheri, *et al.*, ACS Nano, 16, 18968 (2022).

[2] J. O. Brown, *et al.*, preprint at <https://arxiv.org/abs/2307.08047> (2023)

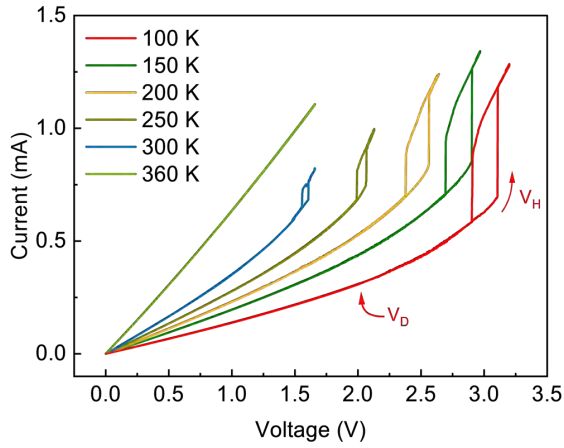


Fig.1: Temperature-dependent I - V characteristics of a $1T$ - TaS_2 thin-film device. The I - V hysteresis results from the transition between the NC - CDW and IC - CDW phases. The hysteresis is used to provide negative feedback for the voltage-controlled oscillators.

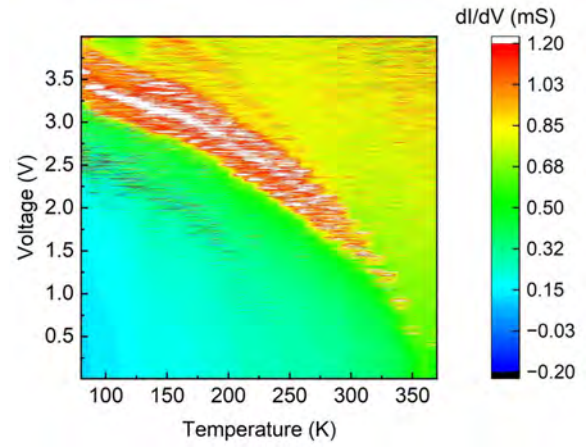


Fig.2: A contour plot representing the current fluctuations (dI/dV) in a thin $1T$ - TaS_2 CDW device (channel thickness of ~ 8 nm). One can trace the NC - CDW – IC - CDW phase transition following the border between the green and red colors.

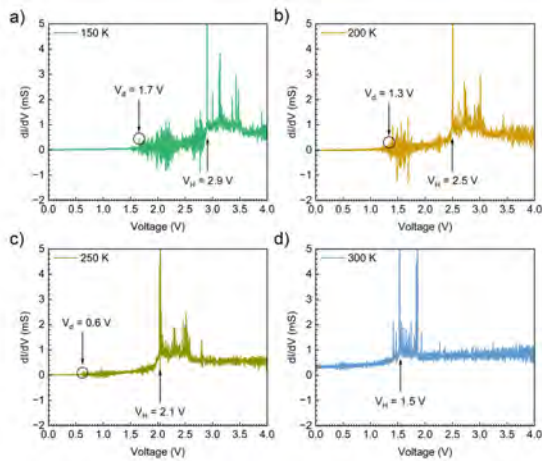


Fig. 3: Current fluctuations (dI/dV) in a thin-film $1T$ - TaS_2 device measured at different temperatures. At 150 K, a large spike (~ 2.9 V) corresponds to the onset of the NC – IC - CDW phase transition (V_H). The burst of conductance fluctuations at lower biases (V_D) indicates CDW domain depinning. Higher temperatures shift the onset of fluctuations and the phase transition voltage to smaller bias values.

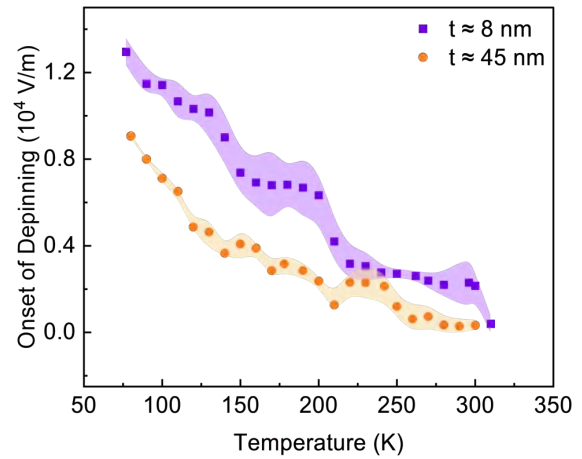


Fig.4: The CDW domain depinning field (E_D) as a function of temperature for two representative $1T$ - TaS_2 devices with different thicknesses. Note the monotonic increase in the threshold field with decreasing temperature. The examined temperature range crosses the transition to the commensurate CDW (C - CDW) phase.

Si:P δ -layer Resonant Tunnel Junctions for TeraHertz applications

D. Mamaluy¹, and J.P. Mendez¹

¹*Cognitive & Emerging Computing, Sandia National Laboratories, Albuquerque, USA*
mamaluy@sandia.gov

Keywords: quantum transport, other advanced devices

Atomic precision advanced manufacturing (APAM) is used to create 2D doped regions in silicon known as δ -layers that simultaneously have single-atom precision [1–2] and extremely high conductivity [3]. Primarily, this technology has been used to explore dopant-based qubits in silicon, but recently APAM has also attracted attention for exploring basic principles of classical-digital computing via novel electronic devices, nano-scale diodes and transistors (e.g. [4]). Previously we have developed an open-system quantum transport treatment [5] that allows to accurately predict the band structure and conductive properties (see Fig. 1) of highly-conductive highly-confined systems such as APAM, including the ultra-sensitive tunnel junction devices [6].

Here we propose, through the predictive quantum transport simulation, a novel type of two-terminal, resonant tunneling junction (RTJ), negative differential resistance (NDR) device for high efficiency dc-to-ac current conversion at extremely high (terahertz) frequencies. The device consists of two Si:P delta-layer tunnel junctions forming a double-barrier structure as shown in Fig. 2 top-right inset. The resulting electrical I-V characteristics shown in Fig. 2 demonstrate a strong NDR region with the excellent amplification characteristics: 1) PVR of 3.75 and 2) extremely high responsivity $\beta > 200$ A/W. The estimated dwell tunneling time is of the order of 10^{-13} seconds, implying the possibility of high TeraHertz applications.

Finally, we discuss the mesoscopic mechanism of the RTJ's extremely high responsivity. It is shown that a charge build-up on the device island eventually leads to a significant change of the island energy (~ 10 mV) even for a very small change of drain voltage (~ 2 mV). Thus, the β value can be understood from the alternative definition of the responsivity as the change of resonator energy per unit of spent power.

- [1] H. F. Wilson *et al.*, Phys. Rev. B 74, 195310 (2006).
- [2] Q. Campbell *et al.*, AVS Quantum Science 4, 016801 (2022),
- [3] B. Weber *et al.*, Science 335, 64 (2012).
- [4] T. Skeren *et al.*, Nature Electronics 3, 524 (2020).
- [5] D. Mamaluy, J.P. Mendez *et al.* Commun Phys 4, 205 (2021).
- [6] J.P. Mendez, D. Mamaluy, Sci Rep 12, 16397 (2022).
- [7] M.B. Donnelly *et al.* Adv. Funct. Mater. 33, 2214011 (2023).

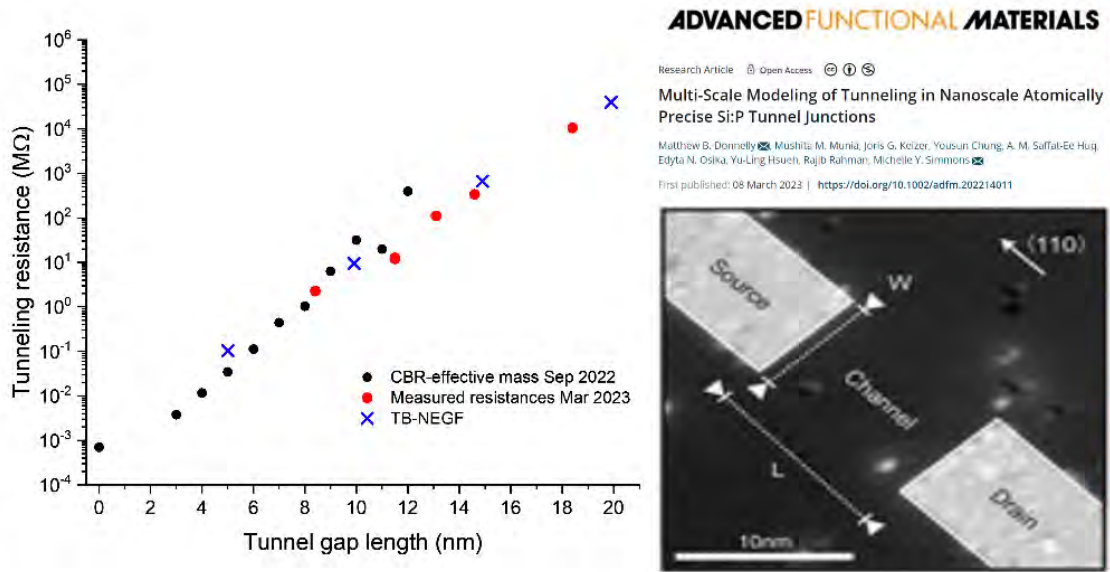


Fig.1: The predicted using CBR-effective mass[6] tunnel resistance vs gap length trend agrees remarkably well with the later experimental measurements [7].

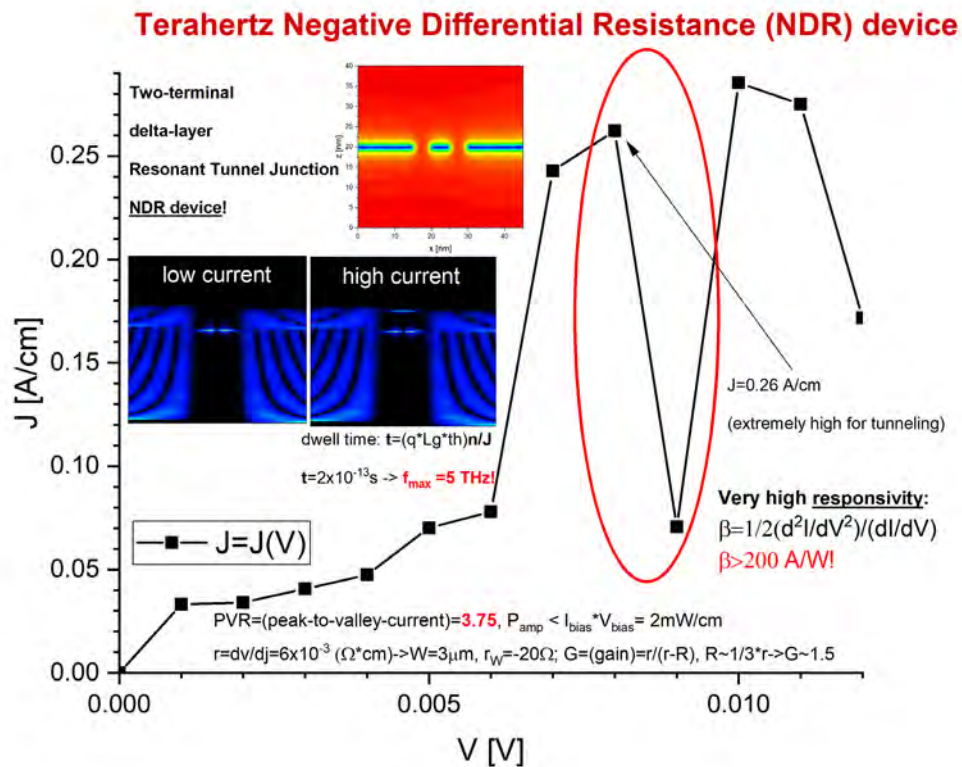


Fig.2: Main plot: the current density (J) vs drain voltage (V) of a two-terminal Resonant Tunnel Junction device (shown in top left inset). When a voltage corresponding to the resonant energy is applied (e.g. $V=7\text{mV}$) a high-energy resonant state forms increasing the current to $J=26\text{nA/nm}$ (mid-left inset shows LDOS with low and high current densities). However, the further increase of the drain voltage ($V=9\text{mV}$) eliminates the resonant state which reduces the current density to about 7nA/nm thus creating a Negative Differential Resistance (NDR) region with PVR \sim 3.7 and the extremely high responsivity $\beta > 200 \text{ A/W}$.

Two-dimensional van der Waals Materials and Their Mixed Low-Dimensional Hybrids for Clean Energy Applications

Chu Te Chen,¹ Yu Fu,¹ Anthony Butler,¹ Huamin Li,² and Fei Yao¹

¹ *Department of Materials Design and Innovation, University at Buffalo, NY 14260, USA*

³ *Department of Electrical Engineering, University at Buffalo, Buffalo, NY 14260, USA*

Email: feiyao@buffalo.edu

Keywords: 2D materials, electrochemical energy storage, and conversion

Abstract

Compared with their 3D counterparts, two-dimensional (2D) van der Waals (vdW) materials exhibit quantum confinement where charge carriers are spatially confined at the physical boundaries. Particularly, when mixing 2D materials with other low-dimensional (LD) materials, they exhibit enormous potential in electrochemical energy applications due to the unique properties arising from reduced dimensionality and, more importantly, material integration synergy [1].

In this work, 2D transition metal dichalcogenides (MoS₂) and their mixed low-dimensional hybrids (MLDHs) are introduced with an emphasis on the hybrid structure construction using the one-step solvothermal synthesis technique (Fig. 1) and their electrochemical applications. Fundamental insight into the synergistic effect of the MLDHs integration in terms of active site exposure, surface area enlargement, electrical conductivity improvement, and structural phase engineering for advancing the development of Li-ion batteries (LIBs) and electrocatalytic hydrogen evolution reaction (HER) will also be discussed. Specifically, in the case of LIBs, 2D-based binary hybrids (i.e., MoS₂/MXene) deliver a Li-ion storage capacity of 540 mA h g⁻¹ at 100 mA g⁻¹ and a stable cycle performance up to 300 cycles, as shown in Fig. 2 [2]. In sharp contrast, the 2D-based ternary MLDHs (i.e., MoS₂/MXene/CNT) exhibit a higher Li-ion storage capacity (1500 mAh g⁻¹ at 100 mA g⁻¹), outstanding cycle stability (up to 300 cycles) and excellent rate capability (500 mAh g⁻¹ at 4000 mA g⁻¹) as an anode of LIBs. In the case of HER, the MLDH heterostructures show an overpotential of 169 mV with a low Tafel slope of 51 mV/dec and can be cycled to 1000 cycles (Fig. 3) [3]. Leveraging the unique microreactor platform (Fig. 4) based on the 2D vdW platform, a mechanistic understanding of charge transport dynamics at the electrified electrode and current collector interface will be highlighted.

The knowledge gained on how mixed-dimensional physics and chemistry will shed light on the design principle of the electrode materials for electrochemical energy storage and conversion and deepen the understanding of the process-structural-property-performance (PSPP) relationship of the vdW-based hybrid structures.

[1] F. Yao *et al.*, MRS Bulletin, just accepted.

[2] F. Yao *et al.*, ACS Appl. Mater. Interfaces 14, 35673–35681, 2022.

[3] F. Yao *et al.*, npj 2D Materials and Applications 6 (1), 25, 2022.

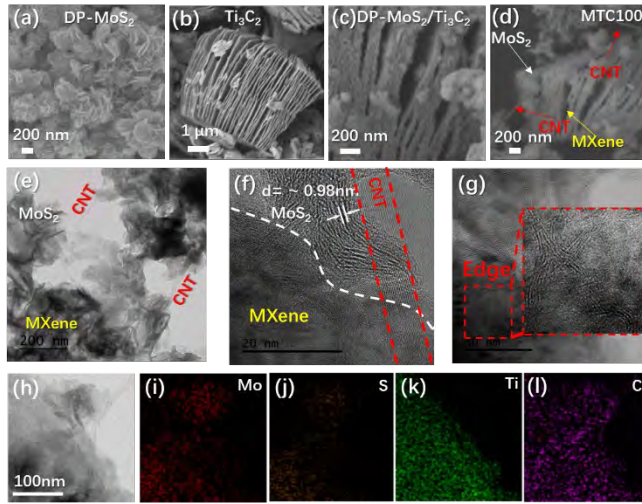


Fig.1: Morphology characterizations of different 2D vdW-based samples. (a)-(d) are the SEM images of pure IT enriched-MoS₂, MXene, MoS₂/Ti₃C₂, and ternary MoS₂/Ti₃C₂/CNT composites, respectively. (e) and (f) are the TEM image and HRTEM image of the ternary composite, respectively. The corresponding EDS elemental mapping is shown in (h)-(l).

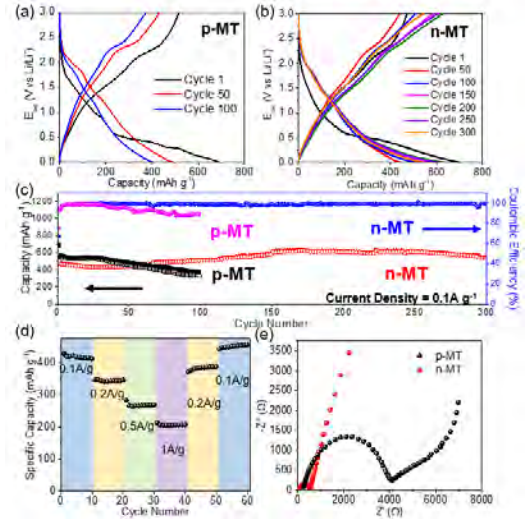


Fig.2: Battery anode performance of 2D vdW-based binary nanohybrids. Galvanostatic charge/discharge profiles of (a) pristine and (b) lithiated MoS₂/Ti₃C₂ nanohybrids. Cycling (c), rate performance (d), and Nyquist plot (e) of the above samples.

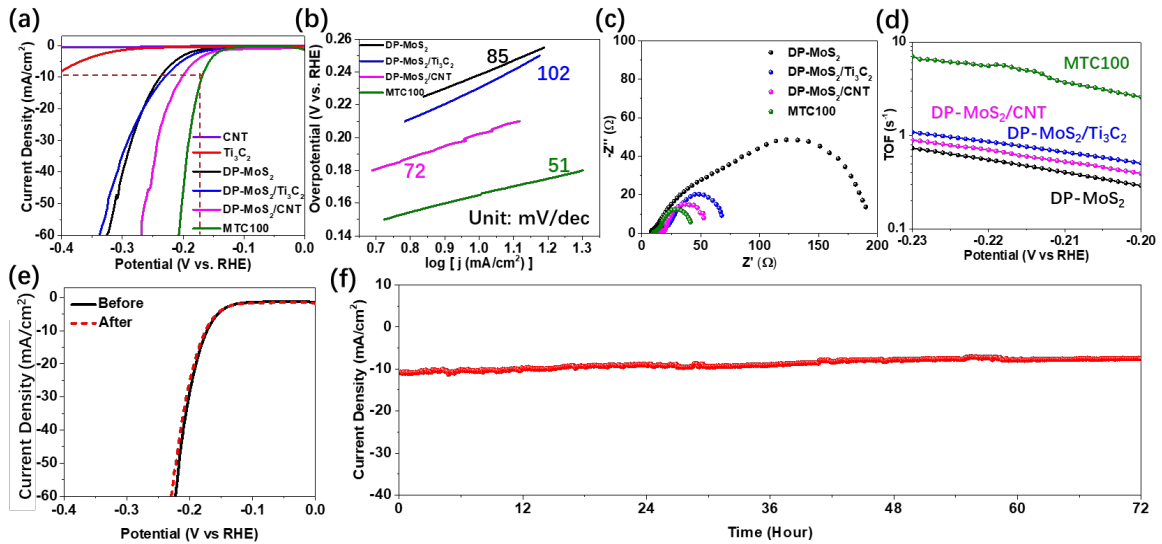


Fig. 3. Electro catalysis performance of 2D vdW-based ternary MoS₂/Ti₃C₂/CNT composites. (a) Polarization curves measured at a scan rate of 5 mV/s and (b) Tafel plots for selected samples. (c) The Nyquist plot of different samples. (d) The turnover frequency versus potential plot. (e) The polarization curves before and after 1000 cycles of CV scans. (f) The time-dependent stability plot.

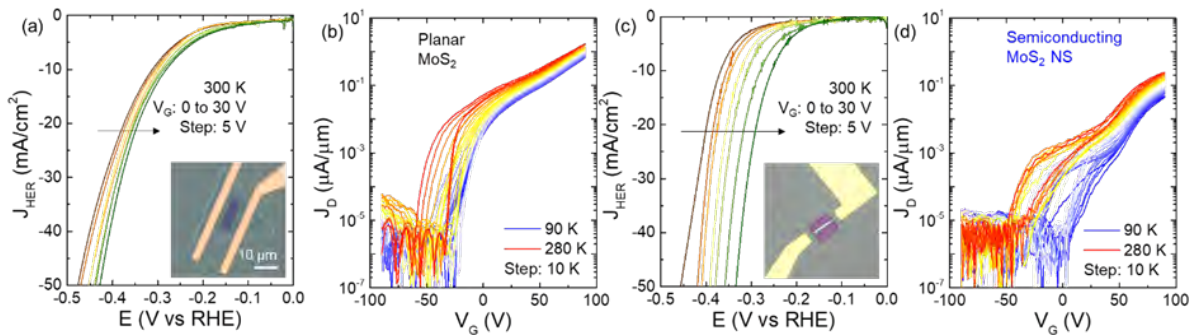


Fig. 4: The electrochemical catalyst performance of MoS₂-based nanostructures. The LSV curves of basal plane (a) and nanoscroll (NS) devices (c) at different gate voltages. (b) and (d) are temperature dependence of the field-effect carrier transport properties shown in (a) and (b), respectively.

Chiral optical nanocavity with atomically thin mirrors

Daniel G. Suárez-Forero¹, Ruihao Ni², Supratik Sarkar¹, Mahmoud Jalali Mehrabad¹,
 Mohammad Hafezi¹ and You Zhou²

¹*Joint Quantum Institute (JQI), University of Maryland, College Park, MD 20742, USA*

²*Department of Materials Science and Engineering, University of Maryland, College Park,
 MD 20742, USA
 mjalalim@umd.edu*

Keywords: 2d materials, light-matter interactions

A fundamental requirement for photonic technologies is the ability to control the confinement and propagation of light. Widely utilized platforms include 2D optical microcavities in which electromagnetic waves are confined between either metallic or multi-layer distributed Bragg reflector dielectric mirrors. However, the high losses in metallic mirrors and fabrication complexities of thick Bragg reflectors have motivated the quest for efficient and compact mirrors. Recently, 2D transition metal dichalcogenides hosting tightly bound excitons with high optical quality were shown as promising atomically thin mirrors (a, b). In this work [3], we propose and experimentally demonstrate a sub-wavelength 2D nanocavity using two atomically thin mirrors (c-f). Remarkably, we show how the excitonic nature of the mirrors enables the formation of chiral tunable cavity modes upon the application of an external magnetic field (g). Our work establishes a new regime for engineering intrinsically chiral sub-wavelength optical cavities and opens avenues for realizing spin-photon interfaces and exploring chiral many-body cavity electrodynamics.

- [1] G. Scuri, Y. Zhou, A. A. High, D. Wild, C. Shu, K. D. Greve, L. A. Jauregui, T. Taniguchi, K. Watanabe, P. Kim, M. D. Lukin, H. Park, *Phys. Rev. Lett.* 120, 037402 (2018)
- [2] P. Back, S. Zeytinoglu, A. Ijaz, M. Kroner, A. Imamoglu, *Physical Review Letters* 120, 037401 (2018).
- [3] Daniel G Suárez-Forero, Ruihao Ni, Supratik Sarkar, Mahmoud Jalali Mehrabad, Erik Mechtel, Valery Simonyan, Andrey Grankin, Kenji Watanabe, Takashi Taniguchi, Suji Park, Houk Jang, Mohammad Hafezi, You Zhou, arXiv:2308.04574 (2023).

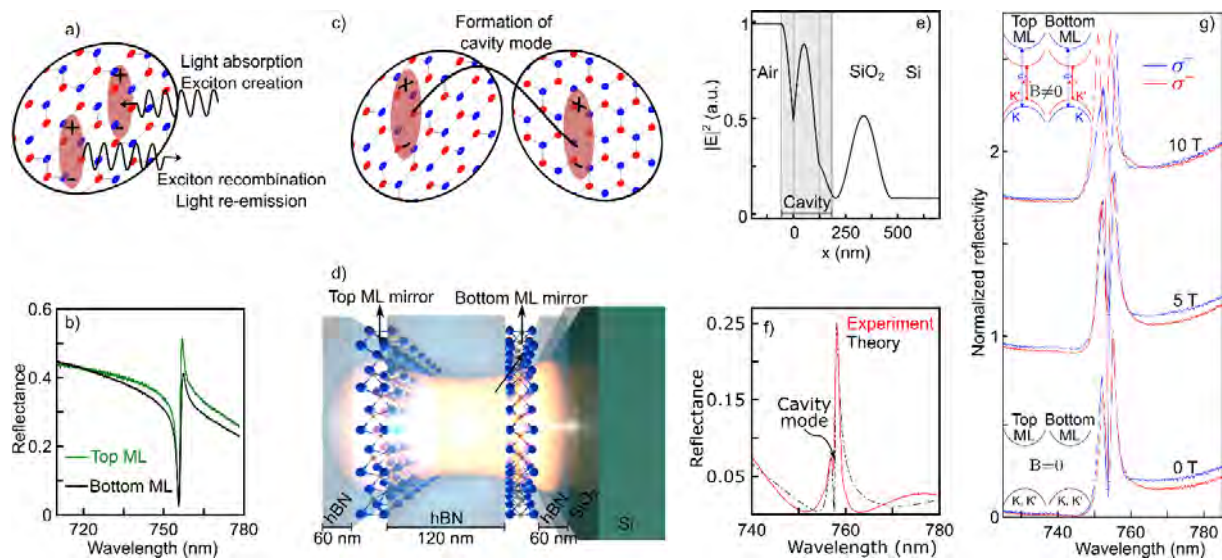


Fig.1: (a-c) Optically induced excitons formed in the 2D layers entail high reflectivity in each TMD ML and form an excitonic cavity when vertically stacked. (d) Schematic of the nanocavity formed from the two layers spaced by hBN. (e) Electric field profile of the nanocavity. (f) Theoretical and experimental spectrum of the cavity mode. (g) Magnetically induced chirality of the nanocavity modes [3].

Can the qubit frequency remain finite even under the very strong Lamb shift from an infinite number of electromagnetic modes?

K. Semba

*National Institute of Information and Communications Technology,
4-2-1, Nukui-kitamachi, Koganei, Tokyo 184-8795, Japan
semba@nict.go.jp*

Keywords: light-matter interactions, superconductivity

We report a qubit frequency that is suppressed by nearly two orders but still finite, observed in a multimode microwave resonator - superconducting flux qubit system in the deep-strong coupling (DSC) regime, where the qubit-resonator coupling strength is comparable to or larger than the qubit and resonator frequencies. The qubit frequency is strongly renormalized by the multimode Lamb shift [1]. The system comprises a superconducting flux qubit (FQ), marked by the dashed orange rectangle in Fig.1, and a quarter-wavelength coplanar waveguide resonator ($\lambda/4$ CPWR) that are coupled inductively through a shared edge, shown as the red part in Fig. 2. The shared edge contains a Josephson junction to enhance the coupling and achieve the DSC regime. Fig. 3 shows the transmission spectrum around the fundamental mode frequency. In the analysis of the observed spectrum, we used the single-mode quantum Rabi Hamiltonian that describes a flux-qubit coupled to the fundamental mode ω_1 of the resonator:

$$\mathcal{H}_1 = -\frac{1}{2}(\Delta'_0\sigma_x + \varepsilon\sigma_z) + \omega_1 a_1^\dagger a_1 + g_1\sigma_z(a_1 + a_1^\dagger) \quad (1)$$

Note that we take $\hbar = 1$. Here, Δ'_0 is a partially renormalized qubit energy i.e., the renormalization from the higher modes other than the fundamental mode are all included. ε is the flux bias. g_1 is the coupling constant of the flux-qubit to the fundamental mode. A strongly renormalized 01 transition of the system is directly observed in Fig. 3b.

In addition to the experimental measurements, we perform theoretical calculations to investigate the naturally occurring high-frequency cutoff in this circuit [2]. As a result, the coupling strength between the qubit and resonator modes increases with mode frequency ω as $\sqrt{\omega}$ at low frequencies and decreases as $1/\sqrt{\omega}$ at high frequencies. We derive expressions for the multimode-resonator-induced Lamb shift in the qubit's characteristic frequency. Because of the natural decoupling between the qubit and high-frequency modes, the Lamb-shift-renormalized qubit frequency remains finite.

[1] Z. Ao, S. Ashhab, F. Yoshihara, T. Fuse, K. Kakuyanagi, S. Saito, T. Aoki & K. Semba, *Scientific Reports* **13**, 11340 (2023).

[2] S. Ashhab, Z. Ao, F. Yoshihara, K. Semba, arXiv:2308.07849

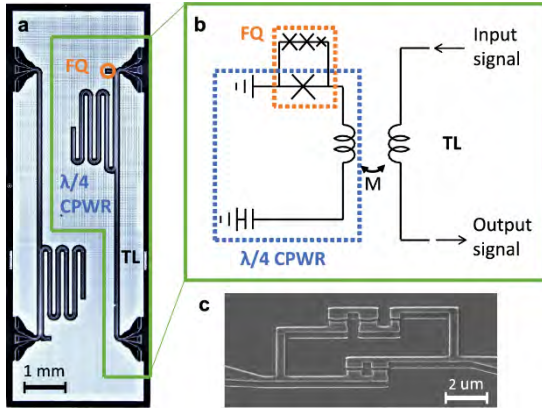


Figure 1 (a) Microscope image of the sample chip. (b) Model of a measurement system. The CPWR is inductively coupled to a transmission line (TL) through the mutual inductance M . The spectroscopy signal is input from one side of the TL and the output signal transmitted to the other side is measured. (c) SEM image of the qubit loop. From Figure 1 of Ref. [1]

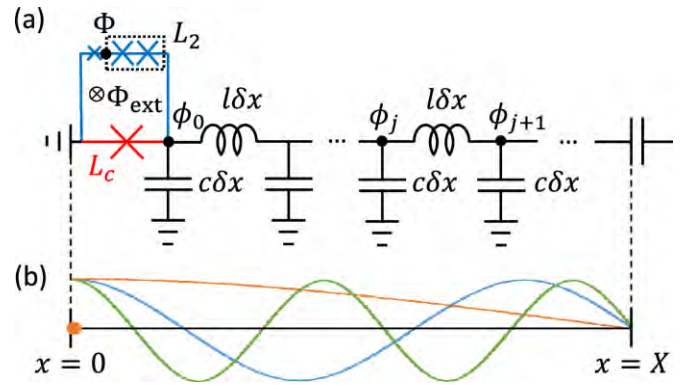


Figure 2 (a) Schematic model of the measured system. The loop formed by the blue and red segments is the FQ loop, while the black and red parts form the CPWR. (b) Three Low-frequency modes in the CPWR. The color of the lines indicates the fundamental (orange), third (blue), and fifth (green) modes. The orange dot indicates the location of the qubit. From Figure 3 of Ref. [1]

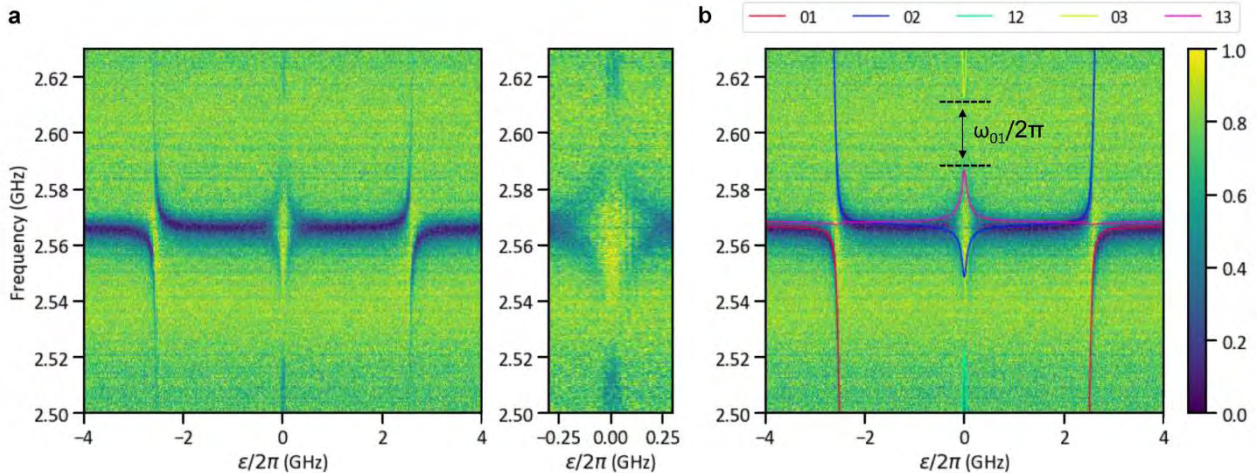


Figure 3 (a) Measured transmission spectrum around the CPWR fundamental mode frequency. The wide panel shows the spectrum over a relatively wide range of flux bias values, while the narrow panel shows a close-up around the symmetry point. The x-axis is the flux bias, relative to the symmetry point, in frequency units. The y-axis is the probe frequency. (b) Same spectrum along with theory curves and the optimized fitting parameters in the Eq. (1): $\omega_1/2\pi = 2.57$ GHz, $\Delta'_0/2\pi = 0.147$ GHz and $g_1/2\pi = 2.39$ GHz. The labels of the theory curves indicate the transitions between pairs of energy eigenstates. For example, the pair 01 means the transition from the ground state $|0\rangle$ to the first excited state $|1\rangle$ of the system. The frequency ω_{01} is the renormalized qubit frequency calculated from the theory curve. The color bar shows the normalized amplitude of the measured output signal. From Figure 2 of Ref. [1]

Strong Coupling of Cd₃As₂ Ribbons and Photons in a Terahertz Photonic Crystal Cavity

T. Aikawa, R. Yahiaoui, P-Y. Chen, Z.A. Chase, and T.A. Searles*

*Department of Electrical and Computer Engineering, University of Illinois at Chicago,
Chicago, IL 60607, USA
tsearles@uic.edu*

Keywords: light-matter interactions, plasmonics

Strong coupling (SC) is a phenomenon that has been observed in various physical systems that have applications in low loss on-chip communication, nonlinear harmonic generation, imaging, and will be important for the architecture of quantum computing. [1,2] It will become increasingly important that this phenomenon is explored in the terahertz (THz) region as it offers a greater communications bandwidth than that is available at microwave frequencies. In this study we present a 200 nm thick ribbon of Cd₃As₂ sandwiched between two quartz slabs capped with a 200 nm thick aluminum coating having precisely cut slits creating a Fabry-Perot resonator with a plasmonic cavity (Fig. 1). This system produces an excitation of a bound states in the continuum (BIC) mode that strongly couple the cavity to the Cd₃As₂ ribbon (Fig. 2a) where the lower polariton and upper polariton are located at 0.372 THz and 0.444 THz. The contour plot of Fig. 2b shows anti-crossing between the upper and lower polaritons. At zero-detuning, a rabbi splitting (Ω_R) of 0.09 shows a value very close to the ultrastrong coupling (USC) region ($\Omega_R > 0.1$) and that slight modifications to the geometries of the slit could push it into the USC region. The Q-factor (Fig. 2c) of the device is highest at a slit length of ~200 μm . In all, we show an enhanced light-matter interaction that can be utilized for various optical applications via BIC modes in a small, compact device.

[1] S. Joseph *et al.*, *Nanophotonics* **10**, (2021).

[2] A. Blais *et al.*, *Phys Rev. A* **69**, 062320 (2004).

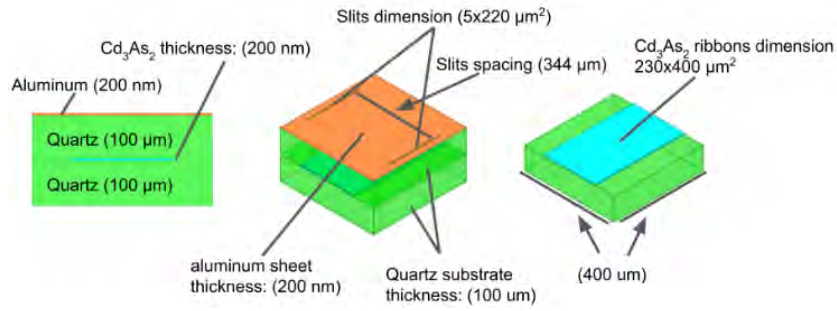


Fig. 1. Schematic of the Cd₃As₂ plasmonic cavity.

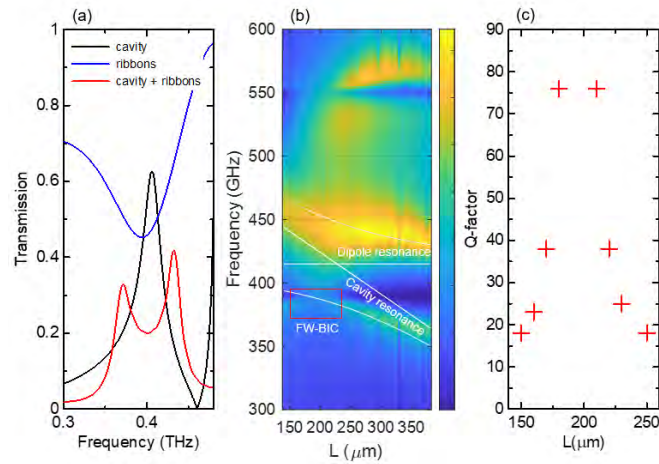


Fig. 2. (a) Transmission versus Frequency plot of the Cd₃As₂ plasmonic-cavity system (red), Cd₃As₂ ribbon (blue), and cavity (black). (b) Conour plot of the Cd₃As₂ plasmonic-cavity system showing the anti-crossing behaviour of the upper and lower polaritons. (c) Quality factor of the cavity eigenmodes close to the BIC.

Superfluorescence-induced optical force in structural environment

H. Shiraki¹, N. Yokoshi², H. Ishihara^{3,4}

¹*Product Reliability, Osaka Research Institute of Industrial Science and Technology, Osaka 594-1157, Japan*

²*Department of Physics and Electronics, Osaka Metropolitan University, Osaka 599-8531, Japan*

³*Department of Materials Engineering Science, Osaka University, Osaka 560-8531, Japan*

⁴*Center for Quantum Information and Quantum Biology, Osaka University, Osaka 560-8531, Japan*

shiraki.hirofumi@orist.jp (e-mail address of the corresponding author)

Keywords: plasmonics (, nanostructures)

Dense quantum emitters in a population inversion state exhibit cooperative emission (superfluorescence) due to their correlated polarizations. Superfluorescence exhibits three main characteristics [1]: the peak intensity of the superfluorescence pulse proportional to the square of the emitter number (N^2), pulse width inversely proportional to N , and the coherence and the directionality (see Figs. 1 and 2). We have designed the properties of superfluorescence, such as emission intensity [2] and directionality [3], by enhancing the correlations between the emitters through environmental structures.

In this study, we discussed optical forces exerted on individual emitters during superfluorescence. Spontaneous emission from asymmetrical emitters or environment generates optical force on emitters. Despite being intuitive, the study of this optical force is still limited. In addition, the behavior of optical forces on emitters during cooperative optical effects in superfluorescence and their motion are completely unknown and not trivial. Thus, we have formulated and applied optical forces from superfluorescence to diverse systems.

We examined force due to superfluorescence on emitters using a simple model. Figure 4 shows the dynamics of the forces acting on the emitters in Fig. 3. The force at each position tends to separate the emitters. In addition, force dynamics correlate with superfluorescence emission pulses. Due to the small absolute magnitude of the force, individual emitters don't visibly shift during a single superfluorescence instance. However, through repeated superfluorescence, optical forces induce significant emitter movement. We also found that a metallic structure can lead to an order of magnitude increase (see Figs. 5 and 6). In this contribution, we will discuss the force due to superfluorescence in more complex systems. We will consider, on a sufficiently long-time scale, how the emitters move under the effects of the environmental structure.

[1] R. H. Dicke, Phys. Rev. **93**, 99 (1954).

[2] H. Shiraki, N. Yokoshi, and H. Ishihara, Phys. Rev. A **106**, 053511 (2022).

[3] H. Shiraki, N. Yokoshi, and H. Ishihara, J. Phys. Soc. Jpn. **92**, 024402 (2023).

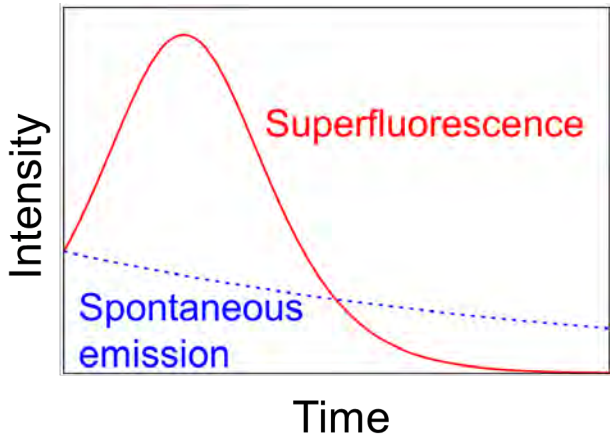


Fig. 1: Time profile of intensity of superfluorescence (solid line) and spontaneous emission (dashed line). Spontaneous emission decreases exponentially, whereas superfluorescence exhibits strong pulsed emission.

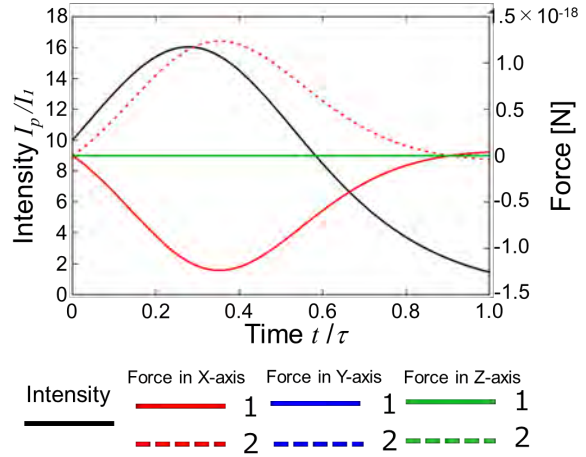


Fig. 4: Time profile of the emission intensity and the forces in each direction exerted on the emitters at the two sites (see legend). The forces in the Y-axis (blue line) and Z-axis (green line) directions are 0.

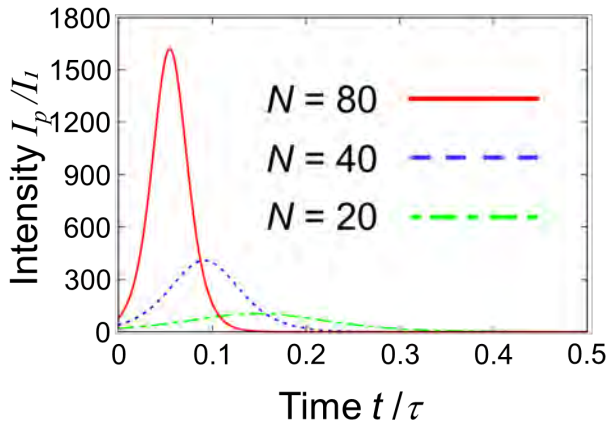


Fig. 2: Peak value of emission intensity is proportional to the square of the number of emitters N and pulse width is proportional to $1/N$. We normalized emission intensity n_p and time using I_1 and τ which is the radiative lifetime of the emitter in a vacuum.

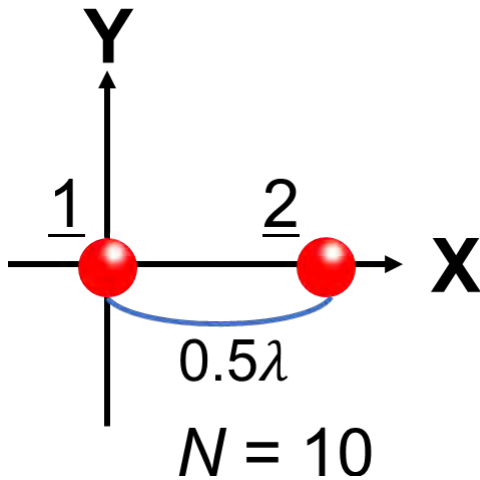


Fig. 3: Schematic diagram of emitters placement for the demonstration calculation of the optical force. We placed 5 emitters in each of the two sites (interval is 0.5λ), i.e., the total number of emitters is $N=10$.

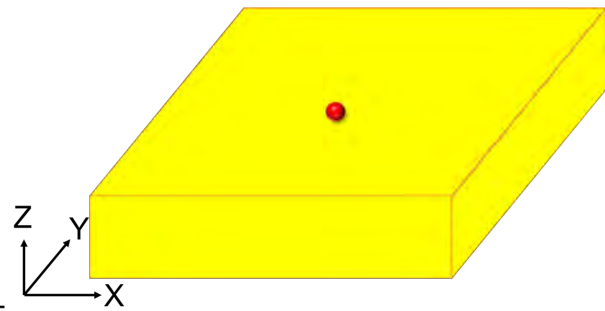


Fig. 5: Schematic diagram of the calculation model. We placed emitters ($N=10$) on a metallic structure (Au).

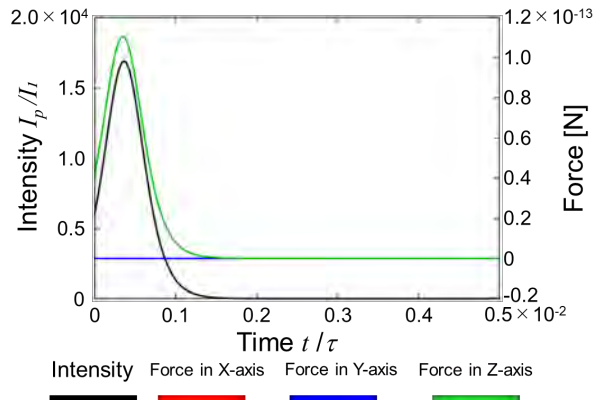


Fig. 6: Time profile of the emission intensity and the forces in each direction exerted on the emitters placed on the metallic structure. The forces in the X-axis (red line) and Y-axis (blue line) directions are orders of magnitude smaller than the forces in the Z-axis direction (green line).

Enhanced optical nonlinearity in graphene nanomeshes

F. Karimi, S. Mitra^{*}, S. Soleimanikhanj, and I. Knezevic

Department of Electrical and Computer Engineering,

University of Wisconsin-Madison, Wisconsin, USA 53706, USA

**smitra8@wisc.edu*

Keywords: quantum materials, light-matter interactions

The interest in nonlinear optical phenomena in nanomaterials is driven not only by scientific curiosity, but also by interest in applications in the field of telecommunication, namely in optical switching, ultrafast optical modulators, as well as biosensing applications. Graphene, an extensively studied two-dimensional (2D) material, has third-harmonic nonlinear optical susceptibility in the range of $10^{-15} \text{ m}^2\text{V}^{-2}$ in the near-infrared frequency range [1]. Here, we present a theoretical study of increasing third-order nonlinear optical response of graphene nanomeshes by patterning graphene with antidots [2]. With proper selection of antidot periodicity, it is possible to excite plasmonic modes as the antidots aid momentum matching necessary to launch plasmonic waves. Graphene nanomeshes can be designed to behave as quasi-one dimensional plasmonic crystals with a large plasmon propagation length.

The plasmonic excitation in a graphene nanomesh are achieved using a TM-polarized wave guided along the x-direction as shown in Figure 1. The electric field along the plasmon-propagation direction can induce surface plasmon polaritons. The time evolution of the electron density matrix, which reveals plasmonic excitations, is calculated using the master-equation formalism [3]. The electron transport is limited by scattering with intrinsic acoustic and optical phonons, ionized impurities, surface optical phonons, and antidot-edge roughness (AER). AER is the dominant scattering mechanism that governs the magnitude of enhancement of the third-order response.

Figure 2(a) shows the loss function as a function of Fermi energy and frequency. Each branch has forward and backward modes. Figures 2(b)-2(d) show the loss function, third-order Kerr and third-harmonic generation (THG), respectively, as function of frequency for a fixed Fermi energy. Figures 2(e)-2(g) represent the same quantities as a function of Fermi energy at 1550 nm wavelength. Our results show third-order Kerr and THG susceptibility as high as 10^{-7} and $10^{-9} \text{ m}^2\text{V}^{-2}$ respectively, a factor of six improvement over unpatterned graphene. In addition, the forward and backward wave switching can be controlled by changing the doping density via gating, thus paving the way toward all-optical switching and modulation.

[1] E. Hendry *et al.*, Phys. Rev. Lett. **105**, 097401 (2010).

[2] F. Karimi *et al.*, Phys. Rev. B **108**, 035414 (2023).

[3] F. Karimi *et al.*, Phys. Rev. B **93**, 205421 (2016).

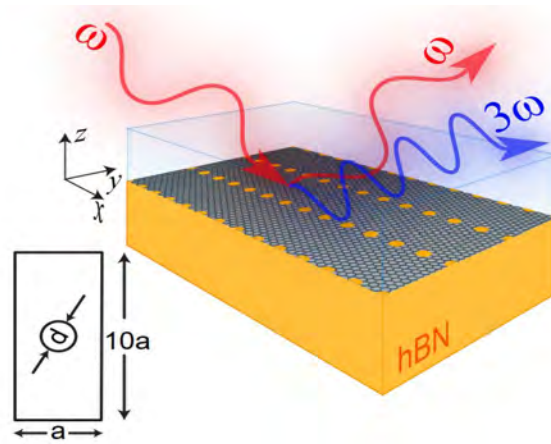


Fig. 1: Schematic representation of the graphene nanomesh structure on top of hBN substrate. Excitation requires TM polarized light with an electric-field component along the x -direction, which is also the propagation direction of the plasmonic wave. Inset shows antidot periodicity $a = 100$ nm and $10a$ along x - and y -directions, respectively, so the nanomesh behaves as a quasi-one-dimensional plasmonic crystal. Each antidot has diameter $d = 30$ nm. Reprinted with permission from F. Karimi, S. Mitra, S. Soleimanikahnoj, and I. Knezevic, *Phys. Rev. B* 108, 035414 (2023).

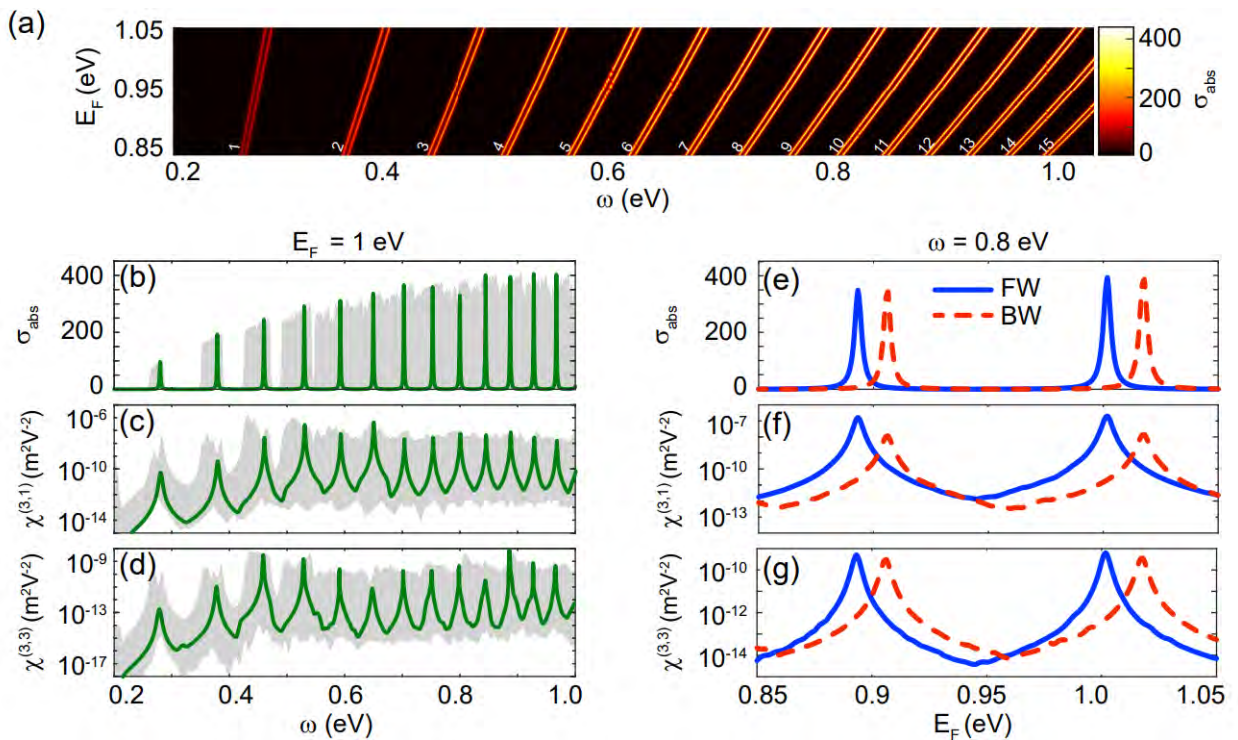


Fig. 2: (a) Loss function of GNM on hBN substrate as function of frequency and Fermi energy. Each branch has forward and backward propagating modes. (b) Loss function, (c) magnitude of third-order Kerr, and (d) magnitude of THG at different frequencies for fixed $E_F = 1$ eV. (e)-(g) The same quantities at different Fermi energies for $\omega = 0.8$ eV. The blue and red lines correspond to forward and backward propagating modes. Reprinted with permission from F. Karimi, S. Mitra, S. Soleimanikahnoj, and I. Knezevic, *Phys. Rev. B* 108, 035414 (2023).

Distinctive high-temperature light emission originating from one-dimensional excitons of carbon nanotubes

T. Nishihara

Institute of Advanced Energy, Kyoto University, Uji, Kyoto 611-0011, Japan.

nishihara.taishi.8x@kyoto-u.ac.jp

Keywords: light-matter interactions, nanostructures

High temperature light emission phenomena in nanostructured materials has attracted much attention in various fields ranging from fundamental science to device applications [1]. Nanostructured materials often exhibit spectrally narrow-band high-temperature light emission reflecting manipulated electronic and/or photonic structures, as opposed to uncharacteristic broadband thermal radiation of bulk materials e.g., blackbody radiation; this characteristic potentially enables highly efficient and functional use of thermal energy such as thermophotovoltaic (TPV) [1]. Among nanostructured materials, for one-dimensional (1D) system in which quasi-particles mainly move only along one axis, the fundamental quantum aspects on their high-temperature light emission properties remained still unclear due to some technical difficulties in experiments.

Here, we will show our recent works on high-temperature light emission of single-walled carbon nanotubes (SWCNTs) [2,3]. SWCNTs are ultrathin cylinders composed of an sp^2 -bonded hexagonal network of carbon atoms, which can be either semiconductors or metals depending on their structure. Recently, we have demonstrated that a semiconducting one exhibits narrow-band near-infrared thermal radiation [2,3] using individual nanotube microscopy [4,5], and it is enabled by exciton states that are hydrogen-like electron-hole pairs (Fig. 1). While excitons are observed in typical bulk semiconductors only at low temperature, even thermal radiation properties above 1,800°C are dominated by excitons in SWCNTs owing to their huge binding energy. In SWCNT assemblies [6] (Fig. 2), this distinct excitonic feature are preserved in SWCNTs' assemblies, which are expected to be a material for wavelength-selective thermal emitter that is a core component of TPV. In this presentation, we will discuss universal features of high temperature light emission of 1D system including metallic species under current injection.

- [1] D. M. Bierman, E. N. Wang *et al.*, *Nat. Energy* **1**, 16068 (2016).
- [2] T. Nishihara, A. Takakura, Y. Miyauchi, K. Itami, *Nat. Commun.* **9**, 3144 (2018).
- [3] S. Konabe, T. Nishihara, Y. Miyauchi, *Opt. Lett.* **46**, 3021 (2021).
- [4] A. Takakura, T. Nishihara, Y. Miyauchi, K. Itami *et al.*, *Nat. Commun.* **10**, 3040 (2019).
- [5] T. Nishihara, A. Takakura, K. Matusi, K. Itami, Y. Miyauchi, *Nano Lett.* **14**, 5818 (2022).
- [6] T. Nishihara, A. Takakura, Y. Miyauchi *et al.*, *Nanophotonics* **11**, 1011(2022).

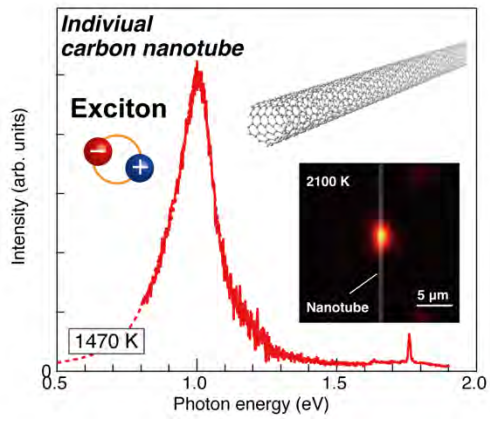


Fig.1: Narrow-band near-infrared thermal radiation of an individual single-walled carbon nanotube, enabled by exciton states.

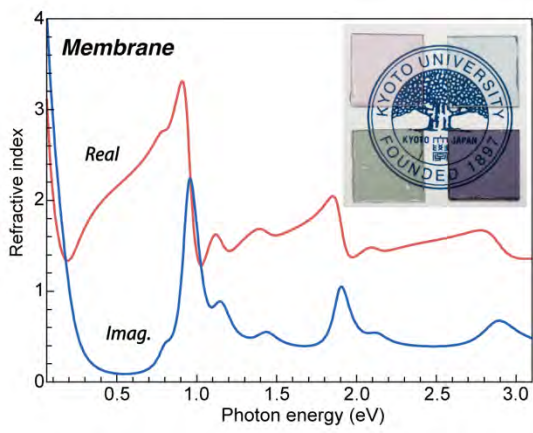


Fig.2: Complex refractive index spectra of carbon nanotube membrane with single chirality.

Single Photon Emitters in 2D Materials

Berend T. Jonker*

Naval Research Laboratory, Washington DC 20375, USA

e-mail: berry.jonker@nrl.navy.mil

Keywords: 2D materials, quantum information

Single photon emitters (SPEs), or quantum emitters, are key components in a wide range of nascent quantum-based technologies. A solid state host offers many advantages for realization of a functional system, but creation and placement of SPEs are difficult to control. We describe here a novel paradigm for encoding strain into 2D materials to create and deterministically place SPEs in arbitrary locations with nanometer-scale precision [1]. We demonstrate the direct writing of SPEs in monolayer WSe₂ using an atomic force microscope nano-indentation process. This *quantum calligraphy* allows deterministic placement and real time design of arbitrary patterns of SPEs for facile coupling with photonic waveguides, cavities and plasmonic structures. Because monolayer WSe₂ is a direct gap semiconductor, SPE emission at a given wavelength is often intermixed with classical light resulting from conventional excitonic recombination, reducing the purity of the quantum emission as quantified by the second order autocorrelation function $g^{(2)}(t=0)$. We show that this undesirable classical emission, arising primarily from defect bound excitonic processes, can be significantly suppressed by electrostatic gating [2] or incorporating the WSe₂ layer in a simple van der Waals heterostructure [3]. Suppression of this classical emission allows a more accurate assessment of the quantum emission character, and results in values of $g^{(2)}$ as low as 0.07 at low temperature. In addition, the SPE intensity at a given wavelength can be strongly modulated by changing the polarity of the gate bias, a feature of technological importance for practical applications. Initial results for SPEs in hBN will also be summarized, time permitting.

[1] M.R. Rosenberger et al, *ACS Nano* **13**, 904 (2019). <https://doi.org/10.1021/acsnano.8b08730>

[2] C.E Stevens et al, *ACS Nano* **16**, 20956 (2022). <https://doi.org/10.1021/acsnano.2c08553>

[3] H.-J. Chuang et al, under review (2023).

*Work done in collaboration with Matthew R. Rosenberger (*Notre Dame*), Hsun-Jen Chuang, Sungjoon Lee and Kathleen M. McCreary (*Naval Research Laboratory*), and Christopher Stevens and Joshua R. Hendrickson (*Air Force Research Laboratory, Wright-Patterson AFB*).

† This work was supported by core programs at NRL.

Enabling Efficient Photon-Mediated Operations Between Spectrally Different Quantum Bits

Herbert F Fotso¹

¹*Department of Physics, University at Buffalo SUNY, Buffalo, New York 14260, USA*

hffotso@buffalo.edu

Keywords: light-matter interactions, quantum information

The discrepancy across properties of the many systems that have separately emerged as successful implementations of quantum bits (or qubits) for quantum information processing (QIP), and their varying efficiencies in key QIP operations raise an important challenge for future QIP technologies. Scalable QIP platforms will most likely be hybrid in nature, with different qubit modalities being utilized for their most advantageous properties. For this reason, optimal light-matter interfaces between different systems are of critical importance. Promising systems include photons, trapped ions, superconducting circuits, quantum dots, nitrogen vacancy centers and other color centers. Besides operating at different frequencies, for certain qubit modalities such as those in the solid state, even when they are nominally identical, the operating frequencies can, despite impressive advances in materials/device manufacturing, feature important variability from one instance to another. We discuss efforts to supplement device manufacturing by designing external field control protocols that can enhance the efficiency of critical photon-mediated operations in QIP. In particular, we aim to demonstrate increased efficiency of two-qubit operations between spectrally different qubits by applying suitable external control fields. We have shown that a periodic sequence of π pulses applied to a two-level system in a dynamic environment can result in an emission that occurs mostly at the pulse carrier frequency [1, 2]. Thus modulating the emission frequency and suppressing spectral diffusion. Through enhanced spectral overlap, as shown in the figures below, this protocol is shown to restore photon indistinguishability between two emitters with different emission frequencies, as indicated by the intensity correlation at the detectors in the Hong-Ou-Mandel two-photon interference operation [3].

[1] H. F. Fotso, A. E. Feiguin, D. D. Awschalom and V. V. Dobrovitski, “Suppressing Spectral Diffusion of Emitted Photons with Optical Pulses,” *Phys. Rev. Lett.* **116**, 033603 (2016).

[2] Herbert F Fotso, “Tuning Spectral Properties of Individual and Multiple Quantum Emitters in Noisy Environments,” *Phys. Rev. A* **107**, 023719 (2023).

[3] H. F. Fotso, “Pulse-enhanced two-photon interference with solid state quantum emitters,” *Phys. Rev. B* **100**, 094309 (2019).

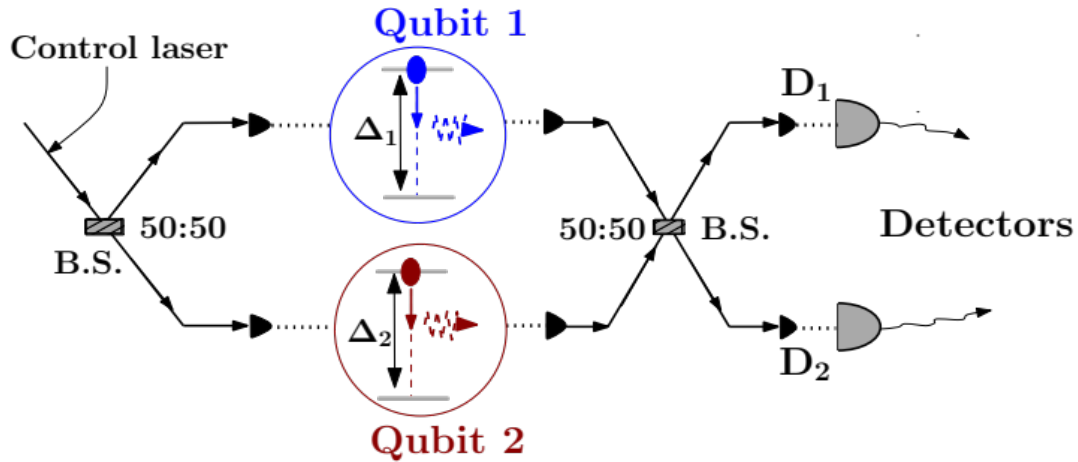


Fig. 1:

Schematic of the pulse-enhanced two-photon Interference from two distant quantum emitters. At spacetime locations 1 and 2, photons from Qubit 1 and Qubit 2 with respective detunings Δ_1 and Δ_2 measured in the frame rotating at the set target frequency ω_0 are sent to input ports of a 50:50 beam splitter and then measured at detectors D_1 and D_2 at spacetime locations 3 and 4. Indistinguishable photons will coalesce and emerge at the same port. The control laser applies a periodic sequence of π pulses, with period τ , to both emitters.

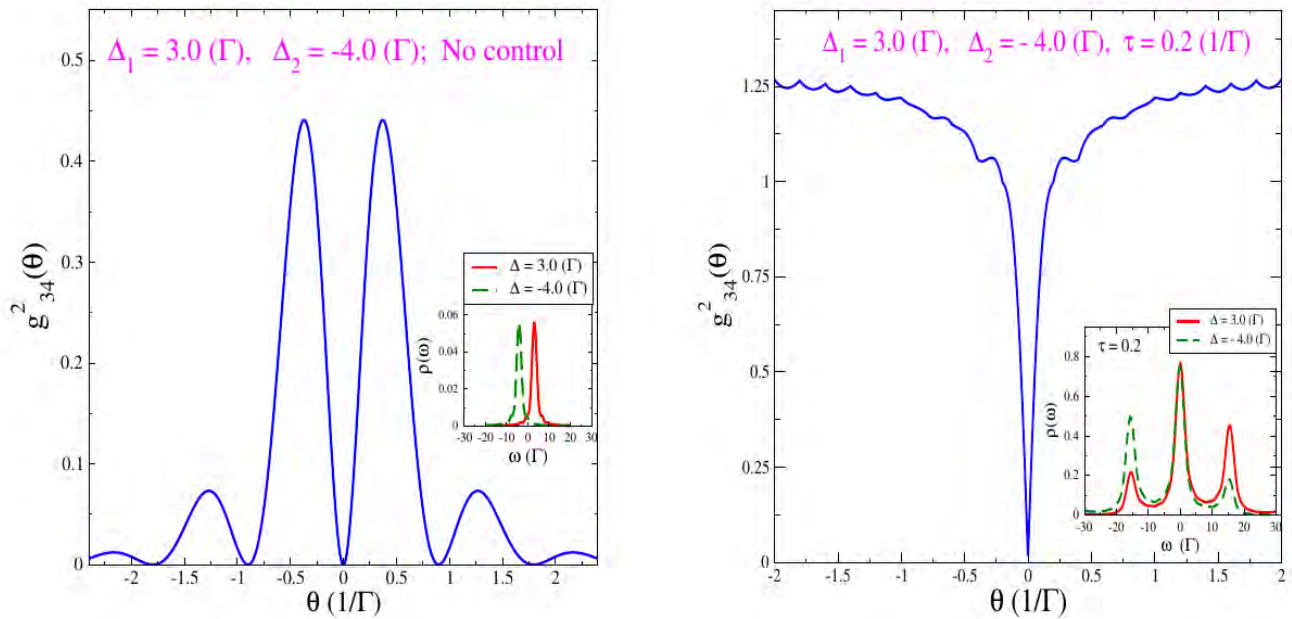


Fig. 2: (From Ref [3]) Intensity correlation at the detectors in the absence of a control protocol (Left) and in the presence of a periodic sequence of π -pulses with period $\tau = 0.2$ (Right) with two independent emitters with detunings $\Delta_1 = 3.0$ and $\Delta_2 = -4.0$ respectively. The insert shows the emission spectra of individual emitters with detunings $\Delta_1 = 3.0$ (solid red line) and $\Delta_2 = -4.0$ (dashed green line). In the absence of any control protocol, they both have Lorentzian line-shapes centered around their respective detunings and have limited spectral overlap. The intensity correlation vanishes at $\theta = 0$ and periodically at $\theta = 2n\pi/\Delta_{21}$, n integer and $\Delta_{21} = |\Delta_2 - \Delta_1|$. When the emitters are simultaneously driven by the same periodic pulse sequence, their emission spectra overlap; the intensity correlation is zero at $\theta = 0$ and finite elsewhere. All energies are measured in unit of Γ , the spontaneous emission rate, and in a frame rotating at the pulse carrier frequency ω_0 . Similarly, times are measured in units of $1/\Gamma$.

Fusion and Braiding of Majorana Zero Modes in Topological Planar Josephson Junctions

Tong Zhou^{1,2,*}, Jong E. Han², Alex Matos-Abiague³, Javad Shabani⁴, and Igor Žutić²

¹*Eastern Institute for Advanced Study, Eastern Institute of Technology, Ningbo, China*

²*Department of Physics, University at Buffalo, State University of New York, Buffalo, USA*

³*Center for Quantum Phenomena, Department of Physics, New York University, USA*

⁴*Department of Physics and Astronomy Wayne State University Detroit, USA*

**e-mail: tzhou@eitech.edu.cn*

Keywords: superconductivity, topology

Majorana zero modes (MZM) with their nonlocal degrees of freedom and non-Abelian statistics have been viewed as a promising candidate for achieving fault-tolerant topological quantum computing. However, despite intensive efforts, experimental support for MZM remains indirect and does not probe their crucial non-Abelian statistics. Here, building on recent experimental advances in two-dimensional semiconductor Josephson junctions (JJs) [1-3], we reveal how to overcome this obstacle in mini-gate controlled JJs and demonstrate non-Abelian statistics through MZM fusion, detected by charge sensing using a quantum point contact [4]. We also propose a novel platform of X-shaped JJs [5], where external flux control of the superconducting phase difference can generate and braid MZM. The feasibility of our proposed preparation, braiding, and fusion of MZM is supported in the fabricated InAs/Al-based JJs and verified by dynamical simulations. Our proposals to identify elusive non-Abelian statistics, as an important milestone towards topological quantum computing, stimulate also further MZM studies in other 2D systems with similar control.

[1] A. Fornieri, *et al.*, *Nature* **569**, 89 (2019).

[2] H. Ren, *et al.*, *Nature* **569**, 93 (2019).

[3] M. Dartiailh, *et al.*, *Phys. Rev. Lett.* **126**, 036802 (2021).

[4] T. Zhou, *et al.*, *Nat. Commun.* **13**, 1738 (2022).

[5] T. Zhou, *et al.*, *Phys. Rev. Lett.* **124**, 137001 (2020).

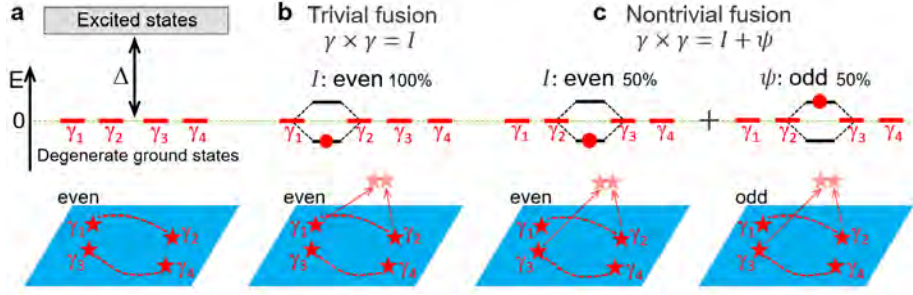


FIG. 1. Schematic of fusion rules. (a) Topological superconductor (blue) hosting MBS, γ_{1-4} . They behave as non-Abelian anyons and lead to the four-fold degeneracy in topological ground states, separated by the energy gap, Δ , from the trivial excited states. (b) and (c) Different fusion outcomes: trivial fusion of 1 and 2, 100% probability to access vacuum, I (Cooper pair condensate), and nontrivial fusion of 2 and 3, equal probabilities to access I or an unpaired fermion, ψ . Red dashed lines: paired MBS. In each case bringing closer MBS leads to the level splitting from the initial zero energy modes.

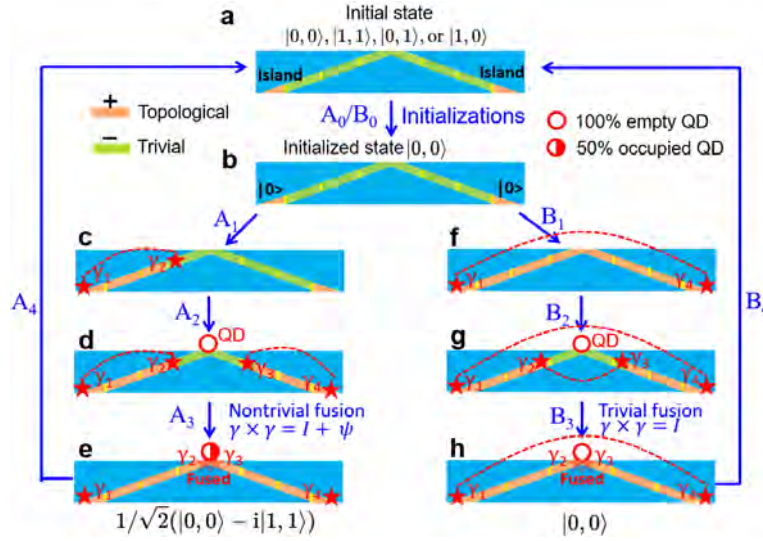


FIG. 2. Probing non-Abelian statistics through MBS fusion in a V-shaped junction (VJ) coupled with a detection quantum dot (QD). The stars indicate the MBS, and the dashed lines link the same MBS pair. (a) Initial trivial state with four possible occupations ($|00\rangle$, $|11\rangle$, $|01\rangle$, and $|10\rangle$) in $-----$ mini gates with V_L and V_R quantum islands. (b) A_0/B_0 : Initialization, where the initial state $|00\rangle$ is prepared. (c) A_1 : changing $-----$ to $++++$, MBS pair (γ_1, γ_2) is created. (d) A_2 : changing $++++$ to $++++$, a second MBS pair (γ_3, γ_4) is created. Then coupling a QD at the apex and making the QD unoccupied (e) A_3 : changing $++++$ to $++++$, the MBS (γ_2, γ_3) are nontrivially fused at the center. As a result, the occupation changes into the superposition of $|00\rangle$ and $|11\rangle$, accessing both vacuum, I , and an unpaired fermion, ψ , with 50% probability. After A_3 , the QPC is used to detect the QD charge number and zero and one charge with the same probability is expected. (f) B_1 : changing $-----$ to $++++$, the MBS (γ_1, γ_4) are created. (g) B_2 : changing $++++$ to $++++$, a second MBS pair (γ_2, γ_3) is created. Then coupling the QD at the apex and making the QD unoccupied. (h) B_3 : changing $++++$ to $++++$, the MBS (γ_2, γ_3) are trivially fused and the occupation is the same as the initial $|00\rangle$, corresponding to I with 100% probability. After B_3 , the QPC is used to detect the QD charge number and zero charge is expected. A_4/B_4 : Reset the system: changing $++++$ to $-----$, and decouple the VJ with the QD. As a result, the system returns to the initial two quantum island states. MBS fusion can be repeated following such operations.

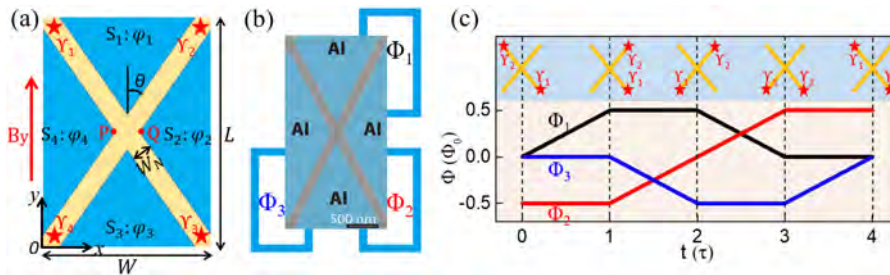


FIG. 3. Schematic of MBS Braiding. (a) X-shaped junction (XJ) schematic formed by epitaxial superconducting (S) regions (blue) covering a 2DEG (yellow). MBS γ_{1-4} (stars) are obtained through modulating the phase differences between ϕ_{1-4} . (b) SEM image for the XJ with schematic external fluxes Φ_1 , Φ_2 , and Φ_3 . (c) MBS exchange with fluxes, τ is the switching time, and Φ_0 is the magnetic flux quantum.

Colloidal Quantum Dot Laser Diodes: Three Decades in the Making

Victor I. Klimov

Nanotechnology and Advanced Spectroscopy Team, C-PCS, Chemistry Division, Los Alamos National Laboratory, Los Alamos, NM 87545, USA

Keywords: light-matter interactions, nanostructures

It has been 30 years since the first demonstration of lasing with semiconductor nanocrystals embedded in glass matrices [1] – the samples akin to standard colored glass filters. Following this discovery, it took three years to realize lasing with epitaxial QDs [2] and six more years to demonstrate the effect of amplified spontaneous emission (ASE) – a precursor of lasing – with colloidal QDs [3].

So far, all reported studies into colloidal QD lasing have utilized optically excited samples. However, most of the prospective technological applications require electrically pumped devices, that is, laser diodes. The realization of such devices has been complicated by multiple problems, widely deemed insurmountable. These include extremely fast nonradiative Auger recombination of optical-gain-active multicarrier states, poor stability of QD films under high current densities required for lasing, and unfavorable balance between optical gain and optical losses in electroluminescent (EL) devices wherein a gain-active QD medium is a small fraction of an overall device stack comprising multiple optically lossy charge-transport layers.

Here we resolve these problems and achieve strong ASE with electrically driven QDs (Figure 1) [4]. To demonstrate this effect, we employ compact continuously graded QDs (ccg-QDs) with strongly suppressed Auger recombination incorporated into a low-loss Bragg-reflector waveguide (BRW) integrated into a pulsed light-emitting diode (LED) with a current focusing charge-injection architecture capable of generating current densities (j) of up to $\sim 2000 \text{ A cm}^{-2}$. These prototype ASE-type laser diodes exhibit strong, broad-band optical gain and demonstrate low-threshold, room-temperature ASE which leads to bright edge-emitted EL whose instantaneous intensity reaches $\sim 2 \text{ kW cm}^{-2}$.

- [1] Vandyshv, Y. V., Dneprovskii, V. S., Klimov, V. I. & Okorokov, D. K. Lasing on a transition between quantum-well levels in a quantum dot. *JETP Lett.* **54**, 442-445 (1991).
- [2] Kistaedter, N., Ledentsov, N. N., Grundmann, M., Bimberg, D., Ustinov, V. M., Ruvimov, S. S., Maximov, M. V., Kopev, P. S., Alferov, Z. I. & Richter, U. Low threshold, large T0 injection laser emission from (InGa)As quantum dots. *Electron. Lett.* **30**, 1416 (1994).
- [3] Klimov, V. I., Mikhailovsky, A. A., Xu, S., Malko, A., Hollingsworth, J. A., Leatherdale, C. A., Eisler, H. J. & Bawendi, M. G. Optical gain and stimulated emission in nanocrystal quantum dots. *Science* **290**, 314-317 (2000).
- [4] Ahn, N., Livache, C., Pinchetti, V., Jung, H., Hahm, D., Park, Y.-S. & Klimov, V. I. Electrically Driven Amplified Spontaneous Emission from Colloidal Quantum Dots. *Nature* **617**, 79 (2023).

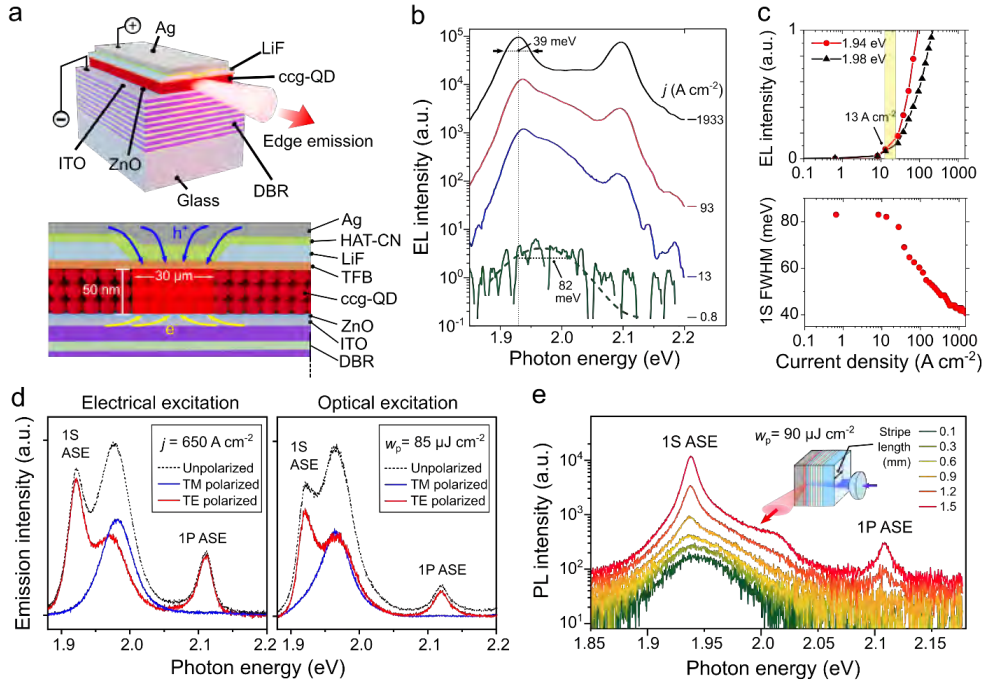


Figure 1. Electrically driven ASE in an LED-like QD device comprising a photonic waveguide. **a**, The device stack is built on top of a distributed Bragg reflector (DBR) made of 10 pairs of Nb_2O_5 and SiO_2 layers (60 and 100 nm thickness, respectively). The DBR and the top silver (Ag) electrode/mirror form a low-loss photonic Bragg-reflector waveguide (BRW). The charge-injection architecture comprises an indium tin oxide (ITO) cathode, a ZnO electron-transport layer, a ccg-QD gain medium (3 QD-monolayers), an organic (TFB) hole transport layer, a LiF interlayer with a rectangular aperture ($30 \times 300 \mu\text{m}^2$) for current focusing, an organic (HAT-CN) hole injecting layer, and an Ag anode. **b**, A progression of edge-emitted electroluminescence (EL) spectra of the BRW device as a function of current density (j) tuned from 0.8 to 1933 A cm^{-2} . The device is excited using pulsed bias with pulse duration $\tau_p = 1 \mu\text{s}$ and pulse-to-pulse separation $T = 1 \text{ ms}$. These spectra show a transition from broad spontaneous emission (82 meV linewidth) observed at low j to sharp 1S and 1P ASE bands (39 meV linewidths) at high j . **c**, (Top) A comparison of j -dependent EL intensities at the peaks of the 1S spontaneous (black) and ASE (red) bands indicates the ASE threshold $j_{\text{th,ASE}} \approx 13 \text{ A cm}^{-2}$. (Bottom) The dependence of 1S emission linewidth on j indicates progressive line narrowing from 82 to 39 meV, typical of the ASE regime. **d**, Polarization characteristics of edge-emitted light of the BRW device in the case of electrical (left, $j = 650 \text{ A cm}^{-2}$) and optical (right, $w_p = 85 \mu\text{J cm}^{-2}$) excitation confirm the ASE origin of sharp emission features. While nonpolarized emission is dominated by a broad 1S spontaneous band, in the TE emission, the sharp 1S and 1P features, attributed to ASE, overshoot spontaneous emission. None of the sharp ASE features is present in the TM polarized spectrum, which corresponds to the “lossy” plasmon-polariton-like mode not capable of supporting the ASE regime. **e**, The variable-stripe-length (VSL) measurements of the optically excited BRW device (inset) indicate the development of the 1S and 1P ASE features with increasing stripe length (l). These measurements utilized 110-fs, 3.6-eV pump pulses with $w_p = 90 \mu\text{J cm}^{-2}$. The sharp ASE bands revealed by the VSL measurements are similar to those observed in the high- j EL spectra (panel **b**) and exhibit similar polarization characteristics (panel **d**). This affirms the realization of ASE with electrical excitation as ASE is unambiguous in the case of optical pumping.

The Josephson Diode effect

Stuart S.P. Parkin

Max Planck Institute of Microstructure Physics, Halle (Saale), Germany
stuart.parkin@mpi-halle.mpg.de

Recently we have discovered a non-reciprocal Josephson diode effect in several Josephson junctions, both lateral and vertical, formed from conventional superconducting electrodes (Nb, NbSe₂) separated by several non-superconducting metals including the 2D van der Waals metals, NiTe₂ [1] and WTe₂ [2], as well as sputtered layers of platinum that are magnetically proximitytized via a magnetic insulator (YIG) [3]. Each of these materials becoming superconducting by proximity to the conventional superconducting electrodes. The superconductivity can be sustained over long distances of, in some cases, up to ~1 micron. The critical supercurrent densities for current flowing in opposite directions within the junction are distinct and can vary by up to 40% or more. For the van der Waals metals the non-reciprocity is only observed in the presence of a small magnetic field oriented perpendicular to the supercurrent, whereas for the Pt based junctions the diode effect is observed in zero field. For vertical Josephson junctions formed from WTe₂ we show that the non-reciprocity depends on the orientation of the magnetic field with respect to the crystal structure of the WTe₂, proving thereby the intrinsic origin of the Josephson diode effect. Such an effect could have important applications as a novel magnetic field detector at cryogenic temperatures, for example, to “read” magnetic domain walls in a cryogenic racetrack memory*.

* Funded through an European Research Council Advanced Grant “SUPERMINT” (2022-2027).

- [1] B. Pal *et al.*, "Josephson diode effect from Cooper pair momentum in a topological semimetal," *Nat. Phys.*, vol. 18, pp. 1228-1233, 2022.
- [2] J.-K. Kim *et al.*, "Intrinsic supercurrent non-reciprocity coupled to the crystal structure of a van der Waals Josephson barrier," *arXiv:2303.13049*, 2023.
- [3] K.-R. Jeon *et al.*, "Zero-field polarity-reversible Josephson supercurrent diodes enabled by a proximity-magnetized Pt barrier," *Nat. Mater.*, vol. 21, pp. 1008-1013, 2022.

Harnessing Laser-Driven Excitations to Control Polarization Switching in Ferroelectric Materials

Bryan M. Wong

Materials Science & Engineering Program, Department of Chemistry, and Department of Physics & Astronomy, University of California-Riverside, Riverside, CA, USA

bryan.wong@ucr.edu

Keywords: light-matter interactions, oxides and ferroelectrics

To enhance the efficiency of next-generation ferroelectric (FE) electronic devices, new techniques for controlling ferroelectric polarization switching are required. While most prior studies have attempted to induce polarization switching via the excitation of phonons, these experimental techniques required intricate and expensive terahertz sources and have not been completely successful. Here, we propose a new mechanism for rapidly and efficiently switching the FE polarization via laser-tuning of the underlying dynamical potential energy surface. Using time-dependent density functional calculations, we observe an ultrafast switching of the FE polarization in BaTiO₃ within 200 fs. A laser pulse can induce a charge density redistribution that reduces the original FE charge order. This excitation results in both desirable and highly directional ionic forces that are always opposite to the original FE displacements. Our new mechanism enables the reversible switching of the FE polarization with optical pulses that can be produced from existing 800 nm experimental laser sources.

Robust and skin-attachable memristor synaptic array for pattern and real-time finger motion recognition

Gunuk Wang

¹ *KU-KIST Graduate School of Converging Science and Technology, Korea University, 145 Anam-ro, Seongbuk-gu, Seoul 02841, Republic of Korea*

² *Department of Integrative Energy Engineering, Korea University, 145 Anam-ro, Seongbuk-gu, Seoul 02841, Republic of Korea*

Keywords: Neuromorphic, advanced devices, flexible electronics

For sustainable advancements in electronics technology, the field of neuromorphic electronics, i.e., electronics that imitate the principle behind biological synapses with a high degree of parallelism, has recently emerged as a promising candidate for novel computing technologies [1]. Toward realizing a massively parallel neuromorphic system, it is essentially required to develop an artificial synapse capable of emulating various synaptic functionality, such as short- and long-term synaptic plasticity with ultralow power consumption and robust controllability [1]. In this talk, I will present uniform and reliable titanium oxide (TiO_x) memristor array devices as constituent device element for in situ hardware neural network [1] and real-time finger motion recognition [2]. In particular, in situ convolutional neural network hardware system is designed and implemented using a multiple 25×25 TiO_x memristor arrays (Fig. 1). The learning rate modulable fast-converging in situ training based on direct memristor operation shows five times less training iterations and reduces training energy compared to the conventional hardware in situ training at $\approx 95.2\%$ of classification accuracy [2]. In addition, an integrated TiO_x memristor array and organic motion sensor that can be conformably attached to a finger and provide real-time motion recognition will be presented [3]. We demonstrate that finger motions for time-resolved digit patterns (0–9) can be learned and recognized with an accuracy of up to 95% at varying strains and up to 100 strain cycles [3].

[1] S. Choi, J. Yang, and G. Wang* **Adv. Mater.** 20044659 (2020).

[2] J. Jang[†], S. Gi[†], I. Yeo, S. Choi, S. Jang, S. Ham, B. Lee* and G. Wang* **Adv. Sci.** 2201117 (2022).

[3] H. Cho[†], I. Lee, J. Jang[†], J.-H. Kim, H. Lee, S. Park* and G. Wang* **Nature Electronics.** in press (2023).

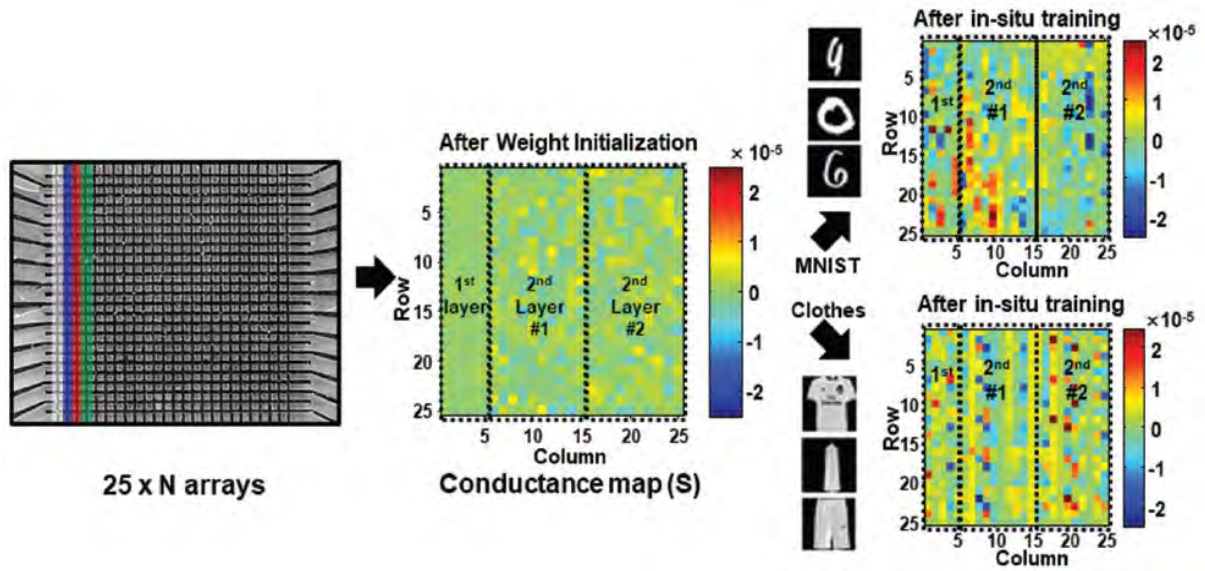


Fig. 1 Implementation of kernel matrix with differential memristor array pairs and an analog conductance map before and after in situ training for two different image data sets (MNIST and Clothes). [2]

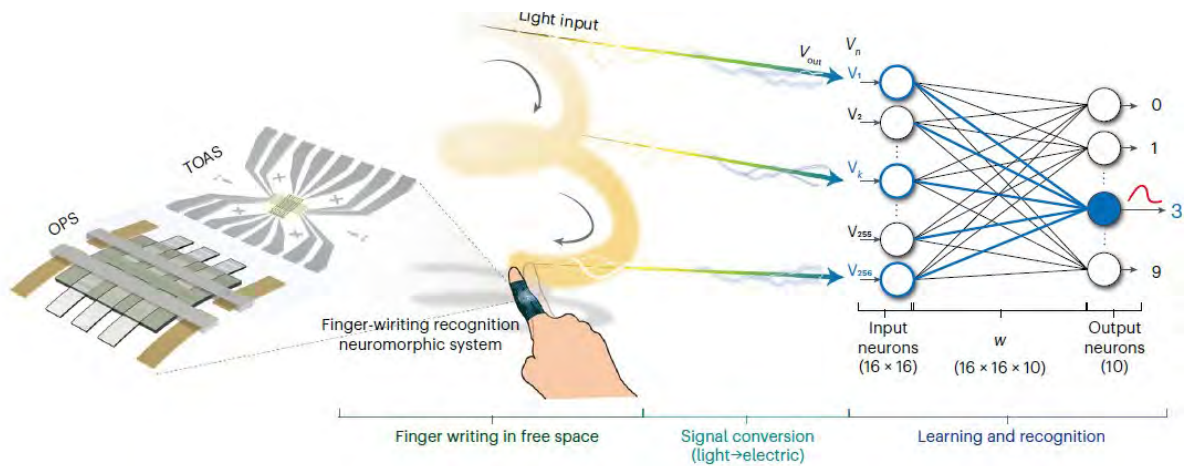


Fig. 2 Schematic of finger-writing recognition neuromorphic system in 3D free space under exposure to light based on the integration of the OPS-TOAS device. [3]

Data-informed prior for Bayesian state tomography

S. Regmi^{1,*}, A. A. Davis¹, A. N. Blackwell¹, A. Khannejad¹, D. E. Jones⁵, R. T. Glasser⁴, J. M. Lukens^{2,3}, S. Lohani¹, B. T. Kirby^{4,5}, T. A. Searles¹

¹*University of Illinois Chicago, Chicago, IL 60607, USA*

²*Arizona State University, Tempe, AZ 85287, USA*

³*Oak Ridge National Laboratory, Oak Ridge, TN 37831, USA*

⁴*Tulane University, New Orleans, LA 70118, USA*

⁵*DEVCOM Army Research Laboratory, Adelphi, MD 20783, USA*

*sangita@uic.edu

Keywords: Machine Learning, Bayesian Technique, Quantum State Tomography, Quantum Hardware

Machine learning (ML) has been extensively applied within the domain of quantum information science, covering areas such as experimental design, state classification, and even explorations into the foundations of quantum physics. In this study, we showcase a learning-based approach to fine-tune prior distributions in Bayesian quantum state reconstruction on table-top optical setup and near-term intermediate-scale quantum hardware. While Bayesian quantum state tomography has been sought after due to its unique advantages, such as natural uncertainty quantification, the ability to provide reliable estimates under various measurement conditions, and minimal mean-squared error, it has faced practical challenges related to lengthy computation times and conceptual difficulties in effectively integrating prior knowledge. Our approach to selecting prior distributions leverages pre-trained neural networks and enables improved inference over standard prior distributions. Utilizing data collected from an experimental design and near-term intermediate-scale quantum (NISQ) hardware, our method decreases the overall time needed for performing high-precision Bayesian inference. In order to validate the proof of concept under realistic experimental conditions, we employ datasets comprising tomographic measurements from entanglement photon source (EPS), and arbitrary quantum states generated by the *ibmq-jakarta* quantum machine, one of the IBMQ Falcon processors. The results provide a promising avenue for the practical implementation of Bayesian quantum state tomography.

Regmi, S., Blackwell, A. N., Khannejad, A., Lohani, S., Lukens, J. M., Glasser, R. T., ... & Searles, T. A. (2023, June). Bayesian quantum state reconstruction with a learning-based tuned prior. In *Quantum 2.0* (pp. QM4B-3). Optica Publishing Group.

Lohani, S., Lukens, J. M., Davis, A. A., Khannejad, A., **Regmi, S.**, Jones, D. E., ... & Kirby, B. T. (2023). Demonstration of machine-learning-enhanced Bayesian quantum state estimation. *New Journal of Physics*, 25(8), 083009.

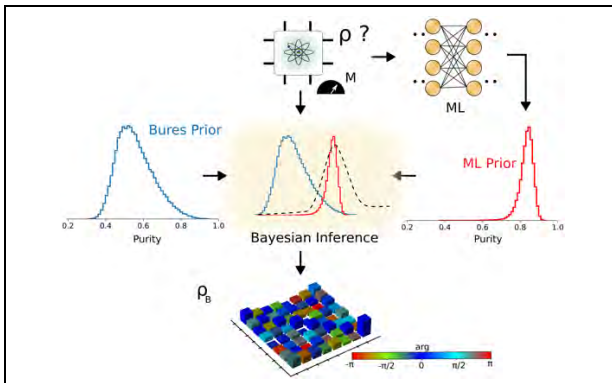


Fig 1: Outline of proposed ML-prior Bayesian estimation method. Shown are the measurement results entering (top of figure) and two different potential prior distributions: a fixed prior in blue (Bures, in this example) and the ML prior, which adapts to measurement results (shown in red). The dashed line represents the actual probability density function of the experimental scenario and emphasizes that the Bures prior is unchanged while the ML-prior distribution adapts by incorporating information from the measurement results. The output of the system is the Bayesian mean density matrix as shown at the bottom of the figure.

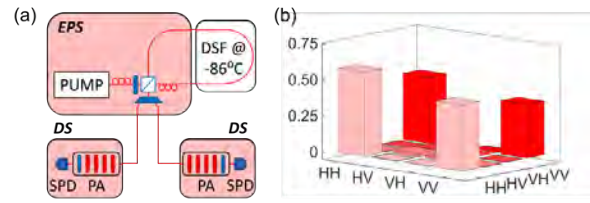


Fig 2: (a) Experimental setup used to compare the purity distribution of states output by a polarization-entangled photon source (EPS) with the ML prior and Bures prior purity distributions. DSF: detector station. PA: polarization analyzer consisting of several wave-plates (red) and a polarizer (blue). SPD: single-photon detector. (b) Real part of an example density matrix calculated by the ML-prior Bayesian estimation method.

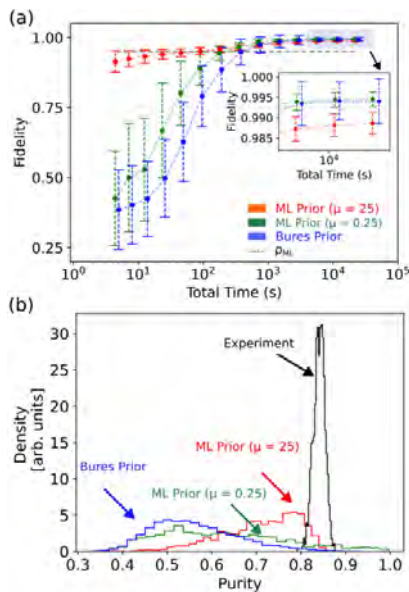


Fig 3: Efficacy of ML-prior method for reconstructing states generated by a polarization-entangled photon pair source. (a) Reconstruction fidelity versus total wall-clock time. (b) Purity distributions for the ML prior, Bures prior, and experimental states. The error bars represent one standard deviation from the mean.

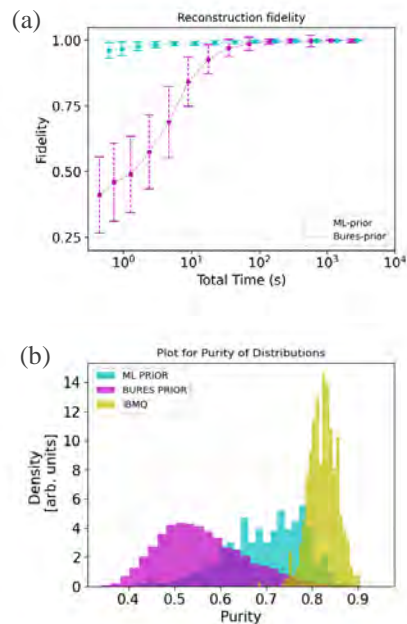


Fig 4: Efficacy of ML-prior method for reconstructing states generated by the IBMQ machine ibmq-jakarta. (a) Reconstruction fidelity versus total wall-clock time. (b) Purity distributions for the ML prior, Bures prior, and IBMQ. The error bars represent one standard deviation from the mean.

Topologically Nontrivial States, Superconductivity, and Ferroelectricity in Few-layer 2M and T_d -TMDs

A. Jindal¹, A. Saha^{2,3}, Z. Li⁴, Y. C. He⁴, A. Strasser⁵, J. C. Hone⁶, T. Biroli³, R. M. Fernandes²,
C. R. Dean¹, A. N. Pasupathy¹, X. F. Qian⁵, and D. A. Rhodes⁴

¹*Department of Physics, Columbia University, New York, NY 10027, USA*

²*School of Physics and Astronomy, University of Minnesota, Minneapolis, MN 55455, USA*

³*Department of Chemical Engineering and Materials Science, University of Minnesota, Minneapolis, MN 55455, USA*

⁴*Materials Science and Engineering Department, University of Wisconsin-Madison, Madison, WI 53706, USA*

⁵*Department of Materials Science and Engineering, Texas A&M University, College Station, TX 77843, USA*

⁶*Department of Mechanical Engineering, Columbia University, New York, NY 10027, USA*
darhodes@wisc.edu

Keywords: 2d materials, superconductivity

In recent years, the 2M and T_d family of transition metal dichalcogenides have been shown, or predicted, to exhibit numerous interesting phenomena: topological superconductivity, quantum spin hall insulator states, and ferroelectricity via interlayer sliding; all tunable by electrostatic doping. Among this family of materials, two stand out: T_d -MoTe₂, which retains a polar crystal structure concomitant with superconductivity and 2M-WSe₂. For MoTe₂, much like WTe₂ [1], we show that the bilayer is ferroelectric and that superconductivity simultaneously exists within the ferroelectric regime [2]. As a result of this coexistence, we observe a field-driven, first-order superconductor-to-normal upon switching of the polarization. Bilayer T_d -MoTe₂ also has a maximum in its superconducting transition temperature, T_c , as a function of carrier density and temperature, allowing independent control of the superconducting state as a function of both doping and polarization. We show that the T_c is maximum when there is compensation of electron and hole carrier densities and that T_c vanishes when one of the Fermi pockets disappears with doping. We interpret this unusual polarization-sensitive superconductivity as being driven by an interband pairing interaction associated with nearly nested electron and hole Fermi pockets. Unlike MoTe₂, for 2M-WSe₂ we show that there is no superconductivity in the few-layer limit. Instead, a band gap opens up, starting at three layers in agreement with expectations from earlier theory [3].

[1] Z. Fei *et al.*, Nature **560**, 336 (2018)

[2] A. Jindal *et al.*, Nature **613**, 48 (2023)

[3] X.F. Qian *et al.*, Science **346**, 1344 (2014)

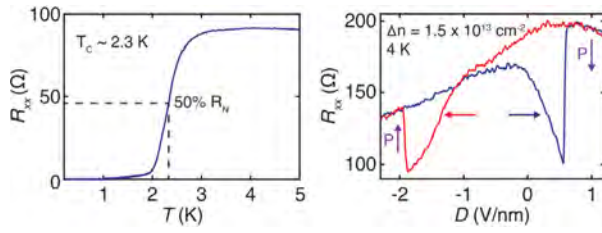


Fig.1: Left, Superconducting transition in bilayer MoTe2 for zero doping. Right, Ferroelectric switching in the normal state in bilayer MoTe₂ with an applied displacement field (D).

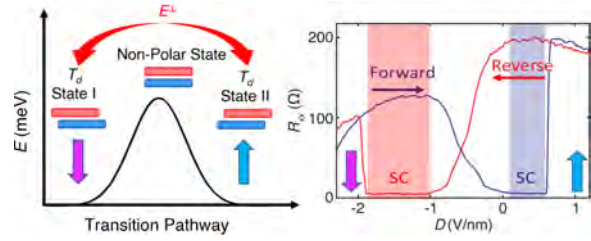


Fig.2: Left, schematic for the transition pathway of the switching of polarization. Right, butterfly loops with bistable normal and superconducting states, indicating coupled ferroelectric and superconducting states. Red and blue arrows denote the direction of the D sweep.

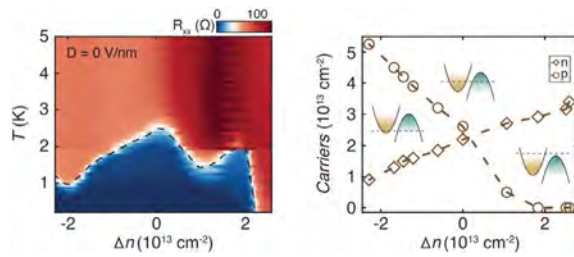


Fig. 3: Evolution of a superconducting dome with electrostatic doping and temperature. Carrier concentration as a function of the gate-induced carrier density, Δn , as extracted by fitting a two-band model to the Hall resistance.

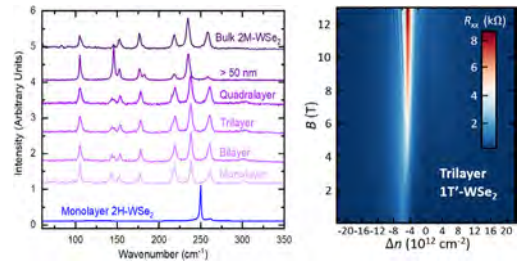


Fig. 4: Left, Comparing Raman spectra of bulk and few-layer 2M-WSe₂ to 2H-WSe₂. Right, Landau fan diagram for trilayer 2M-WSe₂ (isostructural to 1T'). A small gap (~ 5 meV) opens up at $\Delta n = -4 \times 10^{12}$ cm⁻².

Noise mechanisms in short ballistic graphene Josephson junctions

G. Pellegrino^{1,2,3}, G. Falci^{1,2,3} and E. Paladino^{1,2,3}

¹*Dipartimento di Fisica e Astronomia “Ettore Majorana”, Università di Catania, Via S. Sofia
64 I-95123 Catania, Italy*

²*INFN, Sez. Catania, Via S. Sofia 64 I-95123 Catania, Italy*

³*CNR-IMM Catania Univ. Via S. Sofia 64 I-95123 Catania, Italy
elisabetta.paladino@dfa.unict.it*

Keywords: superconductivity, 2d materials, quantum information

The future of quantum technologies lies in hybrid systems achieving multitasking potentialities by combining different physical components with complementary functionalities. In particular, devices based on hybrid Josephson junctions have opened up new possibilities to engineer noise protected qubits being at the same time easily tunable via electrical ports. The recent realizations of graphene-based hybrid systems, such as Josephson junctions (GJJ), make graphene a promising a platform for new generations of devices for topological quantum computing and quantum sensing. To this aim, accurate control of the electronic properties of GJJ in the presence of disorder is essential.

We investigate a short ballistic graphene Josephson junction and show that two points and higher order correlations of carrier density fluctuations of the graphene channel (Fig. 1) lead to fluctuations of the critical current with a characteristic $1/f$ dependence on frequency. Tunability with the Fermi level and temperature dependence of the noise amplitude are clear fingerprints of the underlying material-inherent processes [1], Fig. 2. Remarkably, the same mechanism turns out to be responsible for $1/f$ second spectrum of charge carrier density fluctuations in graphene [2]. These results suggest a roadmap for the analysis of decoherence sources in the implementation of coherent devices by hybrid nanostructures.

In addition, we study the effect of a dilute homogeneous spatial distribution of non-magnetic impurities on the equilibrium supercurrent of the GJJ, see Fig. 3. The potentialities of the supercurrent power spectrum for accurate spectroscopy of the hybridized Andreev bound states-impurities spectrum are highlighted [3].

[1] F. Pellegrino, G. Falci, E. Paladino, *Communication Physics* ,3, 6 (2020).

[2] F. Pellegrino, G. Falci, E. Paladino *Appl. Phys. Lett.* 122, 253102 (2023)

[3] F. Pellegrino, G. Falci, E. Paladino, *Communication Physics*, 5 , 265 (2022).

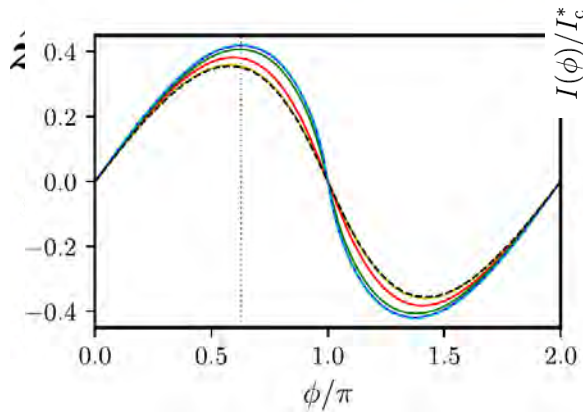


Fig.1: Schematic of the device. a displays the side view, from bottom to top there are a metal gate (green), a substrate (blue), a monolayer graphene (gray), and two superconducting electrodes (yellow). Electron traps are represented with cyan circles randomly distributed inside the substrate. Figure from Ref. [1]

Fig.3: Current-phase relation of a short graphene Josephson junction at zero temperature in the presence of a dilute ensemble of impurities. Colored curves refer to increasing values of the trap energy distribution width (black, yellow, red, green, blue cyan). Figure from Ref. [3]

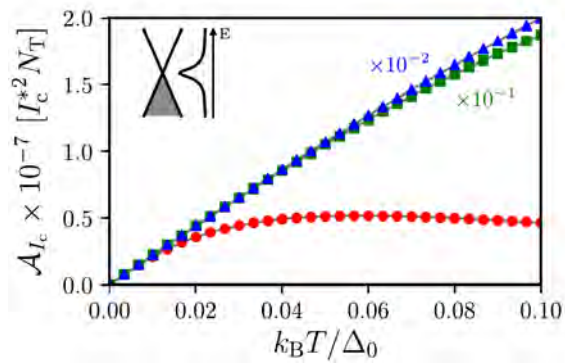


Fig.2: Scaled amplitude of the critical current noise spectrum A_{I_c} as a function of temperature for a trap energy distribution at the charge neutrality point. Different curves correspond to different values of the trap energy distribution width. Figure from Ref. [1]

Tunable Charge Transport at 2D/3D Integrated Interfaces

Simran Shahi¹, Anthony Cabanillas¹, Anindita Chakravarty¹, Asma Ahmed¹, Yu Fu², Chu Te Chen², Fei Yao², and Huamin Li¹

¹*Dept. of Electrical Engineering, University at Buffalo, Buffalo, NY 14260, USA*

²*Dept. of Materials Design and Innovation, University at Buffalo, Buffalo, NY 14260, USA*
huaminli@buffalo.edu

Keywords: 2d materials

With the rise of graphene (Gr), two-dimensional (2D) materials hold a promising future for high-performance energy-efficient nano-electronics, especially through an integration with mature three-dimensional (3D) Si technologies [1-4]. Yet, the impacts of mixed-dimensional interfacial states and metal contacts on the charge transport are still not clear. In this work, we addressed this challenge by investigating the out-of-plane (OoP) charge transport through 2D/3D integrated interfaces. A variety of the 2D monolayers ranging from semimetals (*e.g.*, Gr) to semiconductors (*e.g.*, MoS₂) and insulators (*e.g.*, h-BN) were integrated with 3D Si. The device schematics, microscopy image, and energy band diagram along the OoP direction are illustrated in Fig. 1. Both hybridization and van der Waals (vdW) metal contacts were induced using low and high work function metals (*e.g.*, Ti, Au, and Pd). The 2D monolayers, depending on their thicknesses, bandgaps (E_g), dielectric constants along the OoP direction (ϵ_{OoP}), and equivalent oxide thickness (EOT), play different roles in the OoP charge transport through the 2D/3D integrated interfaces, as shown in Fig. 2. Current-voltage (J - V) characteristics at room temperature for each type of the devices are summarized in Fig. 3. Here Ti provides a hybridized contact with 2D monolayers, whereas Au and Pd maintain a vdW gap between the metal and 2D monolayers [5]. Holes are considered as the majority charge carriers because of the involvement of p-Si for charge transport. The 2D monolayers were electrically transparent for the OoP charge transport from Si to the metals, but governed by either an energy matching (EM) effect or a barrier tunneling (BT) effect for the charge transport in the opposite direction. Furthermore, conductance ($G = \partial J / \partial V_A$) for each type of devices are extracted. The Ohmic carrier transport is also evidenced by the dominance of linearity (~ 1 of the slope) in the logarithmic J - V plots. The deviation from the Ohmic carrier transport in the logarithmic J - V characteristics indicates the possible presence of the trapped (or trap-filled-limited, TFL) and trap-free (or space-charge-limited, SCL) carrier transport mechanisms, which can be attributed to the activation of a variety of defects or disorders involved in the OoP charge transport. Compared to the devices using Gr-enabled EM or Pd contact, the 2D/3D integrations using MoS₂- or h-BN-enabled BT with Ti and Au contact can effectively manipulate the OoP charge transport. By benchmarking with other state-of-the-art MoS₂-based diode devices composed of multi-dimensional materials [6-27], these two devices possess excellent and well-balanced performance to maintain both the high rectification ratio and G simultaneously (up to 5.4×10^4 at 1.3×10^5 S/m² for the Ti-contact MoS₂/Si integration, and 4.3×10^4 at 1.2×10^5 S/m² for the Au-contact MoS₂/Si integration), as shown in Fig. 4. Our work demonstrates the great potential of manipulating the OoP charge transport in the optimized 2D/3D integration, even with only the sub-1-nm thickness of 2D monolayers.

[1] *IEEE IEDM*, 512 (2018). [2] *Nature*, **573**, 507 (2019). [3] *Nat. Mater.*, **18**, 550 (2019). [4] *Nat. Commun.*, **13**, 1392 (2022). [5] *Nat. Mater.*, **14**, 1195 (2015). [6] *Nat. Commun.*, **6**, 6564 (2015). [7] *Adv. Funct. Mater.*, **25**, 5865 (2015). [8] *Appl. Phys. Lett.*, **107**, 183103 (2015). [9] *PNAS*, **110**, 18076 (2013). [10] *Adv. Electron. Mater.*, **5**, 1800976 (2019). [11] *ACS Nano*, **10**, 7451 (2016). [12] *Nano Lett.*, **14**, 4785 (2014). [13] *ACS Nano*, **8**, 8292 (2014). [14] *ACS Nano*, **10**, 3852 (2016). [15] *ACS Appl. Mater. Interfaces*, **10**, 37258 (2018). [16] *Nat. Commun.*, **10**, 4664 (2019). [17] *Nano Lett.*, **14**, 5590 (2014). [18] *Nano Lett.*, **20**, 3651 (2020). [19] *ACS Nano*, **9**, 2071 (2015). [20] *Nano Lett.*, **16**, 1359 (2016). [21] *ACS Nano*, **11**, 9143 (2017). [22] *Nano Res.*, **13**, 1053 (2020). [23] *Mater. Horiz.*, **4**, 274 (2017). [24] *Nanoscale*, **7**, 15442 (2015). [25] *ACS Nano*, **8**, 3042 (2014). [26] *Sci. Rep.*, **4**, 5458 (2014). [27] *Nature*, **526**, 91 (2015).

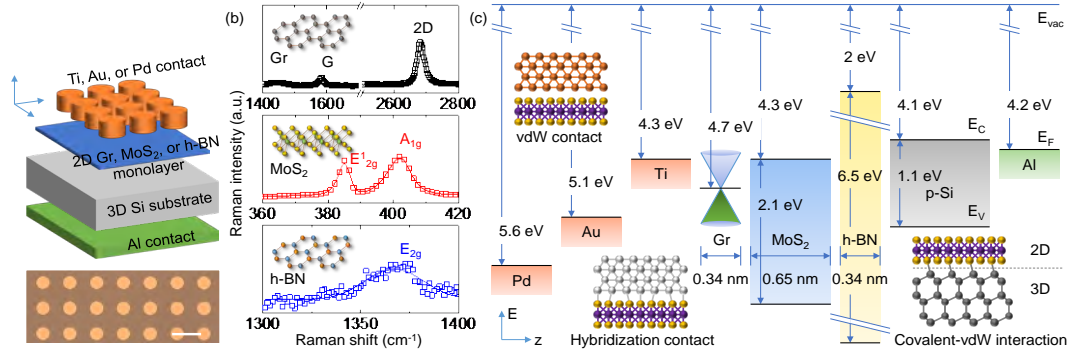


Fig. 1. Large-area 2D/3D integrated junction structures, including (a) schematics of the device structure (top) and a microscopy image (bottom), (b) Raman spectra of the 2D Gr, MoS₂, and h-BN monolayers, and (c) an energy band diagram of the 2D/3D integration along the OoP direction. Here E_{vac} , E_C , E_V , and E_F denote energy at the vacuum, conduction band minima, valence band maxima, and Fermi level, respectively. Schematics of vdw and hybridization contact at metal/2D monolayer interfaces and covalent-vdW interactions at 2D/3D interfaces are also illustrated using 2D MoS₂ monolayer as an example.

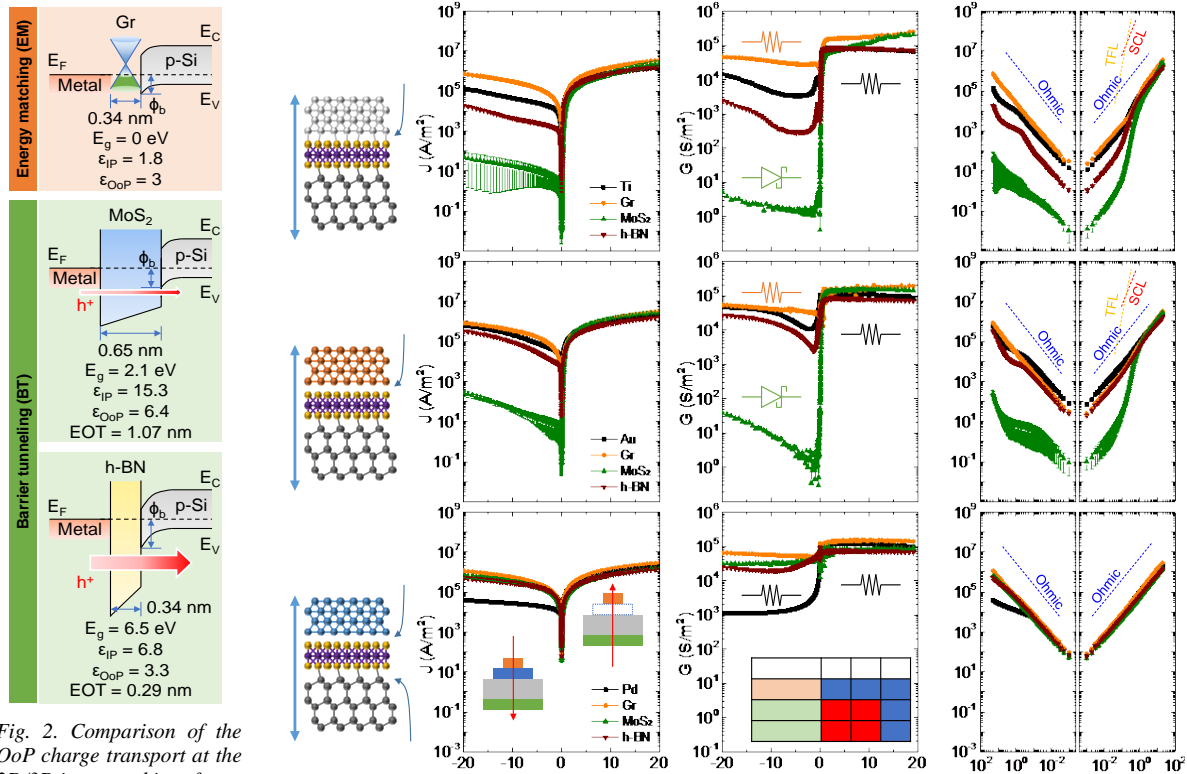


Fig. 2. Comparison of the OoP charge transport at the 2D/3D integrated interfaces, including the Gr-enabled EM effect as well as the MoS₂- and h-BN-enabled BT effect. Other parameters for consideration include the thickness, E_g , ϵ_{IP} , ϵ_{OOP} , and EOT of 2D monolayers.

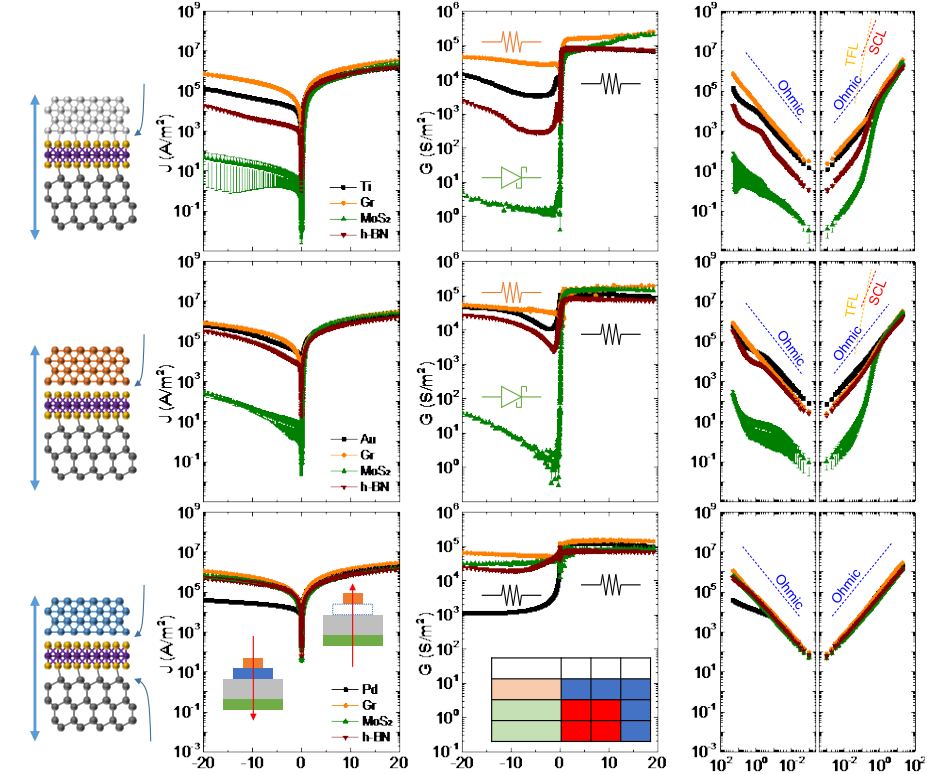


Fig. 3. The OoP charge transport for a variety of 2D/3D integrated device configurations. (a) Schematics of the 2D/3D covalent-vdW interaction (e.g., MoS₂/Si) with hybridization contact (e.g., Ti) and vdw contact (e.g., Au). (b-d) Statistical analysis of J and G as a function of V , in both linear and logarithmic scales, with Ti contact (top), Au contact (middle), and Pd contact (bottom). For the OoP charge transport along the 3D/2D/metal direction, the 2D monolayers act as electrically transparent and provides an Ohmic-like contact using the Gr-enabled EM effect or Pd contact. Along the metal/2D/3D direction, the 2D monolayers create a Schottky-like contact using the MoS₂- and h-BN-enabled BT effect with Ti or Au contact.

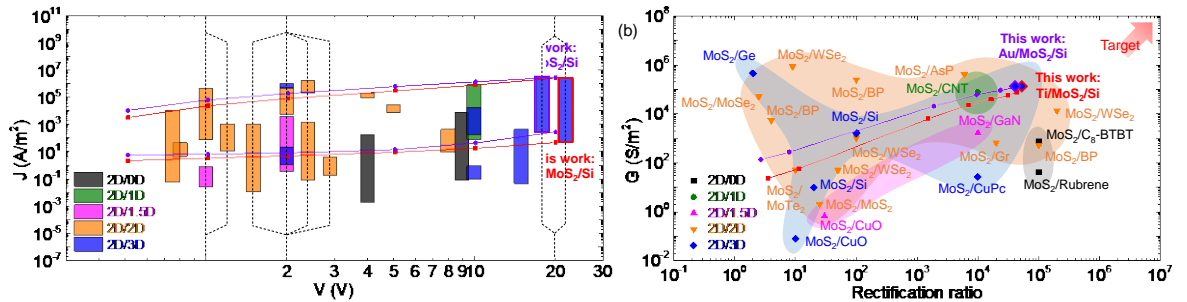


Fig. 4. Benchmarking of the Ti- and Au-contact 2D/3D MoS₂/Si integrated diodes with other state-of-the-art MoS₂-based diodes, including (a) the current rectification versus the required V , and (b) G versus rectification ratios plots. Our devices exhibit a record-high and well-balanced performance to simultaneously maintain high rectification ratio and G in the 2D/3D integrated devices.

Generating free charge carriers in graphene in a van der Waals multilayer heterostructure

R. J. Scott, P. Valencia-Acuna, and Hui Zhao

¹*Department of Physics and Astronomy, University of Kansas, Lawrence, Kansas 66045, USA*
huizhao@ku.edu

Keywords: keyword 1: 2d materials, keyword 2: light-matter interactions

Graphene is a promising material for optoelectronic applications due to its high charge carrier mobilities and wavelength-independent light absorption coefficient. However, when graphene is used alone as an active layer in such devices, separation of photoexcited electrons and holes is challenging, as they can form tightly bound excitons due to their strong Coulomb attraction in its two-dimensional (2D) structure. As neutral particles, excitons do not carry charge currents due to the lack of charge separation, presenting a significant challenge for improving performance of graphene-based optoelectronic devices. Here we show that sophisticated heterostructures combining type-I and type-II interfaces allow for the generation of photoexcited charge carriers. As a model system, we fabricate a 4-layer heterostructure sample of graphene/MoS₂/MoSe₂/graphene. The photoexcited electrons and holes separated at the type-II MoS₂/MoSe₂ interface can be driven to the two graphene layers by the large band offsets at graphene-TMD interfaces. Transient absorption microscopy measurements reveal that these photocarriers are highly mobile free charge carriers. Specifically, the holes in the graphene layer adjacent to MoSe₂ exhibit a diffusion coefficient of 65 cm²/s, corresponding to a mobility as high as 5,000 cm²/Vs at room temperature. In contrast, the electrons in the other graphene layer exhibit superdiffusive behavior. The differing transport properties of the electrons and holes provide strong evidence that they move independently of each other. These results demonstrate that such multilayer heterostructures, with two graphene layers sandwiching a type-II heterobilayer, can serve as active materials for 2D-based optoelectronic devices.

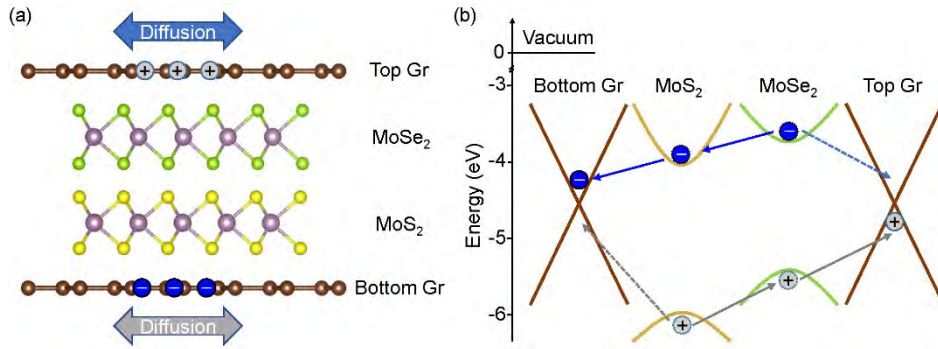


Fig.1: Sample structure and photocarrier dynamics. (a) Schematics of the 4-layer heterostructure of graphene/MoSe₂/MoS₂/graphene. (b) Band alignment and expected photocarrier dynamics.

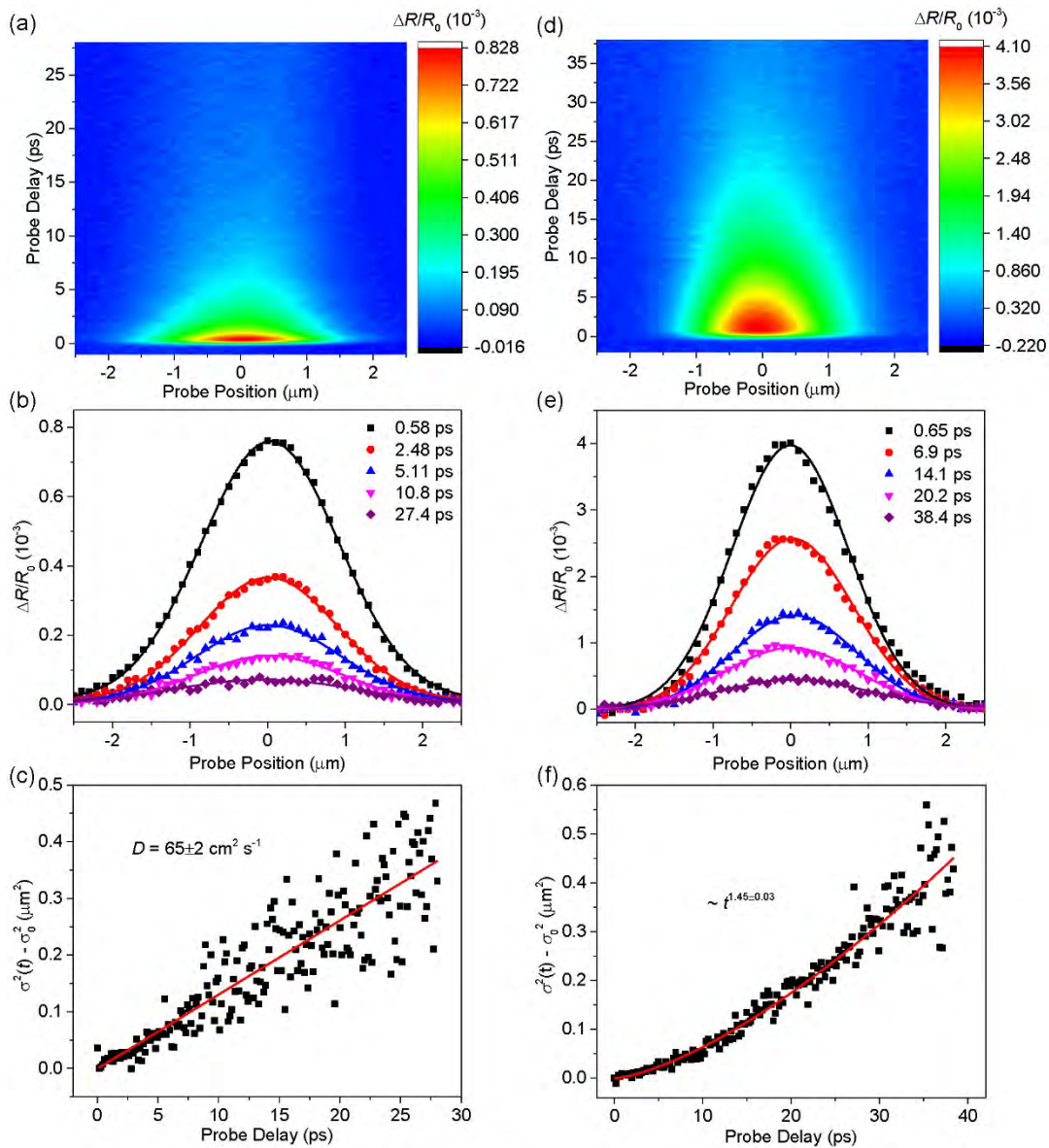


Fig.2: Hole (a-c) and electron (d-e) diffusion in the top and bottom graphene layers, respectively. (a) Spatiotemporally resolved differential reflectance with a 3.10-eV pump and a 1.55-eV probe. (b) Examples of the spatial profiles at various probe delays and the corresponding Gaussian fits (curves). (c) The broadening of the profile. The red line is a linear fit giving hole diffusion coefficient. (d) Spatiotemporally resolved differential reflectance with a 3.10-eV pump and a 1.88-eV probe. (e) Examples of the spatial profiles at various probe delays and the corresponding Gaussian fits (curves). (f) The broadening of the profile. The red curve is a power fit.

Investigation of PtCo Alloy Catalyst Composition for Suppression of H₂O₂ Formation in Polymer Electrolyte Fuel Cell Anodes by First-Principles Calculations

R. Kano¹, S. Fukushima¹, Y. Su^{2,1}, Y. Asano¹, Y. Ootani¹, N. Ozawa^{2,1} and M. Kubo^{1,2}

¹Institute for Materials Research, Tohoku University, Sendai, Miyagi 980-8577, Japan

²New Industry Creation Hatchery Center, Tohoku University, Sendai, Miyagi 980-8579, Japan

kano.ryoya.p8@dc.tohoku.ac.jp

Keywords: other advanced devices

In order to reduce CO₂ emissions and solve energy problems, polymer electrolyte fuel cells (PEFCs) are required to have higher durability and longer lifetime. The degradation of PEFC is a critical issue, and one of the degradation reasons is the decomposition of polymer electrolyte membranes (PEM) due to OH radicals produced from H₂O₂. When an O₂ molecule passes from the cathode to the anode through a PEM, H₂O₂ is generated via the chemical reaction of hydrogen fuel and O₂ on the Pt catalyst. To suppress H₂O₂ formation on the Pt catalyst, Shi et al. experimentally revealed that alloying Pt with Co is an effective approach [1]. However, elution of Co at high voltage negatively affects catalytic activity [2], and a lower amount of Co is desirable. Then, to develop a highly durable PtCo alloy catalyst, the ratio of Co in the PtCo catalyst should be optimized. In this study, to realize the above design, we investigated the relationship between the ratio of Co and H₂O₂ suppression by first-principles calculation.

We constructed Pt catalyst model consisting of Pt_{6-x}Co_x alloy core and a single Pt skin layer (Fig. 1). Moreover, to reproduce the anode environment, hydrogen atoms were placed on the nanoparticles. The H₂O₂ formation process consists of two elementary reaction processes in which HO₂ is formed from H atoms adsorbed on PtCo alloy nanoparticles and O₂ molecules (H + O₂ → HO₂), and H₂O₂ is subsequently formed from HO₂ and adsorbed H atoms (HO₂ + H → H₂O₂) (Fig. 2). To evaluate H₂O₂ formation activity, we calculated the activation energies of HO₂ and H₂O₂ formation (Fig. 3). Here, the higher activation energy of HO₂ and H₂O₂ formation indicates less formation of HO₂ and H₂O₂. To discuss the activity of each model, we compared the activation energies at the rate-determining step. The activation energies at the rate-determining step are 30.77, 15.50, 36.81, 26.74, 20.05, and 13.16 kcal/mol for Pt₃₇Co₁, Pt₃₆Co₂, Pt₃₅Co₃, Pt₃₄Co₄, Pt₃₃Co₅, and Pt₃₂Co₆, respectively. Notably, the Pt₃₅Co₃ nanoparticle, with a Pt₃Co₃ alloy core, exhibits the highest activation energy at the rate-determining step. These findings indicate that composition of the PtCo alloy core, where the ratio of Co to Pt is one, is the most effective at suppressing H₂O₂ formation.

[1] G. Shi et al., *J. Mater. Chem. A*, **8**, 1091-1094 (2020).

[2] R. K. Ahluwalia et al., *J. Electrochem. Soc.* **165**, F3024-F3035 (2018).

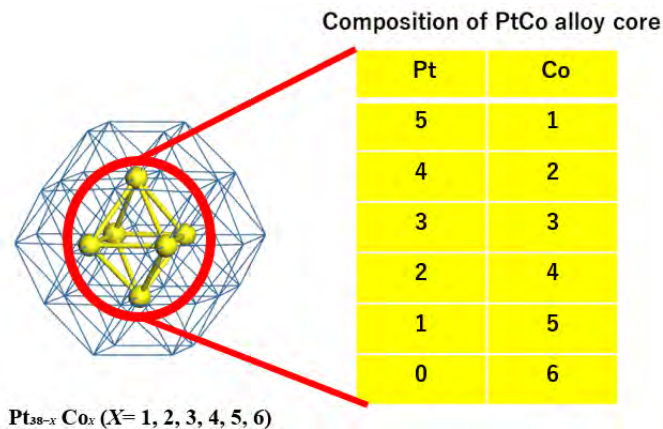
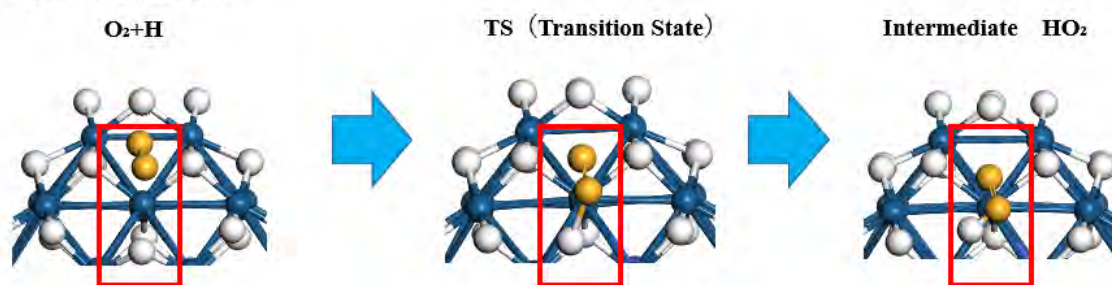


Fig. 1: $\text{Pt}_{38-x}\text{Co}_x$ ($X=1, 2, 3, 4, 5, 6$) nanoparticle model

1) $\text{O}_2 + \text{H} \rightarrow \text{Intermediate HO}_2$



2) $\text{HO}_2 + \text{H} \rightarrow \text{Product H}_2\text{O}_2$

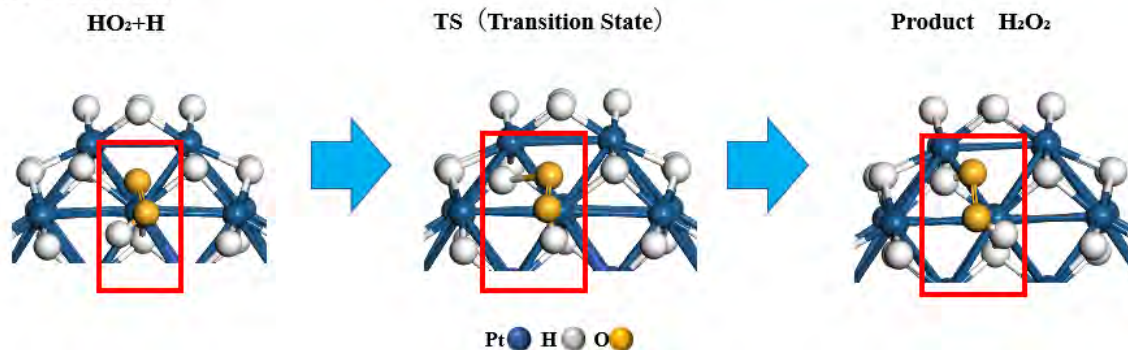


Fig. 2: H_2O_2 formation process on Pt skin layer

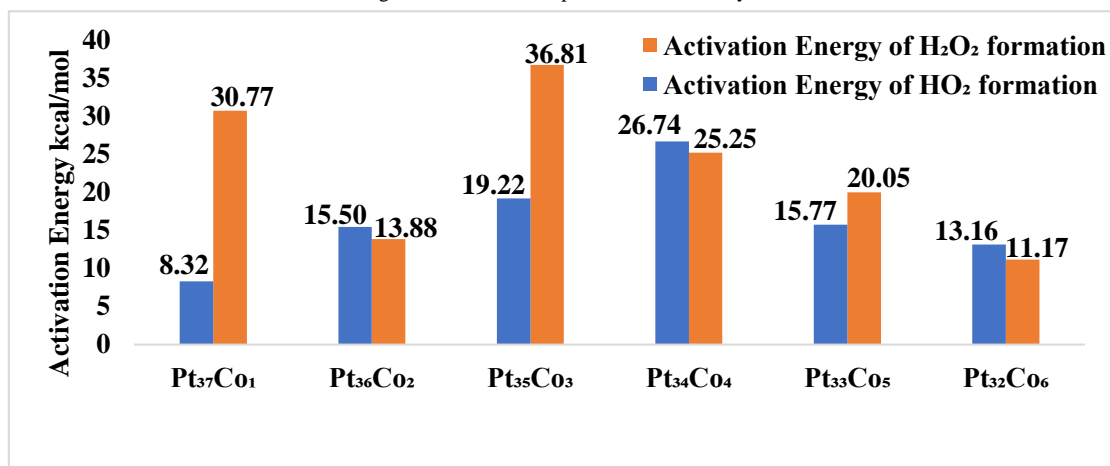


Fig. 3: Activation energies of HO_2 and H_2O_2 formation on $\text{Pt}_{37}\text{Co}_1$, $\text{Pt}_{36}\text{Co}_2$, $\text{Pt}_{35}\text{Co}_3$, $\text{Pt}_{34}\text{Co}_4$, $\text{Pt}_{33}\text{Co}_5$, and $\text{Pt}_{32}\text{Co}_6$ alloy nanoparticles

Molecular Dynamics Simulation on Stress Corrosion Cracking of High Entropy Alloys in Water Environment

Shogo Fukushima¹, Ryutaro Kudo¹, Chang Liu¹, Yuta Asano¹,

Yusuke Ootani¹, Nobuki Ozawa^{2,1}, Momoji Kubo^{1,2}

¹*Institute for Materials Research,*

Tohoku University, 2-1-1 Katahira, Aoba-ku, Sendai 980-8577, Japan

²*New Industry Creation Hatchery Center,*

Tohoku University, 6-6-10 Aoba Aramaki, Aoba-ku, Sendai 980-8579, Japan

Email: shogo.fukushima.d1@tohoku.ac.jp

Keywords: other advanced devices

High entropy alloys (HEAs), containing more than four elements in near-equiatomic proportions, get attention in the field of materials science due to their superior physical and mechanical properties. Despite these excellent properties, they have a critical issue, stress corrosion cracking (SCC) which limits its reliability in practical applications [1]. However, the SCC mechanisms are elusive yet due to the difficulty of experimental observing of atomic-scale deformation mechanisms. Besides the correlation between the number of elements in HEA and mechanical properties such as yield strength is not simple [2]. In this work, we aimed to clarify the effect of the constituent elements of HEA on the tensile behaviors and deformation mechanisms in a corrosive environment such as high-temperature/pressure water. To simulate both the chemical reactions and material deformation mechanisms, we focused on molecular dynamics (MD) simulation with reactive force field (ReaxFF).

We performed atomistic uniaxial tensile simulations using face centered cubic (FCC) type Fe₄₀Ni₄₀Cr₂₀ and Fe₃₀Ni₄₀Cr₂₀Co₁₀ alloys in high-temperature/pressure water environment (Fig. 1). While local body-centered cubic (BCC) phases were mainly created by tensile for Fe₄₀Ni₄₀Cr₂₀ alloy (Fig. 2(a)), the generation of layered hexagonal closest packed (HCP) phases was mainly observed for Fe₃₀Ni₄₀Cr₂₀Co₁₀ alloy (Fig. 2(b)). Because the BCC phase is typically more brittle than the FCC and HCP, leading to a reduced ductility, Fe₄₀Ni₄₀Cr₂₀ alloy shows lower yield strength than that of Fe₃₀Ni₄₀Cr₂₀Co₁₀ alloy as shown in Fig. 3. This result indicates that the addition of Co in FeNiCr HEA induces the increase of mechanical strength of the HEA.

The construction of interatomic potential based on ReaxFF for 5 or more elements is very difficult due to the many numbers of combination of elements. Therefore, we also focused on neural network potentials (NNPs) which can reproduce the interatomic potential of first-principles molecular dynamics (FPMD) by effective parameter fitting based on machine-learning methods. We constructed NNPs which can reproduce the structures of the 5-elements (CrMnFeCoNi) HEA obtained by FPMD simulations. We confirmed that the partial radial distribution functions $g_{\alpha\beta}(r)$ obtained by NNPs are in good agreement with $g_{\alpha\beta}(r)$ obtained by FPMD as shown in Figure 4. In the presentation, we will discuss the SCC mechanisms of CrMnFeCoNi HEA revealed by tensile simulation using NNPs.

[1] S. Mizumachi *et al.*, ISIJ Int. **60**, 175–181 (2020). [2] Z. Wu *et al.*, Acta Mater. **81** 428-441 (2014).

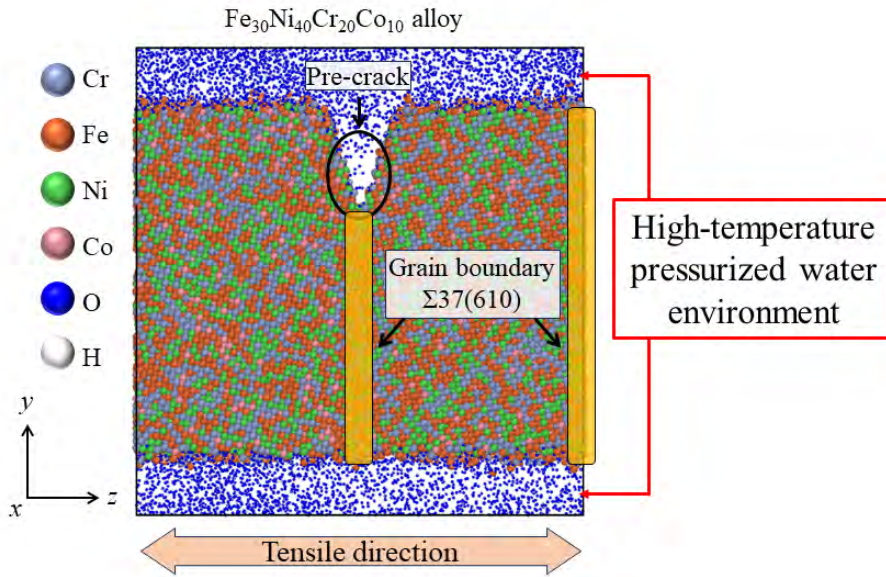


Fig.1: Tensile simulation model of FCC-type $Fe_{30}Ni_{40}Cr_{20}Co_{10}$ alloy in high-temperature/pressure water environments.

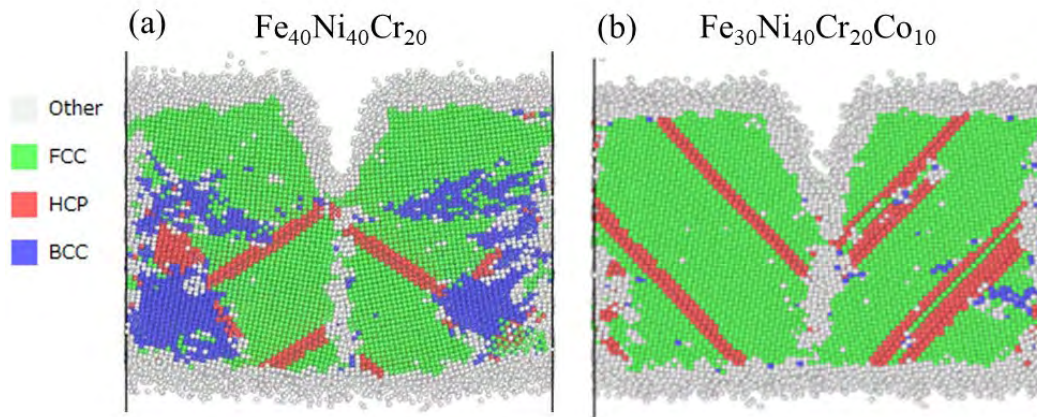


Fig.2: Atomic structures of (a) $Fe_{40}Ni_{40}Cr_{20}$ and (b) $Fe_{30}Ni_{40}Cr_{20}Co_{10}$ alloys in high-temperature/pressure water environment, respectively.

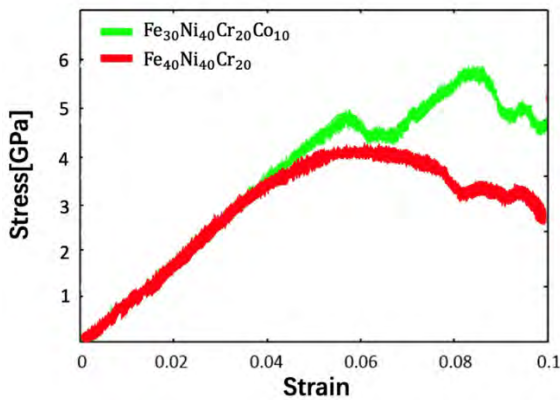


Fig.3: Stress-strain curve of $Fe_{40}Ni_{40}Cr_{20}$ (red) and $Fe_{30}Ni_{40}Cr_{20}Co_{10}$ (green) during the tensile simulations in high-temperature/pressure water environment, respectively.

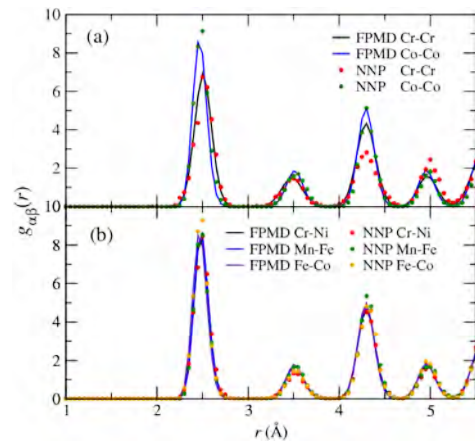


Fig.4: Partial radial distribution functions $g_{\alpha\beta}(r)$ obtained by FPMD (solid lines) and NNPs (dotted lines).

Influence of Deformation Potential Scattering on Impact Ionization and Critical Field in Ultra-Wide Bandgap Materials

J. Shoemaker², R. Vatan¹, T. Biswas², A. Singh², M. Saraniti¹, S.M. Goodnick¹

¹*Department of Electrical Engineering, Arizona State University, Tempe, AZ, USA*

²*Department of Physics, Arizona State University, Tempe, AZ, USA*

stephen.goodnick@asu.edu

Keywords: ultra-wide band-gap materials, computational physics

A major advantage of ultra-wide band gap (UWBG) materials for power electronic applications are the predicted high breakdown voltages limited by avalanche breakdown due to impact ionization. However, experimental data on the impact ionization coefficients in these new class of materials is limited. Theoretical calculations of ionization coefficients using Monte Carlo methods are highly influenced by the choice of deformation potential scattering rates, which in turn are dependent on the phonon deformation potentials used as inputs. In the present paper, we present comparisons of the impact ionization coefficients obtained from first principles with various assumptions of constant deformation potentials, and their resulting critical field estimations in diamond.

The impact ionization and electron-phonon deformation potential scattering rates are computed from Fermi's golden rule. Electronic structures are computed from DFT using Quantum Espresso and from GW using BerkeleyGW. Phonon dispersions are calculated from DFPT using Quantum Espresso and from an empirically fitted valence force field model. K-vector dependent deformation potentials are computed using EPW in Quantum Espresso. Constant deformation potentials are obtained by matching Monte Carlo simulation results to experimental velocity-field measurements. The impact ionization coefficient is calculated from full band cellular Monte Carlo (CMC) simulation as shown in Fig. 3. The critical field is calculated with the avalanche multiplication integral, using the field-dependent impact ionization coefficients in Fig. 3 fitted to the Chynoweth ionization function as input.

Using the GW electronic structure, shown along high-symmetry lines in Fig. 1, as input for the EPW calculation produces the transition rates shown in Fig. 2. The choice of constant deformation potential clearly has a large effect on the electron-phonon scattering rate, which results in large variation in the resulting ionization coefficients, as can be seen in Fig. 3. This demonstrates a need for anisotropic deformation potentials obtained from first-principles.

Using inputs calculated from first principles methods can help to compensate for the shortage of experimental data available for newer materials such as UWBG semiconductors. More traditional approximations, such as constant deformation potential values and empirical electronic and phonon dispersions, are not sufficiently accurate in predicting UWBG material ionization coefficients. GW electronic structures and DFPT phonon dispersions help to produce more accurate ionization coefficients, but it is important to compare the various choices for pseudopotential functions.

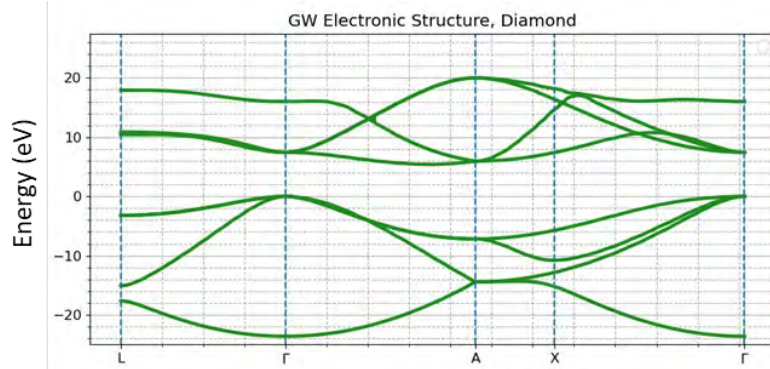


Fig.1: GW band structure of diamond, from BerkeleyGW. Obtained with a wavefunction cut-off of 60 Ryd using BLYP+HGh pseudopotential input and the optimized lattice constant 3.53 Å.

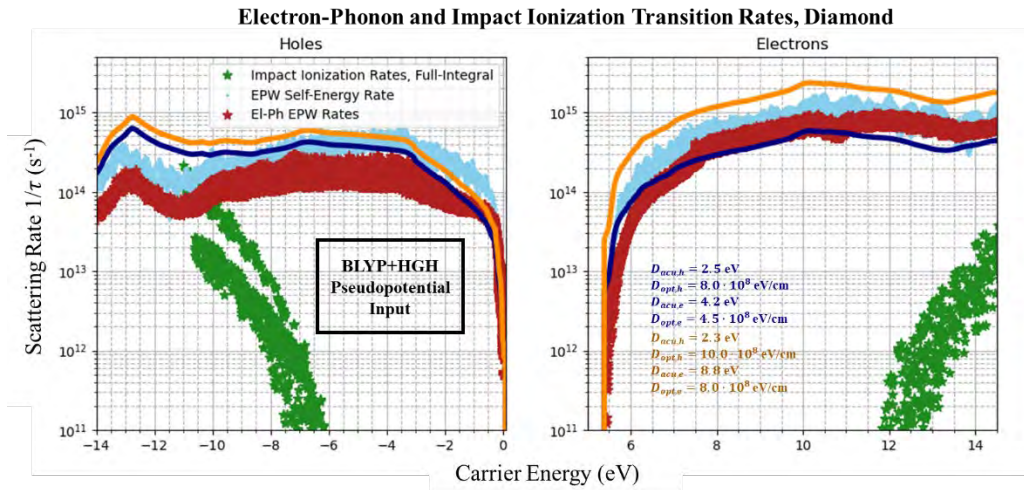


Fig.2: Electron-Phonon deformation potential and impact ionization transition rates of holes and electrons in diamond for anisotropic deformation potentials (red) vs two sets of constant deformation potentials from literature (orange, navy). Rates obtained directly from EPW self-energies are also displayed. Results are obtained with GW energies and wavefunctions as inputs. Impact ionization rates are calculated using Fermi's golden rule.

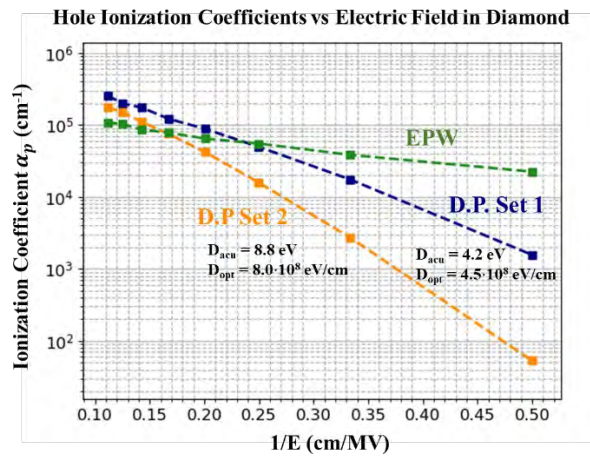


Fig.3: Impact ionization coefficients for holes in diamond, obtained using the fitting parameters shown in Fig.2 in full-band Monte Carlo

TCAD-Optimization Informed Modeling of Commercial SiC MOSFET

X. Gao (xngao@sandia.gov), E. Rhoades, J. E. Manuel, D. R. Hughart, M. L. Breeding, J. M. Young, C. E. Glaser, B. D. Rummel, and T. Buchheit
Sandia National Laboratories, 1515 Eubank SE, Albuquerque, NM 87123, USA

Keywords: wide-gap materials

Commercial-Off-The-Shelf (COTS) silicon carbide (SiC) MOSFETs have become a big interest for space and defense applications due to their high power and radiation tolerance [1]. To understand the radiation responses of SiC COTS parts, we propose a TCAD-Optimization (Charon-Dakota) [2,3] tool coupling approach (Fig. 1) that allows us to determine device details, which are typically unavailable or difficult to obtain for COTS parts, but are essential to build an accurate TCAD model. We applied this approach to model the responses of 3.3 kV SiC power MOSFETs from GeneSiC. We obtained cross-sectional images of the active region through FIB/SEM (Fig. 2, left) to define doping profile geometries, but doping values in a half-finger active region are not yet acquired due to the obstacles associated with doping characterization of sub-micron features. Based on the SEM images, we created a half-finger simulation structure (Fig. 2, right) and identified five necessary device parameters that must be determined for reliable TCAD simulations. First, the drift region thickness and doping determine the device breakdown voltage, so we performed Charon-Dakota breakdown simulations across a wide parameter space of thickness and doping values (Fig. 3). From these simulations, we determined that the drift region thickness is about 27 μm and the doping is around $3 \times 10^{15} \text{ cm}^{-3}$. Next, through simulations, the p-well doping was estimated to be approximately $1.4 \times 10^{17} \text{ cm}^{-3}$ from the fact that it dominates the device threshold voltage, and the JFET n-type doping is about $3 \times 10^{16} \text{ cm}^{-3}$ to maintain a good current path in the typical forward operating regime. Then, a customized field-dependent channel mobility model was implemented in Charon, and its parameters were estimated through Charon-Dakota simulations (Fig. 4). Using the optimized device parameters informed by simulations, we obtain good agreement between simulation and experiment (Fig. 5) in a non-radiation environment. After total ionizing dose (TID) irradiations, the 3.3 kV SiC devices exhibit large threshold voltage (V_{th}) shifts, which saturate at high doses (symbols in Fig. 6). Using a Kimpton-like TID model [4], we can simulate the observed V_{th} shift with dose and the saturation at high doses (Fig. 6). The Charon-Dakota coupling capability enables us to sweep a large range of parameters to achieve more accurate TID simulation results. This simulation approach generalizes and is applicable to other COTS devices.

[1] Q. Yu *et al.*, IEEE Trans. Nucl. Sci., vol. 69, no. 5, pp. 1127–1133, May 2022. [2] <https://charon.sandia.gov/>. [3] <https://dakota.sandia.gov/>. [4] D. Kimpton *et al.*, Solid-State Electron., vol. 37, no. 1, pp. 153-158, 1994.

The authors would like to thank L. Musson, N. A. Modine, D. Vogel, W. Lepkowski, A. Binder, L. Yates, and B. Kaplar for many helpful discussions. Sandia National Laboratories is a multimission laboratory managed and operated by National Technology & Engineering Solutions of Sandia, LLC, a wholly owned subsidiary of Honeywell International, Inc., for the U.S. DOE's National Nuclear Security Administration under contract DE-NA-0003525. The views expressed in the article do not necessarily represent the views of the U.S. DOE or the United States Government.

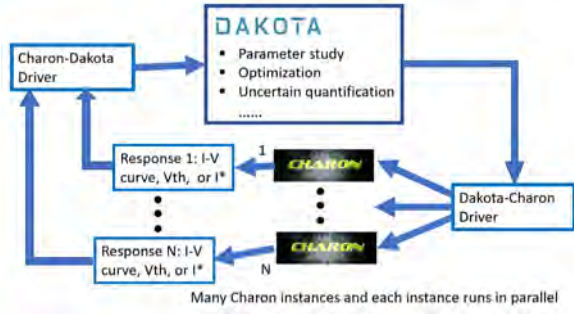


Fig.1: Schematic of Charon [2] and Dakota [3] tool coupling. Dakota is an open-source optimization and UQ tool, which can be coupled with physics-based simulation tools such as Charon, Sandia's open-source TCAD code, to enable fast and parallel simulations. Through the tool coupling, many Charon simulations can run simultaneously on HPC clusters, and each Charon simulation can use as many processors as available.

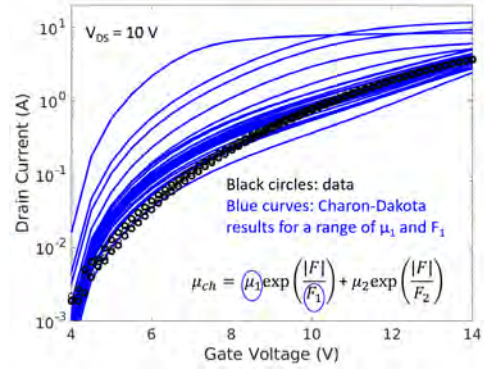


Fig.4: Simulated I_{DS} - V_{GS} curves for a range of channel mobility parameters μ_1 and F_1 obtained from a set of Charon-Dakota simulations. Symbols are measured data. The first exponential component in the model was designed to govern the I-V in the lower voltage region, while the second one has more effect at high voltages. Parameter values were chosen when simulated I-V curves match well with measured data.

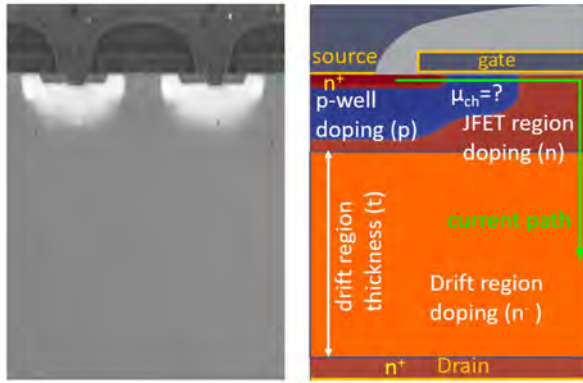


Fig.2 (left) SEM cross-section image of a 3.3 kV SiC power MOSFET from GeneSiC Semiconductor Inc. showing two p-well (white color) and a full JFET regions. (right) Charon simulation structure (half-finger) informed by SEM images showing the current path (green arrow) and five main device parameters that need to be determined from simulations. Source, drain, and gate contacts are also denoted.

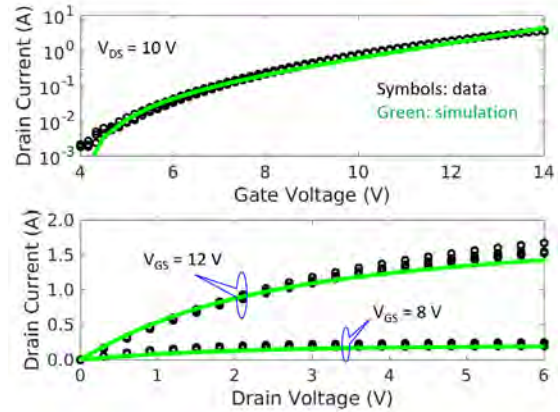


Fig.5 Simulated current-voltage curves (top: I_{DS} - V_{GS} curves with $V_{DS} = 10$ V. bottom: I_{DS} - V_{DS} curves) in comparison with measured data. Simulations were done using the optimized drift region thickness, doping values, and channel mobility informed by Charon-Dakota simulations. Good agreement is achieved between simulation and experiment in a non-radiation environment.

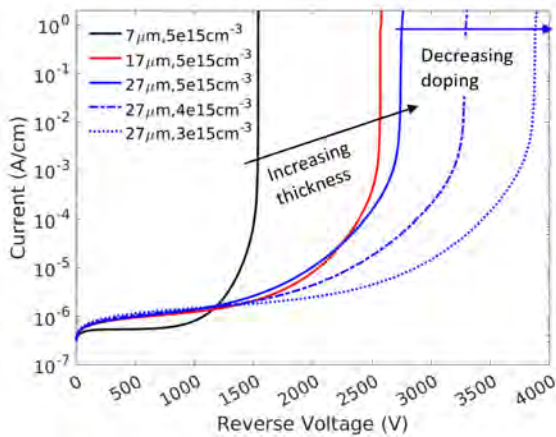


Fig.3: Simulated breakdown current-voltage curves (selected for plot clarity) showing the dependence of breakdown voltage on the drift region thickness and doping. For breakdown simulations, the gate and source contacts are grounded, while the drain contact is positively biased. Charon-Dakota simulations allowed us to quickly determine the drift region thickness and doping values.

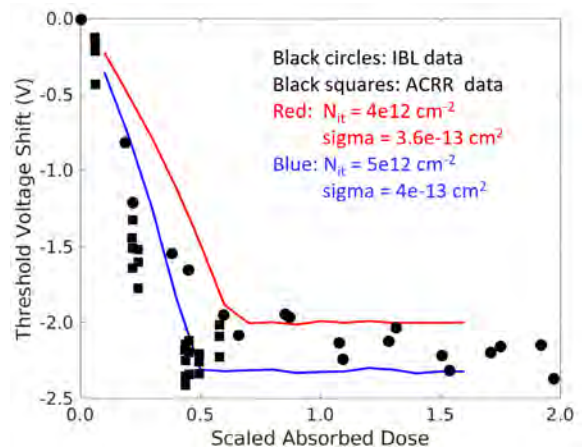


Fig.6: Simulated threshold voltage shifts with scaled absorbed doses in comparison with measured data. Symbols are measured data collected at two radiation facilities (IBL, ACRR) at Sandia. Solid lines are Charon simulation results using a Kimpton-like TID model. Despite some difference, the simulation results capture the saturation of V_{th} shift at high dose as observed in measured data.

Reactive Molecular Dynamics Simulation for Revealing Splitting Phenomena and Mechanism of Ni Particles in Solid Oxide Fuel Cell Anode

T. Ishikawa¹, Y. Su^{2,1}, S. Fukushima¹, Y. Asano¹, Y. Ootani¹, N. Ozawa^{2,1} and M. Kubo^{1,2}

¹*Institute for Materials Research, Tohoku University, Sendai, Miyagi 980-8577, Japan*

²*New Industry Creation Hatchery Center, Tohoku University, Miyagi, Japan*

takashi.ishikawa.q6@dc.tohoku.ac.jp

Keywords: other advanced devices

Solid oxide fuel cells (SOFC) have the advantage of high power generation efficiency without noble metal catalysts. However, a highly humidified hydrogen environment due to hydrogen fuel starvation induces a microstructural change in the Ni/YSZ (Yttria Stabilized Zirconia) at the anode, resulting in the degradation of the electrode reaction activity. Jiao et al.^[1] sputtered Ni on YSZ pellets and polarized them in a highly humidified hydrogen environment. Then, they observed a reduction in the contact angle and splitting phenomena of Ni particles. Since the Ni splitting breaks the conducting path, it is important to clarify the mechanism of Ni splitting phenomena and to develop highly durable anode materials. Therefore, we investigated the behaviors of Ni particles on YSZ(111) in a humidified hydrogen environment by reactive molecular dynamics (MD) simulations.

First, we created a Ni particle/YSZ(111) model (Fig. 1) to observe microstructural changes during power generation in a highly humidified hydrogen environment (50% H₂-50% H₂O). We performed molecular dynamics simulations at 1123 K with and without an external electric field (20 MeV/cm) in the negative direction of the z-axis. The external electric field enhances the interaction between the Ni particle and YSZ(111) by the diffusion of O atoms in the YSZ substrate toward the surface. As a result, the contact angle did not change at 0 MeV/cm, while it continuously decreased at 20 MeV/cm until 250 ps (Fig. 2). When further MD simulation is performed with more time steps, further decrease in the contact angle is expected at the external electric field of 20 MeV/cm.

Then, we considered a further wet state in which the contact angle is further reduced, and investigated the behaviors of Ni particles with initial contact angles of 2.7° (Fig. 3). The MD simulations were performed at a temperature of 1123 K in a highly humidified hydrogen environment (50% H₂-50% H₂O). As a result, the Ni particle is split near the edges of the Ni particles (Fig. 4). To evaluate the degree of Ni splitting phenomena, the Ni particles were projected in the xy-plane and the areas of projected Ni particles were calculated (Fig. 5). The areas of Ni particles were 3.50×10^5 and 3.08×10^5 Å² at 0 (after relaxation at 300 K) and at 62.5 ps, respectively. This indicates that the Ni particle is split by aggregation of Ni at the edge when the contact angle becomes small by the electric field. Thus, we succeeded in simulating the Ni splitting phenomena and revealing mechanism on YSZ(111) at the anode of SOFC.

[1] Z. Jiao *et al.*, J. Electrochem. Soc. **167**, 024516 (2020).

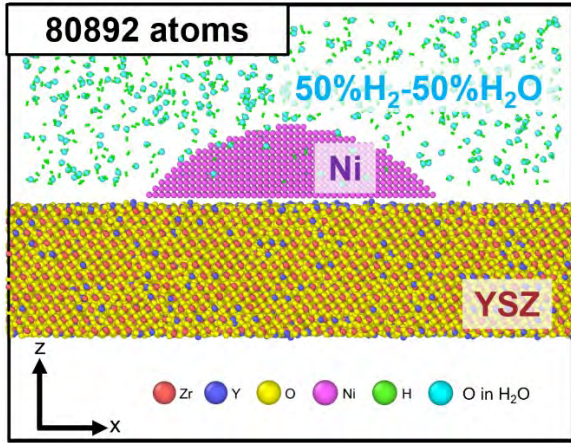


Fig.1: The initial structure of a Ni particle/YSZ(111) model.

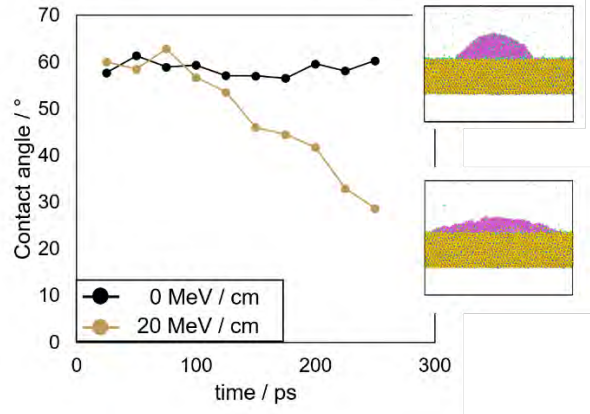


Fig.2: Time variation of Ni contact angle for models with 0 MeV/cm and 20 MeV/cm electric field applied.

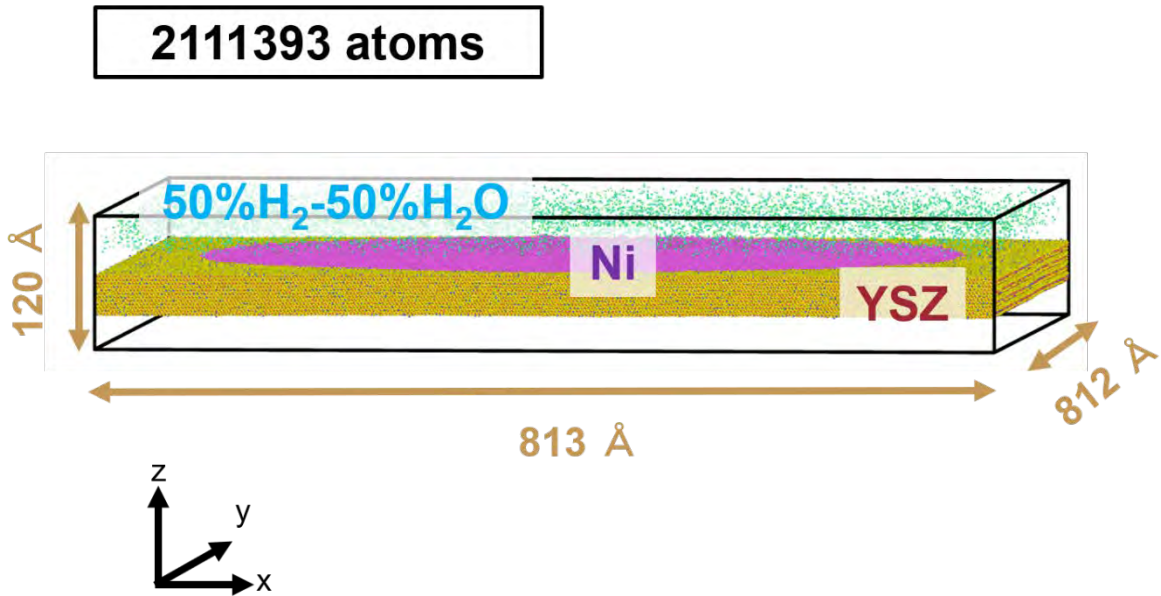


Fig.3: The initial structure of a large-scale Ni particle/YSZ(111) model consisting of about 2 million atoms with a contact angle of 2.7°.

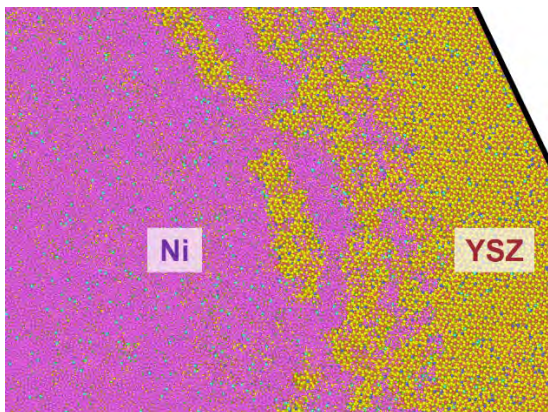


Fig.4: Snapshot of Ni splitting phenomena in a large-scale model with an initial contact angle of 2.7° after 62.5 ps.

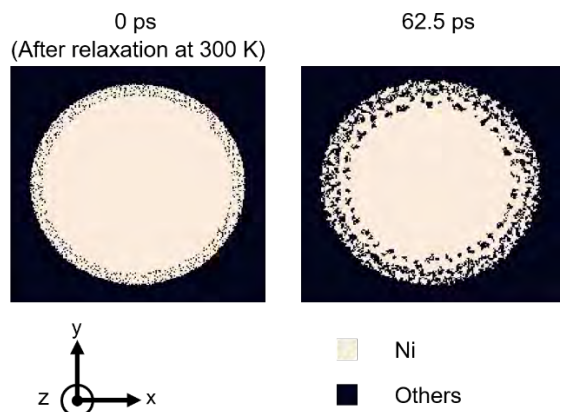


Fig.5: Distribution of Ni particles at 0 (after relaxation at 300 K) and at 62.5 ps projected in the xy-plane.

Effect of Ethylene Glycol Additives on the Water Lubrication of Silicon Nitride - Molecular Dynamics Simulation with Neural Network Potential -

Ryutaro Kudo¹, Kento Hosono¹, Arisa Chiba¹, Mizuho Yokoi¹, Masayuki Kawaura¹, Shogo Fukushima¹, Yuta Asano¹, Yusuke Ootani¹, Nobuki Ozawa^{2,1}, Momoji Kubo^{1,2}

¹*Institute for Materials Research,*

Tohoku University, Katahira, Aoba-ku, Sendai 980-8577, Japan

²*New Industry Creation Hatchery Center,*

Tohoku University, 6-6-10 Aoba Aramaki, Aoba-ku, Sendai 980-8579, Japan

Email: ryutaro.kudo.p2@dc.tohoku.ac.jp

Keywords: nanostructures

Water lubrication is expected to be a clean lubrication method when contamination by oil is undesirable. Currently, Si₃N₄ is known to exhibit super-low friction in aqueous environments due to colloidal lubricant which is produced by tribochemical reactions [1]. However, for practical use, it is necessary to solve the problem that low friction is not maintained under high loads. Alcohols such as ethylene glycol are one of the excellent additives to improve load carrying capacity. It was reported that CN_x film was produced on the surface by tribochemical reactions of alcohol additive. The thin CN_x film is thought to improve load-carrying capacity. [2, 3, 4]. However, the detailed mechanism is still unknown because it is difficult to directly observe the chemical reactions by experiments. Therefore, in this study, friction simulations based on molecular dynamics method were performed.

Figure 1 shows a friction simulation model of Si₃N₄ with ethylene glycol. The friction simulation was performed by fixing the bottom part of the Si₃N₄ substrate, applying a pressure of 1 GPa in the -z-direction to the top part of the Si₃N₄ substrate, and moving the top substrate at a velocity of 100 m/s in the x-direction. In this study, neural network potential (NNP) was used to calculate the interactions between atoms. NNP, in which deep learning is used to evaluate potential energy surfaces, has attracted attention because it can evaluate the potential energy surface with ab initio accuracy at low computational cost. To create a dataset for training, ab initio molecular dynamics simulations were performed on amorphous Si₃N₄ (Fig. 2(a)), a contact interface of ethylene glycol and Si₃N₄ (Fig. 2(b)), and molecules composed of C, H, O, N, and Si (Fig. 2(c)).

Friction simulations confirmed that tribochemical reactions with ethylene glycol produced silicon alkoxide (Fig. 3(a)), N₂ molecules and NH₃ molecules. Condensation of multiple silicon alkoxides is expected to result in the formation of colloidal silica lubricant, whose moderate viscosity causes fluid lubrication when low loads are applied. In addition, the generation of aromatic molecule and chain molecule composed of hydrogen, carbon and nitrogen atoms (Fig. 3(b, c)) was also observed. They can be thought as precursors to two-dimensional CN_x film, which is considered to induce low friction under high loads.

[1] M. Chen, *et al.*, *Wear*, **250**, 246-255 (2001).

[2] S. Yan, *et al.*, *Tribol Int.*, **90**, 386-392 (2015).

[3] Y. Hibi, *et al.*, *Wear*, **231**, 185-194 (1999).

[4] Y. Long, *et al.*, *ACS Appl. Nano Mater.*, **4**, 2721-2732 (2021).

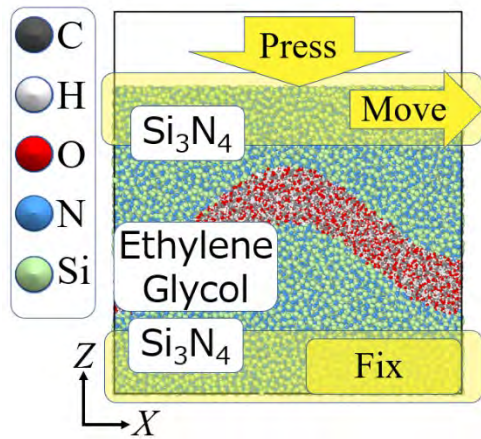


Fig.1: Sliding simulation model of $\text{Si}_3\text{N}_4/\text{Si}_3\text{N}_4$ interface with ethylene glycol.

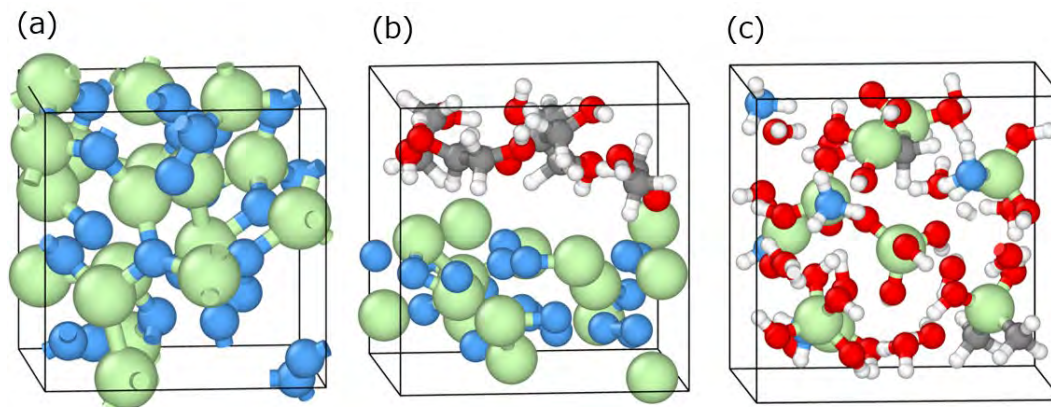


Fig.2: Ab initio molecular dynamics simulation models of (a) Si_3N_4 , (b) contact interface of ethylene glycol and Si_3N_4 and (c) molecules composed of C, H, O, N, and Si.

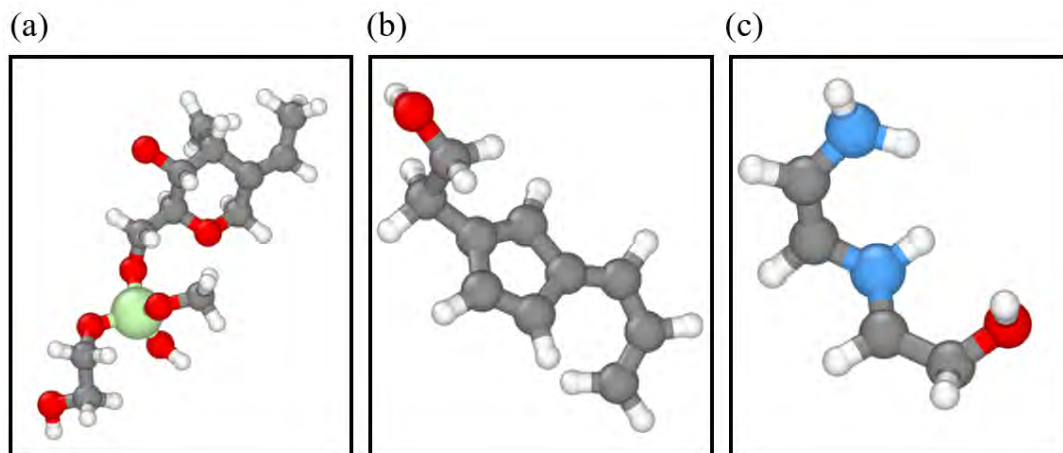


Fig.3: Generated molecules by friction simulation. (a) Silicon alkoxide, (b) aromatic molecule with OH group and (c) chain molecule composed of hydrogen, carbon, and nitrogen atoms.

Shortcut to adiabaticity for adiabatic passage of a single electron spin

X.-F. Liu^{1,2}, T. Fujita^{1,3,4,5}, Y. Matsumoto¹, A. Ludwig⁶, A. Wieck⁶ and A. Oiwa^{1,3,4,5}

¹*SANKEN, Osaka University, 8-1 Mihogaoka, Ibaraki, 567-0047 Osaka, Japan,*

²*Beijing Academy of Quantum Information Science, Beijing 100193, China,*

³*Center for Quantum Information and Quantum Biology (QIQB), Osaka University, Osaka 565-0871, Japan*

⁴*Center for Spintronics Research Network (CSRN), Graduate School of Engineering Science, Osaka University, Osaka 560-8531, Japan,*

⁵*Spintronics Research Network Division, OTRI, Osaka University, Osaka 565-0871, Japan.*

⁶*Lehrstuhl für Angewandte Festkörperphysik, Ruhr-Universität Bochum, Universitätsstraße 150, Gebude NB, D-44780 Bochum, Germany,
oiwa@sanken.osaka-u.ac.jp*

Keywords: quantum transport, quantum information

In an adiabatic quantum process, the quantum state always remains in its instantaneous eigenstates, providing quantum gates robust to noise and dissipation. In quantum technology based on the semiconductor spin qubits, the state transfers based on adiabatic process are expected to be useful for various aspects in scalable quantum computing. However, an ideal adiabatic operation takes an infinitely long operation time. The shortcuts to adiabaticity (STA) provide methods to mitigate the adiabatic drawback. Here, we demonstrate for the first time accelerated adiabatic passage under STA. In addition, the compensation of diabatic errors due to nuclear spin fluctuations using a modified pulse is shown.

We use a double QD formed in a GaAs/AlGaAs heterostructure (Fig. 1). We applied the transitionless quantum driving (TQD) proposed by Chen *et al.*, [2] to the single electron shuttling between two strongly coupled QDs. The counter-diabatic driving pulse designed from the time-dependent Rabi frequency and detuning can suppress the error due to diabatic transition (Fig. 2) [2]. We observed that the spin flip probability for TQD keeps higher value than that for the conventional adiabatic process even at short operation time as shown Fig. 3. The acceleration factor η , which is the operation time ratio of adiabatic and TQD, exceed more than a factor of 2 as shown in Fig. 4. The experimental results can be well described by simulations with a fluctuating nuclear spin noise. To mitigate the influence of the noise, we propose to modify the counter-diabatic pulse shape with a width parameter α (MOD-TQD) and demonstrate the restored state transfer efficiency at short operation time.

[1] D. Guery-Odelin *et al.*, Rev. Mod. Phys. **91**, 045001 (2019).

[2] X. Chen *et al.*, Phys. Rev. Lett. **105**, 123003 (2010).

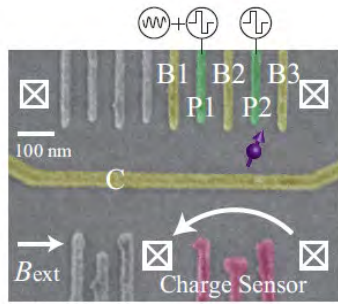


Fig.1: False-colored micrograph of the device, taken from the SEM. The high frequency pulses are applied through the plunger gates P1 and P2, and the MW signal is connected with the gate P1.

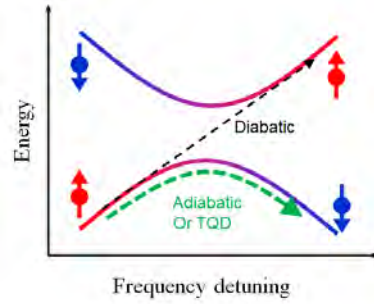


Fig.2: Schematic of Transitionless quantum driving (TQD).

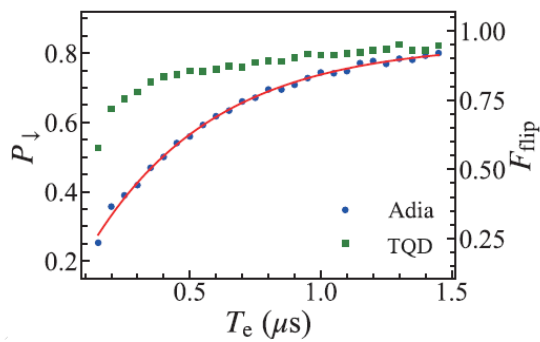


Fig.3: Final spin down probability P_{\downarrow} as a function of the evolution time T_e using the conventional adiabatic evolution and the TQD. The red solid line is the fitting to the Landau-Zener formula of $AP^{LZ} + B$.

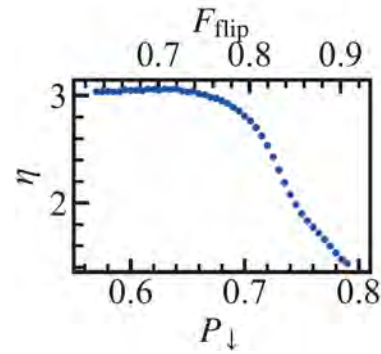


Fig. 4: Speed-up factor η as the functions of P_{\downarrow} and state transfer efficiency F_{flip} .

Controlling Single Electrons by Non-Uniform Magnetic Fields

M. Ballicchia, C. Etl, Mihail Nedjalkov, and J. Weinbub

Institute for Microelectronics, TU Wien, Austria

josef.weinbub@tuwien.ac.at

Keyword: quantum transport

Controlling single electrons is among the core mechanisms in electron quantum optics [1]. There, electron control allows to specifically guide and influence the evolution of individual electrons in transport channels and interaction systems, e.g., interferometers. Particularly important are mechanisms based on electromagnetic fields, providing additional degrees of freedom for electron control. However, very limited experience and understanding of the intricate interplay between electromagnetic fields and the involved single-electron quantum transport is available. We introduce a recently advanced Wigner theory allowing to incorporate non-uniform magnetic fields into the quantum transport model [2,3]. We show simulation studies covering magnetotunneling and snake states where the influence of the electromagnetic fields manipulates the electron evolution. We consider 2D transport in the x, y -plane and a non-uniform magnetic field normal to the plane $B = (0, 0, B(y))$, where $B(y) = B_0 + B_1 y$. Non-interacting electrons are periodically injected (minimum uncertainty Wigner states) at the bottom and center of the simulation domain. Concerning magnetotunneling, the electrons evolve in $+y$ -direction and collide with a 0.3eV and 1nm potential barrier. We consider four different cases for (B_0, B_1) : $(0, 0)$, $(-6\text{T}, 0)$, $(-6\text{T}, 0.2\text{T/nm})$, and $(-2\text{T}, -0.2\text{T/nm})$, see simulated electron densities in Fig.1-4. As can be seen, the electron can in principle tunnel into the upper half of the domain. The mean densities follow the classical paths (indicated lines) in accordance with the Ehrenfest theorem. Fig.1 shows a fine oscillatory structure beyond the barrier, which, however, is destroyed by the electron-bending magnetic field in the case shown in Fig.2. In Fig.3, the magnetic field changes its direction after the barrier, giving rise to a *snake* type of evolution. In addition, a fine oscillatory structure beyond the barrier manifests, like the case shown in Fig.1. This is linked to the magnetic field being zero around the barrier and a local interplay between the magnetic field and the electric field associated with the barrier. Fig.4 considers a case where $B(y)$ is particularly large around the barrier, again suppressing the oscillations. Concerning modeling of snake states, we consider the magnetic field defined by (B_0, B_1) : $(-1\text{T}, 1/300\text{T/nm})$, as shown in the right part of Fig.5. The initial position of the electron is different to the magnetotunneling studies, i.e., at $(x_0, y_0) = (370\text{nm}, 300\text{nm})$ where the magnetic field is positive. This choice makes the state oscillate around the central line due to the symmetry of the magnetic field. The left part of Fig.5 shows the electron density at different time steps. The state is squeezed along its evolution based on the magnetic field. The natural spread of the initial Gaussian state is now suppressed, which shows how a particular configuration of the magnetic field can control the evolution, squeezing, and dispersion of the electron state. [1] H. Edlbauer *et al.*, EPJ Quant. Technol. **9**, 21 (2022). [2] M. Nedjalkov *et al.*, Phys. Rev. A **106**, 052213 (2022). [3] M. Ballicchia *et al.*, Proc. IWCN (2023).

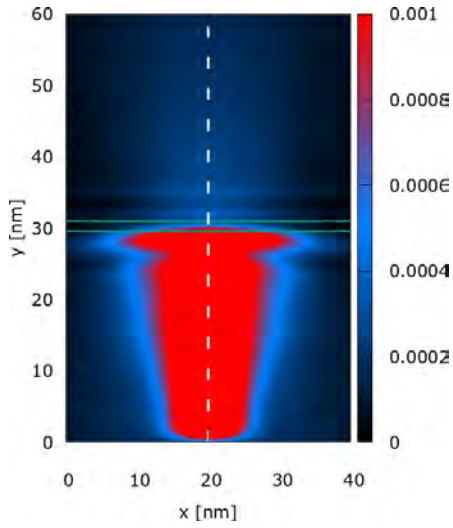


Fig.1: Magnetotunneling electron density for $(B_0, B_1) = (0, 0)$

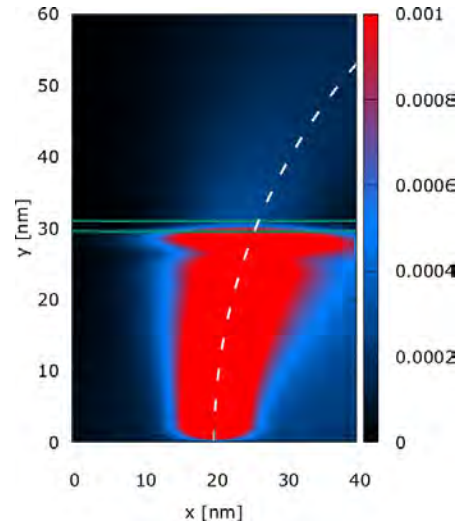


Fig.2: Magnetotunneling electron density for $(B_0, B_1) = (-6T, 0)$

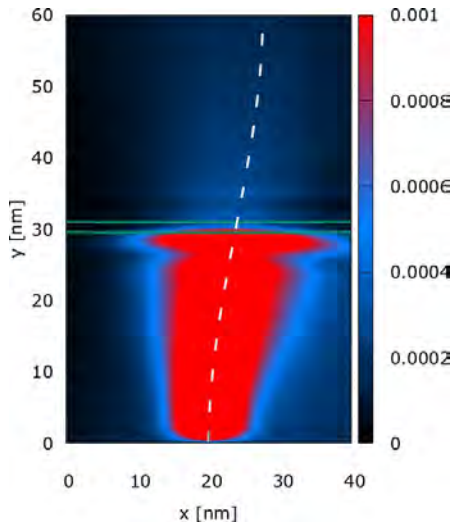


Fig.3: Magnetotunneling electron density for $(B_0, B_1) = (-6T, 0.2 T/nm)$

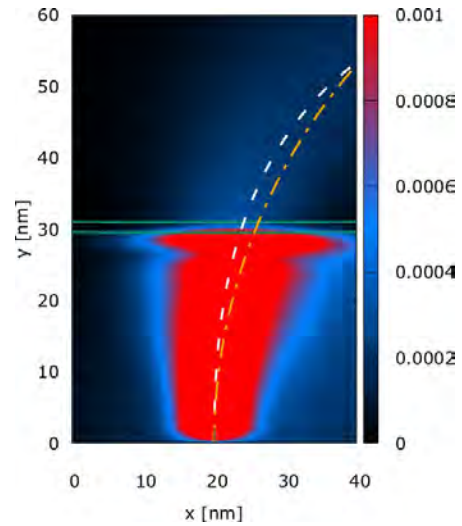


Fig.4: Magnetotunneling electron density for $(B_0, B_1) = (-2T, -0.2 T/nm)$

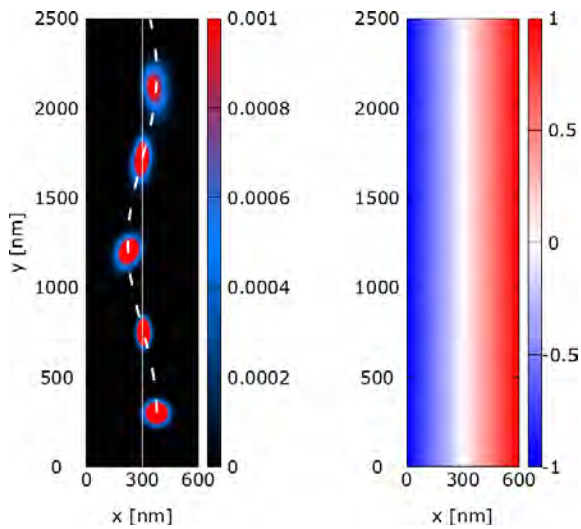


Fig.5: Snake state electron density at different time steps (left) and magnetic field [T] (right)

Acknowledgements: The financial support by the Austrian Science Fund (FWF): P33609 and P37080 is gratefully acknowledged. The computational results have been achieved using the Vienna Scientific Cluster (VSC).

Scattering in the Wigner Equation

S.W. Belling¹, L. Avazpour, and I. Knezevic¹

¹ *Department of Electrical and Computer Engineering, University of Wisconsin – Madison
Madison, WI 53706
swbelling@wisc.edu*

Keywords: quantum transport, nanostructures

The Wigner transport equation is among the widely used formalisms in quantum transport. The Wigner equation is especially well-suited to handling problems with continuous energy spectra, owing to its expression in terms of momentum and position, both of which are continuous variables. Also, the solution to the Wigner equation, known as the Wigner function, $f(x, k, t)$, can be thought of as a quantum analogue to the phase-space distribution in classical statistical mechanics, with negative values of the Wigner function representing regions of phase space where quantum behavior, such as tunneling, occurs [1]. A longstanding problem with utilizing the Wigner equation to describe electron transport in devices and nanostructures is that scattering is difficult to treat exactly, yet commonly employed approximations, such as the relaxation-time approximation, do not hold when there are large regions of space with nonclassical electron behavior and there are several active scattering mechanisms with different energy dependencies. We show how to treat scattering from several mechanisms in the Wigner equation by starting from our previous work [2], where we derived such terms for the density matrix (one of the other popular transport formalisms), and utilizing the Wigner-Weyl transform, which connects the density matrix to the Wigner function. We avoid taking the common rotating-wave approximation, which is only suitable for systems with discrete and widely spaced energy levels (also known as the optical-system limit). Instead, we work with a Markovian master equation for the density matrix in the Schrödinger picture in the Brownian-motion limit of a nearly continuous energy spectrum. With this approach, we arrive at a closed-form and intuitive expression for scattering terms to be used in the Wigner transport equation.

[1] J. Weinbub and D. K. Ferry, *Appl. Phys. Rev.* **05**, 041104 (2018).

[2] F. Karimi, A. H. Davoody, and I. Knezevic, *Phys. Rev. B* **93**, 205421 (2016).

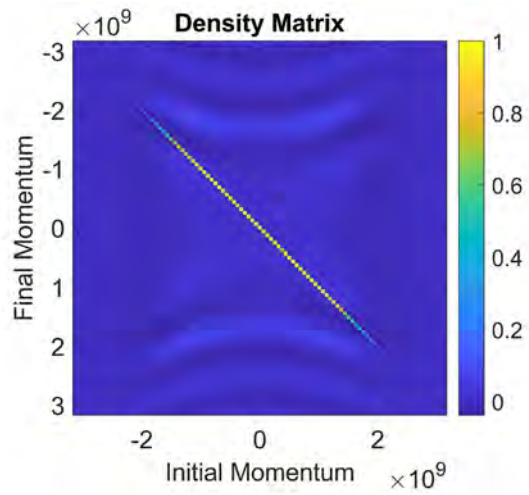


Fig.1: Colorized plot of the density matrix after some scattering from LO phonons.

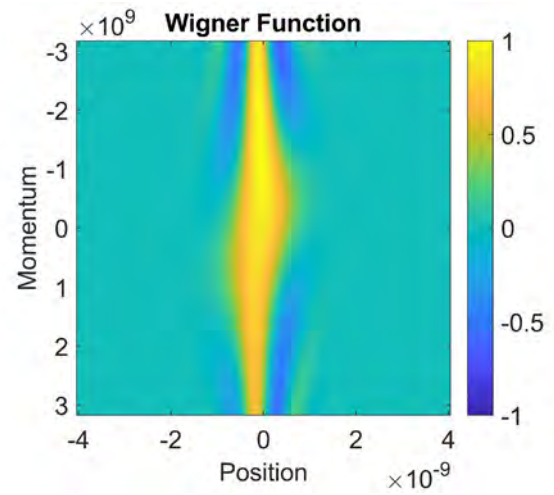


Fig.2: Colorized plot of the Wigner function after some scattering from LO phonons.

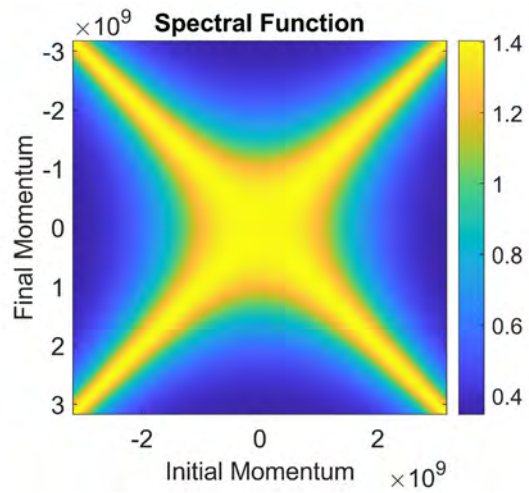


Fig.3: Colorized plot of a one-sided Fourier transform of the phonon-bath spectral function in units of \hbar . The Fourier transform is performed due to the time-dependence of the interaction-picture electronic operators.

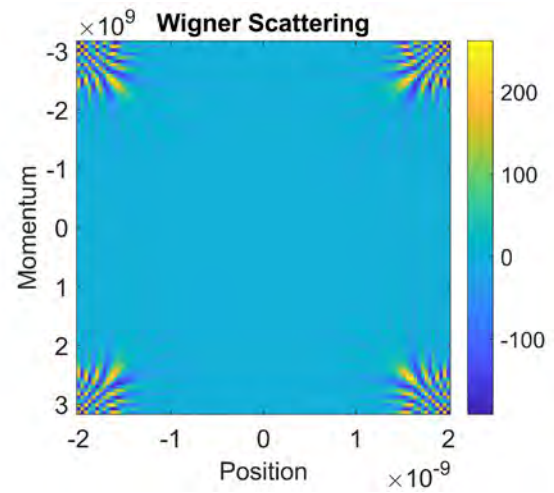


Fig.4: Fourier transform of scattering term, which involves the spectral function in Fig. 3, in units of \hbar . This term appears in the final expression for the collision integral in the Wigner equation.

Atomic Precision Advanced Manufacturing (APAM) devices for quantum sensing

J.P. Mendez¹, and D. Mamaluy¹

¹*Cognitive & Emerging Computing, Sandia National Laboratories, Albuquerque*
jpmende@sandia.gov

Keywords: quantum transport, sensors

Atomic precision advanced manufacturing (APAM) enables the creation of 2D doped regions, also known as delta layers, in a semiconductor. APAM is a process to incorporate dopants, such as P or B, at the atomic scale into Si surface using chemistry surface. APAM has various applications, including the exploration of novel nano-scale electronic devices for classical computing and sensing systems or dopant-based qubits in silicon for quantum computing.

In this work, using our quantum transport framework [1,2,3], we explore the use of APAM devices for charge sensing, in particular delta-layer tunnel junctions. Our device (see Fig. 1) consists of two highly-conductive P δ -layers separated by an intrinsic gap embedded in Si (Si: P delta-layer tunnel junction). Our quantum transport framework [1,2,3] relies on a self-consistent solution of Poisson-open system Schrödinger equation in the effective mass approximation and the Non-Equilibrium Green's Function (NEGF) formalism. Our simulations have revealed that delta-layer tunnel junctions are very sensitive to the presence of charges around the tunnel junction, shedding light on new opportunities for delta-layer systems in semiconductors to be used for charge sensing in many applications.

Fig. 2 shows the computed change of current through the device for different positions of a (negative) charge placed in the middle plane ($y=W/2$) of the device in Fig. 1. Our results show that the tunneling current between delta-layers is strongly affected when the charge is present in the proximity of the tunnel junction. For instance, our simulations predict that the tunneling current increases up to 17 times when a single negative charge is between delta-layers (i.e. $x=20\text{nm}$ and $z=4\text{nm}$) or up to 11 times when the charge is above the delta-layers tunnel junction (e.g. $x=20\text{nm}$ and $z=7\text{nm}$). Fig. 3 shows the local density of states for Si: P δ -layer tunnel junctions. We postulate that the extreme sensitivity of the δ -layer tunnel junction to the presence of charges is due to the strong quantization of the conduction band (shown schematically as white dashed lines in the figure) for these highly-confined systems.

[1] H. R. Khan, *et al.*, Journal of Physics: Conference Series 54, 784–796 (2007).

[2] D. Mamaluy, and X. Gao, Appl. Phys. Lett. 106, 193503 (2015).

[3] X. Gao, *et al.*, Appl. Phys. 115, 133707 (2014).

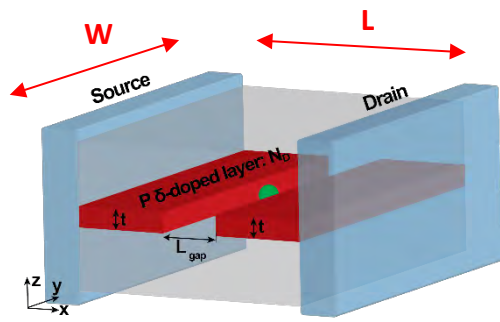


Fig. 1. Si:P δ -layer tunnel junction (TJ). The electrical charge is represented as a green sphere in the figure.

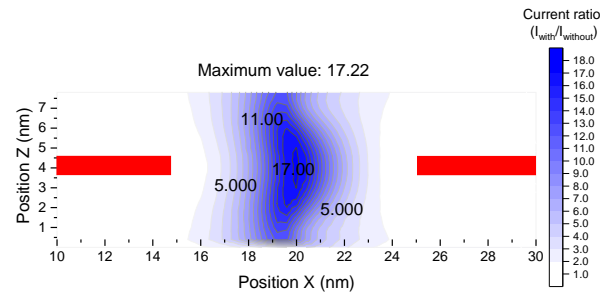


Fig. 2. Computed change of the electrical current for different positions of a (negative) charge (presented as a green sphere in Fig. 1) in the plane $y=W/2$ of the device in Fig. 1. The applied voltage between source and drain is 100mV.

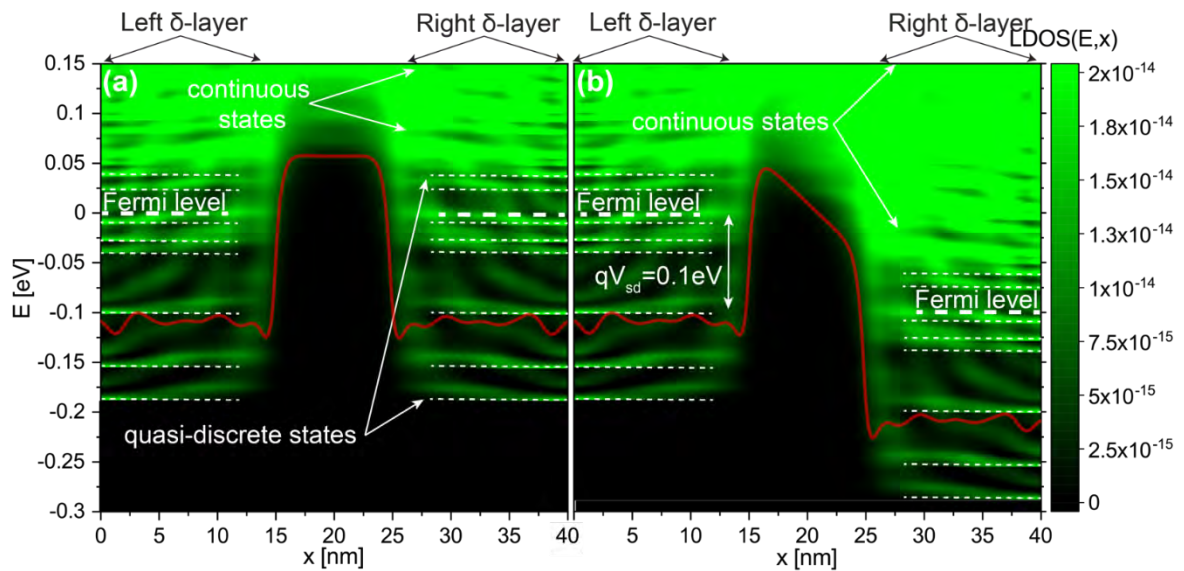


Fig. 3. Local density of state (LDOS) for δ -layer tunnel junction device shown in Fig. 1: (a) for an applied of 1 mV between the source and drain; (b) for an applied of 100mV. The semi-quantized states in the conduction band are indicated with dashed lines.

Magnonic Combinatorial Memory

M. Balinsky and A. Khitun

(Times New Roman, 12pt)

*Electrical and Computer Engineering Department, University of California – Riverside,
California, 92521, USA*

Keywords: spintronics, magnetic memory, combinatorics

In this work, we consider a type of magnetic memory where information is encoded into spin wave propagation routes [1]. The device is an active ring circuit comprising magnetic and electric parts connected in series. The electric part includes a broad-band amplifier, phase shifters, and attenuators. The magnetic part is a mesh of magnonic waveguides with magnets placed on the waveguide junctions. There are amplitude and phase conditions for auto-oscillations to occur in the active ring circuit. The frequency(s) of the auto-oscillation and spin wave propagation route(s) in the magnetic part depends on the mutual arrangement of magnets in the mesh. The propagation route is detected with a set of power sensors. The correlation between the states of electric components and the spin wave propagation route is the base of memory operation. The combination of input/output switches connecting electric and magnetic parts, and electric phase shifters constitute the memory address. The output of power sensors is the memory state. We present experimental data on the proof-of-the-concept experiments on the prototype with three magnets placed on top of a single-crystal yttrium iron garnet $Y_3Fe_2(FeO_4)_3$ (YIG) film. There are three selected places for the magnets to be placed. There is a variety of spin wave propagation routes for each configuration of magnets. The results demonstrate a robust operation with an On/Off ratio for route detection exceeding 35 dB at room temperature. The number of propagation routes scales factorial with the size of the magnetic part. Coding information in propagation routes makes it possible to drastically increase the data storage density compared to conventional memory devices. Magnonic combinatorial memory (MCM) with just 25 magnets can store as much as $25! = 10^{25}$ bits. Physical limits and constraints are also discussed.

[1] M. Balinsky and A. Khitun, <https://arxiv.org/abs/2307.07464> (2023).

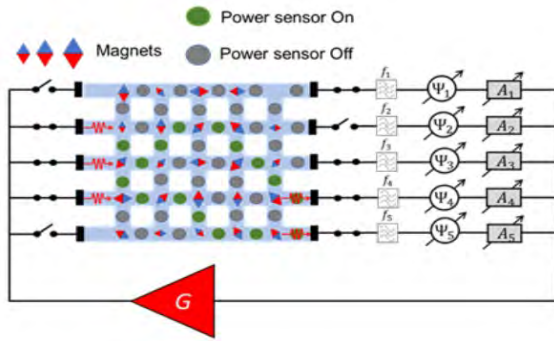


Fig.1: Schematics of MCM. The core of the structure is a mesh of magnonic waveguides shown in the light blue color. There are magnets depicted by the blue-red rhombs placed on top of waveguide junctions. There are power sensors placed on top of the waveguides between the junctions. The mesh is included into an active ring circuit via switches on the left and right sides. There are voltage-tunable frequency filters f_i , voltage-tunable phase shifters Ψ_i , and voltage-tunable attenuators A_i at each output port (right side). There is one broadband amplifier G in the electric part

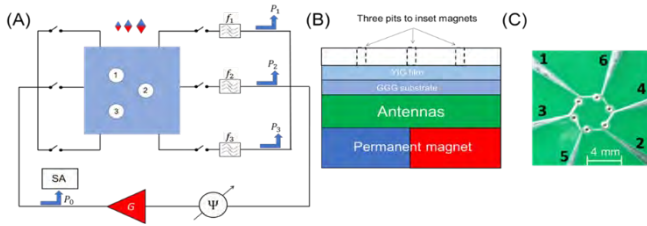


Fig.2: (A) Schematics of the first prototype with just three magnets. (B) The cross-section of the passive magnonic part. It consists from the bottom to the top of a permanent magnet, a Printed Circuit Board (PCB) substrate with six short-circuited antennas, a ferrite film made of GGG/YIG, and a plastic plate with three pits for magnets to be inserted. (C) The photo of the PCB with six antennas. The characteristic size of the antenna is 2 mm in length and 0.15 mm in width.

Switches Input Output	Phase [π]	Magnets Arrangement	Auto-oscillation frequency [GHz]	$P_0(f)$ [dBm]	P_1, P_2, P_3 [dBm]	Memory State
111 111	0	000	2.590	+7.5	-27, -75, -73	100
111 111	0	BWR	2.590, 2.538	+2, +4	-30, -78, -27	101
111 111	0	BRW	2.475	+6	-78, -30, -71	010
111 111	0	WBR	2.539	-1	-72, -71, -39	001
111 111	0	WRB	2.539	+2	-75, -69, -37	001
111 111	0	RBW	2.590, 2.539	+3, +1	-39, -75, -37	101
111 111	0	RWB	2.539	-3	-81, -78, -36	001

Fig.3: Experimental data obtained for the prototype as shown in Fig.2. The data in columns show the combination of input and output switches, the position of the external phase shifter, the magnet arrangement, the frequencies of the auto-oscillations, the power of the auto-oscillation P_0 at different frequencies, the power measured at the three output ports, and the table shows the logic output. It is logic 1 if the output power exceeds -45 dBm and logic 0, otherwise.

BWR	Input Phase [π]	Output State
	0	101
	0.63	111
	1.25	010
	1.75	001

RWB	Input Phase [π]	Output State
	0	001
	0.63	011
	1.25	110
	1.75	011

WBR	Input Phase [π]	Output State
	0	001
	0.63	101
	1.25	011
	1.75	001

Fig.4 Summary of experimental data collected. On the left: magnet arrangement. On the right: memory truth tables for four phases. There are 12 bits stored for each magnet configuration. For comparison, conventional memory with three magnets can store only 3 bits.

Magnetic charge quasi-particle dynamics for spintronics and reservoir computing applications

Deepak K. Singh¹, Jiasen Guo¹, Valeria Lauter², Laura Stingaciu², Piotr Zolnierczuk², Yuwei Zhang³, Risheng Wang³

¹Department of Physics and Astronomy, University of Missouri, Columbia, MO, USA

²Oak Ridge National Laboratory, Oak Ridge, TN, USA

³Missouri University of Science & Technology, Rolla, MO, USA

singhdk@missouri.edu

Keywords: Spintronics, neuromorphic

The dynamic state in artificial honeycomb spin ice is conventionally described in terms of finite size domain wall kinetics that require magnetic field or current application. Contrary to this common understanding, we have discovered that a thermally tunable artificial magnetic honeycomb lattice manifests a perpetual dynamic state due to self-propelled magnetic charge defect relaxation in the absence of any external tuning agent. [1, 2] The topological magnetic charges exhibit strong dynamic property with ps relaxation due to the barrierless kinetics of emergent magnetic charge defect in the underlying lattice. The new finding can have important implications to the design of energetically efficient spintronic and reservoir computing devices where electric current can be used for the tuning of magnetic states, instead of magnetic field application.[3, 4] While the magnetic charge defect's relaxation causes indirect interaction between fluctuating magnetic field, due to the charge defect kinetics, and electric charge carrier spin s (see Fig. 1)—thus causing a net positive drag to electric charge's drift speed, the relaxation time itself can act as synapse for the neuromorphic computing. We have showed that the drag effect enhances electrical conductivity manyfold, thus making the charge defect dynamics a strong alternative proposition for the spintronics application. Similarly, magnetic charge on honeycomb vertices can be tuned by modest current application. We have used contact probe atomic force microscopy to determine the variation in conductivity pattern of charge states after each current cycle, ranging from $\pm 50 \mu\text{A}$ to $\pm 200 \mu\text{A}$ (see Fig. 2). Given the large manifold of 2^n magneto-electric states for a set of n sites occupied charges that can be tuned by modest current, our thermally active honeycomb system provides ideal platform for reservoir computing.

Research at MU is supported by the U.S. Department of Energy, Office of Basic Energy Sciences under Grant No. DE-SC0014461.

[1] J. Guo, P. Ghosh, D. Hill, Y. Chen, L. Stingaciu, P. Zolnierczuk, C. Ullrich and D. K. Singh, "Persistent dynamics magnetic state in artificial honeycomb spin ice", *Nature Communications*, in press (accepted) (2023).

[2] J. Guo, D. Hill, V. Lauter, L. Stingaciu, P. Zolnierczuk, C. Mazzoli, P. Ghosh, C. Ullrich and D. K. Singh, "Uncovering new quasi particle in constricted nanomagnet", in preparation (2023)

[3] Y. Chen, B. Summers, A. Dahal, V. Lauter, G. Vignale and D. K. Singh, "Field and current control of the electrical conductivity of an artificial two-dimensional honeycomb lattice", *Advanced Materials* **31**, 1808298 (2019).

[4] L. J. Heyderman, "Spin ice devices from nanomagnets", *Nature Nanotechnology* **17**, 435 (2022)

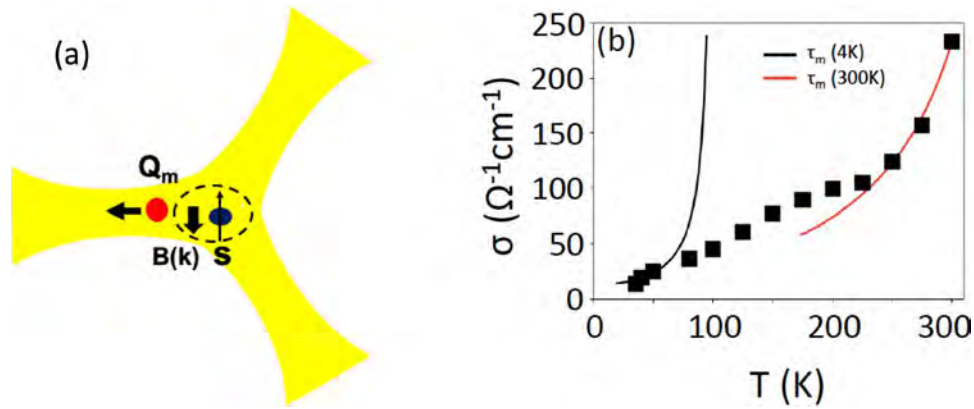


Figure 1: (a) Schematic depiction of interaction between fluctuating magnetic field $B(\mathbf{k})$ (arising due to the longitudinal relaxation of magnetic charge Q_m along honeycomb element) and conduction electron's spin s causes a net faster drift to charge carriers. (b) Faster relaxation at room temperature (~ 50 ps), compared to low temperature (~ 130 ps), propels electrical conduction by more than an order of magnitude.

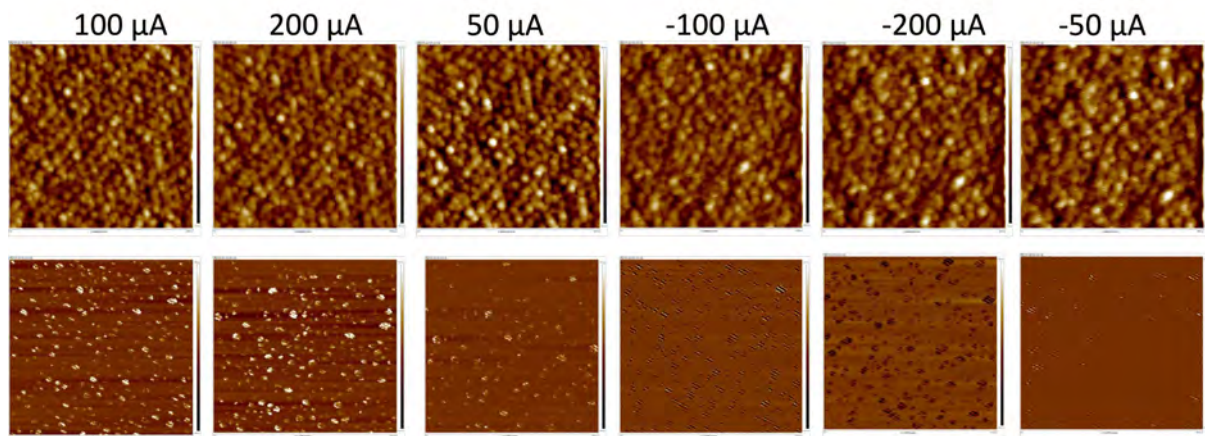


Figure 2: Magnetic charge polarity can be tuned by modest current application. Top Panel- phase image of artificial permalloy honeycomb lattice, obtained from contact probe atomic force microscopy (CAFM). Bottom Panel- conductivity map in CAFM scan after different current input cycle (shown on the top of the figures). The change in pattern is clearly visible as input current changes, thus providing different states that can be trained for reservoir computing purposes.

Interference-based computing using nonlinear spin waves

Adam Papp¹, Gyorgy Csaba¹, Maucha Levente¹, Markus Becherer², Johannes Greil²,
Martina Kiechle², and Wolfgang Porod³

¹Faculty for Information Technology and Bionics, Pazmany University Budapest, Hungary

²Department of Electrical Engineering, Technical University of Munich, Munich, Germany

³Department of Electrical Engineering, University of Notre Dame, Notre Dame, IN

Keywords: spintronics, neuromorphic computing

The notion of analog computing stems from the idea of calculating a problem by an analogous physical system, *i.e.* to map a computing problem to the laws of physics. Since wave phenomena are ubiquitous in physics, it is natural to think of solving computing problems by wave interference. Our research exemplifies this research goal on a specific physical system, namely spin waves (magnons). Spin waves not only show rich interference phenomena, but they also exhibit amplitude-dependent nonlinear behaviors, which is crucial for neural-network-like devices.

In our presentation, we first demonstrate how a magnetic thin film can realize neural computing functions in the spin-wave domain. The film is designed by in-silico machine learning [1] [2], and we employ *Backpropagation Through Time (BPTT)* to design a geometry that performs the desired computing functions. This procedure is referred to as inverse design. Using simulations, we demonstrate that the nonlinearity in the magnetic film is essential to achieve computing.

To show that the inverse design results in physically realizable devices, we show first experimental results on the inverse design of a YIG film. We use Focused Ion Beam (FIB) irradiation to change the properties of a YIG film in a precisely controlled way [3]. The inverse design procedure produces the spatial distribution of the FIB dose that should be applied for the desired functionality. We show experimental data on the realization of a lens (a simple focusing structure) and outline the design of a wave-based signal-processing device using this technology.

[1] Papp, Ádám, Wolfgang Porod, and Gyorgy Csaba. "Nanoscale neural network using non-linear spin-wave interference." *Nature Communications* 12, no. 1 (2021): 1-8.

[2] Wang, Qi, Andrii V. Chumak, and Philipp Pirro. "Inverse-design magnonic devices." *Nature Communications* 12, no. 1 (2021): 1-9.

[3] Kiechle, Martina, Adam Papp, Simon Mendisch, Valentin Ahrens, Matthias Golibrzuch, Gary H. Bernstein, Wolfgang Porod, Gyorgy Csaba, and Markus Becherer. "Spin-Wave Optics in YIG Realized by Ion-Beam Irradiation." *Small* (2023): 2207293.

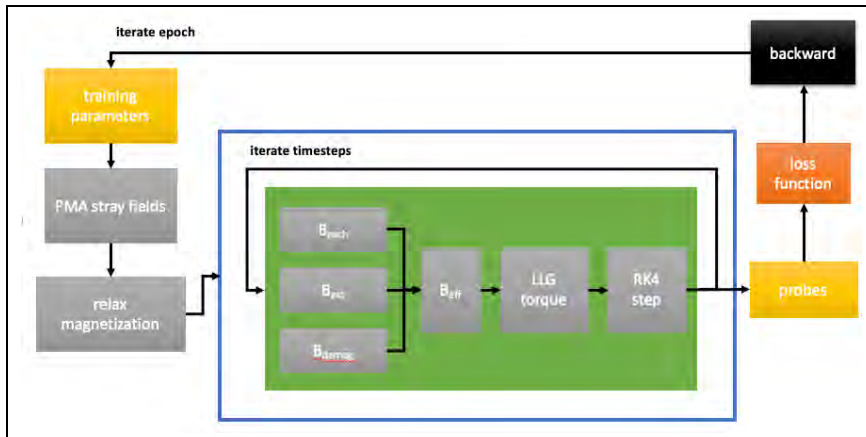


Figure 1 shows the schematic layout of the inverse-design procedure that applies machine-learning methods for designing a spin-wave scatterer geometry.

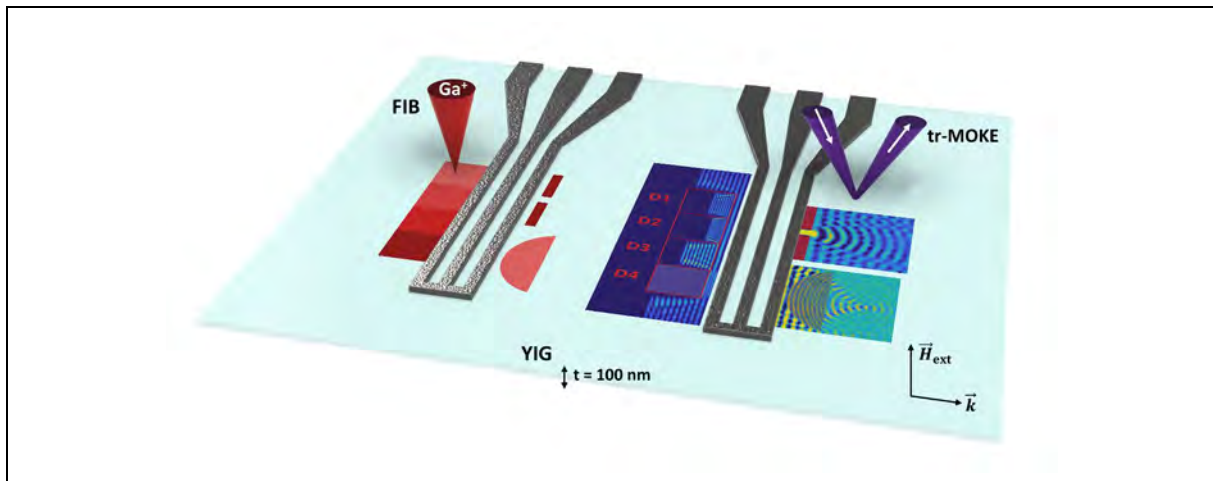


Figure 2 (reproduced from [3]) shows the experimental apparatus: on the left, the FIB-patterning procedure in the vicinity of a waveguide, and the right shows imaging this structure by trMOKE.

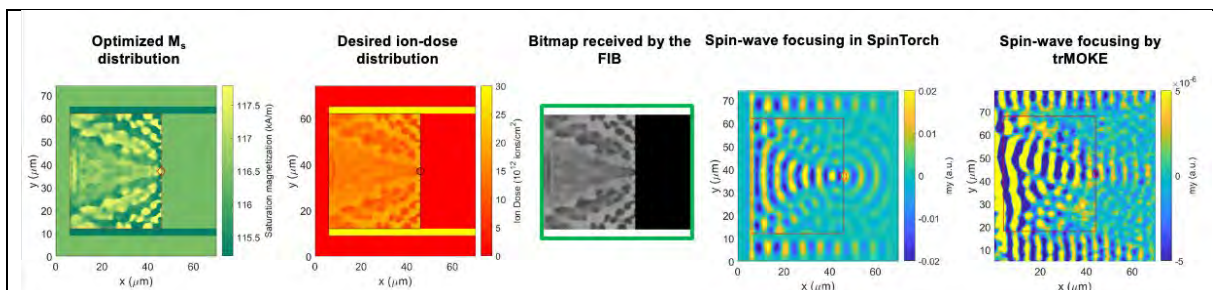


Figure 3 inverse design of a spin-wave lens. The left three images show the design created by the machine-learning algorithm, and the right two images are the simulation and the experimental data of the spin wave pattern, respectively.

Quantum transport in HgTe topological insulators and HgTe-superconductor hybrids

Dieter Weiss

Institut für Experimentelle und Angewandte Physik, Universität Regensburg, 93040

Regensburg, Germany

dieter.weiss@ur.de

Keywords: quantum transport, topology

Strained 3D HgTe, a strong topological insulator, exhibits a pronounced quantum Hall effect (QHE) [1,2], although different classes of electrons participate in transport, including those on the top and bottom surfaces as well as electrons in the bulk conduction band. At low magnetic fields, the carrier densities, as reflected by the periodicity of the Shubnikov-de Haas (SdH) oscillations in transport measurements and the magnetocapacitance oscillations, which involve only top-surface electrons, are strikingly different. This suggests the coexistence of different Landau fans for the three electron species. At high magnetic fields, however, both capacitance and SdH oscillations reflect the same carrier density, suggesting that at sufficiently high B-fields only one Landau fan survives due to charge rearrangement [3].

We fabricate wire structures using this material, which exhibits high carrier mobilities [4]. Topological insulator (TI) nanowires in proximity to conventional superconductors have been proposed as a tunable platform to realize topological superconductivity and Majorana zero modes [5]. The tuning is achieved by using an axial magnetic flux ϕ , which transforms the system from trivial at $\phi = 0$ to topologically non-trivial when half a magnetic flux quantum $\phi_0/2$ threads the wire cross-section. It has been predicted that Majorana-bound states appear in the topological regime, as indicated by the absence of odd Shapiro steps in TI nanowire/superconductor Josephson junctions under microwave irradiation, reflecting the presence of 4π -periodic supercurrents [6]. In our experiments, we observe missing Shapiro steps even at zero flux, suggesting that a trivial mechanism is also at work. However, with increasing axial magnetic flux, the fraction of the 4π -periodic supercurrent with respect to the total supercurrent increases, suggesting that TI nanowires could serve as a platform for studying Majorana-bound states [7]. Work done in collaboration with Ralf Fischer, Johannes Ziegler, Stefan Hartl, Dmitriy A. Kozlov, Wolfgang Himmler, Michael Barth, Jacob Fuchs, Jordi Picó-Cortés, Cosimo Gorini, Gloria Platero, Milena Grifoni, Klaus Richter, N. N. Mikhailov, Sergey A. Dvoretzky, Jürgen Weis, Maximilian Kühn, Lukas Freund und Christoph Strunk.

[1] C. Brüne et al., Phys. Rev. Lett. **106**, 126803 (2011)

[2] J. Ziegler et al., Phys. Rev. Res. **2**, 033003 (2020)

[3] S. Hartl et al., unpublished

[4] J. Ziegler et al., Phys. Rev. B **97**, 035157 (2018)

[5] M. Cook and M. Franz, Phys. Rev. B **84**, 201105(R) (2011)

[6] A. Y. Kitaev, Phys. Usp. **44**, 131 (2001)

[7] R. Fischer et al., Phys. Rev. Res. **4**, 013087 (2022)

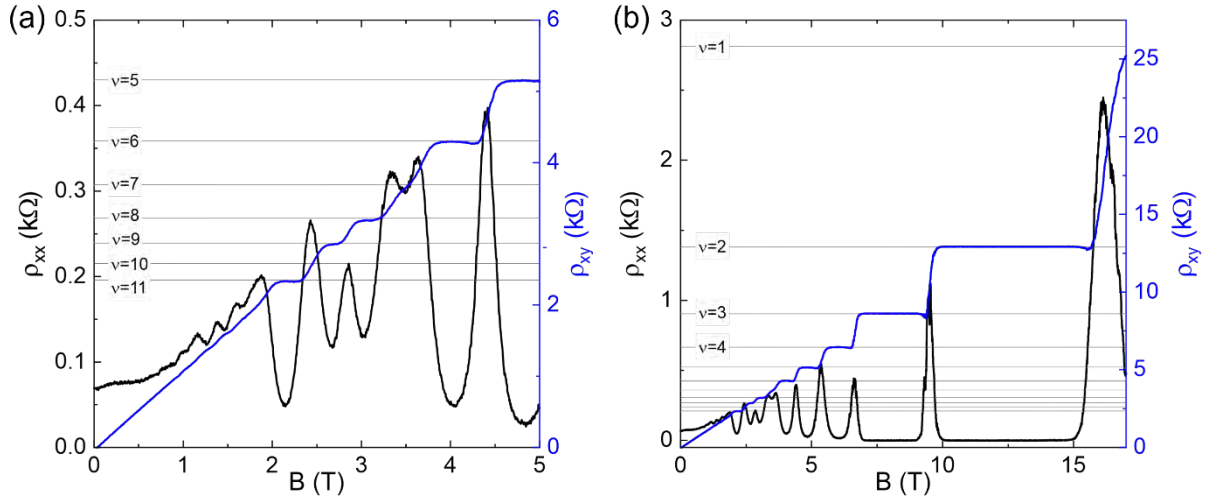


Fig.1: ρ_{xx} and ρ_{xy} in low (a) and high (b) magnetic fields. Well-developed Hall plateaus and zero-resistance states are observed in magnetic fields exceeding 7 Tesla. However, the interplay among different carrier species leads to a more complex scenario at lower field strengths.

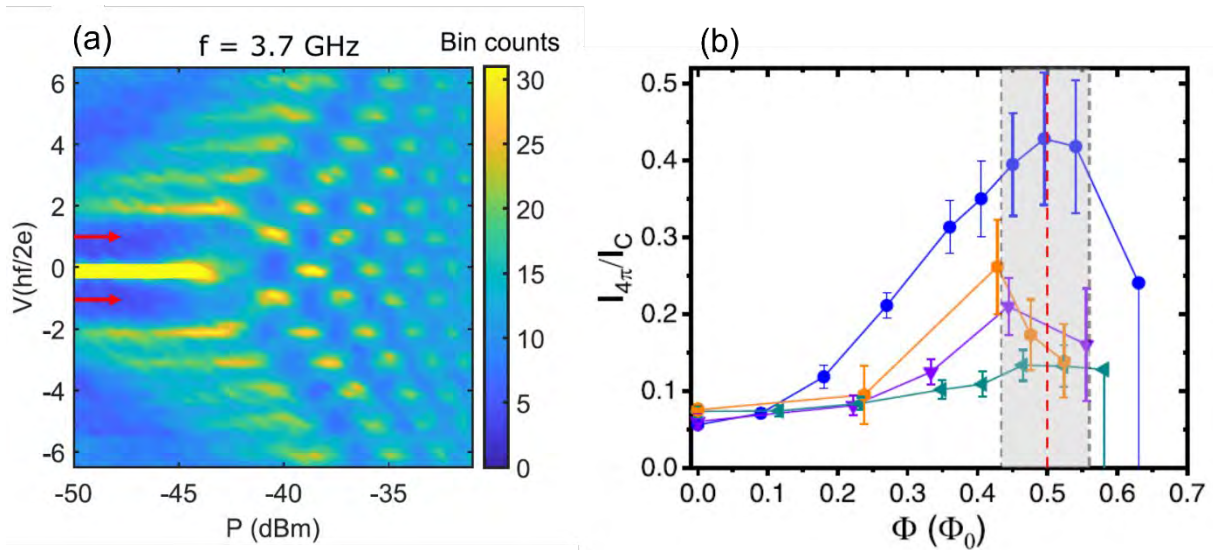


Fig.2: (a) Suppression of the first Shapiro steps, marked by red arrows at a magnetic field of $B = 30$ mT ($\phi/\phi_0 \approx 0.27$). With the normal resistance of the junction $R_N = 216 \Omega$, we estimate $I_{4\pi}/I_C \approx 21\%$ using the resistively shunted junction (RSJ) model. (b) $I_{4\pi}/I_C$ as a function of the axial field for different samples using the RSJ model. Near half a flux quantum $I_{4\pi}/I_C$ has a maximum.

Topological Hall effect in Dirac semimetal

S. Islam¹, E. Steinebronn¹, B. Neupane², K. Yang¹, Y. Wang², C. Liu¹, S. Ghosh³, K. Andre Mkhoyan³, J. Chamorro⁴, T. M. McQueen⁴, and N. Samarth¹

¹*Department of Physics, Pennsylvania State University, University Park, PA: 16802, USA*

²*Department of Physics, University of North Texas, Denton, Texas 76203, USA*

³*Department of Chemical Engineering and Materials Science, University of Minnesota, Minneapolis 55455, USA*

⁴*Department of Chemistry, Johns Hopkins University, Baltimore, Maryland 21218, USA*
ski5160@psu.edu

Keywords: topology, quantum transport

Magnetic skyrmions are chiral spin textures whose non-trivial real space topology is often created by an interfacial anisotropic Dzyaloshinskii-Moriya exchange interaction (DMI) that originates from spin-orbit coupling and broken inversion symmetry [1]. They have been observed in a wide variety of bulk single crystals such as MnSi [2] and thin films such as Fe_{1-x}Co_xSi [3]. More recently, magnetic skyrmions have been probed at ferromagnet/topological insulator interfaces [4] and in magnetic Weyl semimetals [5]. This motivates similar explorations of skyrmion formation in Dirac semimetals (DSMs). We investigated the formation of skyrmions at the interface of a canonical DSM (Cd₃As₂) and a ferromagnetic semiconductor (In_{1-x}Mn_xAs) with perpendicular magnetic anisotropy. Our calculations indicate nonzero spin susceptibility in such heterostructures due to Rashba spin-orbit coupling from broken inversion symmetry, implying the DM interaction necessary for skyrmions. To experimentally test this idea, we grew Cd₃As₂/In_{1-x}Mn_xAs bilayers and mapped out the behavior of the Hall effect as a function of temperature, magnetic field, and gate voltage in electrostatically top gated devices. Below T = 6 K, we observe an emergent gate-tunable topological Hall effect (THE) indicated by an excess Hall resistance (Fig. 1 and Fig. 2). This signature is most pronounced at the charge neutrality point, suggesting the formation of a Dirac-electron mediated chiral spin texture at the DSM/ferromagnet interface. Our study provides a new platform to study the interplay between the topological states in DSMs and the chiral spin textures associated with the THE. Supported by the NSF Graduate Research Fellowship Program (Grant No. DGE1255832).

[1] A. Fert, N. Reyren, and V. Cros, Nat. Rev. Mater., 2, 1 (2017).

[2] S. Mühlbauer et al., Science 323, 915–919 (2009)

[3] X.-Z. Yu et al., Nature 465, 901–904 (2010)

[4] P. Li et al., Nano Lett., 21, 1, 84–90 (2021)

[5] P. Pushpan et al., Phys. Rev. Lett. 124, 017202 (2020)

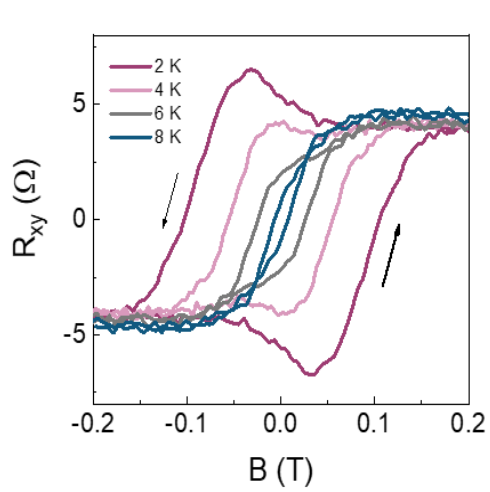


Fig. 1: Hall resistance (R_{xy}) at different temperature (T) showing Excess R_{xy}

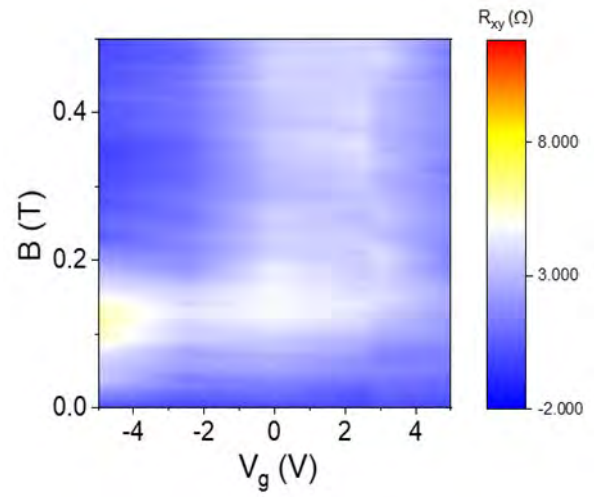


Fig.2: Gate-voltage (V_g) dependence of R_{xy} showing the excess resistance is most pronounced close to the charge neutrality point of the heterostructure

Epitaxial Topological Semimetal Thin Film Platforms for Device Applications

K. Alberi¹

¹*National Renewable Energy Laboratory, Golden CO USA*

Kirstin.Alberi@nrel.gov (e-mail address of the corresponding author)

Keywords: topology

Topological semimetals offer a range of properties that are advantageous for electronic device applications, including high carrier mobility, broadband optical absorption, and the ability to control spin degrees of freedom. To access and utilize these properties, we must learn to integrate them into device structures and master defects, doping, alloying and interfaces, in much the same way we already have with semiconductors. In this talk, I will discuss how we are using epitaxial thin film growth as a tool for understanding and regulating properties in topological semimetals, including Cd₃As₂ and TaAs [1-3]. While we are learning more about how defects, impurities and interfaces influence the Fermi level and electron transport [4-5], I will also touch on the many challenges we still face in realizing the devices we envision.

[1] A.D. Rice *et al.*, Phys. Rev. Mater. **3**, 121201(R) (2019)

[2] A.D. Rice *et al.*, Adv. Funct. Mater. (2022) <https://doi.org/10.1002/adfm.202111470>

[3] J.N. Nelson *et al.*, Matter, (2023) <https://doi.org/10.1016/j.matt.2023.06.018>

[4] J.N. Nelson *et al.* Phys. Rev. B **107**, L220206 (2023)

[5] C. Brooks *et al.* Phys. Rev. B **107**, 224110 (2023)

Phonons in free-standing nanostructured membranes of MoSe and Si

P. Xiao^{1,2}, A El Sachat^{1,#}, E. Chavez-Angel¹, R. C. Ng¹, G. Nikoulis³, J. Kioseoglou³, K. Termentzidis⁵, M. Sledzinska¹, O. Florez¹, M. Poblet¹, M. Albrechtsen⁵, S. Stobbe⁵, J. Ahopelto⁶ and C. M. Sotomayor Torres^{1,*}

¹ *Catalan Institute of Nanoscience and Nanotechnology (ICN2), CSIC and BIST, Campus UAB, Bellaterra, 08193 Barcelona, Spain*

² *Departamento de Física, Universidad Autónoma de Barcelona, 08193 Bellaterra, Spain*

³ *Department of Physics, Aristotle University of Thessaloniki, GR-54124 Thessaloniki, Greece*

⁴ *Univ Lyon, CNRS, INSA Lyon, CETHIL, UMR5008 69621 Villeurbanne, France.*

⁵ *Department of Photonics Engineering, Technical University of Denmark, DK-2800, Kgs, Lyngby, Denmark*

⁶ *VTT Technical Research Centre of Finland Ltd, P.O. Box 1000, FI-02044 VTT, Espoo, Finland*

clivia.sotomayor@inl.int

Keywords: 2d materials, nanostructures

Free-standing membranes of MoS₂ have been nanostructured with phononic crystals resulting in heat locking and in spatially controlled heat transport. The determination of thermal conductivity relies on two-laser Raman thermometry and simulations by equilibrium molecular dynamics considering porosity, film thickness and temperature. We calculated the thermal conductivity reduction factor as a function of thickness up to 40 nm and found it to be a factor of 100 below the amorphous limit cf. patterned Si and SiC. Anisotropy is inherent in 2D materials and here we add directionality in heat propagation in the plane of the membrane which make these layer suitable for possible 2- and 3-D integration in hybrid devices.

While phonon transport in patterned MoS₂ can be understood in terms of phononic crystals, extending membrane patterning to topological phononics, brings in added complexity and technological challenges mainly reflected on the large impact of deviations in critical dimensions, compromising the calculated band gap width at the Dirac point and the symmetry and dispersion of bands in and close to the band gap. We will present a variability study as well as recent light scattering and laser Doppler vibrometry, where both preliminary measurements suggest the presence of topological modes around 2 GHz and in the 10 GHz range, respectively. This preliminary work this time using designs based on topological phonon waveguides, nc-

Present addresses:

Institute of Nanoscience and Nanotechnology, National Center for Scientific Research “Demokritos”, Athens 15341, Greece.

* Intl. Iberian Nanotechnology Laboratory, Av. Mestre José Veiga s/n, 4715-330 Braga – Portugal.

Emergent Wetting Behavior and Strain Engineering in 2D Materials on Nanostructured Substrates

D. Adinehloo¹, J. Hendrickson², P. N. Prasad^{3,1}, and V. Perebeinos¹

¹*Department of Electrical Engineering, University at Buffalo, Buffalo, NY 14228, USA*

²*Sensors Directorate, Air Force Research Laboratory, Wright-Patterson AFB, Ohio 45433, USA*

³*Department of Chemistry and The Institute for Lasers, Photonics and Biophotonics, University at Buffalo, The State University of New York, Buffalo, New York 14260, USA*
vasilipe@buffalo.edu

Keywords: 2d materials, nanostructures

We explore the fascinating realm of strain engineering and wetting transitions in two-dimensional (2D) materials when placed on nanopillar arrays and trench structures. Our investigation encompasses a diverse set of 2D materials, including transition metal dichalcogenides, hexagonal boron nitride, and graphene, with a keen focus on the impact of various parameters such as van der Waals energies, lattice constants, and height profiles. By systematically modulating the van der Waals adhesion of 2D materials to the substrate, we unveil the remarkable potential to tailor the strain in 2D materials on nanopillar arrays. By exploring the intricate interplay between van der Waals adhesion energies, we pinpoint a critical transition in 2D material morphology with two phases having different strain distributions. Our investigation extends to substrate patterning with 1D trenches, where 2D material is predicted to have a similar transition as a function of van der Waals adhesion energies and width of the trenches. Our findings enable comprehension of tunable strain engineering in 2D materials, leading to promising prospects for quantum technologies.

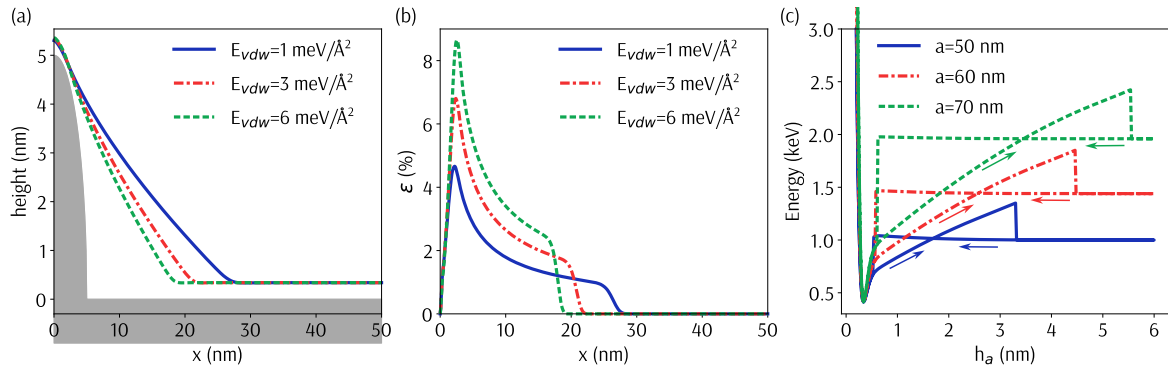


Fig.1: Tailoring MoSe₂ Structure on Nanopillars. (a) Modulating MoSe₂ Behavior on Nanopillar Arrays with Varied van der Waals Energies (E_{vdw}). (b) Unraveling Strain Dynamics in MoSe₂ Structure on Nanopillars across Diverse E_{vdw} Levels. (c) Mapping Energy Landscape with Respect to height profile (h_a) for Different Lattice Constants ($2a$). In (a) and (b), a is consistently set at 50 nm. In (c), $E_{vdw} = 1 \text{ meV}/\text{\AA}^2$, while h_a signifies the height of the 2D material at $x = a$. $h = 5 \text{ nm}$ in all panels. Visualizing MoSe₂ atop nanopillars, (a) uncovers van der Waals energy interplay. Examining strain complexities in (b) reveals MoSe₂ structure's nuanced response to varying E_{vdw} . Profiling energy fluctuations in (c) artistically portrays the structural response to shifts in h_a .

Modeling Long-Wavelength Phonon Dynamics for Enhanced Thermal Transport in Nanomaterials

L. Avazpour, M.K. Eryilmaz, and I. Knezevic

*Department of Electrical and Computer Engineering, University of Wisconsin – Madison,
Madison, WI 53706*

e-mail: laleh.avazpour@wisc.edu; irena.knezevic@wisc.edu

Keywords: 2d materials, nanostructures

Long-wavelength phonons in single-crystalline bulk materials undergo limited phonon–phonon scattering and travel over extended distances, thereby contributing significantly to thermal conductivity. We present an analysis of the role of disorder in thermal transport on two example systems: a) III-V alloy superlattices, akin to those employed in quantum cascade lasers, and b) rough silicon nanowires. The computational approach, informed by experimental data, is based on the finite-difference time-domain (FDTD) solution to the elastic wave equation formulated in the velocity–stress framework and built upon our previously developed code base [1].

The simulation of thermal transport in InGaAs/InAlAs alloy superlattices involves a series of FDTD calculations, encompassing diverse rms roughness values and correlation lengths (Fig. 2). These simulations serve as the basis for a novel neural-network-based machine-learning algorithm. This algorithm leverages the FDTD data to determine optimal rms roughness and correlation lengths, yielding excellent agreement between calculated and measured outcomes [2]. Notably, both experimental data and simulations unveil a distinctive transition from incoherent to coherent phonon transport in alloy superlattices, elucidating the significance of interface density (Figs. 1 and 2).

When examining transport in rough silicon nanowires, we launch a Gaussian longitudinal wave packet from the center of the nanowire towards a rough interface formed between silicon and aluminum top layer (Fig. 3). This wave packet, typically centered around a resonant mode frequency, enables the analysis of frequency-domain characteristics, such as frequency broadening dependent on roughness properties, from which we extract scattering lifetimes. The power-law dependence on the lifetime on frequency provides valuable insights into the role of wire dimensions and roughness features in the dynamics of long-wavelength phonons.

This work underscores the complexity of phonon interaction with disorder and highlights the utility of the FDTD method in understanding phonon dynamics in nanomaterials. By comprehensively modeling long-wavelength phonon behavior and their interactions with interfaces and boundaries, we advance the understanding of thermal transport in nanoscale systems and pave the way for enhanced materials design and applications.

[1] L. N. Maurer, S. Mei, and I. Knezevic, *Phys. Rev. B* **94**, 045312 (2016).

[2] C. Perez, et al., *Appl. Phys. Lett.* **121**, 232201 (2022).

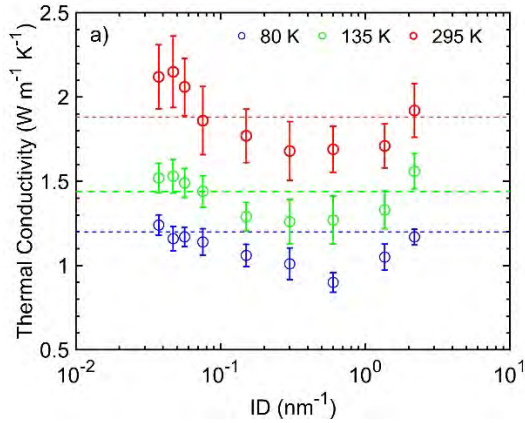


Fig.1: Cross-plane thermal conductivity measurements at three distinct temperatures: 80 K (blue), 135 K (green), and 295 K (red), plotted against interface density spanning from 0.0374 to 2.19 nm⁻¹. Reference values for bulk quaternary alloys with identical stoichiometry as the superlattices are indicated by dashed horizontal lines.

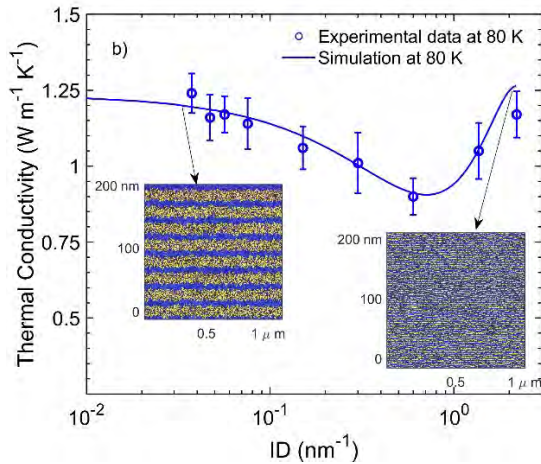


Fig.2: Experimental data (open symbols) and corresponding model predictions (solid curve) of cross-plane thermal conductivity at 80 K, plotted against interface density. Open symbols represent experimental averages with error bars indicating the standard deviation across four measurements. Insets illustrate simulated structures with low and high interface densities. Reprinted with permission from AIP Publishing from *Appl. Phys. Lett.* 121, 232201 (2022).

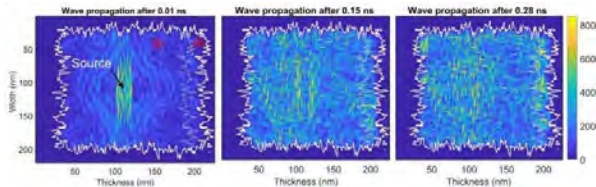


Fig.3: (Preliminary work) A Gaussian wave packet initiated from the center of a silicon nanowire (170 nm width; 200 nm thickness) with an aluminum capping layer (rightmost layer). Snapshots captured at three time points: 0.01 ns (left), 0.15 ns (center), and 0.28 ns (right) following the launch. The irregular surface exhibits exponential correlation with a length scale of 1.7 nm (0.01 of the width) and a rms roughness of 5 nm.

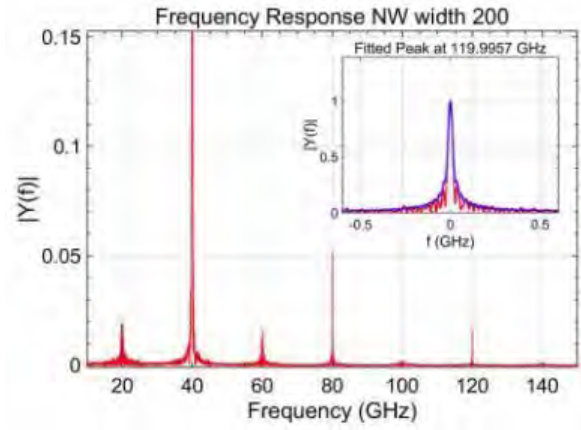


Fig.4: Fourier transform of the time-resolved, spatially averaged velocity magnitude, normalized by the velocity magnitude of the initial Gaussian wave. Each notable peak is subjected to Lorentzian fitting (see inset), where the width of each Lorentzian peak characterizes the scattering rate, representing the inverse of the lifetime influenced by surface roughness, averaged across the entire surface.

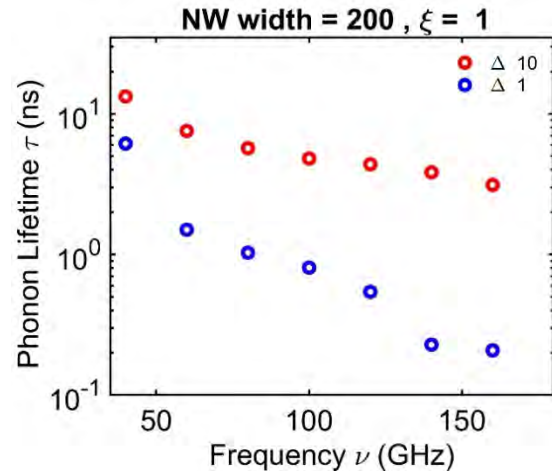


Fig.5: Data illustrating the relationship between lifetime and elastic-wave frequency for two distinct rms roughness values (1 nm and 10 nm) while maintaining constant wire dimensions (200 nm x 200 nm) and correlation length (1 nm). The dependence of lifetime on frequency provides valuable insights into the intricate interplay among factors such as the wire cross-sectional aspect ratio, rms roughness, and the nature of roughness correlation.

Thermal probe of Fractional quantum Hall states in Bilayer graphene

Fereshte Ghahari

Assistant Professor, Department of Physics and Astronomy

George Mason University, Fairfax, USA

fghahari@gmu.edu

Keywords: 2d materials, topology,

Measurement of thermodynamic properties at half-filled LLs such as thermoelectric power (TEP) can offer a view which is distinct from that offered by other techniques. For example, in the case of a clean non-interacting 2D electron system, it has been shown that TEP is proportional to the transport entropy of the 2D electron system. A similar connection between TEP and entropy was later proved to hold for strongly interacting electrons in high magnetic fields. This makes TEP a powerful tool to reveal statistical properties of FQH states as the entropy carried by non-Abelian quasiparticles is predicted to be anomalously larger than that of Abelian quasiparticles. In this talk, I will present magneto TEP studies of high-quality Bernal stacked bilayer graphene devices which exhibit well-developed FQH states including even denominator states at relatively low magnetic fields. Our data indicates that TEP can be a more sensitive probe of FQH states compared to resistivity measurements. The observed FQH states are being studied further by temperature and magnetic field dependence TEP measurement to probe their non-Abelian properties.

[1] N. Sultana, R. Rienstra, K. Watanabe, T. Taniguchi, F. Ghahari, “Thermal probe of fractional quantum Hall states in bilayer graphene,” Under preparation

Note: Since the work is not published yet, I won't be able to share figures

Asymmetric proximity interactions and chiral quantum light generation in 2D magnet/semiconductor van der Waals heterostructures

J. Choi¹, X. Li¹, C. Lane¹, J.-X. Zhu¹, A. Jones¹, H. Zhao¹, V. Chandrasekaran¹, M. Pettes¹, A. Piryatinski¹, M. Tschudin², P. Reiser², D. Broadway, P. Maletinsky², H. Htoon¹, S. A. Crooker¹

¹*NHMFL and CINT, Los Alamos National Laboratory, Los Alamos, NM, USA*

²*Department of Physics, University of Basel, Basel, Switzerland*

crooker@lanl.gov

Keywords: 2D materials, light-matter interactions

Magnetic proximity interactions (MPIs) between atomically-thin semiconductors and two-dimensional magnets provide a means to manipulate spin and valley degrees of freedom in nonmagnetic monolayers, without the use of applied magnetic fields. In such van der Waals (vdW) heterostructures, MPIs originate in the nanometer-scale coupling between the spin-dependent electronic wavefunctions in the two materials, and typically their overall effect is regarded as an effective magnetic field acting on the semiconductor monolayer. Here we demonstrate that this picture, while appealing, is incomplete: The effects of MPIs in vdW heterostructures can be *markedly asymmetric*, in contrast to that from an applied magnetic field [1]. Valley-resolved optical reflection spectroscopy of MoSe₂/CrBr₃ vdW structures reveals strikingly different energy shifts in the *K* and *K'* valleys of the MoSe₂, due to ferromagnetism in the CrBr₃ layer (see Figs. 1 & 2). Density-functional calculations indicate that valley-asymmetric MPIs depend sensitively on the spin-dependent hybridization of overlapping bands, and as such are likely a general feature of such hybrid vdW structures. These studies suggest routes to selectively control *specific* spin and valley states in monolayer semiconductors.

Using a different materials system, we also demonstrate the creation of free-space chiral quantum light emitters (ie, circularly-polarized single photon emitters) via the nano-indentation of WSe₂/NiPS₃ heterostructures at zero external magnetic field [2]. These quantum light emitters exhibit a high degree of circular polarization (0.89) and single-photon purity (95%), independent of pump laser polarization (Figs. 3 & 4). This chiral quantum light emission arises from magnetic proximity interactions between localized excitons in the WSe₂ monolayer, and the out-of-plane magnetization of defects in the antiferromagnetic order of the NiPS₃, both of which are co-localized by the strain fields associated with the nanoscale indentations.

[1] J. Choi, C. Lane, J.-X. Zhu, & S.A. Crooker, Asymmetric magnetic proximity interactions in MoSe₂/CrBr₃ van der Waals heterostructures, *Nature Materials* **22**, 305 (2023).

[2] X. Li, A.C. Jones, J. Choi, H. Zhao, V. Chandrasekaran, M.T. Pettes, A. Piryatinski, M.A. Tschudin, P. Reiser, D. Broadway, P. Maletinsky, N. Sinitsyn, S.A. Crooker, & H. Htoon, Proximity-induced chiral light generation in strain-engineered WSe₂/NiPS₃ heterostructures, *Nature Materials* (August 2023).

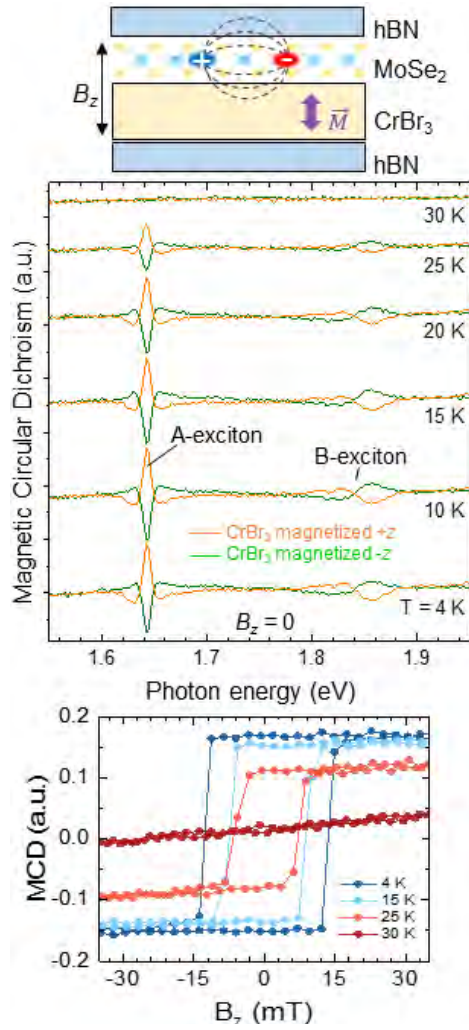


Fig.1: MoSe₂/CrBr₃ structure. MCD at $B_z=0$ shows a strong magnetic circular dichroism (MCD) response from the (non-magnetic) MoSe₂ below $T_c \sim 28$ K, due to MPIs. Bottom: Hysteresis of MCD. From [1].

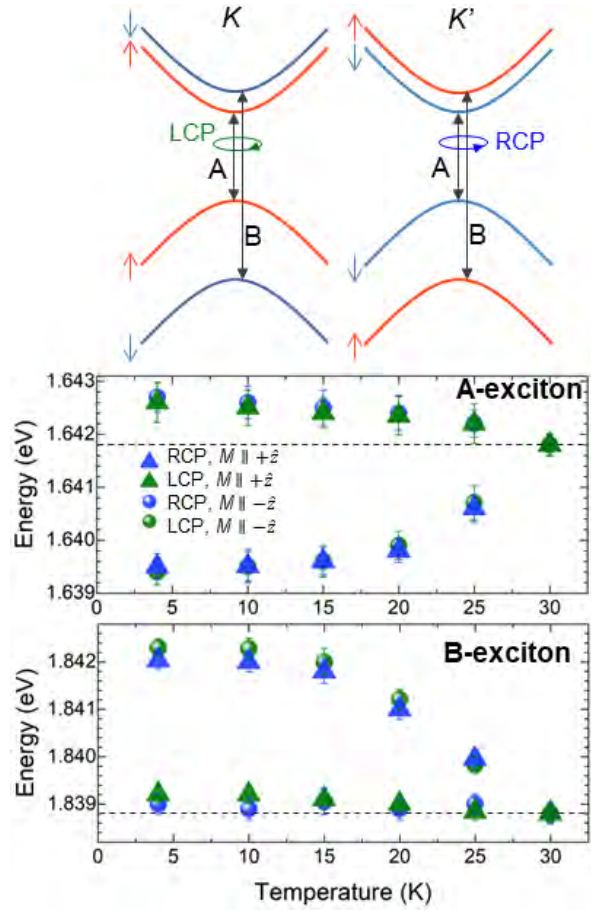


Fig.2: Optical transitions of spin-up/down bands in K/K' valleys shift asymmetrically due to MPIs (in contrast to effect of real magnetic fields). From [1].

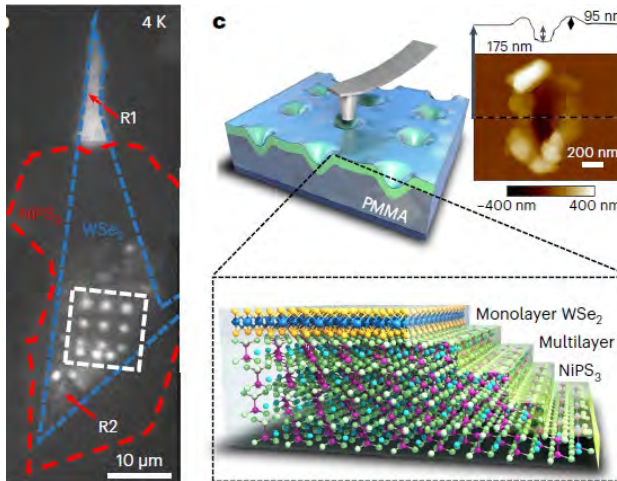


Fig.3: Photoluminescence (PL) image and schematic of a nanoindented WSe₂/NiPS₃ van der Waals heterostructure. The indentations create single photon emitters, that emit circularly polarized light due to MPIs with the underlying NiPS₃. From [2].

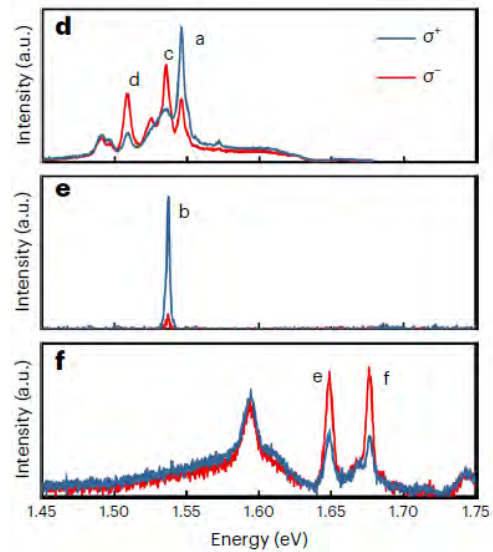


Fig.4 Representative σ^+ and σ^- resolved PL spectra at 4 K from different individual nanoindentations, acquired under linearly polarized laser excitation at zero magnetic field. From [2].

Terahertz Spin-Light Coupling in Proximitized Dirac Materials

K. S. Denisov¹, I. V. Rozhansky¹, S. O. Valenzuela^{2,3}, and I. Zutic⁴

¹*Ioffe Institute, 194021 St. Petersburg, Russia*

²*Catalan Institute of Nanoscience and Nanotechnology, CSIC and BIST, Barcelona, Spain*

³*Institucio Catalana de Recerca i Estudis Avancats (ICREA) Barcelona 08010, Spain*

⁴*Department of Physics, University at Buffalo, State University of New York, Buffalo, NY 14260, USA*

zigor@buffalo.edu

Keywords: 2d materials, spintronics, light-matter interactions, quantum materials

The atomically thin nature of two-dimensional (2D) materials makes them highly susceptible to the influence of their neighbors, thereby enabling the design of their electronic band structure by proximity phenomena [1]. Here, we reveal a remarkable terahertz (THz) spin-light interaction in 2D Dirac materials that arises from proximity effects of magnetic and spin-orbital character [2]. We demonstrate theoretically that the electric dipole spin resonance of Dirac electrons displays distinctive features in the THz range, upon emerging spin-pseudospin proximity terms in the Hamiltonian. To capture the effect of fast pseudospin dynamics on the electron spin, we develop a mean-field theory and complement it with a quantum-mechanical treatment. As a specific example, we investigate the THz response of a single graphene layer proximitized by a magnetic substrate, using realistic parameters. Our analysis demonstrates a strong enhancement of the THz-light absorption with the increase of the spin-pseudospin coupling, pointing towards promising prospects for THz detection and efficient generation and control of spins in spin-based quantum devices.

[1] I. Zutic *et al.*, *Mater. Today* **22**, 85 (2019).

[2] K. S. Denisov, I. V. Rozhansky, S. O. Valenzuela, and I. Zutic, preprint.

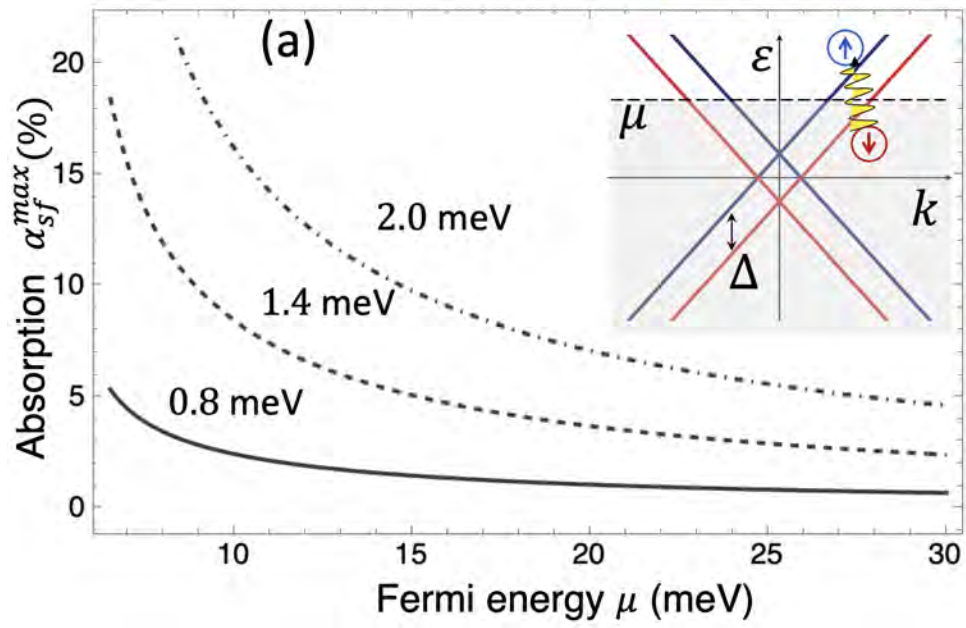


Fig.1: The evolution of a giant increase in electron dipole spin resonance absorption with the Fermi energy, μ , and spin-orbit coupling strength (0.8, 1.4, and 2.0 meV). Insert: Linear spectrum with proximity induced spin splitting, Δ .

Electron Transport in Vertical Quasi-Two-Dimensional Antiferromagnetic Semiconductor Devices

S. Ghosh^{1,2}, Z. E. Nataj^{1,2}, F. Kargar^{1,2}, and A. A. Balandin^{1,2}

¹*Department of Materials Science and Engineering, UCLA, California 90095 USA*

²*Department of Electrical and Computer Engineering, UCR, California 92521, USA*

fkargar@ece.ucr.edu

Keywords: 2D materials, magnetism

Recent years witnessed a growing interest in the exploration of magnetism within low-dimensional systems for enabling novel spintronic applications [1-3]. This pursuit started with the discovery of ferromagnetic properties in single-layer quasi-two-dimensional (quasi-2D) transition-metal dichalcogenides, denoted as MX₂, in which M and X are transition metal and chalcogen, respectively. It was found that quasi-2D transition metal phospho-trichalcogenides (MPX₃) are among the very rare compounds that host a variety of antiferromagnetic (AFM) spin ordering in the few and single atomic layer limits [1]. Generally, these AFM compounds are semiconductors with electronic band gaps spanning from 1.3 eV to 3.5 eV [1-3]. In their intrinsic form, they are highly electrically resistive making their electrical transport characterization a formidable task. To overcome this challenge, we fabricated large-area short-channel vertical *h*-BN/FePS₃ heterostructure devices and conducted cross-plane electron transport measurements (Figs. 1 – 2). Our results show that the resistance, *R*, of the devices, decreases with temperature rise, consistent with the semiconductor nature of FePS₃ AFM material (Fig. 3). Notably, the temperature-derivate of the resistance, *dR/dT*, exhibits a sharp minimum at the Néel temperature of FePS₃ at *T_N*~115 K, indicating a possible electron-magnon interaction at the magnetic phase transition (Fig. 4). The obtained results suggest a possibility of the interplay of the AFM and semiconductor properties of these quasi-2D materials that can be potentially used for achieving novel device functionalities.

F.K. and A.B.B. acknowledge funding from the National Science Foundation (NSF), Division of Material Research (DMR) *via* the project No. 2205973 "Controlling Electron, Magnon, and Phonon States in Quasi-2D Antiferromagnetic Semiconductors for Enabling Novel Device Functionalities." A.A.B. acknowledges the support from the Vannevar Bush Faculty Fellowship.

[1] X. Wang, *et al.*, Adv. Mat. 1804682 (2018)

[2] S. Ghosh, *et al.*, Adv. Electron. Mater., 2100408 (2021)

[3] F. Kargar, *et al.*, ACS Nano **14**, 2424 (2022)

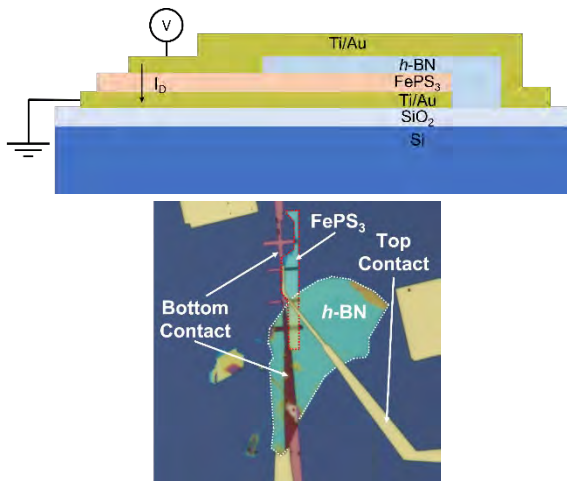


Fig.1: Schematic and optical microscopy image of the vertical device with antiferromagnetic FePS₃ semiconductor as the channel. The arrow in the top image shows the direction of the current.

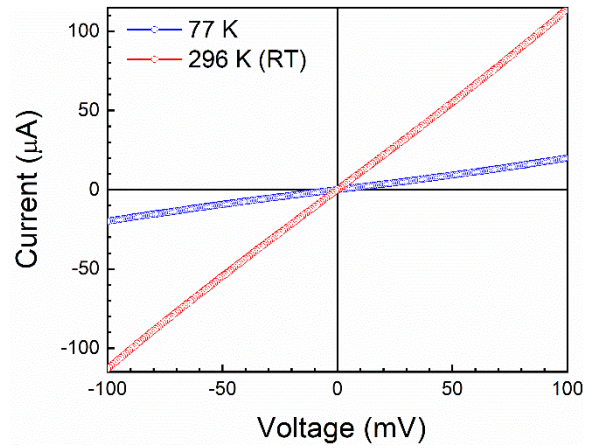


Fig.2: The I-V characteristics of the device measured at 77 K and near room temperature. The fabricated contacts exhibit Ohmic behavior at small biases.

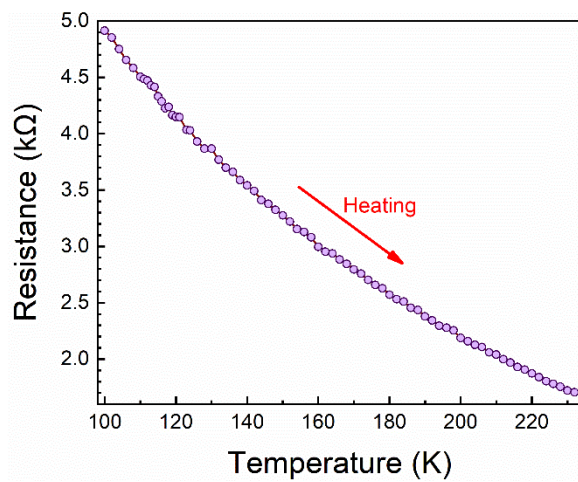


Fig.3: Electrical resistance of the device measured as a function of temperature. The resistance decreases with increasing temperature confirming the semiconductor nature of the channel.

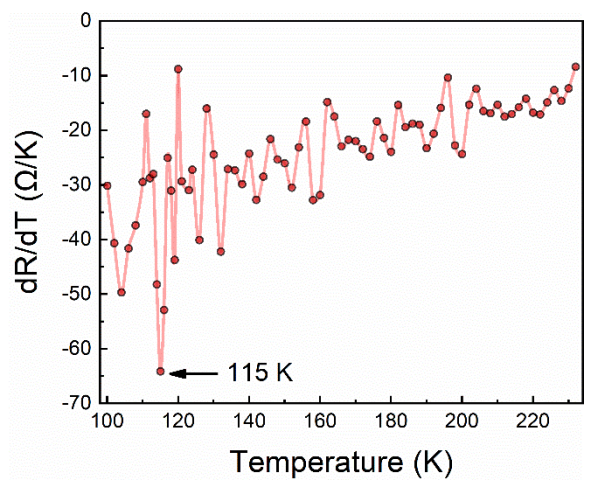


Fig.4: The temperature-derivative of the resistance plotted as a function of the temperature. The data shows fluctuations and a sharp minimum at $T_N \sim 115$ K indicating the interplay of semiconductor and antiferromagnetic properties.

Correlated phases in proximitized (untwisted) graphene multilayers

J. Fabian

*Department of Physics, University of Regensburg, Universitatstrasse 40, 93040 Regensburg,
Regensburg, Germany
jaroslav.fabian@ur.de*

Keywords: 2d materials, spintronics

Electronic correlations play an important role in forming novel correlated phases in both twisted and untwisted multilayer graphene. The underlying reason is the existence of nearly flat bands which increase the importance of the Coulomb interactions. Since flat bands are susceptible to proximity spin interactions due to encapsulating layers of strong spin-orbit materials such as WSe₂ or van der Waals magnets such as Cr₂Ge₂Te₆ (CGT) it is natural to expect that proximity effects [1] can strongly influence the character of the correlated phases. Indeed, this is what we predict for ABC trilayer [2] and Bernal stacked bilayer [3] graphene within the RPA. For ABC graphene encapsulated by WSe₂ and MoSe₂, we show the existence what we call spin valley coherence states, which is an emerging state with coupled spin and valley degrees of freedom. In this state the effective single-particle Hamiltonian enable spin-flip-valley-flip coupling, not possible in uncorrelated systems [2]. For Bernal stacked bilayer we demonstrate the possibility to swap correlated states by either doping or displacement field, in an ex-so-tic heterostructure formed by a bilayer encapsulated by WSe₂ from one side and magnetic CGT from the other. Such an ex-so-tic heterostructure enables one to switch between spin-orbit and exchange coupling proximity effects, and swap between spin-orbit and exchange coupling driven correlated phases [3]. The proposed emergence of spin-valley interactions facilitated by electronic correlations in the presence of SO coupling is particularly exciting, as it can enable new spintronic phenomena in van der Waals heterostructures.

Support from DFG SPP1244, EU Graphene Flagship, and DFG SFB 1277 is acknowledged.

[1] K. Zollner and J. Fabian, Physical Review Letters 128, 106401 (2022).

[2] Y. Zhumagulov, D. Kochan, and J. Fabian, arXiv:2305.14277.

[3] Y. Zhumagulov, D. Kochan, and J. Fabian, arXiv:2307.16025.

Materials screening for spin orbit torque in two- dimensional van der Waals heterostructures

Jinying Wang^{1*}, Dmitri E Nikonov³, Hongyang Lin², Dain Kang², Raseong Kim³, Hai Li³,
Gerhard Klimeck^{1, 2*}

1. *Network for Computational Nanotechnology, Purdue, West Lafayette, IN 47907, USA*
2. *School of Electrical and Computer Engineering, Purdue, West Lafayette, IN 47907, USA*
3. *Components Research, Intel, Hillsboro, Oregon 97124, USA*

gekco@purdue.edu

Keywords: keyword 1 2d materials, quantum transport

Progress in the field of spin orbit torque (SOT) technology within two-dimensional van der Waals (2D vdW) materials has not only pushed the boundaries of spintronic devices to atomic scales but has also unveiled unconventional torque phenomena and innovative spin-switching mechanisms. The diversity of SOT effects observed in numerous 2D vdW materials begs the question which material might be best suited for realistic applications. A systematic and fast screening approach to identify materials optimal for torque device performance is desirable to guide experimental explorations. However, such a screening process has not yet been developed. The challenge in the screening process is that full Non-Equilibrium Function Theory Spin Torque calculations are computationally expensive and cannot easily be scaled to larger disordered systems. Simpler and faster DFT calculations may be able to guide the selection of materials faster. We develop a figure of merit that relates DTF-based results to spin orbit torque to rapidly search through materials. As such we employ a combination of density functional theory and non-equilibrium Green's function methods to compute SOT properties in various 2D vdW bilayer heterostructures. Our investigation leads to the identification of three high SOT systems: WTe₂/CrSe₂, MoTe₂/VS₂, and NbSe₂/CrSe₂. Future work will explore more material systems and disordered systems




SC-SOC/M-FM 	M-SOC/M-FM 	M-SOC/SC-FM 
MoTe ₂ /CrSe ₂	NbSe ₂ /CrSe ₂	NbSe ₂ /CrI ₃
MoTe ₂ /VSe ₂	NbSe ₂ /VSe ₂	NbSe ₂ /CrGeTe ₃
MoTe ₂ /VS ₂	WTe ₂ /CrSe ₂	WTe ₂ /CrI ₃
MoSe ₂ /CrSe ₂	WTe ₂ /VSe ₂	WTe ₂ /CrGeTe ₃
MoSe ₂ /VSe ₂		WTe ₂ (1T')/CrI ₃
MoSe ₂ /VS ₂		WTe ₂ (1T')/CrGeTe ₃
WSe ₂ /CrSe ₂		
WSe ₂ /VSe ₂		
WSe ₂ /VS ₂		

Table 1: The 2D vdW bilayer heterostructures in this study

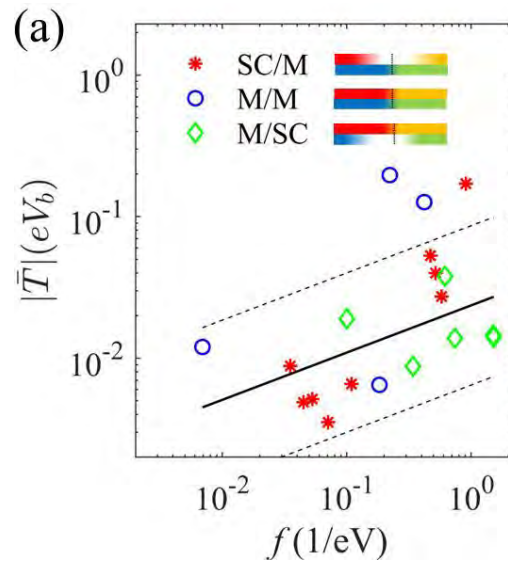


Figure 1 – Heterostructure spin orbit torques versus our newly developed Figure of Merit (f).

Phase-space approach for the topological phase transitions in silicene

M. Kalka¹, P. Pigoń¹ and B. J. Spisak¹

¹*AGH University of Krakow,*

Faculty of Physics and Applied Computer Science,

al. Mickiewicza 30, 30-059 Kraków, Poland

bjs@agh.edu.pl

Keywords: 2d materials

Under the influence of interaction with an external field in 2d materials described by the Kane-Mele Hamiltonian, a topological phase transition can occur. In silicene, which is a topological insulator (TI), under the influence of the interaction of spin-orbit and external field, a change into a band insulator (BI) has been observed. Recently, it has been shown that measures of information (such as Fisher information, complexity measure, or Rényi entropy) can indicate such topological phase transition (TPT) [1].

On the other hand, the phase-space formulation of quantum mechanics based on the Wigner function has widespread applications and it is gaining popularity in the condensed matter field [2], particularly in two-dimensional materials interacting with magnetic and electric fields [3]. Accordingly, in our work an analytical form of the Wigner function for silicene interacting with a perpendicularly directed magnetic field has been calculated. Using this result, Wigner-Rényi 's phase-space entropy has been employed to detect the TPTs.

[1] J. C. Bolivar and E. Romera, *Phys. Lett. A* **381**, 1753 (2017)

[2] J. Weinbub and D. K. Ferry, *Appl. Phys. Rev.* **5**, 041104 (2018)

[3] Y. Betancur-Ocampo, E. Díaz-Bautista, and T. Stegmann, *Phys. Rev. B* **105**, 045401 (2022)

Novel probe metal pads design for IC test in DRAM

Bonhwi Gu^{1,2}, Sukho Shin², Dongwon Lim², Byoungdeog Choi¹

¹*Department of Electrical and Computer Engineering, Sungkyunkwan University, Suwon-Si, Gyeonggi-do 16419, Korea, Republic of (South)*

²*Samsung Electronics Co., Hwaseong-si, Gyeonggi-do 18448, Korea, Republic of (South)*
bdchoi@skku.edu

Keywords: nanostructures

Introduction

As DRAM devices shrink, the spaces of metal routing become smaller. So, it is necessary to lower the dielectric constant k of the inter layer dielectric (ILD). The ILDs of the metal layer have been replaced with porous SiCOH, a low- k material [1]. But a failure of sawing had occurred when low- k ILDs were applied to SAMSUNG's 18nm node DRAM as shown in Fig. 1. In particular, the probe metal pads used for IC test blocked the sawing pass, resulting in a failure. Here, we developed a new design of probe pads.

Design and Result

Existing probe pads were located right above the sawing area in the form of 1-by-24 as shown in Fig. 2. In this case, the laser easily cut the low- k ILDs during sawing, but the cutting was not completed because it was blocked by the metal pads. To solve this, the probe pads had to be redesigned, also a new probe card and probing method had to be devised. We finally rearranged the probe pads to both sides, connected them with metals, and developed a new 2-by-12 type probe card as shown in Fig. 3. The new design allowed the metal pads to be repositioned over the MAIN chips on both sides of the sawing area. Since the pads that blocked the sawing pass were moved out of the sawing area, chips could be perfectly cut without any defects during laser cutting. As shown in Fig. 4, the existing design could not secure the reliability of sawing. But with the new design, rate of failure decreased. In addition, normal testing results were obtained during the IC test. Although the design of the probe pads was changed, the results were same as the existing IC test values.

Conclusion

The failure could be solved with the novel pads design, while maintaining the probing function. Therefore, to apply low- k ILDs to DRAM products, it is essential to consider the probe metal pads design and a new probe card. When changing materials in the DRAM R&D stage, it is necessary to research not only the relevant step, but also the subsequent process.

[1] Gambino, J. P. *et al.*, VLSI Tech. Systems and Appl., 5872228 (2011).

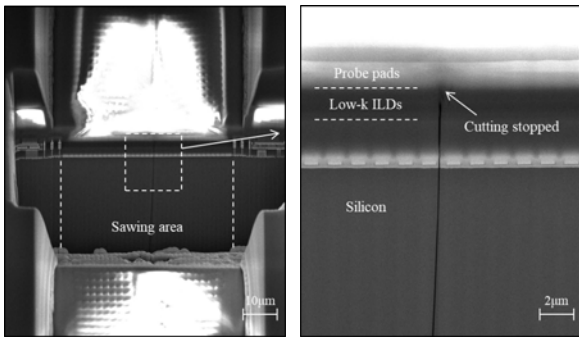


Fig.1: FIB images of sawing failures in SAMSUNG's 18nm node DRAM.

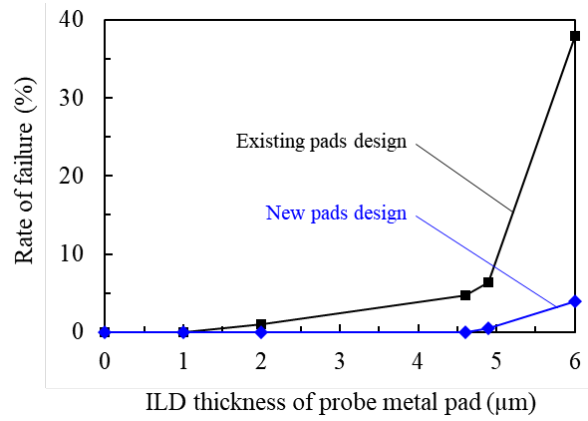


Fig.4: Reduced rate of failure through the new design.

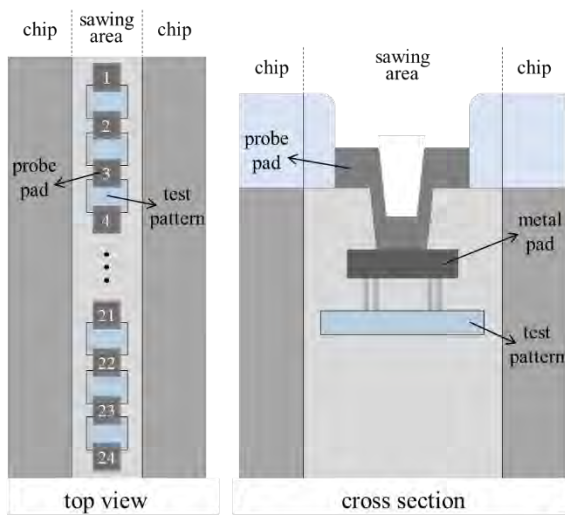


Fig.2: Existing probe metal pads design.

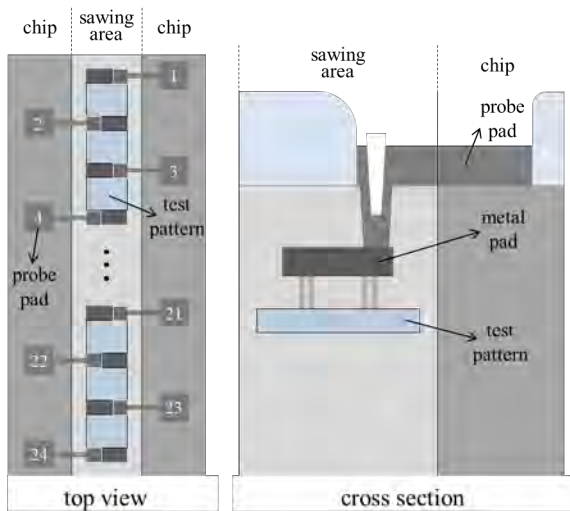


Fig.3: Novel probe metal pads design.

The mask stack efficiency for improving gate oxide reliability of DRAM

Hyojin Park^{1&2}, Byoungdeog Choi¹

¹*Department of Semiconductor and Display Engineering, Sungkyunkwan University, Suwon-si, 16419, Korea*

²*DRAM Process Architecture team, Samsung Electronics, Hwaseong-si, 18448, Korea*
bdchoi@skku.edu

Keywords: nanostructures

Abstract

As the market demand for semiconductors is increased rapidly, the feature size of DRAM products is shrunken a lot, and it became hard to enhance gate oxide reliability while meeting other conditions. To get over this, we usually focus on the gate oxide quality or electric voltage, and in this paper, we try to find out the novel way making better structure to decrease the electrical field because there are not many options to choose. To figure out the new way, we performed the simulation, and with the result of simulation, we could see the possibility of mask stack efficiency. So, in this paper, we changed the gate structure by changing mask stack, which is not considered before and figured out the improvement of gate structure by TEM and verified breakdown voltage by the voltage ramping test of EDS (Electric Die Sorting).

Experiment and results

To figure out the new way to make more reliable structure, we performed the simulation and as the result, we found the novel way to change the gate structure. As the result, gate structure could be changed by the height of mask layer like Fig.1 and this is because the difference of mask layer uniformity is affect to make less round corner like Fig.2. So we increased the mask stack height 70Å to change the uniformity of mask layer and evaluated the gate structure after cleaning process with TEM. In this experiment, the mask height is made same by CMP process to reduce the possibility of height itself, so the uniformity is only varied by increasing mask layer as shown in Fig.3. As the result, the corner roundness of STI is increased 3% shown in Fig.4 and breakdown voltage is also proved 2.5% like Fig.5. This showed the possibility of making more reliable structure by changing the mask stack. The semiconductors we tested are made in the sub-14nm DRAM process of Samsung electronics.

[1] C. P. Chang et al., International Electron Devices Meeting. IEDM Technical Digest, Washington, DC, USA (1997) 661-664.

[2] Stathis. J, Journal of Applied Physics, Vol. 86 No. 10 (1999) 5757–5766.

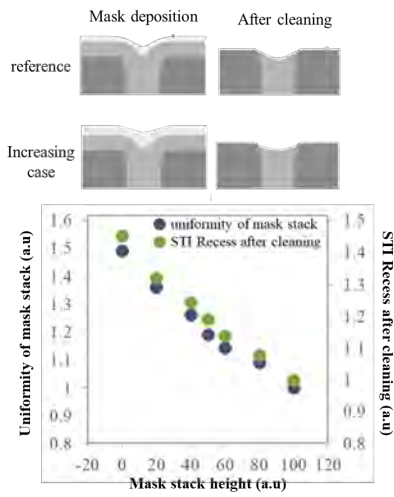


Fig.1: Results of simulation.

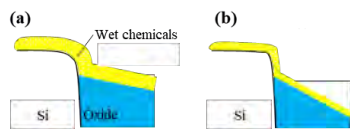


Fig.2: Effect of various mask stack uniformity: (a)increasing case (b)reference

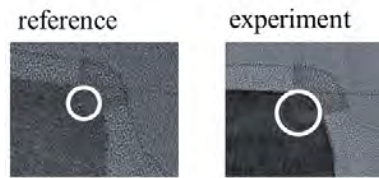


Fig.4: TEM analysis after wet cleaning process

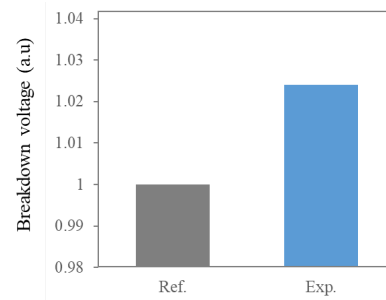


Fig.5 Gate breakdown voltage by voltage ramping test.

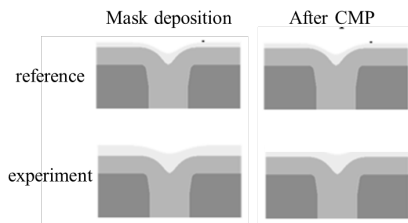


Fig.3: Experimental process

Charge-to-spin conversion in twisted graphene on transition metal dichalcogenides

I. Wojciechowska¹, A. Dyrdał¹

¹*Department of Mesoscopic Physics, ISQI, Faculty of Physics, Adam Mickiewicz University in Poznan, ul. Uniwersytetu Poznanskiego 2, 61-614 Poznan, Poland*

Keywords: 2d materials, spintronics

The discovery of magic angle in twisted bilayer graphene and extraordinary phase transitions in such structures initiated enormous interest in the research field called twistrionics, particularly in twisted-angle van-der-Waals structures. The possibility of exploring the dependence of proximity-induced spin-orbit coupling on a twisted angle in such heterostructures can lead to other interesting transport phenomena in which electric or spin signals can be tuned externally. Under main interest are twisted structures containing graphene and semiconducting transition metal dichalcogenides (TMDCs), where the crucial role plays proximity-induced effects.

We will present a theoretical analysis of charge-to-spin conversion effect - **spin hall effect**[1] in twisted graphene on selected TMDCs such as MoS₂, WS₂, MoSe₂, and WSe₂ modelled by an effective Hamiltonian derived based on symmetry considerations and DFT study (see e.g., [2,3]). We present the behaviour of Berry curvature as a function of twisted angle and parameters defining the Hamiltonian, and focus on its impact on valley and spin Hall effects. Moreover we discuss the behaviour of current-induced spin polarization and show how it depends on the twist angle and radial Rashba angle. Our analysis can be applied to different TMDCs materials.

[1] A.Dyrdał and J.Banaś, 2D Materials 4, 034003 (2017),

[2] Thomas Naimier, Klaus Zollner, Martin Gmitra, JPhys. Rev. B 104, 195156 (2021),

[3] M. Gmitra, D. Kochann, P. Hogg, and J. Fabian Phys. Rev. B 93, 155104 (2016).

This work has been supported by the Norwegian Financial Mechanism 2014-2021 under the Polish-Norwegian Research Project NCN GRIEG “2Dtrionics” no. 2019/34/H/ST3/00515.

Electronic and Topological Properties of a Topological Insulator Thin Film Sandwiched between Ferromagnetic Insulators

P. Pigoń¹, A. Dyrdał²

¹*Faculty of Physics and Applied Computer Science, AGH University of Science and Technology, al. Mickiewicza 30, 30-059 Kraków, Poland*

²*Faculty of Physics, Adam Mickiewicz University in Poznań, ul. Wieniawskiego 1, 61-712 Poznań, Poland*
ppigon@agh.edu.pl

Keywords: 2d materials, topology

We consider a thin film of a topological insulator (TI) sandwiched between two ferromagnetic (FM) insulators under external gate voltage. The TI surface states are magnetized due to the magnetic proximity effect to the ferromagnetic layers. The magnetization of ferromagnetic layers can be changed by applying an external magnetic field or by varying the thickness of the topological insulator. The change of magnetic configuration in the system affects the transport properties of surface electronic states.

Using the Green function formalism, we calculated spin polarization, anomalous Hall effect and magnetoresistance of the system. We will present a detailed study of transport characteristics as a function of gate voltage and magnetizations of the top and bottom FM layers. We focus, among others, on the role of hybridization between surface states, which decreases with increasing the thickness of TI. We will show how changing of voltage, magnetizations of FM layers and hybridization of surface states can lead to the quantum topological phase transition from trivial to quantum anomalous Hall insulator state.

Acknowledgment

This work has been supported by the National Science Centre in Poland under the project Sonata-14 no. 2018/31/D/ST3/02351.

[1] A. G. Moghaddam, A. Qaiumzadeh, A. Dyrdał, and J. Berakdar, *Highly Tunable Spin-Orbit Torque and Anisotropic Magnetoresistance in a Topological Insulator Thin Film Attached to Ferromagnetic Layer*, Phys. Rev. Lett. **125**, 196801 (2020).

[2] P. Pigoń, A. Dyrdał, to be published; arXiv 2023.

Asymmetrically Engineered Nanoscale Transistors for On-Demand Sourcing of Terahertz Plasmons

B. Barut¹, X. Cantos-Roman², J. Crabb², A. Mundaganur¹, S. Mundaganur¹, T. Sugaya³, E. Einarsson¹,

J. M. Jornet², J. P. Bird¹, and G. R. Aizin⁴

¹*Department of Electrical Engineering, University at Buffalo, Buffalo, NY 14260, USA*

²*Department of Electrical and Computer Engineering, Northeastern University, Boston, USA*

³*AIST, Tsukuba, Ibaraki 305-8568, Japan*

⁴*Kingsborough College, The City University of New York (CUNY), NY 11235*

jbird@buffalo.edu

Keywords: plasmonics, other advanced devices

Plasma oscillations in semiconductors are appealing for use in high-frequency communication schemes [1]. The possibility of realizing sustained plasma oscillations in high-electron-mobility transistors (HEMTs) was first proposed by Dyakonov and Shur [2], who predicted that a dc current through a transistor can become unstable to plasma wave generation (the Dyakonov–Shur (DS) instability). The spontaneous onset of plasma oscillations requires a geometry in which the (ac) impedance (Z_s) between source and gate corresponds to a short circuit, while that between gate and drain is infinite (*i.e.*, an open circuit). While the DS instability has previously been explored experimentally, the issue of the required impedance mismatch, and its impact on the instability, has not been carefully addressed. Here, we describe a scheme for engineering HEMT devices, to realize the conditions required for the DS instability. Our approach [3] involves the placement of its nanoscale gate in close proximity to an etched trench that ensures the high impedance needed at the drain side of the device (Figs. 1 & 2). The transistor curves of these devices exhibit negative differential conductance (Fig. 3) that is connected to the onset of the DS instability. In temperature-dependent studies, we demonstrate how control of the electron density in the plasmonic cavity below the gate can extend the survival of the instability beyond room temperature, due to a crossover between the hydrodynamic and ballistic regimes of electron-electron scattering. The asymmetric plasmonic devices that we have implemented have considerable potential for use as local oscillators that may be used to source high-frequency on-chip signals for future communication systems.

Work supported by the US AFOSR and the Coherent/II-VI Foundation.

[1] M. Polese *et al.*, IEEE Communications Magazine **58**, 48 (2020).

[2] M. Dyakonov and M. Shur, Physical Review Letters **71**, 2465 (1993).

[3] B. Barut *et al.*, Nano Letters **22**, 2674 (2022).

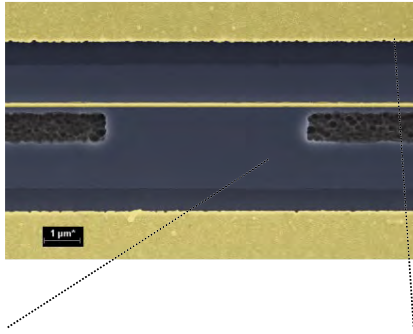


Fig.1: Colorized electron micrographs of a gated 2DEG plasmonic cavity. The full mesa width is $115\ \mu\text{m}$, and the images show an expanded view around the center region where both the etched trench and unetched region can be seen.

Fig.2: Schematic (not to scale) of the layer structure of our devices. The image represents the structure as seen along the dashed line AB in panel a. Silicon delta-doping layers are inserted in the upper (8 nm) InGaAs layer, where the source and drain contacts (at Ground and V_d , respectively) are formed, and in the 18 nm InAlAs spacer. An additional delta-doped layer is also present at the interface between the InGaAs and the InP etch-stop layer. Also denoted in the figure are the capacitive impedances between the gate and the source (Z_s) and the gate and the drain (Z_d). Z_s is governed by the distance between the 2DEG and the gate ($\sim 21\ \text{nm}$), while Z_d is essentially determined by the distance between the gate and 2DEG on the other side of the trench ($\sim 1\ \mu\text{m}$).

Fig.3: The main panel shows transistor curves measured at 3 K in a representative device such as that of Figs. 1 & 2. From top to bottom at $V_d = 4\ \text{V}$, the different curves correspond to increasing negative gate voltage. Curves plotted with filled symbols exhibit NDC at a positive drain bias that is absent upon reversal of the polarity of V_d . The three- (upper-left inset) and two- (lower-right inset) dimensional color contours show the detailed evolution of drain current with V_g and V_d . Both contours use the calibration scale included as the lower-left inset of the main panel. In the lower-right inset, the white-dotted line encloses the range of NDC.

Circuit-level device modeling for framework analyzing hot carrier injection failure in gate-all-around (GAA) charge trapping flash (CTF) memory devices based on new experimental methodology

Sunghwan Cho^{1,2} and Byoungdeog Choi³

¹*Dep. of Semiconductor and Display Engineering, Sungkyunkwan University, Suwon, Korea*

²*Samsung Electronics Company, Ltd., Hwaseong 445-701, Korea*

³*Dep. of Electrical and Computer Engineering, Sungkyunkwan University, Suwon, Korea*

bdchoi@skku.edu

Keywords: advanced devices

To overcome the limitation of conventional planar flash memory in scaling down, gate-all-around (GAA) charge trapping flash (CTF) memory gradually become the most promising alternative due to remarkably larger storage and less disturbance. However, as stacking more layers vertically and getting smaller in feature size, it is inevitable that device failures attributed to interference or leakage such as band-to-band tunneling (BTBT) and hot carrier injection (HCI) increase rapidly. Furthermore, a suitable framework to analyze failure mechanisms and optimize design by using circuit simulation is insufficient. In this paper, we proposed circuit-level device modeling as a framework focused on HCI failure analysis in GAA CTF, which is achieved by establishing new method in measuring HCI effect and optimizing model parameters by derived formula. As shown in Fig. 1, threshold voltages in non-programmed memory cell can be increased unexpectedly by HCI effect, which results in critical failure and degradation of performance. In conventional junction-less GAA CTF memory devices, electrons generated by BTBT in a large gap in boosted channel potential and high electric field in vertical direction contribute to HCI effect. As a result, circuit-level modeling for accurate calculation of boosted channel potential and determination of gate voltages in a cell string is essential in analyzing HCI effect. Fig. 2(a) and (b) illustrate single modeling structure and equivalent circuit attaching voltage-controlled-current sources which execute essential current flow in GAA CTF such as Fowler-Nordheim (FN) tunneling, BTBT and HCI leakage by using derived formula in our work. By connecting single modeling units serially as shown in Fig. 2(c), circuit-level modeling structure with a cell string unit is proposed which makes prediction of boosted channel potential and BTBT/HCI current more accurate. Fig. 3 presents mechanisms of HCI in the proposed experimental method. Since the amount of HCI leakage is determined by 2 dominant conditions which are potential difference in lateral direction generating BTBT and electric field in vertical direction, we separated 2 measurement conditions, as shown in Fig. 3(a) and (b), to extract model parameters compactly by breaking down 2 terms. Furthermore, since HCI failure commonly occurs at the end of channel, we enhanced experimental progress by measuring near gate select line (GSL) transistor, as shown in Fig. 3(c). Finally, the fitting results show good agreement with experimental data, as shown in Fig. 4, which means the proposed model would equip designer of GAA CTF by analyzing failure mechanism and optimizing the performance.

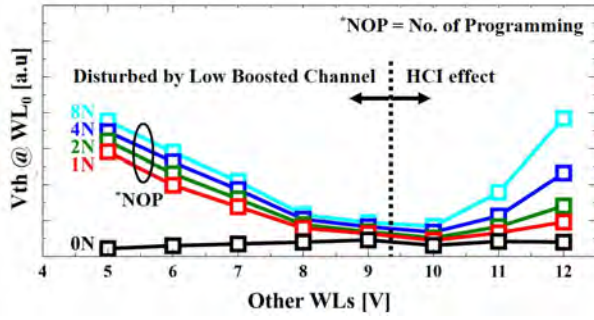


Fig. 1: Experimental data for HCI effect in the end of string. Note that threshold voltage increases as gate voltage and NOP increases by HCI effect.

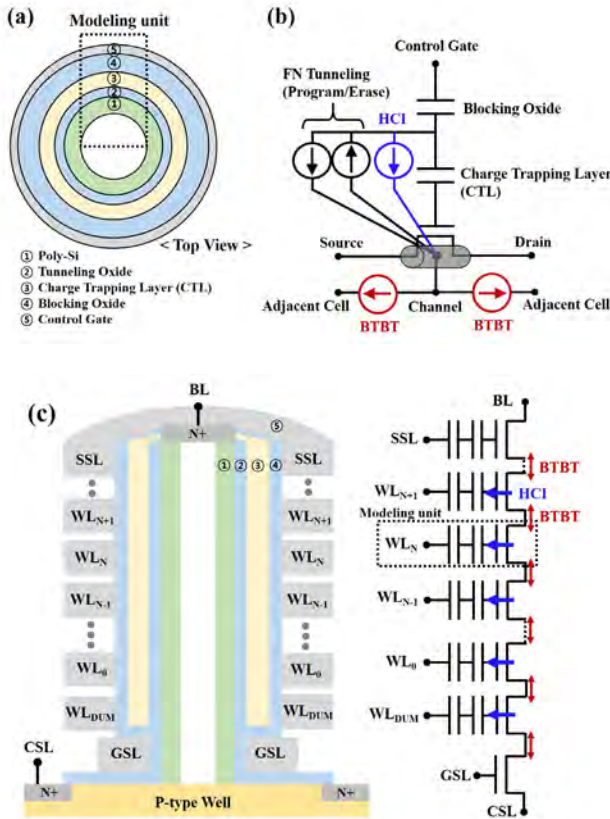


Fig. 2: Schematics for proposed modeling structure and corresponding equivalent circuit. (a) Illustration for top view of GAA structure in CTF devices and corresponding (b) single modeling unit and (c) string-level modeling unit

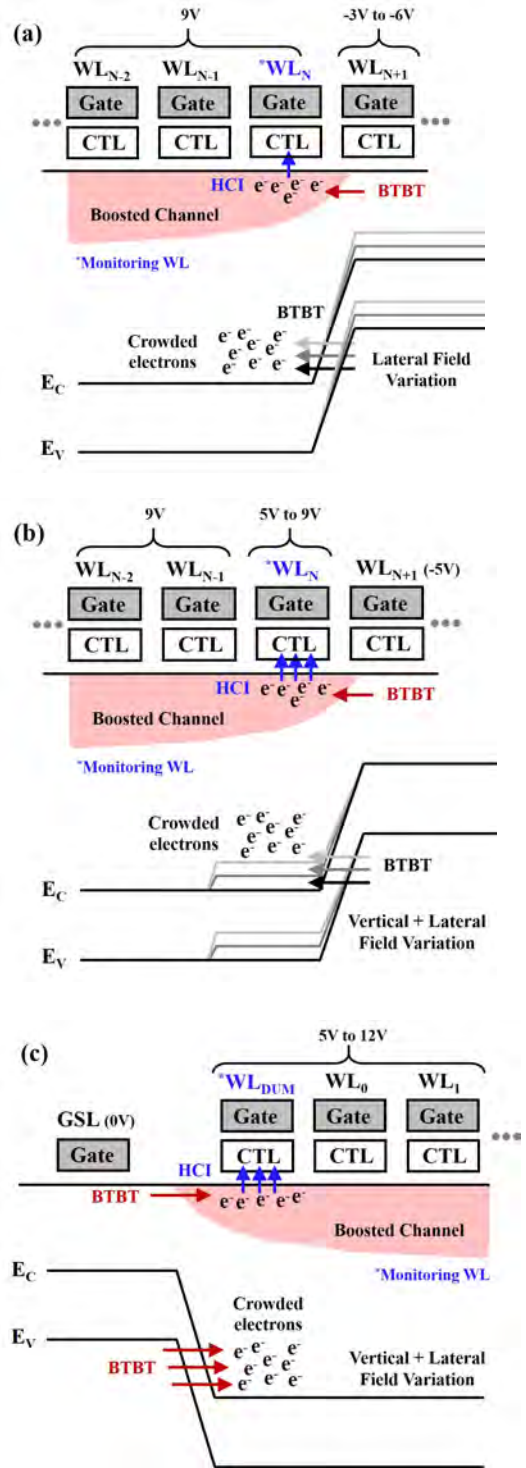


Fig. 3: Illustrations for proposed experimental method in our work. Band diagrams are used to clarify each mechanism and bias conditions and we recommend sequential progress from (a) to (c) to break down terms and extract model parameters compactly.

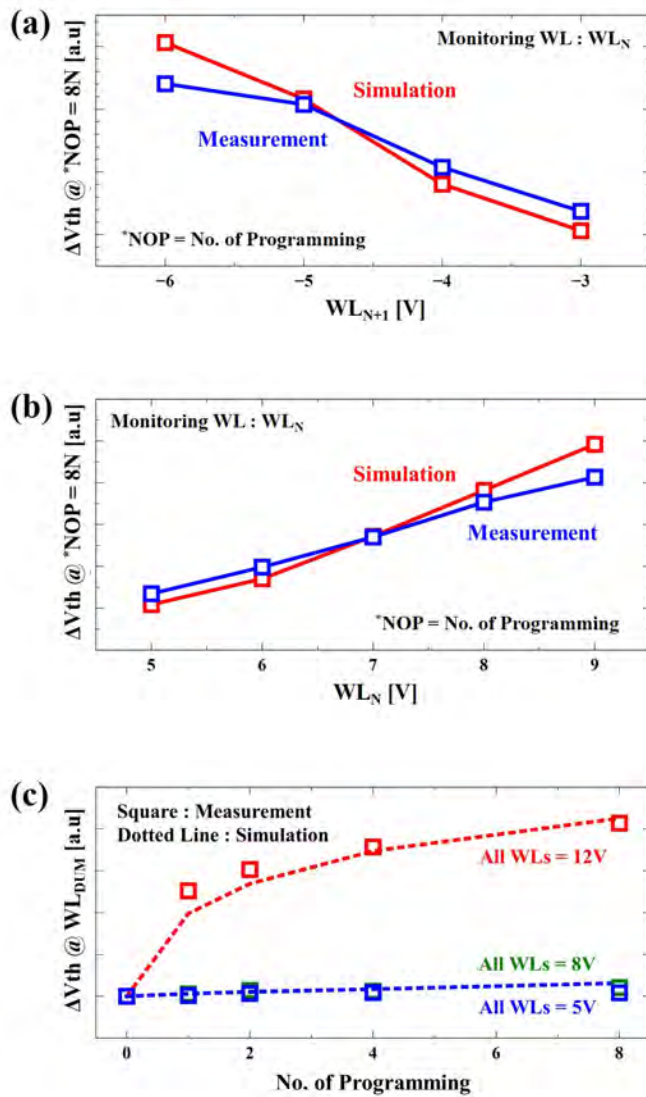


Fig. 4: Optimized results by fitting the proposed model to experimental data which we present in Fig. 3 using simulation program with integrated circuit emphasis (SPICE) simulation.

Coarse-grained molecular dynamics simulation study on the dispersion mechanism of organically modified nanoparticles in mixed solvent -Analysis of nanoparticle/solvent/nanoparticle interface structure-

Kota Jojima¹, Yuta Asano¹, Yusuke Ootani¹, Nobuki Ozawa^{2, 1}, and Momoji Kubo^{1,2}

¹*Institute for Materials Research, Tohoku University, 2-1-1 Katahira, Aoba-ku, Sendai 980-8577, Japan*

²*New Industry Creation Hatchery Center, Tohoku University, 6-6-10 Aoba, Aramaki, Aoba-ku, Sendai 980-8579, Japan*
momoji@tohoku.ac.jp

Keywords: nanostructures

Nanoparticles (NPs) have unique optical, thermal, and magnetic properties because of their quantum size effect. Therefore, NPs can achieve high functionality for variety of applications. Basically, NPs are handled in organic solvents. Since their individual structure must be retained to preserve superior properties. NPs are organically modified (OM) to promote dispersion in the organic solvents. However, it is widely reported that the dispersibility of OMNP cannot be estimated by the affinity between organic modifier and solvent molecules. On the other hand, recent studies revealed that the addition of a small amount of hexane solvent, which disperse NP well, significantly improves NP dispersibility in solvent which does not disperse NP well such as tetradecane [1]. The detailed insights into the dispersity in single and mixed solvent is useful to improve the dispersibility of OMNP. However, the mechanism is still in debate. In this work, we investigated the OMNP/solvent/OMNP interface structure by coarse-grained molecular dynamics (CGMD) simulations for single and mixed solvent system.

The simulations of two OMNPs were performed in single tetradecane solvent, and mixed tetradecane/hexane solvent (Fig. 1). OMNPs were placed at a distance where they almost touched each other. To evaluate interface structures quantitatively, we calculated the orientational order parameter between modifier and solvents (Fig. 2). Fig. 3 shows the distribution of the order parameters for tetradecane and mixed tetradecane/hexane cases. The solvent molecules highly oriented to modifiers in single tetradecane case compared to mixed tetradecane/hexane case. Figure 4 shows the snapshot of the CGMD simulation colored by order parameters. As shown in Fig. 4(a), in tetradecane, solvent molecules oriented parallel to modifiers were shared between modifier shell of each OMNP; solvent molecules connect two OMNPs. On the other hand, in tetradecane/hexane, the solvent shared by two modifier shells were not found (Fig. 4(b)). These results suggest that, in tetradecane solvent, aggregation of OMNP occurs because the highly oriented solvent molecules connect OMNPs. In contrast, in mixed tetradecane/hexane solvent, the solvent molecules do not connect because the solvent molecules do not orient to modifiers, thereby dispersibility of OMNP is improved in mixed solvent.

[1] Tomai, T. et al., *J. Colloid Interface Sci.* **587**, (2021) 574-580.

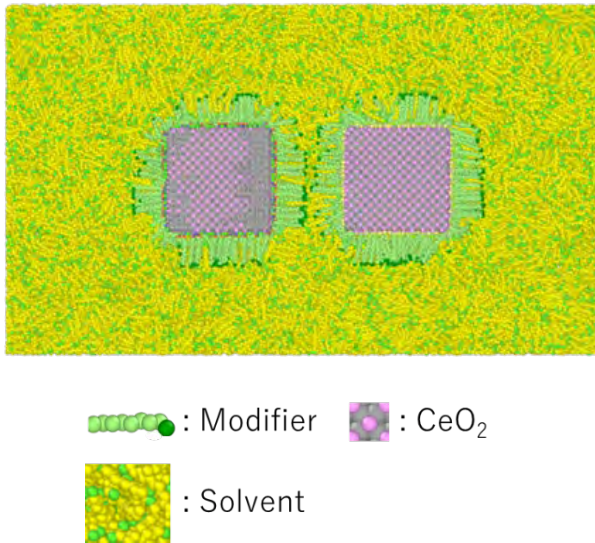


Fig.1: Cross section view of two OMNPs model.

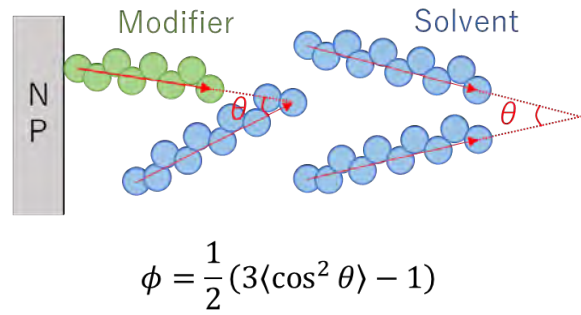


Fig.2: The definition of the orientational order parameter ϕ which ranges from -0.5 to 1, where $\phi=-0.5$ when the solvent is perpendicular to modifier or solvent and $\phi=1$ when the solvent is parallel to modifier or solvent.

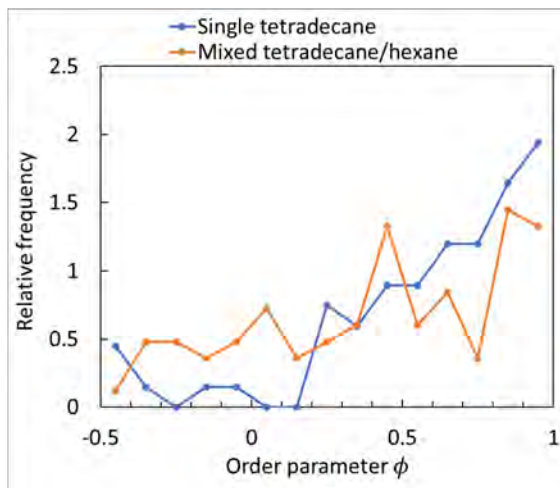


Fig.3: The distribution of orientational order parameter of solvent molecules located between two OMNPs.

$\phi=-0.4$ perpendicular $\phi=0.9$ parallel

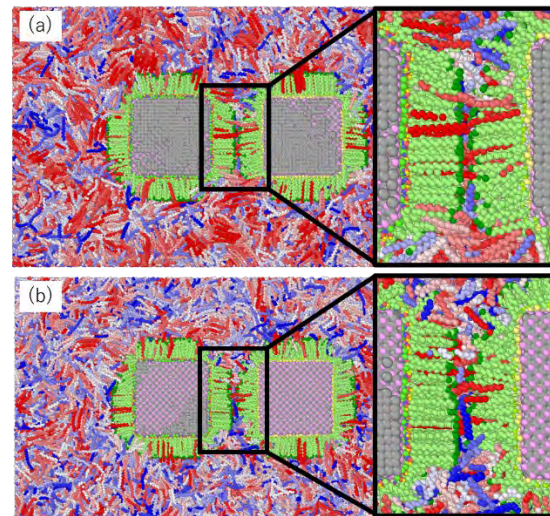


Fig.4: Snapshots of the CGMD simulation for (a) single tetradecane and (b) mixed tetradecane/hexane case. The solvent molecules are colored according to orientational order parameters.

2.1 eV AlGaInP photovoltaic device for use in radiation environment

Y. Shoji¹ and T. Fujiwara¹

¹ National Institute of Advanced Industrial Science and Technology (AIST), 1-1-1 Umezono,
Tsukuba, Ibaraki 305-8568, Japan
y.shoji@aist.go.jp

Keywords: wide-gap materials, other advanced devices

The generation of radioactive wastes associated with using nuclear power plants is a serious social issue. However, these wastes possess enormous amounts of energy and would be a great energy source if they could be effectively utilized. This paper proposes a III-V semiconductor device that generates electricity using radiation. III-V solar cells have been used as the power source for space applications such as artificial satellites because they can obtain high conversion efficiencies under sunlight illumination, and their performance is superior in terms of radiation resistance. This study presents an AlGaInP photovoltaic device that uses radiation down-converted through a scintillator to generate electricity. We fabricated photovoltaic devices with 2.1 eV AlGaInP absorbers shown in Fig. 1. The layer structures were grown by metal-organic vapor phase epitaxy. Fig. 2 shows the electroluminescence from the sample, with an emission peak at a wavelength of ~590 nm. First, we characterized the performance as a solar cell. Fig. 3 shows the current-voltage curves under air mass 1.5 global (AM1.5G) spectrum illumination and dark condition. The 2.1 eV AlGaInP devices achieved the short-circuit current density, open-circuit voltage, fill factor, and photoelectric conversion efficiency of 6.53 mA/cm², 1.52 V, 0.816, and 8.10%, respectively. Fig. 4 shows the external quantum efficiency (EQE) spectrum measured using a monochromatic light with a flux of 1×10^{14} photons/cm². The maximum EQE of the fabricated samples was approximately 60%. The EQE value can be improved by optimizing the device structure and crystal growth conditions^[1]. Fig. 5 shows the photoelectric conversion efficiency when irradiating monochromatic light with a power density of 50 μW/cm². The horizontal axis represents the wavelength of incident light. The photoelectric conversion efficiency of 25–27% was obtained for light with wavelengths of 500–570 nm. Finally, we measured the power-voltage curve of the sample with the illumination of visible light down-converted from X-rays via a GAGG:Ce scintillator (Fig. 6). The X-ray tube voltage and current were 320 kV and 4.65 mA, respectively. The exposure dose rate was ~100 Gy/min. The peak emission wavelength of the scintillator used in this study was ~520 nm. We have obtained a maximum power density of 54 μW/cm² by X-ray irradiation. This result demonstrates that photovoltaic power generation is available from radiation and indicates one of the ways to utilize radioactive wastes.

[1] E. E. Perl *et al.*, Proc. of IEEE 42nd PVSC (2015).

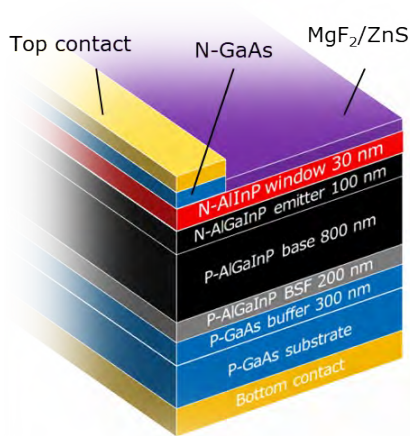


Fig.1: Schematic sample structure.

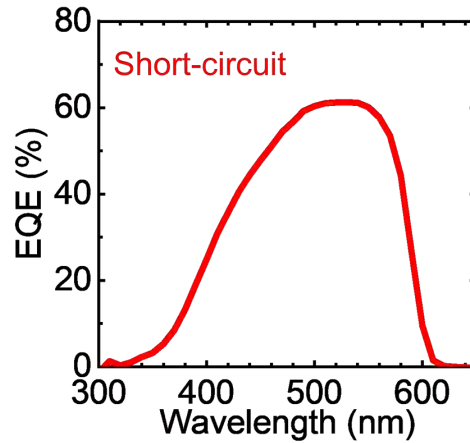


Fig.4: External quantum efficiency measured at short-circuit condition.

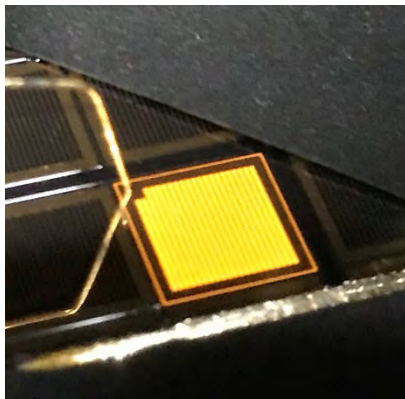


Fig.2: Light emission from the sample with current injection.

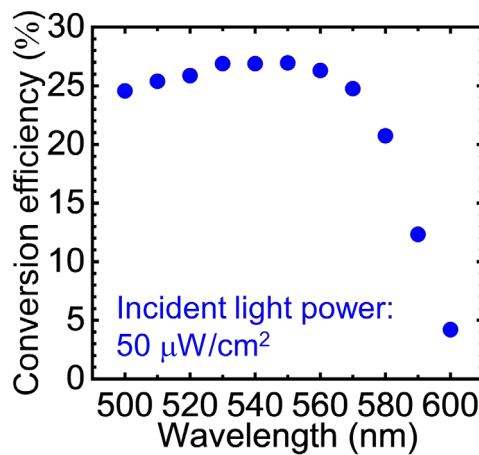


Fig.5: Photoelectric conversion efficiency for monochromatic light.

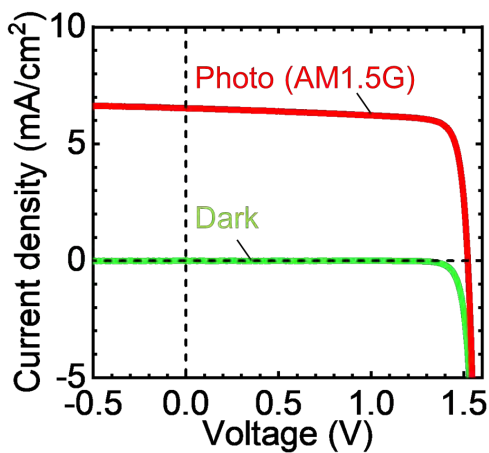


Fig.3: Current-voltage curves under airmass 1.5 global spectrum illumination and dark condition.

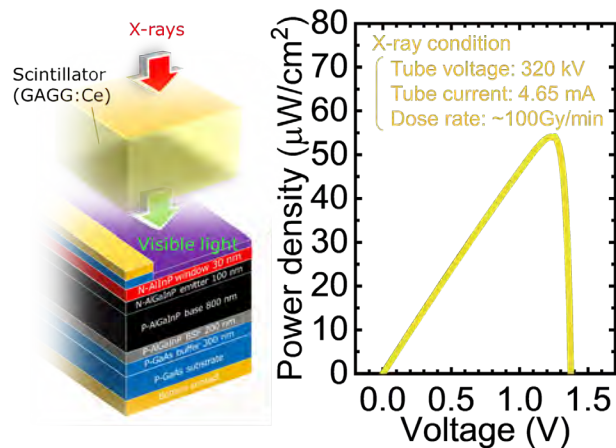


Fig.6: Power-voltage curve under X-ray irradiation. The X-rays are down-converted to visible light by the GAGG:Ce scintillator and then illuminated into the device.

Proximity effect of an emergent field from spin ice in an oxide heterostructure

M. Ohno¹, T. C. Fujita¹ and M. Kawasaki^{1,2}

¹*Department of Applied Physics and Quantum-Phase Electronics Center (QPEC),
University of Tokyo, Tokyo 113-8656, Japan*

²*RIKEN Center for Emergent Matter Science (CEMS), Wako 351-0198, Japan
kawasaki@ap.t.u-tokyo.ac.jp*

Keywords: topology, oxides and ferroelectrics

Geometrical frustration imparts magnets with macroscopically degenerate ground states, giving rise to exotic spin structures and field-induced quantum phenomena. Such magnets, known as quantum magnets, exhibit non-coplanar spin textures and serve as a viable platform for an “emergent field” driven by their scalar spin chirality that generates the topological Hall effect. However, most of quantum magnets are insulators, posing challenges in electrical detection of emergent fluctuations and excitations associated with the degeneracy. Here, we present the detection of magnetic transition in the archetypal quantum magnet, spin-ice insulator $\text{Dy}_2\text{Ti}_2\text{O}_7$, through emergent magnetotransport phenomena at the heterointerface with a non-magnetic metal $\text{Bi}_2\text{Rh}_2\text{O}_7$. We discover distinct peaks in the field angle dependence of longitudinal resistivity appeared at the magnetic phase boundaries of spin ice $\text{Dy}_2\text{Ti}_2\text{O}_7$ due to domain boundary scattering. Moreover, we observe field induced sign change in the anomalous Hall resistivity, reflecting the sign inversion of the emergent field triggered by the magnetic transition in $\text{Dy}_2\text{Ti}_2\text{O}_7$. These findings based on the sophisticated epitaxial technique bridge the gap between fundamental research on insulating quantum magnets and their potential electronic applications, possibly leading to a transformative innovation in quantum technologies reliant on their exotic spin states and transitions.

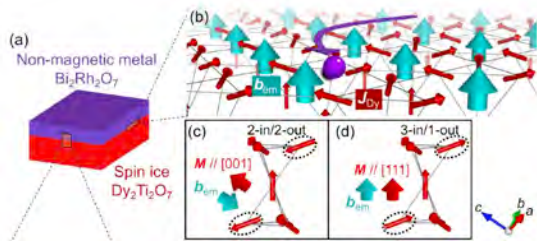


Fig.1: (a) A schematic of the heterostructure composed of non-magnetic metal $\text{Bi}_2\text{Rh}_2\text{O}_7$ (BRO) and magnetic insulator $\text{Dy}_2\text{Ti}_2\text{O}_7$ (DTO) with spin ice configuration. (b) A schematic of the BRO/DTO interface. The charge carrier (purple) on the BRO side flows through the proximity-induced emergent field b_{em} (green) penetrating from DTO with 3-in/1-out (3/1) configuration of local spins J_{Dy} (red), resulting in the transverse Hall current (curved purple arrow). The net b_{em} and magnetization M in a pair of tetrahedrons consisting of Dy spins with (c) 2-in/2-out (2/2) and (d) 3/1 configurations under magnetic field along [001] and [111] directions. When the magnetic field is rotated from [001] to [111] directions, the spins surrounded by the dotted ellipses in (c) are flopped to those in (d), resulting in a transition from 2/2 to 3/1 configurations.

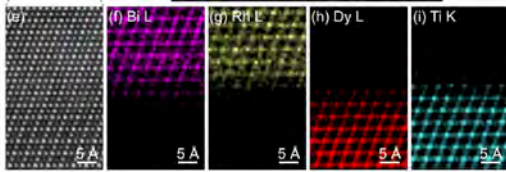


Fig.2: (e) High resolution high-angle annular dark-field (HAADF) scanning transmission electron microscopy (STEM) image of the film. The corresponding energy dispersive x-ray (EDX) spectrometry maps for (f) Bi L, (g) Rh L, (h) Dy L, and (i) Ti K edges.

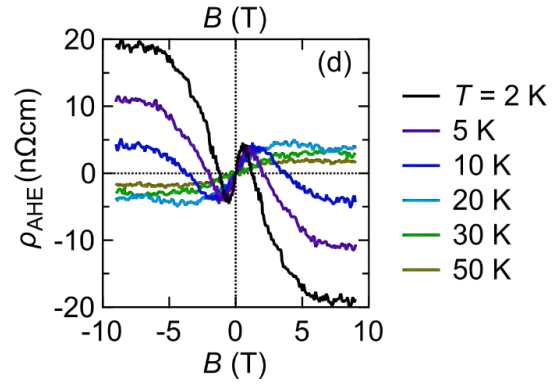


Fig.3: Anomalous Hall resistivity ρ_{AHE} obtained by subtracting the ordinary Hall term.

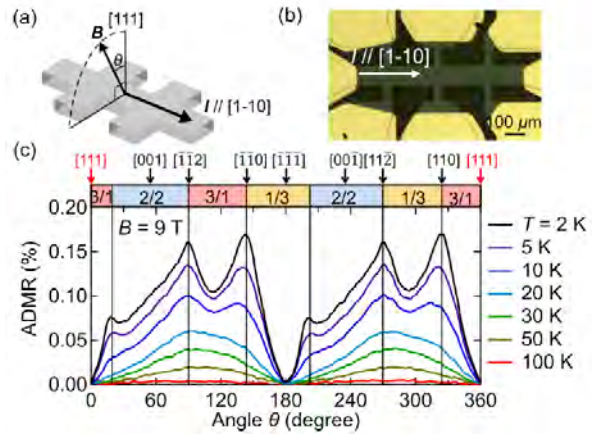


Fig.4 (a) A schematic of measurement configuration. The field angle θ is defined from the surface normal [111] direction. (b) A top-view photograph of the measured Hall-bar device structure with a channel width of $100 \mu\text{m}$. (c) The top panel denotes the corresponding crystallographic directions and expected magnetic structures of the Dy 4f moments under high field limit: 2/2, 3/1, and 1/3 represent “2-in/2-out”, “3-in/1-out”, and “1-in/3-out” configurations, respectively. The bottom panel shows the angle-dependent magnetoresistance ratio ($\text{ADMR} \equiv \rho_{xx}(\theta)/\rho_{xx}(0^\circ) - 1$) for several temperatures at 9 T.

Dominant Surface State Transport in HfTe₅ thin films

J. Liu¹, R. A. Welser¹, S. Yopez-Rodriguez¹, M. A. Delmont², M. T. Pettes³, L. A. Jauregui¹

¹*Department of Physics and Astronomy, University of California, Irvine CA 92697, USA*

²*Department of Mechanical and Aerospace Engineering, University of California, Irvine, CA 92697, USA*

² *Center for Integrated Nanotechnologies (CINT), Materials Physics and Applications Division, Los Alamos National Laboratory, Los Alamos, NM 87544, USA*

lajaure1@uci.edu (e-mail address of the corresponding author)

Keywords: 2d materials, topology, quantum materials, quantum transport, nanostructures.

Controlling materials to create and tune topological phases of matter could potentially be used to explore new phases of topological quantum matter and to create novel devices where the carriers are topologically protected. It has been demonstrated that a trivial insulator can be converted into a topological state by modulating the spin-orbit interaction or the crystal lattice. However, there are limited methods to controllably and efficiently tune the crystal lattice and at the same time perform electronic measurements at cryogenic temperatures. Here, we show two methods to create dominant surface state transport in high quality pentatellurides. First, we use large controllable strain to demonstrate the topological phase transition from a weak topological insulator phase to a strong topological insulator phase in HfTe₅ samples. After applying high strain to HfTe₅ and converting it into a strong topological insulator, we found that the sample's resistivity increased by more than two orders of magnitude (24,000%) and that the electronic transport is dominated by the topological surface states at cryogenic temperatures. Second, we create devices based on thin layers of HfTe₅ that show an enhanced surface to bulk contribution. When thin down to less than 100 nm we observe interesting quantum transport phenomena such as strong anomalous Hall effect and correlated effects. Our findings show that HfTe₅ is an ideal material for engineering topological properties, and it could be generalized to study topological phase transitions in van der Waals materials and heterostructures. These results can pave the way to create novel devices with applications ranging from spintronics to fault-tolerant topologically protected quantum computers.

[1] J. Liu *et al.*, Arxiv:2304.09072 (2023).

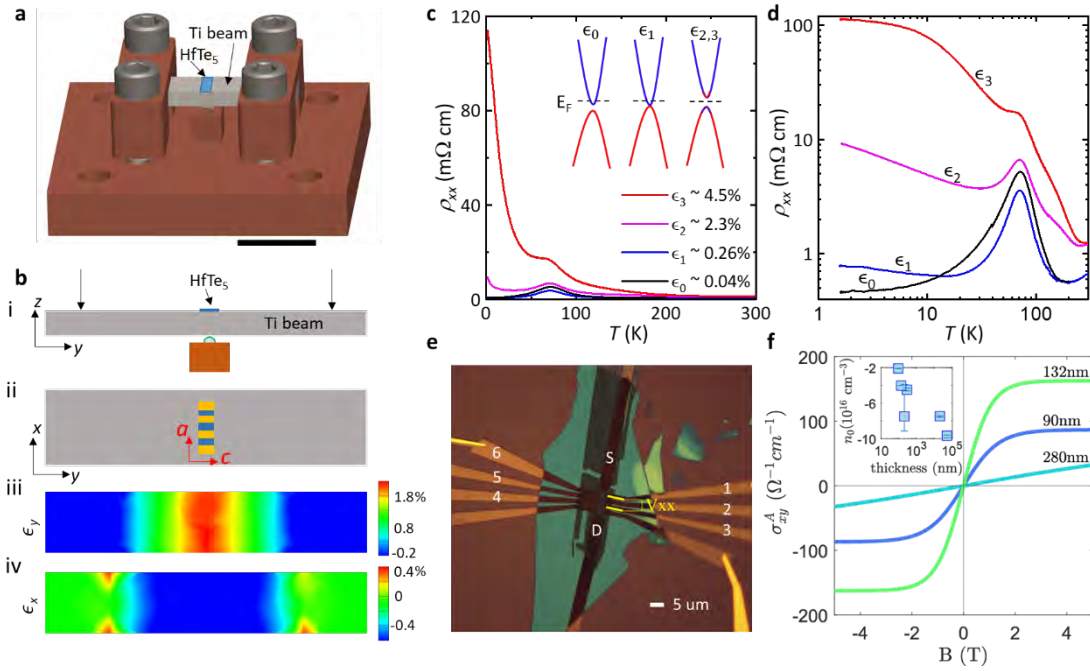


Figure 1 **a**, A model of the “bending station” with a sample mounted at the center of the beam’s top surface. The scale bar represents 1 cm. **b**, **i**. Schematic of how the beam is bent. The two black arrows represent the force load. **ii**. Top view of the sample configuration relative to the beam for applying strain along the sample’s c axis. **iii**. and **iv**. show the strain distribution of ϵ_y and ϵ_x on the beam under a moderately high load, which results in a strain of $\epsilon_y = 2.2\%$ near the sample area. **c & d**, ρ_{xx} as a function of temperature (T) for the HfTe₅ sample under different strains, plotted in log-log scale in **d** for clarity. Inset of **c**: Schematics of the Dirac bands around Γ under different strain cases. **e** Optical image of a Boron Nitride encapsulated 32 nm thick HfTe₅ sample. **f** Extracted anomalous Hall conductivity for three different samples at $T = 2\text{K}$. Inset: extracted carrier density with sample thickness.

Quasi-two-Dimensional Chromium Telluride: Thickness Dependent magnetism and Strain-tunable Berry curvature

Valeria Lauter¹, Hang Chi^{2,3}, Yunbo Ou^{2*}, Tim B. Eldred⁴, Wenpei Gao⁴, Sohee Kwon⁵, Joseph Murray⁶, Michael Dreyer⁶, Robert E. Butera⁷, Haile Ambaye¹, Jong Keum¹, Alice T. Greenberg³, Yuhang Liu⁵, Mahesh R. Neupane^{3,5}, George J. de Coster³, Owen A. Vail³, Patrick J. Taylor³, Patrick A. Folkes³, Charles Rong³, Gen Yin⁸, Roger K. Lake⁵, Don Heiman^{2,9}, Jagadeesh S. Moodera^{2,10}

(lauterv@ornl.gov)

¹Neutron Scattering Division, Neutron Sciences Directorate,

Oak Ridge National Laboratory, Oak Ridge, Tennessee 37831, USA

²Francis Bitter Magnet Laboratory, Plasma Science and Fusion Center,

Massachusetts Institute of Technology, Cambridge, Massachusetts 02139, USA

³U.S. Army CCDC Army Research Laboratory, Adelphi, Maryland 20783, USA

⁴Department of Materials Science and Engineering,

North Carolina State University, Raleigh, North Carolina 27695, USA

⁵Department of Electrical and Computer Engineering,

University of California, Riverside, California 92521, USA

⁶Department of Physics, University of Maryland, College Park, Maryland 20740, USA

⁷Laboratory for Physical Sciences, College Park, Maryland 20740, USA

⁸Physics Department, Georgetown University, Washington, District of Columbia 20057, USA

⁹Department of Physics, Northeastern University, Boston, Massachusetts 02115, USA

¹⁰Department of Physics, Massachusetts Institute of Technology,

Cambridge, Massachusetts 02139, USA

Keywords: 2d materials, topology, nanostructures

In recent years, a variety of novel two-dimensional (2D) van der Waals magnets have been discovered, founding the active field of 2D magnetism¹. Among these prospective compounds, binary chromium tellurides $\text{Cr}_{1-\delta}\text{Te}$ are attractive owing to their rich magnetic properties, as well as inherent chemical and structural compatibility when forming heterostructures² with other topological systems. Magnetic transition metal chalcogenides form an emerging platform for exploring spin-orbit driven Berry phase phenomena owing to the nontrivial interplay between topology and magnetism. Here we show that the anomalous Hall effect in pristine Cr_2Te_3 thin films manifests a unique temperature dependent sign reversal at nonzero magnetization, resulting from the momentum-space Berry curvature as established by first-principles simulations. The sign change is strain tunable, enabled by the sharp and well-defined substrate/film interface in the quasi-two-dimensional Cr_2Te_3 epitaxial films, revealed by scanning transmission electron microscopy and depth-sensitive polarized neutron reflectometry.

This Berry phase effect further introduces hump-shaped Hall peaks in pristine Cr_2Te_3 near the coercive field during the magnetization switching process, owing to the presence of strain-modulated magnetic layers/domains³. The versatile interface tunability of Berry curvature in Cr_2Te_3 thin films offers new opportunities for topological electronics.

[1] Burch, K. S., Mandrus, D. & Park, J.-G. Magnetism in two-dimensional van der Waals materials. *Nature* **563**, 47-52 (2018). <https://doi.org/10.1038/s41586-018-0631-z>

[2] Gong, C. & Zhang, X. Two-dimensional magnetic crystals and emergent heterostructure devices. *Science* **363**, eaav4450 (2019). <https://doi.org/10.1126/science.aav4450>

[3] Chi, H., et al. Strain-tunable Berry curvature in quasi-two-dimensional chromium telluride. *Nat Commun* **14**, 3222 (2023). <https://doi.org/10.1038/s41467-023-38995-4>

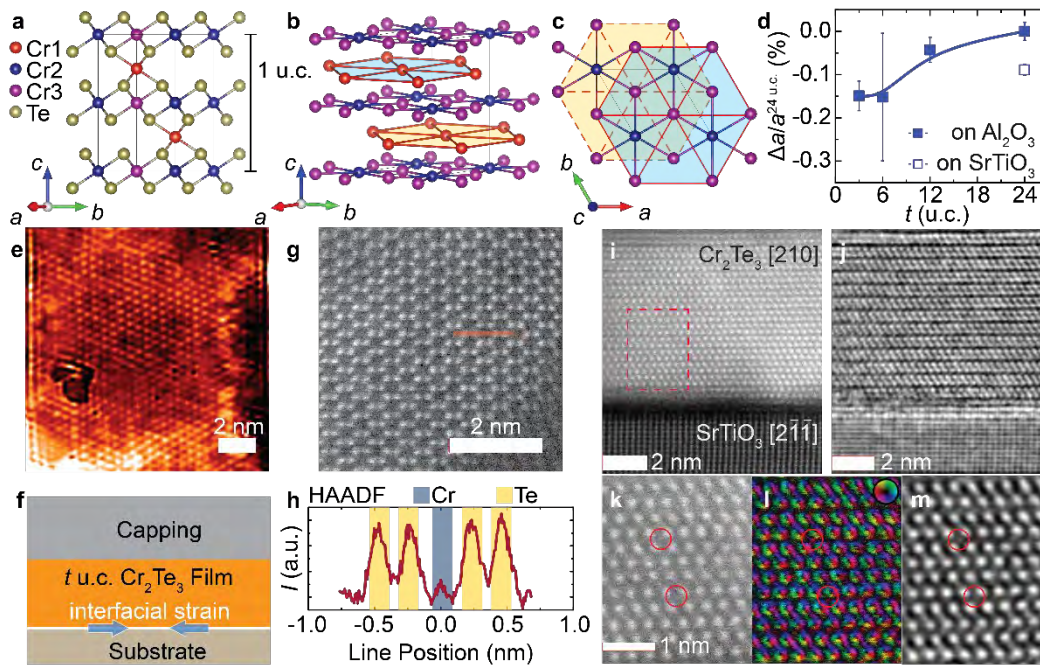


Figure 1. Crystal structure of Cr_2Te_3 thin films. *a*, Atomistic structure of Cr_2Te_3 viewed along the crystallographic [210] direction. *b*, Among the three Cr species, Cr1 (red) form sparse honeycombs that are stacked between those of Cr2/Cr3 (purple/blue) with six-fold in-plane symmetry (*c*). *d*, Enhanced in-plane compressive strain at reduced thickness t , quantified by the relative change of the a lattice parameter via XRD for Cr_2Te_3 grown on $\text{Al}_2\text{O}_3(0001)$ (solid) or $\text{SrTiO}_3(111)$ (open). *f*, Schematic of the film stacks. Atomically resolved STM morphology (*e*) and planar HAADF STEM image (*g*) of Cr_2Te_3 confirm the honeycomb-like Te lattice and Cr sites (*h*). *i-m*, Cross-sectional images of Cr_2Te_3 films on $\text{SrTiO}_3(111)$. The HAADF (*i*) and iDPC (*j*) imaging. The enlarged view (dashed box region in *i*) of HAADF (*k*), DPC (*l*), and iDPC (*m*) images identify the random distribution of the interlayer Cr1 (circles), which deviates from the ideal Cr_2Te_3 structure with full occupancy.

Evidence of 1D propagating topological superconducting mode along edge of Fe(Te,Se)

Wenyao Liu¹, Gabriel Natale¹, and Kenneth S. Burch¹

¹ *Department of Physics, Boston College, Chestnut Hill, MA 024*

ks.burch@bs.edu (corresponding author)

liucnp@bc.edu (presenter)

Keywords: Superconductivity, Topology

The combination of topological surface states and superconductivity has paved a new way to realize exotic quasiparticle excitations, such as Majorana modes, which has stirred significant excitement in the condensed-matter physics. Recent works suggest that Fe(Te,Se) is a putative topological superconductor, hosting the 0D Majorana bound state as topological vortex modes [1]. Intriguingly, predictions also indicate the presence of high-order topological superconducting edge states in Fe(Te,Se) due to its unconventional sign-changing superconductivity and potential time-reverse-symmetry broken [2,3]. Here, we present evidence supporting the existence of a 1D propagating topological superconducting state in Fe(Te, Se). This conclusion is based on comprehensive transport measurements, Andreev-reflection spectroscopy, and specialized fabrication techniques. Firstly, our observations highlighted an anomalous perfect-Andreev-reflection (PAR) signal from contacts on the Fe(Te, Se) edge. In contrast, the signal from contacts on its bulk are still normal Andreev-reflection feature, hinting at a unique 1D mode along the edge. Furthermore, we determined that this PAR signal is absent in the absence of the topological surface state, suggesting that this edge mode is under the topological protection. Most critically, when we disconnect the edge channel linking the source and drain contacts, the PAR signal was extinguished, which confirms the ballistic transport channel's origin from the topologically protected edge state. Thus, our findings offer compelling evidence of the 1D propagating high-order topological superconducting mode in Fe(Te,Se).

[1] Wang, D. *et al.*, Science 362, 333–335 (2018).

[2] Zhang, R.-X. *et al.*, Phys. Rev. Lett. 122, 187001 (2019).

[3] Yan, Z. *et al.*, Phys. Rev. Lett. 121, 096803 (2018).

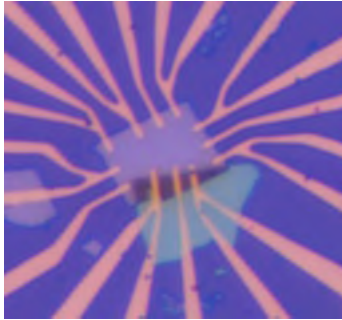


Fig.1: Color image of the exfoliated device.

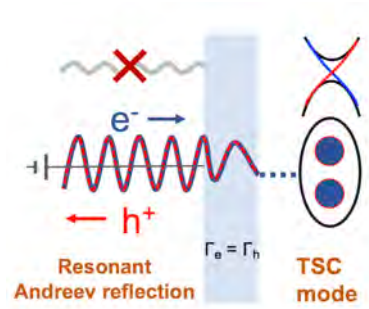


Fig.2: Perfect Andreev reflection through topological superconducting channel

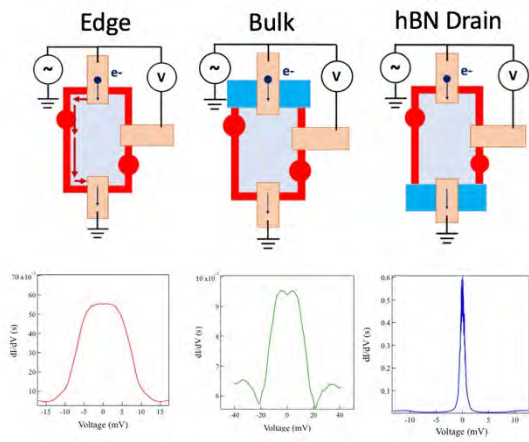


Fig.3: Contacts configuration and corresponding transport measurement. Left to right: topological edge channel case, bulk contacts case; topological edge channel disconnect case.

Multi-bit Operation in an MRAM Cell with a Composite Free Layer

V. Sverdlov^{1,2}, M. Bendra^{1,2}, N. Jorstad¹, B. Pruckner¹, T. Hadamek¹, W. Goes³, S. Selberherr¹

¹ Christian Doppler Laboratory for Nonvolatile Magnetoresistive Memory and Logic at the

² Institute for Microelectronics, TU Wien, Gußhausstraße 27-29/E360, 1040 Vienna, Austria

³ Silvaco Europe Ltd., Cambridge, United Kingdom

sverdlov@iue.tuwien.ac.at

Spin-transfer torque magnetoresistive random access memory (STT-MRAM) is nonvolatile, fast and scalable, possesses high endurance, and requires only a few additional masks for fabrication. The main element of an MRAM cell is a magnetic tunnel junction (MTJ) which is typically composed of a CoFeB reference layer (RL) and a free magnetic layer (FL) separated by an MgO tunnel barrier (TB). An MTJ with perpendicular RL and FL magnetization (pMTJ) reduces the cell footprint and increases the memory density. In advanced MRAM cells with a single-digit nanometer footprint, the perpendicular anisotropy is boosted by introducing an additional MgO TB along the FL and elongating the FL [1]. For modeling MRAM cells with a composite FL shown in Fig.1a, we employ the recently developed approach to evaluate spin torques in multilayered structures [2].

Fig.1b shows the FL magnetization switching from the anti-parallel (AP) to parallel (P) alignment of the FL and RL at a bias of 1.5V applied. The spin polarizations at the TBs between the RL and FL₁, and FL₁ and FL₂ are 0.6 and 0.5, respectively. Initially, the torques acting on FL₁ from the RL and FL₂ are additive. The FL₁ magnetization rapidly inverts, followed by a slower inversion of the one in FL₂. A plateau at $m_x = 0$ develops, confirming the composite FL's sequential switching [3]. Fig.2 demonstrates P to AP switching at -1.5V. For lengths of FL₁ = FL₂ = 5nm the magnetization reversal proceeds in the inverse order to that of AP to P switching (Fig.5, c1-c3). However, for shorter FLs, the magnetization returns to $m_x = 0$ at longer pulse durations. Fig.3 shows the magnetization at the final state for several lengths of FL₁ and FL₂. It indicates that, after achieving the AP state, FL₂ flips back to become AP to FL₁ (Fig.5, c4). This back hopping is due to the torque from FL₁ favoring the AP configuration of FL₁ and FL₂. The torque from FL₂ acting on FL₁ favors the P configuration of FL₁ and FL₂. However, this is counteracted by the torque from the RL on FL₁, and FL₁ remains AP to the RL and FL₂. To flip FL₁ (Fig.5, c5), one can increase the spin polarization of the TB in the FL to 0.9. Fig.4 demonstrates a cycling switching due to back hopping effect, at the *same voltage polarity*. Using the parasitic back hopping effect [4], a multi-bit operation in an MRAM cell with a composite free layer is achieved (Fig.6).

[1] B. Jinnai *et al.*, IEDM 2020, p.24.6.1.

[3]. S. Fiorentini WINDS 2022, p. 44.

[2]. S. Fiorentini *et al.*, Sci. Rep.**12**, 20958 (2022).

[4]. C. Abert *et al.*, Phys.Rev.Appl. **9**, 054010 (2018).

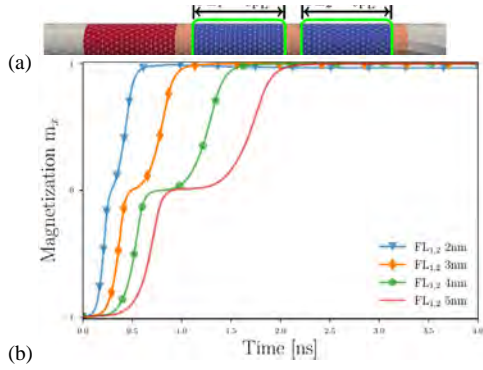


Fig.1: (a) MRAM cell with a composite elongated FL consisting of the two parts FL₁ and FL₂ separated by a TB. (b) AP to P switching for several FL lengths in a symmetric configuration (FL parts of the same length).

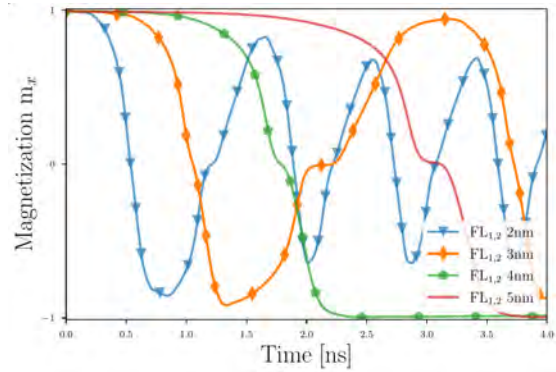


Fig.4: Cyclic magnetization switching for the same voltage polarity is achieved, if the polarization of the TB in the FL is increased to 0.9.

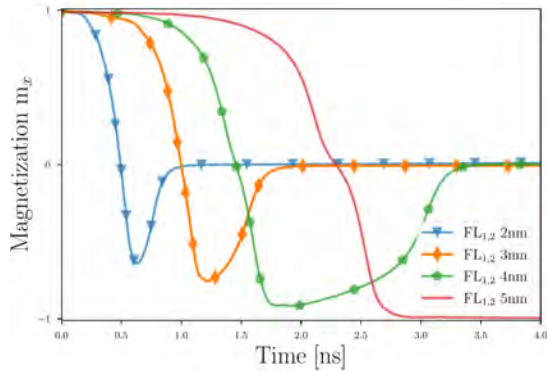


Fig.2: P to AP switching for several FL lengths in a symmetric configuration. For shorter FLs, the magnetization does not stay in AP configuration.

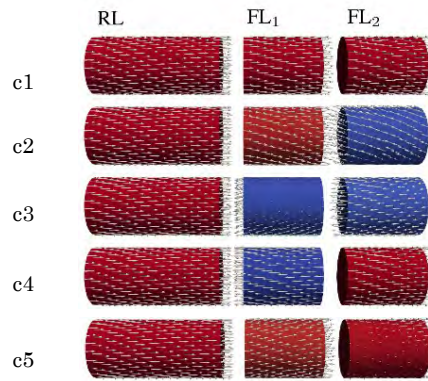


Fig.5 Snapshots of four logic states of the FL. The pin polarization of 0.9 at the FL tunnel barrier is larger than that at the barrier between RL and FL. The configuration c5 is equivalent to c1.

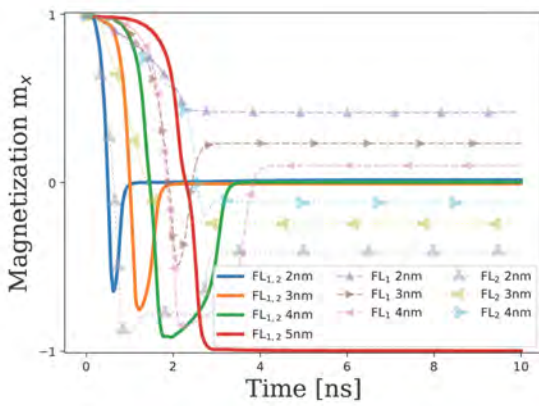


Fig.3: P to AP switching for asymmetric configuration. Except for FL₁=FL₂=5nm, the magnetization in the final state equals $(FL_2 - FL_1)/(FL_2 + FL_1)$ indicating FL₂ flipped to become P with RL.

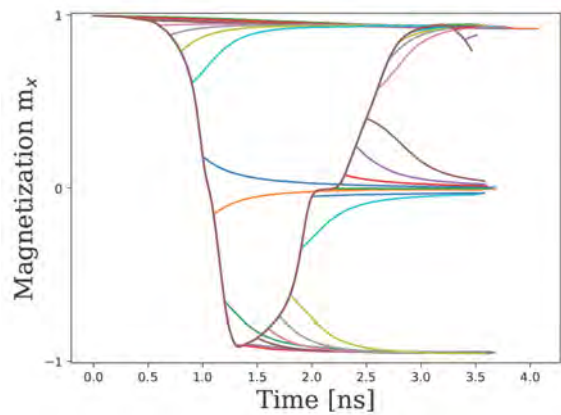


Fig.6: Magnetization state after a pulse of increasing duration is applied. The pulse increase is 0.1ns. A clear relaxation of the magnetization of the FL to four logic states is observed.

Electron Tunneling between Vibrating Cu Atoms in a Cu Filament in a Neuromorphic ReRAM Device

A. Chakraborty, M. Al-Mamun, and M. Orlowski,

*Bradley Department of Electrical and Computer Engineering, Virginia Tech
Blacksburg, Virginia 24061, USA, m.orlowski@vt.edu*

Keywords: electron atom-to-atom tunneling, quantum conductance, 1D & 2D contact interfaces, neuromorphic device & computing

Thermal cross-talk between neuromorphic ReRAM cells within a crossbar array (Fig. 1) can lead to either permanent or transient erasure of filaments in neighboring cells that have been programmed (Fig. 2). Additionally, the electric conductivity, facilitated by the conductive Cu filament (CF), might spontaneously recover [1] displaying quantum conduction effects. We attribute transient erasure and recovery to vibrations of Cu atoms in the CF, modulated by heat transfer. This phenomenon results in a modulation of electron tunneling effects, where the average tunneling distance between vibrating Cu atoms varies proportionally to \sqrt{T} (T abs. temperature). The Cu filament establishes either 1D or 2D contact (Fig. 3) with the driving Cu electrode within the TaO_x oxide, contingent on the robustness of the Cu filament. This filament and its 2D interface are modeled using a resistive network of individual Cu atoms (Fig. 4). A unit resistance of $R_0=1/G_0=h/(2e^2t)$ is assigned between two Cu atoms, where the quantum conductance G_0 follows Landauer's formula: $G_0=(2e^2/h)\times t$, and t represents the tunneling transmission probability between neighboring Cu atoms. For a weak CF, the cross-sectional area of the CF's constriction at the Cu electrode interface comprises only a small number of Cu surface atoms, ranging from 1 to 9. Our observations include temporary erasure of cells X_i and Y_i , followed by spontaneous recovery to a preset value. This recovery typically occurs within 50 to 100 s after the heating has ceased, see Fig. 5. Notably, Fig. 5(b) highlights that resistance decreases in distinct steps, corresponding electron tunneling in statistically distributed decreases in Cu atom oscillations. As temperature rises, the average tunneling distance increases, leading to a significant reduction in tunneling probability, and consequently, a marked increase in transient resistance. The manifestation of quantum conductance in memristive device is evident in Fig. 6. These neuromorphic devices have served as synapses, storing weight values from spiking neural networks with threshold functions for device activation. Mitigating cell-to-cell heat transfer has proven effective in minimizing cycle-to-cycle switching variations [2].

[1] M. Al-Mamun, M. Orlowski, "Electron Tunneling between Vibrating Atoms", Scientific Reports, 11:7413, 2021

[2] H. An, M. Al-Mamun, M. Orlowski, "3D Neuromorphic Computing with Memristive Synapses" IEEE Trans. Comp.-Aided Design Integrated Circuits. & Systems, 41, 400, 2022

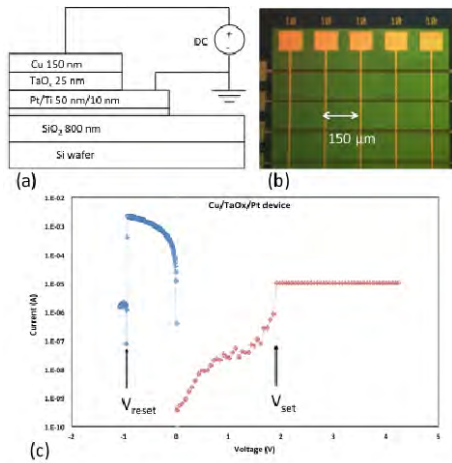


Fig.1: (a) Cross-sectional view of a Cu/TaO_x/Pt resistive switching cell with layer thicknesses indicated. (b) Optical microscope picture of an array of Cu and Pt lines with Cu/TaO_x/Pt cells at the intersections. (c) Typical switching cycle with set and reset operations with the threshold voltages V_{set} and V_{reset} respectively.

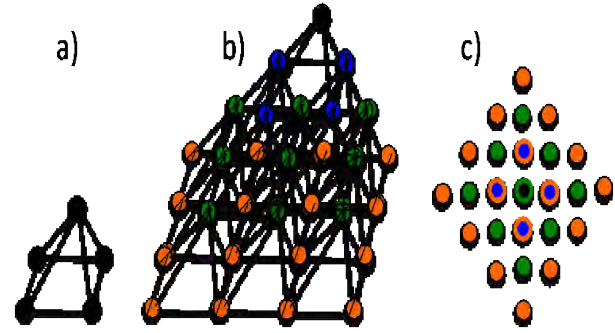


Fig.4: (a) Every Cu atom is connected to four Cu atoms in the next subjacent layer. Each connection between the Cu atoms corresponds to a unit resistance of $R_o=1/G_o$. (b) Pyramidal 3D resistor network with one atom at the top and three subjacent layers shown. (c) Projection of the pyramid on the plane of the base of the pyramid.

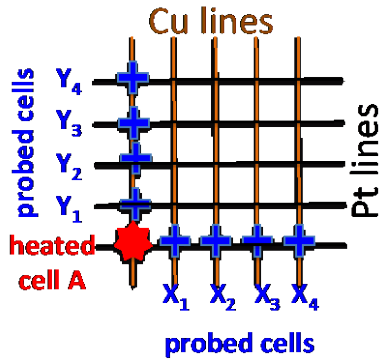


Fig.2: A memory array of Cu/TaO_x/Pt cells. The red cell A represents the heated cells by repeated set-reset cycles. Immediately after the heating of cell A has been completed the cells X_i and Y_j are tested to find their state of conductivity.

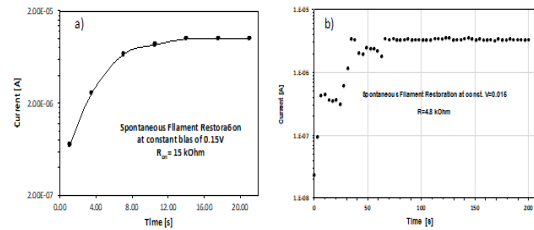


Fig.5: (a) evolution of the current through a preset X₁ cell to R_{on}=15kΩ at a constant bias of 0.150V just after the heating by cell A. (b) evolution of the current through a preset Y₁ cell to R_{on}=4.8 kΩ at a constant bias of 0.015V just after the heating by cell A.

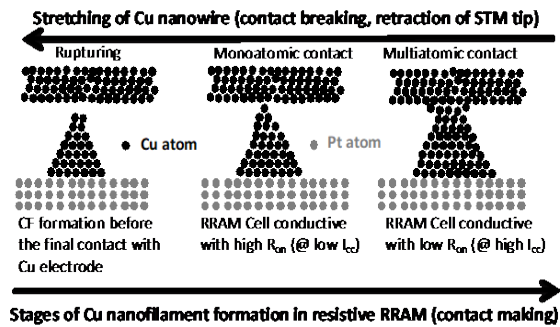


Fig. 3 Equivalency between making a monoatomic contact by elongation of an indented Cu wire in a free space and formation of a chain of Cu atoms in the matrix of a thin dielectric (TaO_x) in a neuromorphic ReRAM cell and a method for monoatomic 1D and 2D contact formation using STM. For both types of point contacts, quantum conductance in units $G_o=2e^2/h$ has been observed.

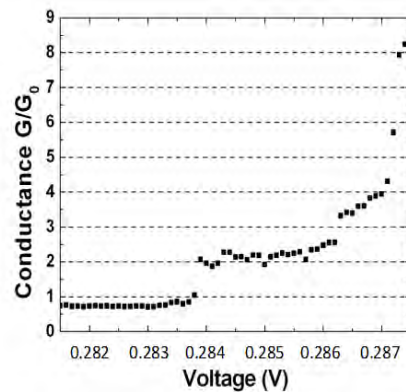


Fig.6: Quantum conduction observed in the I-V characteristic of Cu/TaO_x/Pt memory cells at room temperature. The sweep rate is 0.002 V/s allowing a high time resolution of the voltage sweep.

Experimental evidence of a novel mechanism of hole injection into quantum wells of long wavelength GaN-based LEDs

S. Marcinkevičius¹, R. Yapparov¹, J. Ewing², F. Wu², S. Nakamura², and J. S. Speck²

¹*Department of Applied Physics, KTH Royal Institute of Technology, AlbaNova University Center, 10691 Stockholm, Sweden*

²*Materials Department, University of California, Santa Barbara, California 93106, USA*
sm@kth.se

Keywords: wide-gap materials, nanostructures

GaN-based RGB (red-green-blue) lighting is expected to have more functionalities and higher efficiency than traditional blue LED and phosphor devices. For that, efficient green and red LEDs are required. In such LEDs the InGaN/GaN quantum wells (QWs) are deep, which prevents thermionic hole transport across the QWs [1]. Thus, carrier distribution in the multiple QWs of the LED active region is expected to be nonuniform. Highly populated QWs on the *p*-side of the device would experience an increased nonradiative Auger recombination reducing the overall LED efficiency. Nevertheless, an exceptionally high wall plug efficiency (WPE) of ~30% for yellow LEDs has recently been reported [2]. It has been suggested [3] that the high WPE is related to the carrier injection into all QWs of the active region via semipolar QWs located at the $\{10\bar{1}1\}$ facets of the hexagonal V-defects that terminate threading dislocations. Experimentally, though, such an injection mechanism has not been confirmed.

In this work, we have tested existence of this V-defect injection mechanism by electroluminescence (EL) and time-resolved photoluminescence (TRPL) measurements on a specially-designed green LED. In the device, the QW furthest away from the *p*-side was deeper and served as an optical marker for injected electron-hole pairs. Strong EL from the marker well confirmed that, indeed, the holes were injected into this QW, which could only take place via the sidewall semipolar QWs. In addition, TRPL transients for the marker QW did not possess the slow PL rise component, which is an indicator of the thermionic carrier transport from the top GaN layer across the QWs [1], confirming that the vertical interwell transport did not take place. Thus, unlike the direct interwell transport by thermionic emission, the transport via the V-defects allows populating all QWs of the active region in spite of the high potential barriers in long wavelength InGaN/GaN QWs.

[1] S. Marcinkevičius *et al.*, Appl. Phys. Lett. **114**, 151103 (2019).

[2] F. Jiang *et al.*, Photonics Res. **7**, 144 (2019).

[3] C. H. Ho, J. S. Speck, C. Weisbuch, and Y.-R. Wu, Phys. Rev. Appl. **17**, 014033 (2022).

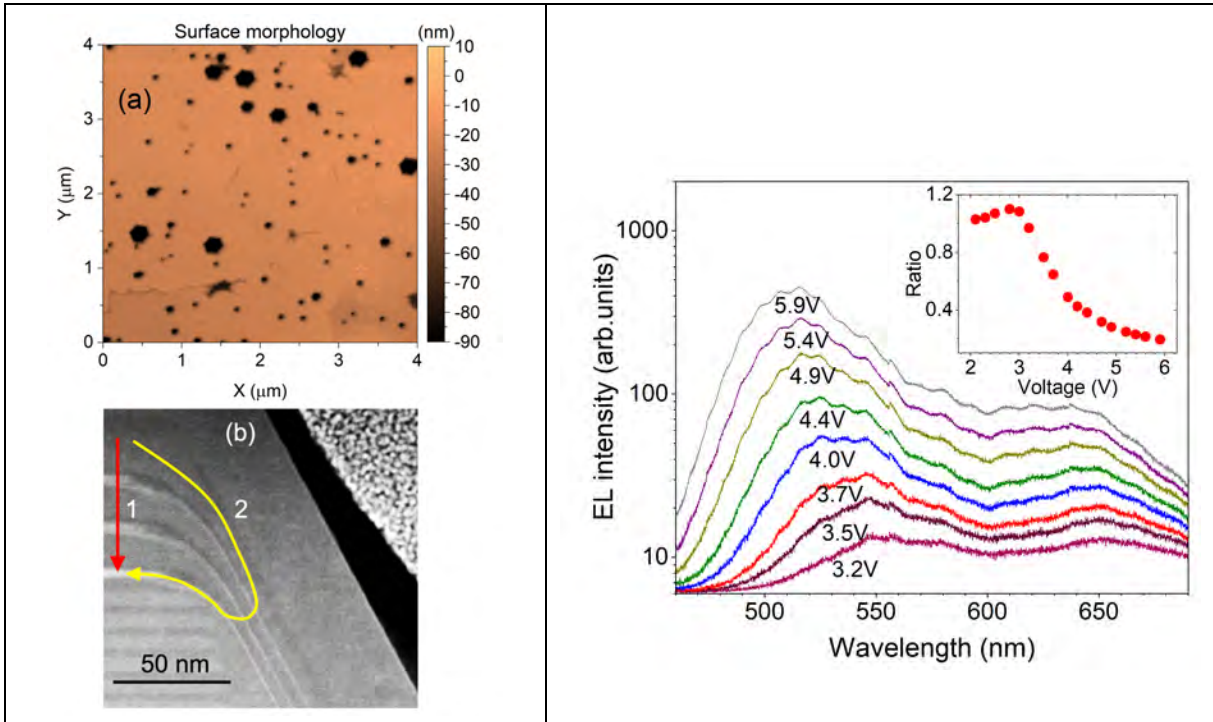


Fig.1: Atomic force microscopy (AFM) image of the LED structure displaying small and large hexagonal V-defects (a). High angle annular dark field scanning transmission electron microscopy (HAADF-STEM) image of the structure in the vicinity of a large V-defect with schematically illustrated paths of the hole transport toward the detector QW (DQW) directly across the green QWs (1), and via semipolar QWs at the V-defect facets (2) (b).

Fig.2: EL spectra at different bias voltages. The peak at 500-550 nm corresponds to the emission of the regular QWs, and the peak at 650 nm – of the DQW. The inset shows the integrated EL intensity ratio between the green QWs and DQW as a function of bias.

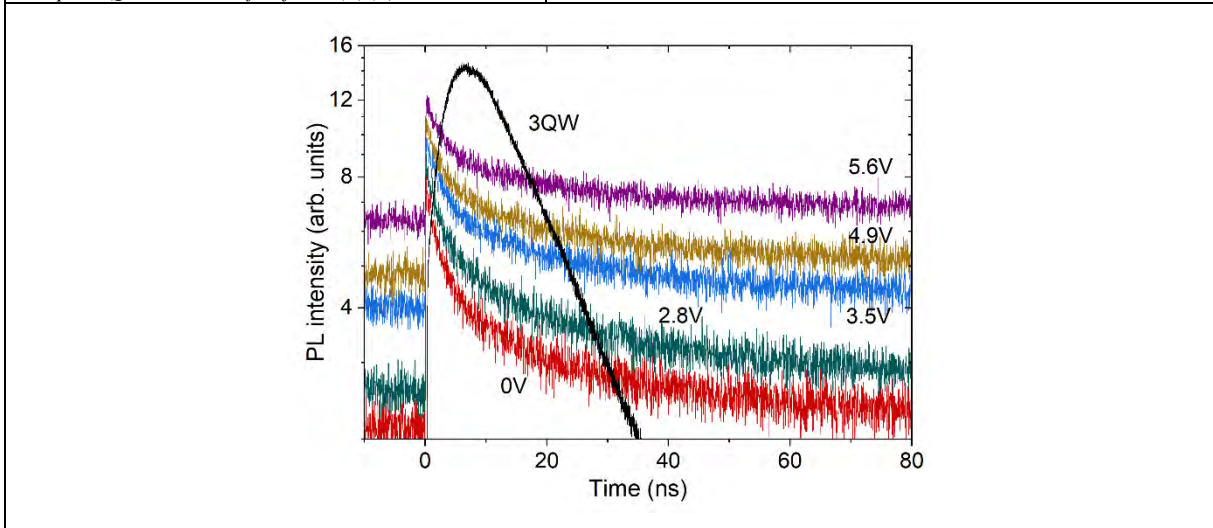


Fig.3: Detector QW PL transients at different biases. The black curve labelled 3QW is for the DQW PL of a structure containing three $In_{0.12}Ga_{0.88}N/GaN$ QWs [1].

New Method for Improving Al Void and Refresh Characteristics in sub 25nm DRAM

Dongsik Park^{1,2}, Byoungdeog Choi¹

¹*Department of Semiconductor and Display Engineering, Sungkyunkwan University, Suwon-Si, Gyeonggi-do 16419, Korea, Republic of (South)*

²*Samsung Electronics Co., Hwaseong-si, Gyeonggi-do 18448, Korea, Republic of (South)*
bdchoi@skku.edu

Keywords: DRAM, Al Void, Double Depo Aluminum, static refresh

Over the recent years, scaling down of design rule appears to face serious limitations such as void issues originated from the shrink of aluminum metal line in DRAM product. Various stress issues from the drastic changes of the surrounded insulating layer and the process steps affect the grain size of aluminum metal layers, these can lead to the severe void problems during its high temperature process of 300~400°C as shown in Fig. 1 [1], [2]. In order to resolve the Al void formation originated from the severe stress issues, Double Depo Aluminum (DDA) layer process is proposed. This novel metallization process can be effectively and simply performed with the native oxide such as Al₂O₃ between the upper and lower Al metal layer by ex-situ deposition technique. (Fig. 3). The Al voids was induced by controlling the temperature of the following HDP deposition. As shown in Fig. 4-(a), it was difficult to identify any big differences of Al void formation compare to our previous metal line formation process with top view SEM images. However, from the TEM image of this void containing point, no Al void can be observed at the area of lower Al layer beneath the thin Al-oxide layer and also we can suppose the current flows through the lower layer. Table.1 shows that the DDA process has excellent Al void immunity against temperature stress of following process. There is a trade-off relationship between Ti thickness and static refresh characteristics of DRAM. However, by adapting DDA process, significant improvement of Al void issues have been verified with no additional increase of its barrier metal thickness. Fig.5 shows the comparison of the median values of static-refresh failure bits of each die in wafer as a function of the barrier-metal thickness. The static-refresh characteristics is improved by almost 20% by using DDA process with 100Å –Ti thickness. This result clearly explains that our DDA process is easier and effective method for improving both Al voids and static refresh characteristics than that of conventional process

[1] Heryanto, A., et al. "The effect of stress migration on electromigration in dual damascene copper interconnects." *Journal of Applied Physics*, Vol. 109, No. 1 (2011), p 013716. doi:10.1063/1.3531393

[2] Suzuki, A., et al. "A strategy using a copper/low-k BEOL process to prevent negative-bias temperature instability (NBTI) in p-MOSFETs with ultra-thin gate oxide." 2002 Symposium on VLSI Technology. Digest of Technical Papers, IEEE, Honolulu, HI, August 2002, p 216-217. doi:10.1109/VLSIT.2002.1015458

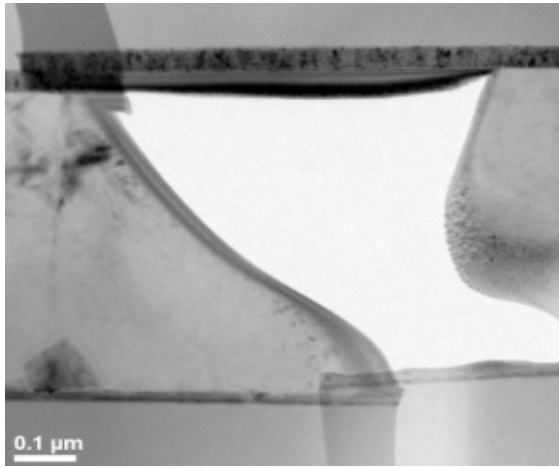


Fig.1: TEM image of voids in Al metal-line in DRAM products.

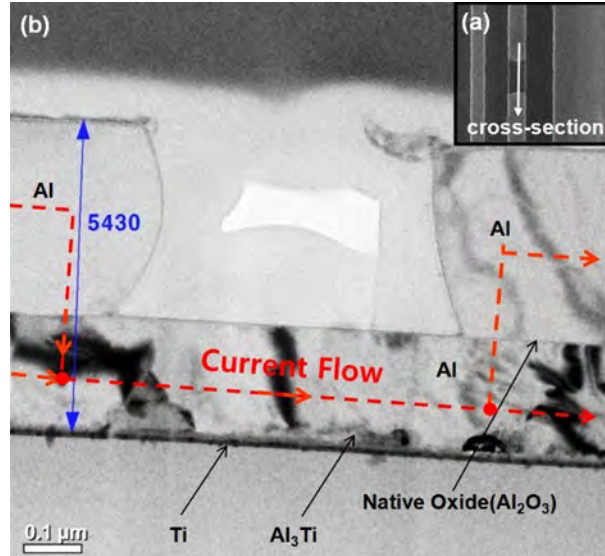


Fig.4: (a) Top view SEM image and (b) cross-sectional TEM images of Al void caused by intentional temperature stress with the DDA process.

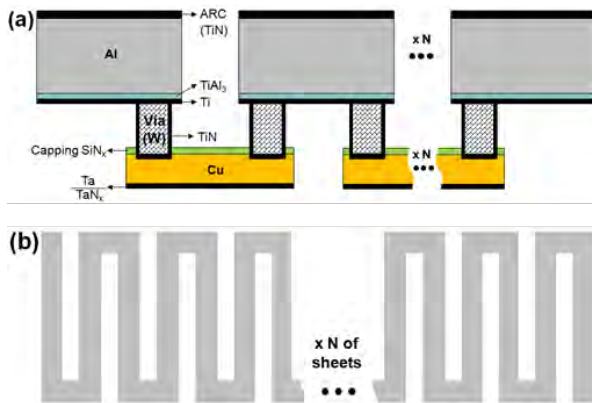


Fig.2: Structures of TEG's for evaluating the resistance of Al metal-lines. : (a) Via contact string in vertical view and (b) Continuous 'line & space' pattern in top view layout.

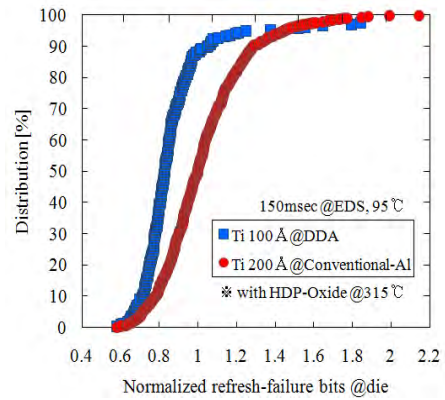


Fig.5 Distributions of static-refresh failure bits in wafer level with different barrier-metal Ti thickness and Al deposition process.

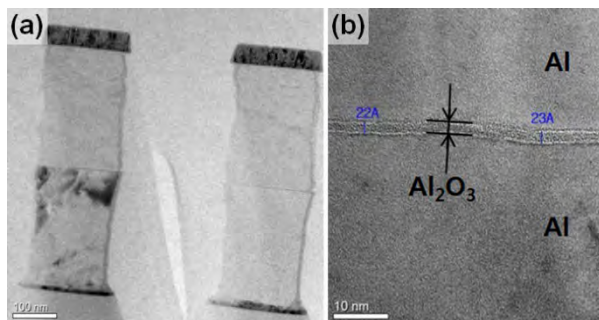


Fig.3: Cross-sectional TEM images of Al formed by the DDA process. : (a) vertical view and (b) magnified view of the interface between the upper and the lower Al layer.

wafer temperature *(chuck cooling gas pressure : inner/outer-area [ton])		335 °C *(5/7)	315 °C *(7/9)	276 °C *(10/12)	268 °C *(11/13)	260 °C *(12/14)
No. of failed dies	conventional	0	0	0	0	243
	DDA	0	0	0	0	124

Table.1 Failed-dies comparison on EDS representing voids.

A novel technology for edge patterning in processes using SOH masks in sub-20nm DRAM

Minhyung Kim^{1,2}, Yunseok Kim¹

¹School of Advanced Material Science and Engineering, Sungkyunkwan University, Suwon-si, 440-746, Republic of Korea

²Samsung Electronics Co., Hwaseong-si, Gyeonggi-do 18448, Republic of Korea

E-mail: kimmh9009@gmail.com

Keywords: nanostructures

Abstract

With the development in the semiconductor integration, the width of circuit line has been decreased. Correspondingly, it is necessary to create narrow and deep pattern. In particular, LP (landing pad) is one of the smallest patterns in DRAM and it serves to connect the GBC (gate buried contact) and capacitor. As shown in Fig.1. hard mask is used to create LP pattern under photoresist. However, because SOH (spin on hard masks) is deposited using a rotating manner, the thickness at the wafer edge becomes thicker especially for 300mm wafer. With the conventional etching method, SOH remains on the wafer edge even after etching. It makes the LP patterns stick together as described in Fig.3. It has a big impact on yield loss. To address this issue, we employed a technology for controlling the gas flow rate at the edge of the gas plate as shown in Fig.4. Without changing the flow rate of the inner part, we increase the O₂ gas flow rate at the edge of the plate and strengthen the reaction. Simultaneously, we introduce a sidewall passivation technique using C₄F₈ gas to prevent the unintended reduction of LP pattern caused by excessive SOH etch (see Fig.5). As a result, it can reduce the failure rate of LP pattern as shown in Fig.6. and attained the same pattern as the inner pattern without side effects.

Reference

[1] Park, J.M., et al. "20nm DRAM: A new beginning of another revolution." 2015 IEEE International Electron Devices Meeting IEDM. IEEE, 2015.

[2] Hwang, Yoosang, et al. "An overview and future challenges of high-density DRAM for 20nm and beyond." Proceedings of the Extended Abstracts of the 2012 International Conference on Solid State Devices and Materials, Kyoto, Japan. 2012.

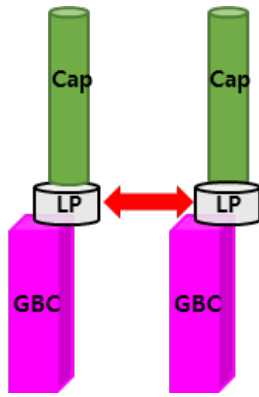


Fig.1: LP serves as a connection between the GBC and the Capacitor structure in DRAM

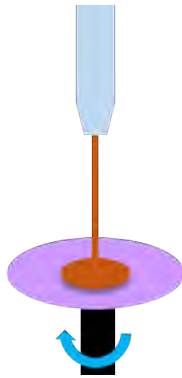


Fig.2: SOH is coated using the spin-coating method

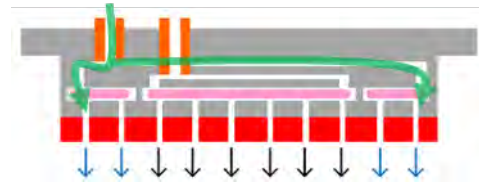


Fig.4: Edge gas control by using gas plate

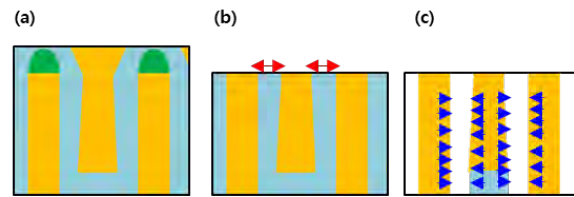


Fig.5: SOH mask etch profiles (a) During SOH mask etching (b) SOH etch enhancement region (c) Passivation region

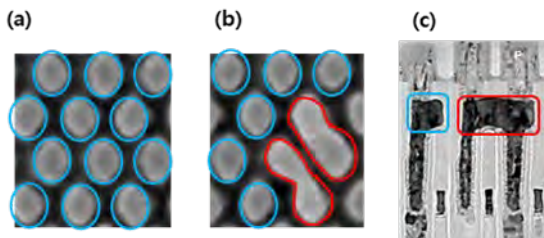


Fig.3: Wafer edge LP pattern attached to another cell: (a) Good region (b) Defective region (c) Vertical view.

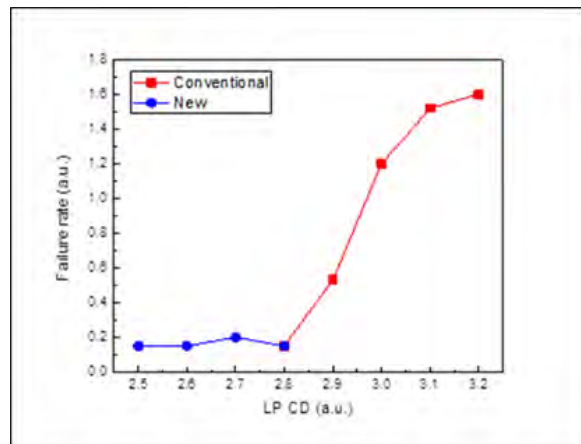


Fig.6: Reduced rate of failure through new technology

